Cophasing LINC-NIRVANA
and
Molecular gas in low-luminosity QSO host and cluster galaxies

INAUGURAL-DISSERTATION

zur

Erlangung des Doktorgrades

der Mathematisch-Naturwissenschaftlichen Fakultät

der Universität zu Köln

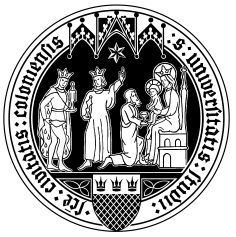

vorgelegt von

Thomas Bertram
aus Köln

Köln 2007

Berichterstatter: Prof. Dr. A. Eckart
Prof. Dr. J. Jolie

Tag der mündlichen Prüfung: 24. Oktober 2007

Abstract

This thesis consists of two parts. The first part reports on the development of a fringe tracking system for LINC-NIRVANA, the near-infrared homothetic imaging camera for the Large Binocular Telescope (LBT). LINC-NIRVANA allows for a coherent combination of the light entering the two primary mirrors. The fringe pattern in the focal plane is required to be stable in time to preserve the high spatial frequency information in long exposure images. Atmospheric differential piston causes the position of the fringes to change with time. A fringe tracker is a servo system that measures and corrects for atmospheric differential piston in real-time. In the first part, numerical simulations of atmospheric turbulence are used to investigate the problem of angular anisoplanatism of differential piston. The fringe tracking concept and the top-level requirements are introduced, followed by a presentation of the mechanical design of the system. This design includes a solution for a device that is capable of positioning a detector with high precision within a cryogenic environment. A fitting algorithm determines the amount of differential piston in the point-spread function of a reference target. The performance of this algorithm under different signal-to-noise conditions is investigated. First polychromatic fringes obtained with a testbed interferometer conclude the first part.

Measurements of millimeter CO transitions in extragalactic targets are the basis for the two observational studies in the second part of this thesis. The molecular gas content in low-luminosity QSO host galaxies is investigated and discussed together with far-infrared data. Unlike in most published studies, a far-infrared selection criterion was not applied. It is shown that the majority of low-luminosity QSO host galaxies is rich in molecular gas. These objects show different CO emission properties, depending on their central activity. The second study deals with a potential dependency of the molecular gas content in cluster galaxies on their distance to the center of the cluster. A deficiency of molecular gas in galaxies that are located in the vicinity of the center is indicated in a sample of Abell 262 galaxies. A model is presented that predicts a drop of gas and dust and explains it with the stripping of cirrus-like clouds.

Zusammenfassung

Die vorliegende Dissertationsschrift dokumentiert Arbeiten auf zwei der Astronomie zugeordneten Gebieten: der Entwicklung von astronomischer Instrumentierung und der beobachtenden Astrophysik. Dabei kamen unterschiedliche Methoden zur Anwendung, unter anderem numerische Simulationen, Systemanalysen, mechanische Konstruktion, Software-Entwicklung, Messungen und Tests im Labor, aber auch Beobachtungen mit Teleskopen, die Analyse der gewonnenen Daten sowie deren astrophysikalische Interpretation. Wie der Titel bereits nahelegt, besteht die Dissertation aus zwei Teilen, die jeweils eines der beiden Gebiete repräsentieren.

Der erste Teil befasst sich mit der Entwicklung eines sog. "Fringe Trackers" für LINC-NIRVANA; einem Nahinfrarot Kamerasystem, welches am "Large Binocular Telescope (LBT)" zum Einsatz kommen und dort die Möglichkeiten der interferometrischen Überlagerung von Licht, die das Teleskop bietet, voll ausnutzen wird. Diese Kamera wird, sobald sie den Betrieb aufgenommen hat, eine bisher unerreichte Kombination aus hoher Winkelauflösung, hoher Sensitivität und großem interferometrischen Bildfeld bieten. Um eine effiziente Nutzung sicherstellen und lange Integrationszeiten ermöglichen zu können, ist der Einsatz eines Fringe Trackers unerlässlich. Dieses Subsystem der Kamera unterdrückt mit Hilfe eines geschlossenen Regelkreises die durch die Atmosphäre verursachte ständige Bewegung des Interferenzmusters in der Bildebene der Kamera. Erfolgt diese Unterdrückung nicht, so geht bei längeren Integrationszeiten der Gewinn an Winkelauflösung verloren, der mit Hilfe der interferometrischen Überlagerung gegenüber herkömmlichen optischen Großteleskopen erzielt wird. Die Arbeit am Fringe Tracker umfasst, von der konzeptionellen über die detailliertere Entwurfsphase bis hin zum Test von ersten Hard- und Softwarekomponenten, alle bisher durchlaufenen Phasen des Projektes. Leider sind noch einige Schritte zu gehen, bevor LINC-NIRVANA am LBT die ersten stabilen Interferenzmuster produzieren kann (derzeit geplant für 2010).

Der zweite Teil der Dissertation präsentiert Studien über die Menge molekularen Gases in Galaxien, die Quasistellare Objekte (QSO) in ihren Zentren beheimaten, und über die Menge molekularen Gases in ausgewählten Galaxien des Galaxienhaufens Abell 262. Diese Studien basieren auf Messungen von CO-Übergängen im Millimeter-Wellenlängenbereich, die mit verschiedenen Teleskopen, in einem Fall auch mit einem lokalen Interferometer, durchgeführt wur-

den. Die Wechselwirkung zwischen Galaxien, die häufig gerade auch in Galaxienhaufen beobachtet werden kann, und das QSO-Phänomen sind möglicherweise miteinander verknüpft in einer evolutionären Sequenz. Um diesen potentiellen Zusammenhang aber genauer studieren zu können, bedarf es, in jedem zu untersuchenden Wellenlängenbereich, Beobachtungsmöglichkeiten mit hoher Winkel-auflösung und großem Bildfeld. LINC-NIRVANA wird im nahinfraroten Bereich über diese geforderten Qualitäten verfügen.

Die Kapitel 1 und 4 enthalten einleitende Informationen zu den beiden Teilen der Arbeit. Folgende Aspekte werden in den Kapiteln 2, 3, 5 und 6 behandelt:

Kapitel 2: Simulationen atmosphärischer Turbulenzen

Der Fringe Tracker analysiert das Licht einer Punktquelle, um den variablen Phasenversatz zwischen den beiden Armen des Interferometers bestimmen und kompensieren zu können. Wenn das zu beobachtende Objekt und die als Phasenreferenz dienende Punktquelle nicht identisch sind und einen Winkelabstand zueinander besitzen, so propagieren die Wellenfronten der beiden Quellen durch teilweise unterschiedliche Bereiche der Atmosphäre und erfahren damit unterschiedliche Störungen, bevor sie das Teleskop erreichen. Sobald ein gewisser Winkelabstand überschritten ist, kann die Information über den Phasenversatz in Richtung der Referenzquelle nicht mehr als repräsentativ für die zu beobachtende Quelle angesehen werden. In dieser Studie werden Simulationen der turbulenten Atmosphäre dazu verwendet, den Bereich einzugrenzen, innerhalb dessen die Dekorrelation der Phaseninformation zwischen zwei Punkten unterhalb einer bestimmten Toleranzschwelle bleibt. Verschiedene Atmosphären-Bedingungen werden dazu simuliert. Außerdem wird gezeigt, dass die Verwendung der Adaptiven Optik von LINC-NIRVANA einen positiven Einfluss auf die Größe dieses Bereiches haben kann.

Eines der meistuntersuchten Objekte ist das Galaktische Zentrum. Aufgrund seiner südlichen Koordinaten ist es kompliziert, dieses Objekt mit dem LBT zu beobachten. Im hinteren Teil des Kapitels wird anhand einer Simulation gezeigt, dass es sich unter bestimmten Umständen trozdem lohnt, solche Beobachtungen durchzuführen. Die Simulation lässt vermuten, dass eine Strehl-Verteilung von 10% - 15% erzielbar ist.

Kapitel 3: Der Fringe Tracker für LINC-NIRVANA

Der Fringe Tracker ist ein Servo-System, welches den variierenden Phasenversatz in Echtzeit misst und kompensiert. Die zur Messung benötigte Analyse der Punktquelle beinhaltet die Anpassung eines analytischen Modells des Inter-

ferenzmusters an das Profil der Punktverteilungsfunktion. Zur Aufnahme der Punktquelle dient ein Nahinfrarotdetektor, der der Trajektorie der Quelle in der Fokalebene folgen muss. Die Positionierung muss dabei innerhalb einer kryogenen Umgebung präzise (auf 5 μm genau) und über eine relativ große Strecke hinweg (30 cm) erfolgen. Es wird in diesem Kapitel das Konzept des Fringe Trackers für LINC-NIRVANA dargestellt, die wesentlichen Anforderungen an das System erläutert und das mechanische Design mit der avisierten Lösung der Positionierungs-Problematik vorgestellt.

Fehler des Messalgorithmus wirken sich direkt auf die Gesamt-Fehlerbilanz des Systems aus. Die Verhalten des Messalgorithmus bei verschiedenen Signal-zu-Rauschen Verhältnissen und bei verschiedenen Wellenlängen wird in diesem Kapitel dargestellt. Um Erfahrungen im Umgang mit einem Fringe Tracker zu sammeln, bevor das System letztendlich am Teleskop installiert wird, wurde ein Interferometer im Labor realisiert. Dieses ermöglicht die Erzeugung eines Interferenzmusters, das dem des LBTs entspricht. Phasenversatz-Sequenzen können vorgegeben werden, um atmosphärische Turbulenz zu simulieren. Alle Komponenten, die für ein Servosystem notwendig sind, sind ebenfalls vorhanden. Am Ende dieses Kapitels wird der Aufbau erläutert und die ersten mit diesem Testaufbau erzeugten polychromatischen Interferenzmuster gezeigt.

Kapitel 5: Molekulares Gas in nahen, QSO umgebenden Galaxien

Es werden die Ergebnisse einer Studie über die globalen Eigenschaften des molekularen Gases in einer Stichprobe aus Galaxien, die ein QSO beherbergen, dargestellt. Ein großes Gas-Reservoir ist notwendig, um die Leuchtkraft sowohl des aktiven Kerns als auch der den Kern umgebenden massiven Sternentstehungsregionen zu unterhalten. Nahe, relativ leuchtschwache QSO sind gut geeignet, um die sie umgebende Galaxie näher zu untersuchen. Eine Stichprobe dieser Objekte wurde ausgewählt, die nicht auf einem Infrarot-Auswahlkriterium basiert. Alle Objekte stammen aus dem Hamburg-ESO Katalog heller QSO und ihre Rotverschiebungen sind jeweils kleiner als z = 0.06.

Zwei CO-Übergänge wurden mit dem IRAM 30 m Teleskop gemessen. In 27 von 39 Galaxien wurde CO nachgewiesen – und Massen molekularen Gases im Bereich von $0.4 \cdot 10^9 M_\odot$ bis $9.7 \cdot 10^9 M_\odot$ berechnet. Der Vergleich der CO- mit den Ferninfrarot-Leuchtkräften lässt zwei Trends mit unterschiedlicher Steigung erkennen: ein Potenzgesetz, welches die Seyfert I Population mit geringer Aktivität beschreibt und eines, welches die leuchtstarken QSO repräsentiert. Diese Trennung ist möglicher Weise das Resultat unterschiedlicher Kompaktheit der Emmissionsregionen. Ein einfaches Modell, welches die beiden Fälle beschreibt, wird in diesem Kapitel vorgeschlagen.

Kapitel 6: Verlust von molekularem Gas in Abell 262?

Spiralgalaxien, die sich im Zentrum eines galaxienreichen Clusters befinden, weisen eine, verglichen mit isolierten Galaxien gleichen Typs, geringere atomare Gasmasse auf. Dieser Umstand ist ein klarer Hinweis auf das Vorhandensein von Wechselwirkungen zwischen der interstellaren Materie der Galaxien auf der einen und des intra-cluster Mediums auf der anderen Seite. Molekulares Gas hingegen wird in wesentlich geringerem Maße von solchen Mechanismen beeinflusst. Das liegt an der höheren Konzentration des molekularen Gases im zentralen Teil der Galaxie und der stärkeren gravitativen Bindung. In diesem Kapitel wird, anhand der Beobachtungsdaten von 24 Galaxien des Abell 262 Clusters, trotzdem ein Zusammenhang zwischen molekularer Gasmasse und Abstand zum Zentrum des Clusters diskutiert. Die Messungen des ^{12}CO(1−0) Übergangs wurden mit dem IRAM 30 m Teleskop, dem Onsala 20 m Teleskop und dem Nobeyama 45 m Teleskop durchgeführt. Ein möglicher Verlust molekularen Gases der Galaxien im Zentrum des Clusters wird mit einem Modell in Zusammenhang gebracht, bei dem weniger stark gebundene cirrusartige Molekülwolken durch Interaktion verloren gehen.

Zusätzlich zu den Messungen der globalen Gaseigenschaften der Stichprobe wurde exemplarisch für eine Galaxie auch die Verteilung des Gases mit Hilfe interferometrischer Beobachtungen untersucht. In diesem Fall war es möglich, neben der zentralen Konzentration des Gases auch eine weitere Quelle nachzuweisen.

Contents

CHAPTER 0

Overview

Work in two fields of activity in astronomy is presented in this thesis: in instrumentation and in observational astrophysics. A variety of different methods were applied in the present studies, including numerical simulations, system analyses, mechanical engineering, software development, laboratory work, but also astronomical observations, data reduction, and their interpretation in extragalactic contexts. As its title already suggests, the thesis is divided into two parts, each representing one of the two branches.

The first part reports on the development of a fringe tracking system for LINC-NIRVANA, a near-infrared imaging camera for the Large Binocular Telescope (LBT). Once operational, it will provide an unprecedented combination of angular resolution, sensitivity and field of view, achieved through a coherent combination of the light that is collected by the two primary mirrors. To operate this interferometer in an efficient way a fringe tracker is mandatory. The task of this cophasing system is to assure a time-stable interference pattern in the focal plane of the camera. If this is not given, any gain in resolution compared to current optical telescopes is lost in long exposure images. The work on the fringe tracker covered all phases, starting at the conceptual level, followed by a design phase and the realization and testing of first hard- and software components. Unfortunately, there are still many steps to take before cophased imaging with LINC-NIRVANA at the LBT will take place (current schedule: 2010).

In the second part, studies are presented on the molecular gas content in the host galaxies of nearby low-luminosity quasistellar objects (QSOs) and in the members of the galaxy cluster Abell 262. These studies are based on observations of millimeter CO transitions, carried out with several single dish telescopes, and in one case also with a local telescope array. Galaxy interaction, which is commonly observed in clusters of galaxies, and the QSO phenomenon are potentially linked in an evolutionary sequence. Detailed studies in either the near-infrared or the mm wavelength domain, however, require data with a combination of exceptionally high angular resolution and large field of view – such a combination will be provided in the near-infrared by LINC-NIRVANA.

Chapters 1 and 4 contain more detailed introductions into the two parts of the thesis. The following aspects will be discussed in the corresponding chapters:

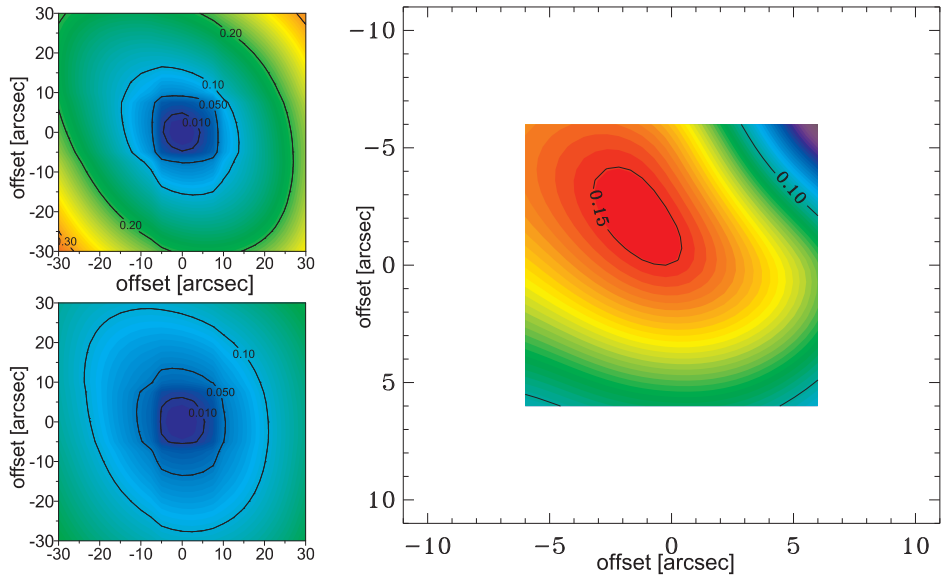

Left: The size of the isopistonic patch increases with the use of LINC-NIRVANA's adaptive optics (contours in λ). Right: Strehl map of the Galactic Center region (contours in %).

Chapter 2: Simulation of atmospheric turbulence

A fringe tracker uses the light of a point source as reference to determine and compensate for varying phase offsets between the arms of an astronomical interferometer. If science target and the fringe tracking phase reference are not identical and exhibit a certain angular separation, then their wavefronts partially travel through different regions of the atmosphere and experience different perturbations. If the angular separation is large, the phase distributions related to the two directions may not any longer be correlated. In this case the phase offset obtained for the reference source is not representative for the phase offset in direction of the science target. The presented study uses simulations of atmospheric turbulence to investigate the size of the region (the isopistonic patch) in which the correlation remains at an acceptable level. The influence of different atmospheric conditions is simulated. Moreover, it is shown, that the adaptive optics systems, which are part of LINC-NIRVANA, improve this size.

One of the most intensely studied objects is the Galactic Center. It is difficult to observe from the LBT site. In the second part of the chapter, a simulation of a potential observation with LINC-NIRVANA is presented. Under certain conditions, such observations can indeed be fruitful, despite the northern latitude of the LBT. A simulated Strehl map indicates that about 10% - 15% of flux concentration of a diffraction limited telescope is achievable.

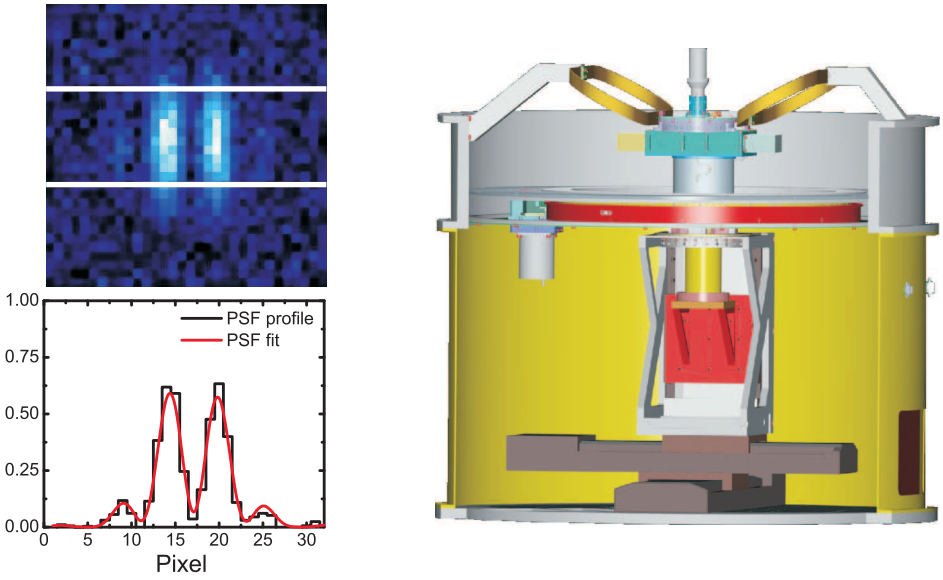

Left: A profile of the point-spread function is used to determine phase offsets. Right: The cryo–ambient mechanical design of the fringe tracking system

Chapter 3: Cophasing LINC-NIRVANA

The fringe tracker of LINC-NIRVANA is a real-time servo system. To sense varying phase offsets, it fits an analytic model to the profile of the point-spread function of the reference star. A near-infrared focal plane array detector has to be placed at the position of the point source in the field of view and has to follow its trajectory as the field rotates. The detector has to be moved with high precision over large distances (30 cm) within a cryogenic environment. This chapter introduces the concept of the fringe tracking system for LINC-NIRVANA, discusses the top-level requirements and presents its mechanical design, including the solution for the detector positioning problem. Measurement errors of the phase offset directly effect the error budget of the system. The performance of the fitting algorithm is investigated for different signal-to-noise conditions and different combinations of science and fringe tracking wavelength.

A testbed interferometer was set up, to obtain hands-on experience before going to the telescope. It allows to generate point-spread functions that are similar to the LBT case. Defined, fast varying phase offsets can be introduced to simulate different atmospheric conditions. All components of a servo loop are also included. In this chapter the setup and first polychromatic fringes are presented.

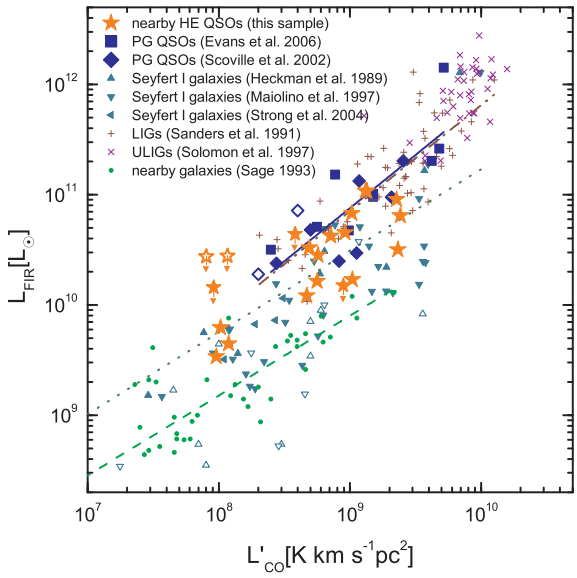

Far-infrared luminosity versus CO luminosity of galaxies with different levels of activity.

Chapter 5: Molecular gas in nearby QSO host galaxies

This chapter addresses the global molecular gas properties of a representative sample of galaxies hosting low-luminosity QSOs. An abundant supply of gas is necessary to fuel both the active galactic nucleus and any circum-nuclear starburst activity of QSOs. Nearby low-luminosity QSOs are ideally suited to study the properties of their host galaxies because of their higher frequency of occurrence compared to high-luminosity QSOs in the same comoving volume and because of their small cosmological distance. A sample of nearby low-luminosity QSO host galaxies was selected that is free of infrared excess biases. All objects are drawn from the Hamburg-ESO survey for bright UV-excess QSOs and their redshifts do not exceed z=0.06.

Two CO transitions were observed with the IRAM 30 m telescope. The observations and results are presented in this chapter. Twenty-seven out of 39 galaxies in the sample have been detected. Their molecular gas masses range from $0.4 \cdot 10^9 M_\odot$ to $9.7 \cdot 10^9 M_\odot$. When comparing the far-infrared with the CO luminosities, the distribution can be separated into two different power-laws: one describing the lower activity Seyfert I population and the second describing the luminous QSO population. The separation may be explainable with differing degrees of compactness of the emission regions. A simple model is provided that describes the two power-laws.

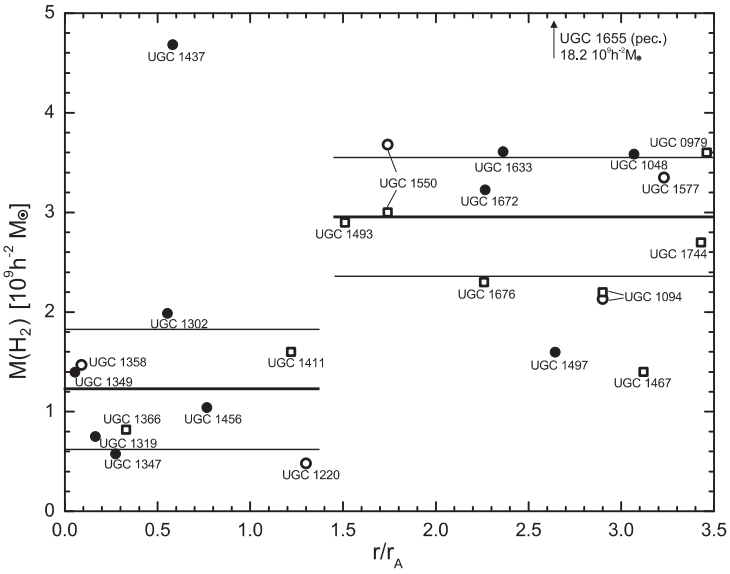

Molecular gas content of Abell 262 galaxies as function of the projected distance to the center of the cluster.

Chapter 6: Molecular gas stripping in Abell 262?

Strong evidence of interaction between the interstellar medium of galaxies and the intra-cluster medium is the lack of atomic gas in those spiral galaxies that are located in the vicinity of the centers of rich clusters. The deficiency of atomic gas is explained with ram pressure stripping, as the galaxy moves through the dense gas in the core of the cluster. Molecular gas is much less affected by the gas stripping mechanisms, because of its concentration and the stronger binding within the potential in the center of the galaxy.

In this chapter, CO observations of 24 galaxies within the Abell 262 cluster are discussed in the context of a possible molecular gas deficiency within the region of the cluster center. The observations were carried out with the IRAM 30 m telescope, the Onsala 20 m telescope and the Nobeyama 45 m telescope. Several indications of the presence of such a deficiency are highlighted and connected to a model of cirrus-like cloud stripping.

In addition to results for the global CO content of the galaxy sample, high-resolution interferometric CO(1−0) observations of one of the cluster members, UGC 1347, exemplify the spatial distribution of the molecular gas in a galaxy of the cluster. It was possible to confirm the existence of a bright off-nuclear CO-emission source and to derive molecular masses and line ratios for this source and the nucleus.

CHAPTER 1

Ground-based homothetic imaging

1.1 Astronomical interferometry

Angular resolution and sensitivity are key parameters in astronomical instrumentation. Within this section it is implicit that diffraction is the limiting factor of the angular resolution. In this case, both parameters are defined by the size of the telescope: the larger the aperture, the better the performance in these terms. The disproportional growth of complexity with the diameter of a telescope, however, practically limits the size that is technically feasible with reasonable effort. A natural approach to overcome these practical limitations is the joining of two or more smaller (and technically feasible) telescopes to a large synthetic aperture: an astronomical interferometer.

1.1.1 Beam combination

To obtain a gain in angular resolution compared to its individual telescopes, the interferometer has to preserve the temporal coherence when combining the light. If this is given, the superposition of two light beams of a single source at the point of combination results in an interferometric *fringe* pattern:

$$I = I_1 + I_2 + 2\sqrt{I_1 I_2}\,|\gamma_{12}| \cos\left(\frac{2\pi \cdot P}{\lambda} - \phi\right) \tag{1.1}$$

where (in a quasimonochromatic case) I_1 and I_2 represent the intensities of the fields probed by the individual telescopes of the interferometer, γ_{12} represents the normalized complex degree of spatial coherence, and P denotes the *optical path-length difference* (OPD) between the two paths of the interferometer up to the point of interference. γ_{12} depends on the brightness distribution $B(\alpha, \delta)$ of the source. The *van Cittert-Zernike theorem* states:

$$|\mathcal{F}(B(\alpha, \delta))| = |\gamma_{12}| \tag{1.2}$$

where the left side is the modulus of the normalized spatial Fourier transform of the brightness distribution in a plane. The highest degree of spatial coherence is achieved for compact, point-like sources.

Many beam combining concepts can be realized. Mariotti (1992) classifies the different beam combining concepts by four different criteria:

- Field access. Is the field of view (FoV) limited to a field that corresponds to the diffraction limit of the telescope apertures (single-mode) or can a larger FoV be accessed (multi-mode)? All radio interferometers are single-mode interferometers.
- Beam direction. Are the beams approaching the point of superposition from the same direction (coaxial) or are the beams approaching it from different directions (multi-axial)?
- Combination plane. Does the beam combination take place in the image plane or in the pupil plane of the telescope?
- Pupil geometry. What is the relation between entrance and exit pupil. The size of the interferometric FoV depends on certain constraints related to the pupil geometry (cf. Sect. 1.1.2).

This thesis will focus on a multi-mode multi-axial image plane interferometer that obeys the homothetic pupil condition.

1.1.2 Homothetic pupil interferometry

Already in 1868, Fizeau suggested to place a mask with two holes in front of a telescope and to use the telescope as beam combiner for the two sub-apertures. The interferometric FoV in this setup corresponds to that of the underlying telescope. The resolution of the Fizeau interferometer, however, depends on the separation of the sub-apertures and is limited by the size of the beam combining telescope. To overcome this limitation, separate telescopes can be used as apertures. To preserve the large FoV, Traubs *golden rule of separated telescopes* has to be obeyed (Traub 1986): "As viewed from a point in the focal plane, beams from separated telescopes must be recombined so that they appear to be coming directly from a single large telescope which has been masked so as to reproduce exactly the ensemble of collecting telescopes." Figure 1.1 shows the required geometry of such a system. It has to guarantee that the parts of a wavefront emerging the interferometer from an off-axis direction do not experience any OPD on their way to the point of superposition. The condition is fulfilled, if the exit pupil of the optical system forms a scaled version of the entrance pupil. A single telescope with a masked pupil is commonly referred to as *Fizeau interferometer*, while a an interferometer consisting of more than one aperture that obeys the golden rule is referred to as *homothetic imager*.

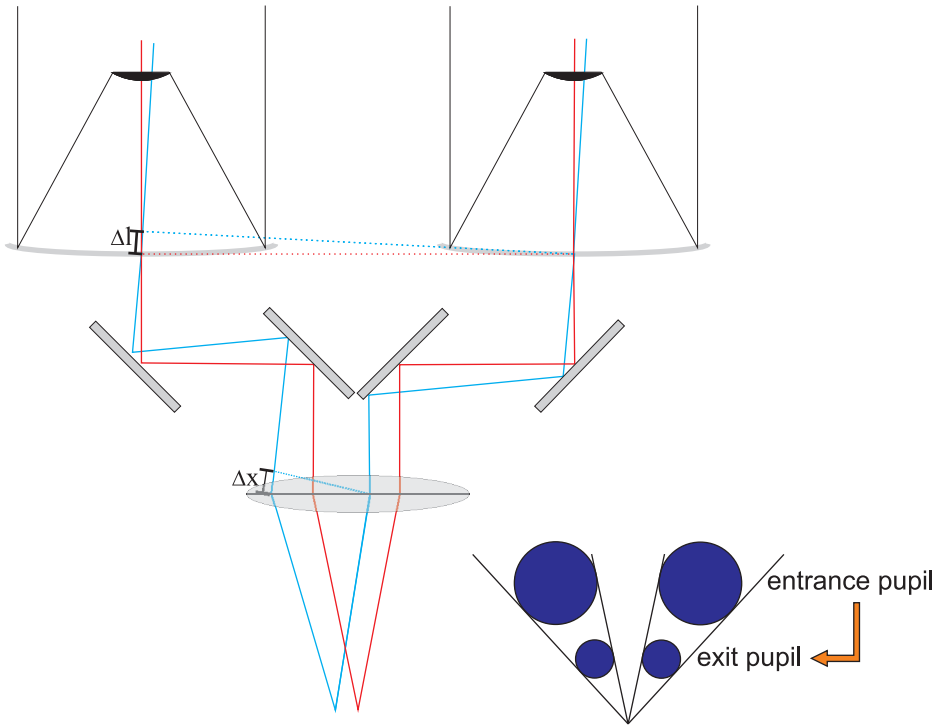

Figure 1.1: *Homothetic pupil condition. For wavefronts emerging at an angle with respect to the optical axis, the optical design has to guarantee zero optical path-length difference (OPD) at the focal plane, i.e. $\Delta l = \Delta x$, just as it is the case for telescope with a masked aperture. In other words: the exit pupil has to be a scaled version of the entrance pupil.*

1.2 Observing through the atmosphere

Before the light of an astronomical target is observed on the ground, it has traveled the distance between source and observer virtually undisturbed. Only on the last few ten kilometers, a tiny fraction of the overall distance, the emerging wavefronts get severely distorted as they travel through the turbulent atmosphere.[1] In the following the influence of the atmosphere on the imaging capabilities is outlined and measures to improve the data quality are introduced. A more detailed discussion of the following can be found in Roggemann et al. (1997).

[1] As a matter of fact, the astronomical light may be influenced by various other effects along the line-of-sight, such as absorption by interstellar or intra-cluster medium, gravitational lensing, etc. While signatures of these line-of-sight effects are out of reach and may be interesting in themselves, the astronomer generally wants to minimize the atmospheric impact on the data quality.

1.2.1 Fluctuations of the refractive index in a turbulent medium

The Reynolds number, the relation between inertial and viscous forces, is used to distinguish between laminar and turbulent fluid motion:

$$Re = \frac{v_\mathrm{a} l}{\nu_\mathrm{v}}, \tag{1.3}$$

where v_a denotes the average velocity of a viscous fluid of characteristic size l and ν_v its kinematic viscosity. High values for Re, e.g. $Re \sim 10^6$ in the case of atmospheric air flow (Ishimaru 1978), correspond to turbulent fluid motion. The atmosphere resembles a turbulent medium with a refractive index n, that depends on both temperature T and pressure p (Cox 1999):

$$n_1 \simeq n - 1 \approx 7.76 \cdot 10^{-5} \frac{p\,[\mathrm{mbar}]}{T\,[\mathrm{K}]}. \tag{1.4}$$

Since n is dependent on T, the random temperature distribution in the turbulent atmosphere naturally yields a random distribution of n. Fluctuations of the refractive index occur on a wide range of spatial and time scales. Areas in the air with uniform n are called *turbulent eddies*.

For a statistical formulation of these fluctuations, Kolmogorov (1961) assumed that the kinetic energy of large-scale motions in the turbulent flow (large eddies characterized by the *outer scale length* L_0) is transferred into smaller and smaller scale motions. The corresponding Reynolds number decreases with the size of the eddies until a critical value is reached for the *inner scale length* l_0. For smaller entities the kinetic energy is converted into heat by viscous dissipation. Within the range of $[l_0, L_0]$, turbulent motion is assumed to correspond to a homogeneous and isotropic random field. The statistical distribution of the size and number of these eddies can be characterized by the spatial power spectral density $\Phi_n(\vec{\kappa})$, with $\vec{\kappa}$ being the spatial wave number vector. In the Kolmogorov turbulence model, $\Phi_n(\vec{\kappa})$ follows for spatial wave numbers $\kappa = \frac{2\pi}{l}$ in the range $\kappa_0 = \frac{2\pi}{L_0} \leq \kappa \leq \frac{2\pi}{l_0}$:

$$\Phi_n^K(\vec{\kappa}) = 0.033 C_n^2 \kappa^{-11/3}. \tag{1.5}$$

C_n^2 is called the *structure constant* of the refractive index fluctuations and has units of $\mathrm{m}^{-2/3}$. To overcome the difficulties associated with the truncation at the outer and inner scale, a modification of the Kolmogorov model, the von Karman model was introduced:

$$\Phi_n^V(\vec{\kappa}) = \frac{0.033 C_n^2}{\left(\kappa^2 + \kappa_0^2\right)^{11/6}} \cdot \exp\left[-\frac{\kappa^2}{\kappa_m^2}\right], \tag{1.6}$$

with $\kappa_m = 5.92/l_0$. For low wave numbers and $L_0 \to \infty$, it follows that $\Phi_n^V(\vec{\kappa}) \to \Phi_n^K(\vec{\kappa})$. The actual value for L_0, which limits the contribution of low spatial frequencies to the power spectrum, depends on the local conditions at the telescope site. Experimentally determined values range from several m to more than 100 m (Nightingale & Buscher 1991; Linfield et al. 2001; Conan et al. 2003). Since the spatial power spectral density is dominated by the lowest spatial frequencies, L_0 gains in importance as the aperture of the telescope increases (e.g. in the case of interferometers or Extremely Large Telescopes[2]).

The variation of the refractive index between two spatially separated points is of particular interest for the treatment of wave propagation through the turbulent atmosphere. The refractive index structure function $D_n(\vec{r})$ is defined as the variance of the refractive index at any two points $\vec{r}_0$ and $\vec{r}_1$:

$$D_n(\vec{r}) = \left\langle |n(\vec{r}_0 + \vec{r}_1) - n(\vec{r}_0)|^2 \right\rangle \tag{1.7}$$

It can be shown that for conditions following Kolmogorov statistics the refractive index structure function results in

$$D_n(\vec{r}) = C_n^2 \cdot r^{2/3}, \tag{1.8}$$

In ground-based astronomy, the object of interest is observed through a column of air with C_n^2 being dependent on the altitude z. $C_n^2(z)$ is dependent on various geographical and seasonal conditions, such as time of the year, time of the day, influence of streams, geographical location and altitude of the telescope site, local environment of the telescope such as the construction of the dome, presence of trees etc. Common to most sites is the particular strength of the atmospheric layer in the first few kilometers above the ground. To be able to determine C_n^2 profiles that are representative for the specific conditions at a telescope site, $C_n^2(z)$ has to be measured over several years. Information on initial SCIDAR[3] measurement campaigns for the LBT site on Mt. Graham can be found in Egner (2006).

1.2.2 Wave propagation through the turbulent atmosphere

As shown in the previous section, atmospheric turbulence causes fluctuations of the refractive index in the air along the line of sight. The phase of an initially flat wavefront emerging from a distant source is perturbed as it propagates through

[2] ELT is a commonly used term describing concepts of optical telescopes with diameters from ~30 m up to 100 m.

[3] SCintillation Detection And Ranging is one of many methods to determine C_n^2 profiles

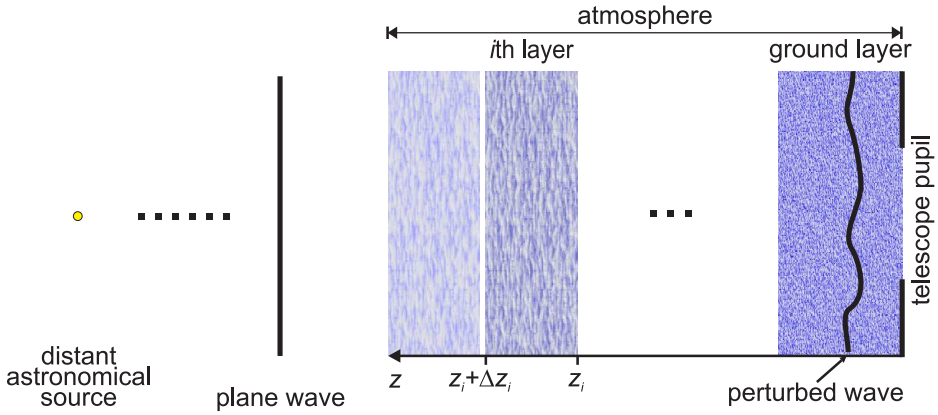

Figure 1.2: *Wave propagation through the atmosphere. For the sake of simplicity, a discrete number of atmospheric layers is assumed, each represented by its own constant $C_{n_i}^2$. The incident plane wave is perturbed as it propagates through the different atmospheric layers.*

each turbulent atmospheric layer. In the following a finite number of atmospheric layers are assumed, each of them representing regions of similar turbulence (cf. Fig. 1.2). The same notation as in Roggemann et al. (1997) is used here: $C_{n_i}^2$ describes the turbulence of the ith layer with altitude z_i and thickness Δz_i. $\Delta\vec{x}$ denotes the vector separation of two points in the plane perpendicular to the direction of propagation (z). $u_i(\vec{x})$ is used to represent the complex optical field in the telescope pupil after propagation through the ith layer. The corresponding spatial correlation function $\Gamma_{p_i}(\Delta\vec{x})$ of the optical field in the pupil is given by

$$\Gamma_{p_i}(\Delta\vec{x}) \equiv \left\langle u_i(\vec{x}) u_i^*(\vec{x}-\Delta\vec{x}) \right\rangle = \exp\left[-\frac{1}{2} D_{\psi_i}(\Delta\vec{x})\right], \tag{1.9}$$

where the phase perturbations caused by refractive index fluctuations in the ith layer are represented in the phase structure function

$$D_{\psi_i}(\Delta\vec{x}) = \left\langle k^2 \left(\int_{z_i}^{z_i+\Delta z_i} \mathrm{d}z \left[n_1(\vec{x}, z) - n_1(\vec{x}-\Delta\vec{x}, z) \right] \right)^2 \right\rangle. \tag{1.10}$$

$k = \frac{2\pi}{\lambda}$ is the optical wave number. Assuming Kolmogorov statistics and a thickness of layer i that is significantly larger than $|\Delta\vec{x}|$, the phase structure function results in (Fried 1966)

$$D_{\psi_i}(\Delta\vec{x}) = 2.91 k^2 \Delta z_i C_{n_i}^2 |\Delta\vec{x}|^{5/3}. \tag{1.11}$$

Fried (1966) defined a fundamental parameter that allows to characterize the spatial extent of the phase perturbations:

$$r_0 = 0.185 \left(\frac{4\pi^2}{k^2 \sum_{i=1}^{N} C_{n_i}^2 \Delta z_i} \right)^{3/5}, \tag{1.12}$$

or in a more general notation considering the angular zenith distance γ and a continuous $C_n^2(z)$ distribution:

$$r_0 = \left(0.423 k^2 \sec\gamma \int C_n^2(z)\, \mathrm{d}z \right)^{-3/5}. \tag{1.13}$$

With the Fried parameter the phase structure function for the propagation through the entire atmosphere reduces to

$$D_\psi(\Delta\vec{x}) = 6.88 \left(\frac{|\Delta\vec{x}|}{r_0} \right)^{5/3} \tag{1.14}$$

and the total spatial correlation function of the optical field in the telescope pupil results in

$$\Gamma_p(\Delta\vec{x}) = \exp\left[-\frac{1}{2} D_\psi(\Delta\vec{x}) \right] = \exp\left[-\frac{1}{2} \cdot 6.88 \left(\frac{|\Delta\vec{x}|}{r_0} \right)^{5/3} \right]. \tag{1.15}$$

r_0 represents the diameter of a cell, over which the statistical phase error (RMS) amounts to ~1 rad. Since $r_0 \propto \lambda^{6/5}$, the cell sizes increase with increasing λ.

A convenient way of dealing with the turbulence-propagation through a discrete number of atmospheric layers is the introduction of two-dimensional phase screens. Each screen is associated with a nominal altitude and characterizes the phase perturbation of the corresponding layer. In numerical simulations (Chapter 2) the treatment as phase screens simplifies the calculation of wavefront propagation.

1.2.3 Phase variations and interferometers

The phase structure function $D_\psi(\Delta\vec{x})$ describes the variance of the phase variations between two points in the pupil. Of specific interest when dealing with interferometers is the standard deviation σ_ψ of the phase variations between two distinct points in the pupil plane: the regions of the individual apertures that form the interferometer. The separation of these regions is given by the baseline B. Kolmogorov statistics then yields:

$$D_\psi(\Delta\vec{x}) = \sigma_\psi^2 = 6.88 \left(\frac{|\Delta\vec{x}|}{r_0} \right)^{5/3} \rightarrow \sigma_\psi(B) = 2.62 \left(\frac{B}{r_0} \right)^{5/6} \tag{1.16}$$

This quantity is directly related to the standard deviation of atmospherically induced OPD between the two arms of the interferometer (cf. Sect. 1.3.3).

$$\sigma_{\mathrm{OPD}}(B) = \frac{\lambda}{2\pi}\sigma_{\psi}(B) = \frac{2.62}{2\pi}\lambda\left(\frac{B}{r_0}\right)^{5/6} \tag{1.17}$$

It is important to note that σ_{OPD} is achromatic and only dependent on the separation B, since $r_0 \propto \lambda^{6/5}$.

1.2.4 Anisoplanatism

Especially in the context of adaptive optics (AO; cf. Sect. 1.3) the question arises, whether the phase distributions of wavefronts emerging from two distinct directions are statistically correlated. The degree of correlation depends on the angular separation of the sources. Each of the two wavefronts propagates through slightly different regions in the atmosphere, experiencing slightly different phase perturbations. This effect is known as anisoplanatism.

The *isoplanatic angle* θ_0 is defined to be the largest angular separation of two sources (such as science target and AO reference star) such that the phase decorrelation remains below 1 rad^2:

$$\theta_0 = 0.0581\lambda^{6/5}\left[\int \mathrm{d}z\, C_n^2(z)\cdot z^{5/3}\right]^{-3/5} \tag{1.18}$$

(Fried 1982). The isoplanatic angle is proportional to $\lambda^{6/5}$ (just like r_0, cf. Eq. 1.13). Observing at longer wavelengths, thus, not only is less sensitive to turbulence with fewer Fried cells across the aperture. It also allows for a larger sky coverage of AO assisted telescopes, since it permits the selection of the reference star in a larger region around the source of interest. A typical value for θ_0 is 20″ at λ =2.20 μm.

1.2.5 Temporal evolution of turbulence

Taylor's frozen-flow hypothesis is commonly used in the discussion of the temporal evolution of atmospheric turbulence. It assumes that the segments of an atmospheric layer remain frozen over the period in which they translate across the telescope beam with uniform wind velocity. "Frozen" means that any temporal evolution of the refractive index occurs on timescales larger than the crossing time. In this case temporal refractive index variations can be ignored. Associated with each atmospheric layer are a structure constant $C_{n_i}^2$ and a uniform wind component $\vec{v}_i$ perpendicular to the direction of propagation. The spatial

phase structure function can then be extended to a space-time structure function $D_\psi(\Delta\vec{x}, t_2 - t_1)$. When considering the disturbance of all layers, it follows

$$D_\psi(0,t) = \left(\frac{t}{\tau_0}\right)^{5/3} \tag{1.19}$$

with

$$\tau_0 = 0.314\frac{r_0}{\bar{v}}, \tag{1.20}$$

where $\bar{v}$ is the ($C_{n_i}^2$ weighted) average of the wind velocities of all layers. τ_0 is the *atmospheric coherence time*, a characteristic timescale for the temporal evolution of phase perturbations, as turbulence cells are blown across the telescope aperture.

For interferometers the *differential piston time constant* t_0 is of special interest. This is the characteristic time in which the variance of differential piston does not exceed 1 rad^2. For small apertures and large baselines B with $B \gg L_0$ the phase variations at the individual apertures are not correlated, thus (Kellerer & Tokovinin 2007)

$$t_0 = 2^{-3/5}\tau_0 = 0.66\tau_0 \tag{1.21}$$

If $B \gg L_0$ is not given, t_0 is between $0.66\tau_0$ and τ_0. In interferometers employing larger telescopes with diameters d of several r_0, the phase variations are averaged across each aperture. For this case Kellerer & Tokovinin (2007) state a modified interferometric time constant t_1

$$t_1 = 0.273\left(\frac{r_0}{\bar{v}}\right)\left(\frac{d}{r_0}\right)^{1/6} \tag{1.22}$$

These equations assume time intervals $t < \frac{B}{\bar{v}}$. For larger intervals the piston values of the two apertures cannot be considered as independent – the differential piston time constants can only be used in structure functions to represent the short-time behavior.

1.2.6 Imaging through the atmosphere

The influence of phase perturbation on the formation of images can be conveniently expressed in the framework of Fourier optics. Let $\vec{r}$ and $\vec{R}$ represent positions in the object plane and image plane respectively. An image $I_i(\vec{R})$ of a brightness distribution $I_0(\vec{r})$ is formed by convolution with the *point-spread function* (PSF) $\mathcal{S}(\vec{r})$:

$$I_i(\vec{R}) = I_O(\vec{r}) * \mathcal{S}(\vec{r}) \tag{1.23}$$

or, expressed in the spatial frequency domain by applying the convolution theorem:

$$\mathcal{F}\left\{I_i(\vec{R})\right\} = \mathcal{F}\left\{I_O(\vec{r})\right\} \cdot \mathcal{F}\left\{\mathcal{S}(\vec{r})\right\} \tag{1.24}$$

The Fourier transform of the PSF is the (unnormalized) *optical transfer function* (OTF):

$$\mathcal{F}\left\{\mathcal{S}(\vec{r})\right\} = \mathcal{T}(\vec{f}). \tag{1.25}$$

It transfers the frequency spectrum of the object's brightness distribution into the image frequency spectrum. The complex OTF represents the full telescope-atmosphere system. It is the product of the atmospheric transfer function $\mathcal{T}_A(\vec{f})$ and the telescope transfer function $\mathcal{T}_T(\vec{f})$:

$$\mathcal{T}(\vec{f}) = \mathcal{T}_A(\vec{f}) \cdot \mathcal{T}_T(\vec{f}). \tag{1.26}$$

The diffraction limited telescope transfer function is the autocorrelation of the telescope pupil function $\mathcal{P}(\vec{x})$ (if aberrations are neglected) or, equivalently, the inverse Fourier transform of the diffraction limited PSF:

$$\mathcal{T}_T(\vec{f}) = \mathcal{F}\left\{\mathcal{S}_T(\vec{r})\right\} = \mathcal{F}\left\{\left|\mathcal{F}\left\{\mathcal{P}(\vec{x})\right\}\right|^2\right\} \tag{1.27}$$

In the *long exposure* case the atmospheric transfer function is the pupil field correlation function $\Gamma(\lambda\vec{f})$. With Eq. 1.15 follows:

$$\mathcal{T}_{A_{LE}}(\vec{f}) = \exp\left[-\frac{1}{2} \cdot 6.88\left(\frac{\lambda|\vec{f}|}{r_0}\right)^{5/3}\right] \tag{1.28}$$

1.2.7 Angular resolution and atmospheric seeing

One of the key parameters in astronomy is the angular resolving power of a telescope. A well established definition is the Rayleigh criterion, in which any two equally luminous stars are said to be just resolved with a circular diffracting aperture of diameter D, when the center of one Airy disk coincides with the first Airy minimum of the other star:

$$\theta_{\text{telescope}} = 1.22\frac{\lambda}{D} \tag{1.29}$$

The Airy disk is seen in the diffraction limited PSF of a circular aperture. This definition suggests that the resolving power of a telescope increases with the size of the aperture.

However, as discussed in Sect. 1.2.6, the OTF is the product of the telescope transfer function and the atmospheric transfer function. Any degrading effects of

the atmosphere are ignored in the Rayleigh criterion. To consider the influence of the atmospheric transfer function on the angular resolution, the angular diameter (full width at half maximum, FWHM) of the long exposure PSF under the influence of atmospheric turbulence can be calculated. The FWHM of this PSF is denoted as *seeing angle*:

$$\theta_{\text{seeing}} \approx \frac{\lambda}{r_0}, \tag{1.30}$$

with the Fried parameter introduced in Sect. 1.2.2. Thus, r_0 can be seen as a critical telescope diameter. Telescopes with diameters exceeding r_0 are dominated by seeing. A typical value for r_0 in the visible wavelength domain is ~10 cm.

1.2.8 Regaining the diffraction limit

For the traditional ground-based astronomy in the visible (or NIR) wavelength domain, the increase of the aperture size beyond 0.1 m (0.6 m) does not result in any gain in terms of angular resolution (however, it does in terms of sensitivity). Several routes can be taken to circumvent the profound degradation due to the atmosphere, and to improve the resolving power – in the ideal case up to the fundamental limit imposed by the diffracting aperture:

- Airborne or space telescopes
- Speckle interferometry
- Adaptive optics

Space telescopes
The idea is simple but expensive. By installing the telescope on a space craft outside of the atmosphere, a time-invariant PSF can be achieved, that is limited only by the diffracting aperture and optical aberrations. The maximum diameter of the telescope, however, is limited by the payload of available space vehicles. A current, ambiguous project is the James Webb Space Telescope. It will be installed in the Lagrangian point L2 of the earth-sun system and will operate in the wavelength regime from 1 μm-24 μm. The primary mirror diameter of 6.5 m will allow for an angular resolution of 30 mas when observing at 1 μm.

Speckle interferometry
Among the earth-bound solutions, speckle interferometry is the technically less complex approach and was first realized in 1970 (Labeyrie 1970). The idea beyond this concept is that short exposure images contain more high-spatial-frequency information than long exposure images. If the exposure time is of

the order of the coherence time of the atmosphere, the atmospheric perturbation of the phase can be assumed as frozen over the integration. The resulting image contains a pattern of bright spots, called *speckles*. They are the result of interference between wave segments that traveled through different seeing cells. These r_0 sized cells divide the telescope aperture into several sub-apertures. The number of speckles $\sim (D/r_0)^2$ depends on the number of Fried cells across the telescope pupil. To first order each speckle covers an area that corresponds to the diffraction limit of the telescope. The structure of the speckle cloud changes randomly with time. A simple summation of an ensemble of these statistically uncorrelated speckle clouds results in the long exposure image with reduced angular resolution (Sect. 1.2.7). More advanced post-detection processing of the short exposure images, such as shift-and-add, allows to conserve the high-spatial-frequency information.

Each of the large number of short exposures, needed to reconstruct the high-resolution image, contain the readout noise of the detector electronics. This limits the sensitivity that can be achieved with this method.

1.3 Adaptive optics

To be able to conserve high-spatial-frequency information while integrating over longer periods of time, the perturbations of the incoming phases have to be actively compensated before the wavefront reaches the detector array. This is the task of adaptive optics systems, different variants of which nowadays are part of almost every 8 m class optical telescope. There are conceptual differences on the component level of these servo systems, but the basic idea is always the same. Adaptive optics is not only incorporated in single aperture telescopes, but it is used also for telescope arrays. A fringe tracker is a system that is unique to interferometers. In the following the basic principle of single and multi-aperture adaptive optics is presented.

1.3.1 Zernike polynomials

The phase of a wave segment $\psi(D\rho, \theta)$ passing through an optical system with a circular aperture of diameter D can conveniently be expressed by a series of Zernike polynomials.

$$\psi(D\rho, \theta) = \sum_J c_J \cdot Z_J(\rho, \theta) \tag{1.31}$$

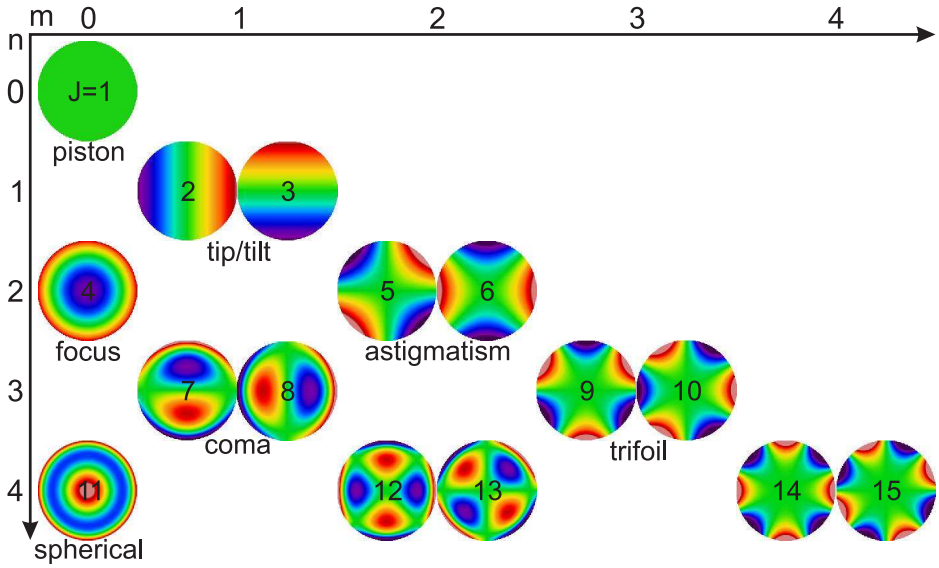

Figure 1.3: *Surface plots of the first 15 Zernike modes. The name of the corresponding optical aberration is stated below each plot.*

These are orthonormal on the unit circle. The following definition follows Noll (1976):

$$\begin{aligned} Z_J &= \sqrt{n+1}R_n^0(\rho) && m = 0 \\ Z_{J_{\text{even}}} &= \sqrt{n+1}R_n^m(\rho)\sqrt{2}\cos m\theta && m \text{ even} \\ Z_{J_{\text{odd}}} &= \sqrt{n+1}R_n^m(\rho)\sqrt{2}\sin m\theta && m \text{ odd} \end{aligned} \tag{1.32}$$

with

$$R_n^m(\rho) = \sum_s^{\frac{n-m}{2}} (-1)^s \frac{(n-s)!}{s!\left(\frac{n+m}{2}-s\right)!\left(\frac{n-m}{2}-s\right)!}\rho^{n-2s} \tag{1.33}$$

The azimuthal order m and radial order n have to fulfill: $m \leq n$ and $n-m =$ even. Surface plots of the first orders are shown in Fig. 1.3.

1.3.2 Single aperture adaptive optics

Every wavefront perturbation can be represented by a superposition of discrete Zernike modes. Static aberrations are caused by the implementation of non-perfect optical components in the system. Time invariant solutions may potentially be introduced to compensate for these aberrations.

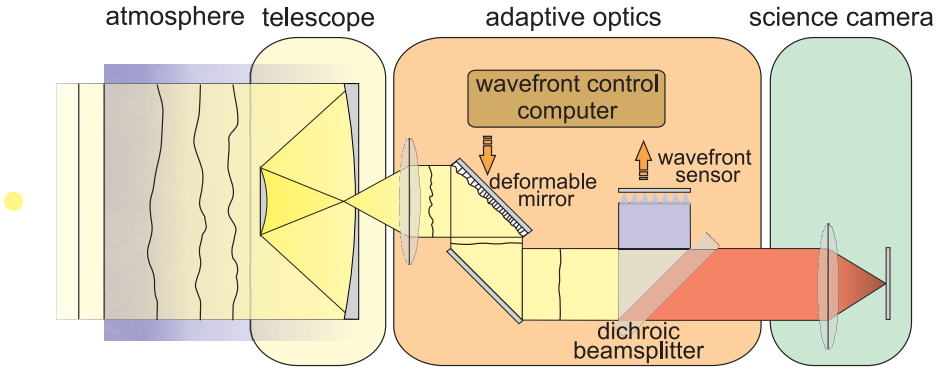

Figure 1.4: *Schematic view of a ground-based telescope system featuring adaptive optics. The propagation of the light is from left to right: Initially flat wavefronts get perturbed by the atmosphere, enter the telescope, are corrected by the AO system, and finally form the image on the science detector. Within the AO servo loop, the wavefront perturbations are measured by a wavefront sensor, then a correction matrix is calculated and applied to the deformable mirror. In the optical path the wavefront sensor is located behind the deformable mirror. Thus, it senses only the residual wavefront perturbations that remain after the correction by the deformable mirror calculated in a previous loop cycle. Only the short wavelength part of the spectrum is used by adaptive optics. The longer wavelengths are available to the science camera.*

To be able to correct for the fast varying atmospheric perturbations in real-time, however, an adaptive system has to be employed. Such a system has to be able to continuously measure and correct phase perturbations in a closed loop. The servo loop frequency must be faster than the characteristic timescale of the atmospheric disturbances.

The correction of a perturbed wavefront can be accomplished by a reflection on a surface that is shaped like the perturbation. Deformable mirrors (DMs) serve this purpose. Their shape can be adjusted with the help of a large number of actuators on the back side of the reflecting surface. The number of actuators limits the number of Zernike modes that may be corrected with the help of that DM. Just like the number of sub-apertures covered by the wavefront sensor, the number of actuators $N \approx \left(\frac{D}{r_0}\right)^2$ should correspond to the number of Fried cells across the aperture.

Current wavefront sensors are based on different techniques. Two common sensor types are the Shack-Hartmann sensor and the pyramid wavefront sensor. In a Shack-Hartmann sensor, an array of micro-lenses splits the aperture in a grid of subapertures, each producing a low-resolution image of the reference source in the focal plane of the sensor. The shift of each image with respect to the theoretical position provides information on the local tilt of the wavefront at the corresponding lenslet array coordinate. In pyramid wavefront sensors, the tip of

a four-sided pyramid is placed at the position of the reference PSF in the focal plane. The pyramid splits the light into four beams, each of which is used to produce a pupil image on a CCD. The information on the phase perturbation at a certain position in the pupil is encoded in the intensity distribution between the four associated pixels in the four pupil images.

The basic setup of an AO system is outlined in Fig. 1.4. In the optical path, the AO system is located before the science camera. Light entering the telescope usually is spectrally divided into an AO and a science channel. Due to the wavelength dependence of r_0 (cf. Sect. 1.2.2), the shorter waveband is exploited by the AO system to provide a good correction at longer wavelengths.

Phase reference

A phase reference source has to be accessible by the wavefront sensor, independent of the technology used to sense the wavefront. The light of this reference is used to measure the phase perturbations. This imposes certain constraints on the nature of the reference target, such as apparent magnitude and distance to the target of interest. Any reference source has to provide a sufficient photon flux density to allow for wavefront measurements at the required sampling rate. It has to have an angular separation from the target of interest that is lower than the isoplanatic angle (cf. Sect. 1.2.4). These constraints significantly limit the region of the sky in which AO assisted observations are possible.

A natural guide star, in some cases the science source itself, or an artificial light source outside of the atmosphere (or at least in the outer regions of the atmosphere) may serve as reference. Such an artificial light source may be a patch of sodium atoms in a thin layer in the outer atmosphere, excited by a laser. Laser-based references may be a solution to increase the sky coverage of AO assisted observations. However, these artificial light sources still require a (potentially fainter) natural reference star for tip-tilt correction: the laser beam direction varies, because it has to travel through the same turbulent medium in opposite direction.

A different approach to increase the sky coverage is the use of layer-oriented Multi-Conjugate Adaptive Optics. In this concept, the light of several faint natural reference stars can be optically coadded. Therefore, the system does not depend on the presence of a single bright reference source to overcome the limiting magnitude for wavefront sensing (cf. Sect. 1.5).

1.3.3 Fringe tracking

In imaging systems with only one circular aperture, the J=1 Zernike mode does not not affect the quality of the obtained images. In interferometric systems with

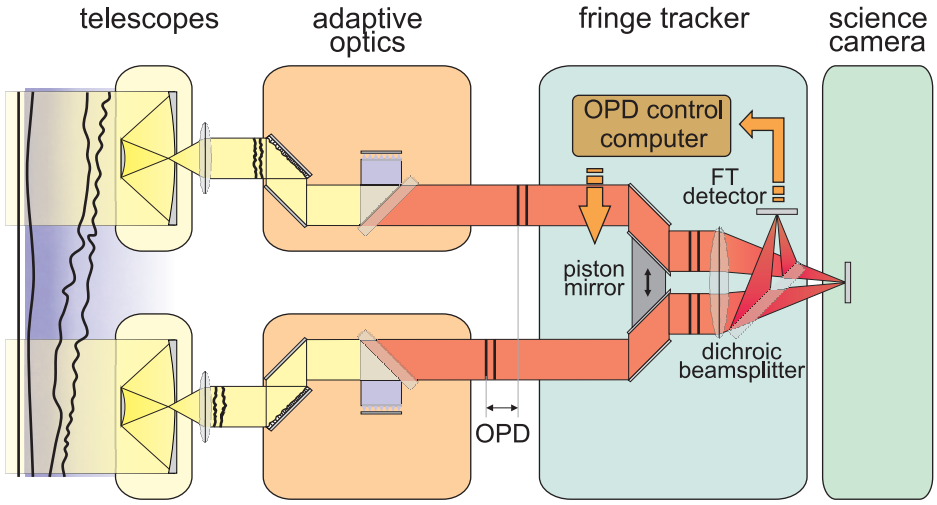

Figure 1.5: *Schematic view of a ground-based optical interferometer featuring adaptive optics and a fringe tracker. Perturbed wave segments passing through the interferometer are corrected for each channel individually (cf. Fig. 1.4). The remaining perturbation is differential piston, or optical path-length difference (OPD), between the channels. In the fringe tracking servo loop, differential piston is measured by analyzing the fringe pattern of a reference target in the combined focal plane. A correction signal is determined and a compensating OPD is introduced by moving the piston mirror. Just like in the AO loop, the fringe tracking detector is located behind the piston mirror in the optical path. Thus, the sensor measures the residual differential piston after the correction applied in previous cycles.*

more than one aperture, however, this piston mode gains in relevance. Any wavefront approaching the interferometer is probed by each aperture of the system. For a coherent combination, the wavefront segments in each aperture that correspond to a common wavefront have to coincide in space and time. Therefore, a difference between the piston values (differential piston) of these wavefront segments must not be present at the surface at which the coherent beam combination should take place.

Fringes are only detectable as long as the differential piston is smaller than the coherence length:

$$l_c = \frac{\bar{\lambda}^2}{\Delta\lambda}, \tag{1.34}$$

where $\bar{\lambda}$ is the mean wavelength and $\Delta\lambda$ the width of the observed band, which is illuminated by a grey source with a flat spectrum across the transmission range of the filter in use. Differential piston is most likely the sum of several effects causing static or variable phase delays. Two basic classes of effects causing differential piston with different power-spectra can be identified:

- Atmospheric differential piston. Any emerging wavefront forms a corrugated but still continuous surface. The piston term of the wavefront segment cut by each aperture of the interferometer corresponds to the phase average across this aperture. Only low-order atmospheric phase perturbations on scales exceeding the size of each aperture cause differential piston.
- Instrumental effects. OPD between the arms of the interferometer preclude a coherent beam combination, too. Many reasons for instrumental OPD can be identified:
  - static misalignment
  - flexure
  - vibrations
  - non-perfect AO correction
  - tracking errors

Fringe tracking is applied in interferometers to continuously monitor and correct for differential piston. A fringe tracker is a servo system just like single aperture AO systems, except that it deals only with the J=1 Zernike mode. Three different concepts of fringe tracking can be employed, depending on requirements imposed by the interferometer type and purpose:

- Coherencing. A coherencing system ensures the availability of fringes by controlling OPD in a way that it remains within the coherence length. In this concept no attempt is made to freeze the fringe motion. The time for each fringe measurement has to be short compared to the characteristic fringe motion timescale.
- Phase tracking. A phase tracker stops the fringe motion over periods much longer than the characteristic timescale of the differential piston variation. Differential piston is continuously controlled to remain at a constant value within the coherence length. The residual piston is kept below a certain threshold (e.g.: $\frac{\lambda}{4}$ or $\frac{\lambda}{10}$).
- Cophasing. In a cophasing system phase tracking is performed on the white light (i.e. central) fringe. In other words: differential piston within the system is continuously controlled to remain at zero.

In Fig. 1.5 a conceptual representation of an interferometer equipped with AO systems and a fringe tracker is shown as an example. Every fringe tracker depends on the presence of a phase reference within the FoV, just as it is the case

for single aperture AO systems. In observations with stellar interferometers the science target often also serves as phase reference. Homothetic imagers allow to select off-axis reference stars for fringe tracking. Similar restrictions apply to AO and fringe tracking phase references: an upper limit for the apparent magnitude and a maximum angular distance to the target of interest (cf. Sect. 2.2).

1.4 The Large Binocular Telescope

On Mt. Graham in Arizona, one of the most ambiguous telescope projects has reached a state which allows to produce first scientific images. Once fully operational, the Large Binocular Telescope (LBT) will be the largest "single" telescope for the visible to the thermal-infrared wavelength domain that has been built so far. It is a joint undertaking by a consortium of U.S. American, German and Italian institutions. Most fields in observational astrophysics will benefit from the LBT being a powerful general purpose instrument that is intended to prepare the ground for the next generation of ELTs. For a more detailed description of the project see Hill & Salinari (2004) and Hill et al. (2006).

1.4.1 LBT design

The LBT uses two 8.4 m diameter primary mirrors with a center-to-center distance of 14.4 m supported by a common alt-az mount to produce a total collecting area of $\sim$110 m^2 (cf. Fig 1.6). Their static arrangement in a common plane perpendicular to the line of sight provides a time-invariant input pupil geometry[4] (cf. Fig. 1.7). In phased arrays this constellation has a great advantage over the use of individually mounted telescopes with time-variant projections of the entrance pupil on a plane perpendicular to the line of sight. There is no need for long optical delay lines, which have to be implemented in most stellar interferometers to compensate for the OPD between the individual telescopes of the array. The LBT setup allows for 3 basic modes of operation:

1) Individual beam mode. The two individual 8.4 m telescopes can be pointed either to the same position on the sky or to neighboring fields up to a few arcminutes apart.

2) Incoherent beam combination mode. In this mode the light-gathering power of the effective aperture is equivalent to a 11.8 m circular aper-

[4] Actually the undersized secondary mirrors constitute the aperture stops of the telescopes, hence they define the entrance pupils

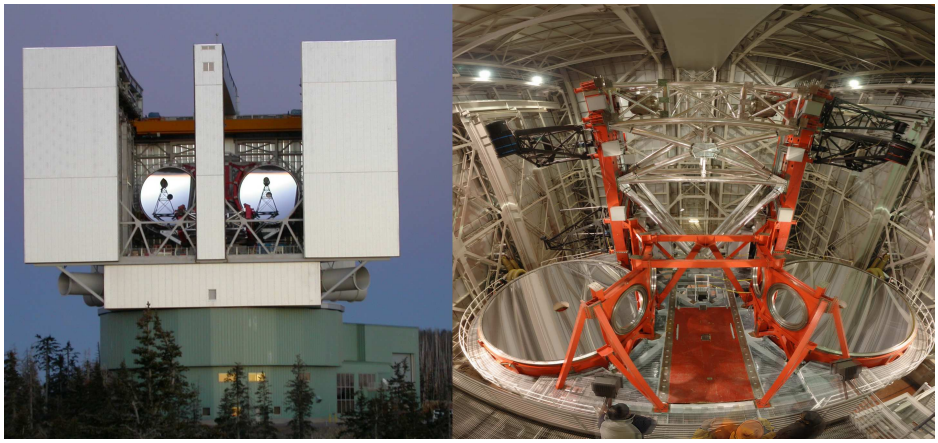

Figure 1.6: *The Large Binocular Telescope (LBT) in the beginning of 2007. The two primary mirrors are aluminized and the two prime focus cameras LBC red and LBC blue are in place. LBC blue is commissioned and produces first scientific images. Right: Movable swing arms allow to insert either the prime focus cameras or secondary and tertiary mirrors into the optical path. One of the swing arms for a secondary mirror and one for a tertiary mirror is mounted. LINC-NIRVANA will be installed on the central instrument platform and will occupy the left and right bent Gregorian foci in the front of the image. Image courtesy: J. Hill and W. Rujopakarn*

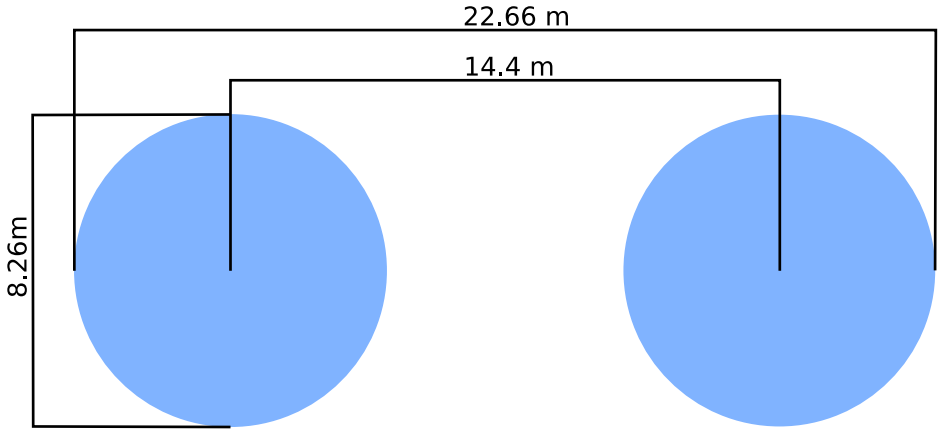

Figure 1.7: *Basic dimensions of the time-invariant LBT pupil that will be available to both interferometric instruments. The undersized secondary mirrors form the aperture stops of the single-eye telescopes. Their images through the primaries form the entrance pupil at a distance of ~100 m in front of the telescope. This is the conjugation altitude of the ground-layer adaptive optics system. To allow for homothetic imaging with a large interferometric FoV, the pupil configuration has to be conserved, i.e. the exit pupil has to be a scaled version of the entrance pupil.*

ture telescope. The spatial resolution in the diffraction limit, however, is driven by the 8.26 m pupils.

3a) Coherent beam combination mode. In this mode the additional complexity of the LBT approach compared to the use of two individual, unlinked telescopes starts to pay off. The coherent combination preserves the phase information that results in a gain in spatial resolution by the sampling of larger spatial frequencies (cf. Sect. 1.4.2) of up to 22.8 m.

3b) Homothetic imaging. The full elegance of the LBT design unfolds in this mode in which the coherent beam combination is paired with the preservation of the homothetic pupil condition (cf. Sect. 1.1.2), which allows for high spatial resolution over a larger field of view. In terms of angular resolution the LBT will outperform the imaging capabilities of existing 8-10 m class telescopes by a factor of ∼3 (cf. Sect. 1.4.2).

Instruments can pick up the field at 12 focal stations: two prime foci, two fiber pickups, two straight Gregorian and a total of six bent f/15 Gregorian Foci. The set of instruments that is currently being built facilitates either mode 1 or mode 3. The first generations of instruments will consist of two wide field cameras (LBC, optimized for red and blue respectively), a set of two multi-object spectrographs (MODS) for the visible, two NIR long-slit and multi-object spectroscopic units (LUCIFER), a high-resolution échelle spectrograph (PEPSI) and two interferometers: the LBT Interferometer (LBTI) and LINC-NIRVANA. LBTI will provide imaging and nulling capabilities and will work at wavelengths longer than K-band. LINC-NIRVANA will be the NIR homothetic interferometric imaging camera for the LBT (cf. Sect. 1.5). The use of swing arms and turnable tertiary mirrors enables to quickly switch between the instruments (cf. Fig. 1.6).

Since adaptive optics is a key issue in state-of-the-art ground-based telescopes (cf. Sect. 1.3), the LBT will be equipped with two adaptive secondary mirrors of 672 voice-coil actuators each.

1.4.2 Spatial resolution

The monochromatic diffraction limited PSF reflects the uniqueness of the pupil geometry of the LBT, when used as a phased array (cf. Fig. 1.8, panel 4). It is described by an envelope function that corresponds to the diffraction limited PSF of a circular aperture with a diameter of ∼8.3 m. The envelope function is modulated by a fringe pattern (sine function) that results from the coherent combination of the two circular apertures. The fringe modulation is purely dependent on the center-to-center distance between the two circular apertures (14.4

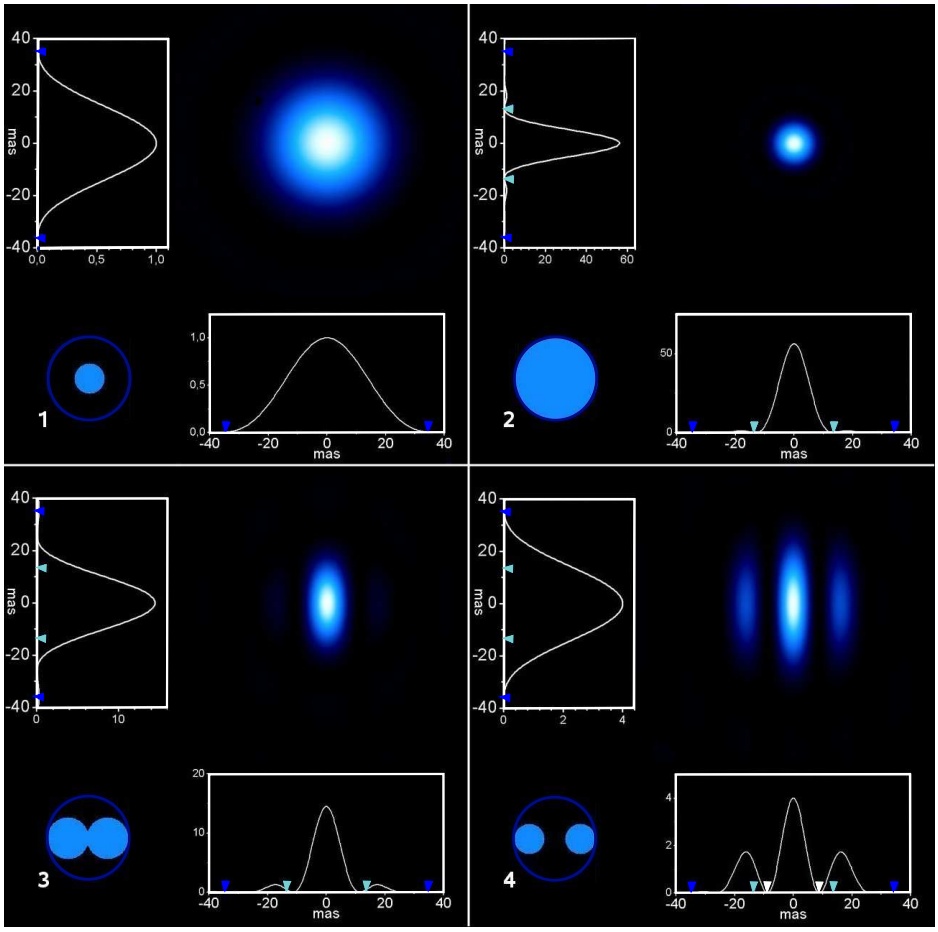

Figure 1.8: *The point-spread functions of 1.) an 8.3 m circular aperture telescope, 2.) of a 23 m telescope, 3.) of two circular apertures with diameters and a center-to-center distance of 11.5 m, and 4.) of the LBT. In vertical direction, the LBT PSF does not differ from the PSF of an 8.3 m telescope, while in the direction of high spatial resolution the fringe spacing is even narrower than the Airy radius of a 23m telescope (the positions of the minima are marked with small triangles). The fringe spacing is depending on the center-to-center distance of the mirrors and not on the largest spatial frequency that can be achieved over the full aperture.*

m) and the wavelength. A Young experiment with a ratio of pinhole diameter to separation of $\frac{8.26\text{m}}{14.4\text{m}}$ results in the same intensity distribution as the PSF of the LBT.

A comparison of the LBT PSF with the PSFs resulting from other pupil geometries is shown in Fig. 1.8. Because of the fringe modulation, the diffraction limited PSF is not circular symmetric but shows a principal direction of maximum angular resolution perpendicular to the orientation of the fringes. Along this direction the LBT allows for an angular resolution of $\sim$ 5 mas in J-band. Perpendicular to the direction of maximum resolution, however, no gain over the diffraction limited resolution of a single aperture is achieved.

Nevertheless, there is a way of obtaining images with high angular resolution along all axes of the image. Due to the alt-azimuth mounting of the LBT, the observed field rotates with time in the image plane of the camera (cf. Fig. 1.9). For each hour angle the parallactic angle η describes the orientation of the field. Because of the fixed baseline geometry of the LBT, the direction of maximum angular resolution remains fixed with respect to the detector (if the detector is not derotated). The earth rotation can thus be used to obtain images of the target of interest at different parallactic angles. For each parallactic angle the direction of the maximum spatial resolution with respect to the object is different. A set of 3 or more images of the target of interest, each exhibiting a different orientation of the object, can then be combined by image reconstruction algorithms (Hofmann et al. 2005; Desiderá et al. 2006) to obtain an image with a uniform resolution.

1.5 LINC-NIRVANA

LINC-NIRVANA is the NIR homothetic imaging camera for the LBT and combines two ambiguous technologies in ground-based instrumentation in one instrument: cophased imaging and Multi Conjugate Adaptive Optics (MCAO; Ragazzoni et al. 2000). Initially introduced as LINC, the LBT INterferometric Camera, LINC is now the first step in the implementation towards the final goal: NIRVANA, the Near-IR/Visible Adaptive iNterferometer for Astronomy. The difference between the two phases of implementation are the capabilities (and the complexity) of the adaptive optics systems. LINC incorporates a single on-axis wavefront sensor per telescope while NIRVANA provides full MCAO capabilities. The realization of LINC-NIRVANA is a joint undertaking by German and Italian institutes.

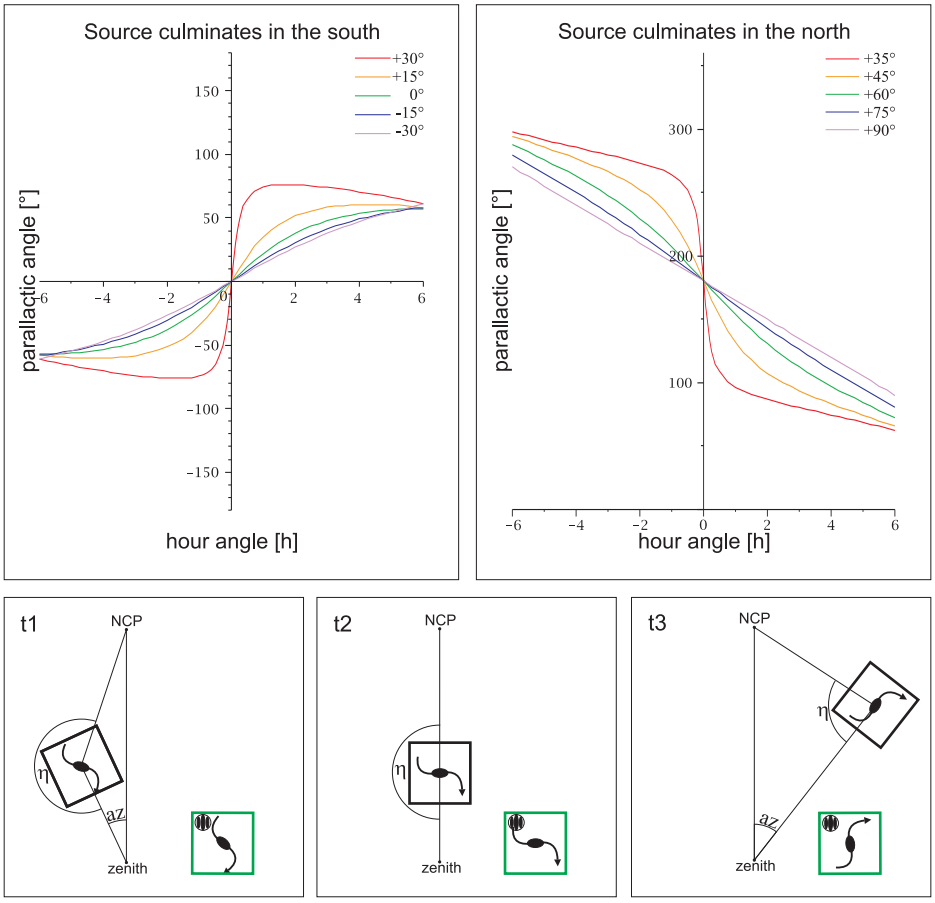

Figure 1.9: *Parallactic angle η as function of the hour angle. In this comparison a latitude of 32.7°(the latitude of the LBT) is considered. The alt-azimuth mounting of the LBT causes the target's image to rotate in the focal plane as the hour angle changes. In the bottom panels this effect is sketched for a target that is culminating in the north. 3 successive hour angles are shown: before (t1), at (t2), and after (t3) meridian transit. Because of the rotation of the earth the target appears to be rotating around the north celestial pole (NCP). To follow the target on the sky, the azimuth angle of the telescope has to change and with the azimuth angle the parallactic angle η changes, too. The highest velocities $\frac{d}{dt}\eta$ are achieved for objects that are near the zenith at meridian transit (cf. also Sect. 3.2.3). In the green boxes the image of the target is shown as it appears on the detector.*

1.5.1 Cophased imaging

Because it obeys the homothetic pupil condition (cf. Sect. 1.1.2) in its imaging concept, LINC-NIRVANA can profit from the resulting large interferometric FoV in two ways: It provides a large interferometric science FoV that is merely limited by the cost of NIR focal plane arrays (FPAs). In addition, it allows to exploit the full FoV to choose from a larger pool of off-axis reference stars for fringe tracking. The beam combination is realized by a Cassegrain telescope within the cryostat of LINC-NIRVANA. The fringes in the image plane of the beam-combiner telescope comprise the phase information preserved by the coherent combination. This is the case also for off-axis sources that are imaged by LINC-NIRVANA.

To be able to integrate on the science detector for longer than fractions of a second without loosing fringe contrast and the respective gain in spatial resolution, fringe tracking (cf. Sect. 1.3.3) is mandatory. The Fringe and Flexure Tracking System (FFTS), therefore, is the adaptive optics system that is inherently necessary to operate LINC-NIRVANA as a cophased imaging camera.

1.5.2 Multi Conjugate Adaptive Optics

The layer-oriented MCAO units forseen for LINC-NIRVANA are sophisticated systems that allow to correct for disturbances occurring in different layers of the atmosphere. Up to three deformable mirrors in each arm of the interferometer, all conjugated to atmospheric planes with different distances to the entrance pupil of the telescope, can be used to introduce corrections for the corrugated wavefront. Pyramid wavefront sensors (Ragazzoni 1996) are implemented in each unit. Each pyramid is placed at the position of a natural reference star PSF. The pupils of the reference stars are optically coadded and imaged on a single CCD. Several, possibly faint, natural reference stars contribute to the measurement of the phase distortion. Different from classical AO systems, this method is not limited by the magnitude of a single reference star but rather by the magnitude of the combined light of several natural reference stars. This advantage directly translates into a gain in sky coverage (Arcidiacono et al. 2003).

A ground-layer wavefront sensor (GWS) unit and a mid/high-layer wavefront sensor (MHWS) unit are forseen for each arm of the interferometer. The GWS will exploit guide stars in an annular field with a radial distance to the center of the FoV of $2'$- $6'$. Up to 12 pyramids can be employed in these units. The adaptive secondary mirrors, which are conjugated to the ground-layer at a height of $\sim$100 m above the telescope, are used as actuators. The MHWS units use the visible part of the light in the central two arcminutes to determine the phase

Table 1.1: *Imaging parameters of LINC-NIRVANA*

Field of View (interferometric)	
scientific:	10″x10″
FFTS:	60″x 90″
Field of View (single telescope)	
GWS:	annulus ⌀2′- 6′
MHWS:	⌀2′
Pixel scale (science FPA)	5 mas pixel^{-1}
Number of pixels	2048x2048
Wavelength coverage (science channel)	1.0 μm - 2.45 μm

distortions in more distant atmospheric layers. The corresponding conjugation altitudes of the DMs are adjustable in the collimated optical beams. A total of 8 pyramids can be used in each MHWS unit.

1.5.3 Optical design

A detailed description of the optical design (cf. key parameters in Table 1.1) can be found in Bizenberger et al. (2006). The light coming from the two bent Gregorian foci enters the instrument on opposite sides of the optical bench (cf. Fig. 1.10). Annular mirrors direct the outer field to the GWS units. The central part is collimated and reflected twice on DMs that are conjugated to different heights[5]. A dichroic beamsplitter directs the visible part of the light to the MHWS units. Light with a wavelength longer than 0.9 μm is transmitted to the piston mirror. This wedge-shaped monolithic mirror is the piezo driven actuator for the fringe tracking loop (cf. Sect. 3.1.4). It folds the optical paths of both arms of the interferometer and directs them parallel in vertical direction towards the beam combining Cassegrain telescope in the cryostat. To obey the homothetic pupil condition, it is crucial to exactly align the two parallel, collimated beams entering the beam combiner.

All detector devices that are sensitive to thermal radiation are located within the cryogenic environment of the dewar (Bizenberger et al. 2004; Laun et al. 2006). Both, science detector and FFTS detector, are located in the focal plane of the beam combiner telescope. The science field is folded by dichroic beamsplitters into the direction of the 2048x2048 pixel HAWAII-2 focal plane array. A filter wheel allows to select the required NIR bandpass for the science observation. The detector itself is mounted on a device that allows to rotate the center of the detector around the optical axis to compensate for field rotation during

[5]Because of the high costs of DMs, only one DM per arm in addition to the secondary mirror will be implemented in the beginning.

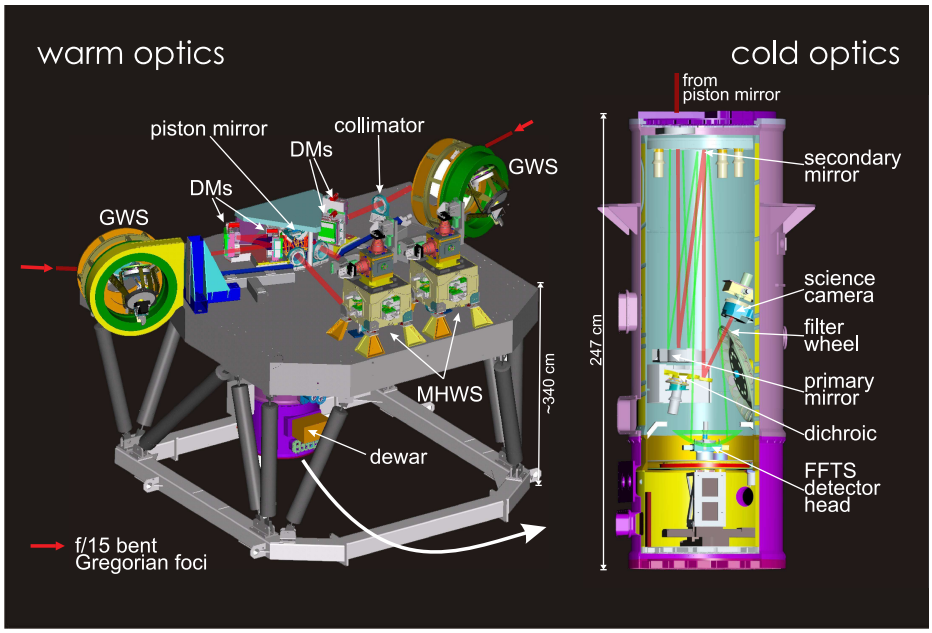

Figure 1.10: *LINC-NIRVANA cold and warm optics. The left and right arm of the interferometer are symmetrical. The warm optics are mainly assigned to the single-eye adaptive optics systems. Stellar light sources in an annulus of 2′ - 6′ around the optical axis of the telescopes are used by the ground-layer wavefront sensor (GWS). The light passing through in the center is collimated and reflected on DMs. A dichroic beamsplitter directs the visible light to the mid/high-layer wavefront sensor (MHWS) while the NIR light is reflected by the piston mirror to the Cassegrain beam combiner telescope in the cryostat. A dichroic wheel in the cryostat allows to chose the band that is reflected to the science detector. The remaining light is available to the Fringe and Flexure Tracking System (FFTS).*

long exposures. However, the direction of the fringes remains fixed with respect to the telescope geometry. By rotating the detector, the direction of lowest spatial resolution changes on the detector and causes a loss in fringe contrast in the long exposure images. Therefore, the maximum derotation angle is limited to 30°. Light that is transmitted by the dichroic beamsplitter in the central ~15″ is available to the Fringe and Flexure Tracking System (FFTS). So is the light in the outer region of the FoV, that is not covered by the science detector. A detailed description of the FFTS follows in Chapter 3.

CHAPTER 2

Simulation of atmospheric turbulence

Many parameters that are crucial for the design of adaptive optics systems of LINC-NIRVANA are not known in advance and have to be simulated or derived from theoretical considerations. Statements on the expected performance of these systems can only be based on numerical simulations. This chapter deals with a set of simulations that have been carried out to quantify the size of the isopistonic patch, a quantity that is directly related to the interferometric performance of LINC-NIRVANA. Furthermore, the performance of LINC-NIRVANA on a very prominent astronomical target, the Galactic Center, is discussed.

2.1 The Layer-Oriented Simulation Tool

All simulations presented in this chapter are based on *LOST*, the *Layer-Oriented Simulation Tool* (Arcidiacono et al. 2004). This Interactive Data Language (IDL) based numerical simulation code was developed by Italian members of the LINC-NIRVANA consortium, mainly to analyze the performance of Multi-Conjugate Adaptive Optics in a layer-oriented approach. In order to study the interferometric performance of LINC-NIRVANA, the code was extended in collaboration with Carmelo Arcidiacono to allow for the analysis of differential piston.

Setup

LOST simulates the response of an adaptive optics system to a simulated atmosphere. A simulation setup consists of a large number of parameters characterizing the telescope geometry, wavefront sensor type and setup, noise contribution and diagnostics. The atmosphere is parameterized by the number of layers that should be considered and the strength of the turbulence $\frac{D}{r_0}$, transverse wind velocity v and altitude z for each layer. An optional outer scale length L_0 can be specified for each layer (cf. Sect. 1.2.1). If this is the case, the simulation of the atmosphere will be based on the von Karman model, otherwise the Kolmogorov model is used to generate the atmosphere. The asterism, i.e. the distribution of reference stars is defined by their positions in the field of view and their apparent magnitudes. A more detailed description can be found in Arcidiacono (2004).

Simulation
A LOST simulation consists of three consecutive steps: the calculation of the model atmosphere, the simulation of the AO loop and the deduction of the results:

1. Calculation of the model atmosphere. For each atmospheric layer a random phase screen is generated that follows the power spectrum of the specified turbulence model. $\frac{D}{r_0}$ is used to quantify the strength of the turbulence in each screen. The transverse wind direction, i.e. the direction of translation of the screen is randomly chosen. LOST is based on the frozen-flow assumption (cf. Sect. 1.2.5). The phase screens themselves do not evolve with time – only their position changes as they are translated across the telescope pupil. The generated phase screens can be saved and reloaded to be able to reuse the same atmosphere for a different simulation runs.

2. Simulation of the AO loop. The atmospheric evolution is simulated in a loop with defined time increments. Each cycle represents an evolution of a specified value of milliseconds. The evolution time increment defines the base frequency of the simulation. All other loops involved in the simulation (AO loops, diagnostic loops) have time intervals that are integer multiples of the evolution time increment.

   In each evolution cycle, the phase screens are moved according to their transverse wind directions and velocities. For each reference star the total phase perturbation resulting from all phase screens are calculated. Only the sections of the phase screens that fill the footprint of the reference star are considered in the perturbation sum. The footprint of the reference star on the phase screen is the geometrical projection of the telescope pupil on the screen in direction of the reference star. Thus, it depends on the star's position with respect to the center of the FoV and the altitude associated with the phase screen.

   To obtain the AO corrected wavefront for each reference star at loop cycle t, the latest corrections, calculated in previous AO loop cycles of all DMs in the system, are subtracted from the perturbation sum. For the wavefront of the lth reference star follows

$$\psi_l(\vec{x},t) = \sum_{i=1}^{N_{\text{layers}}} L_i\left(\vec{x} - z_i\vec{\theta}_l, t\right) - \sum_{j=1}^{N_{\text{DM}}} DM_j\left(\vec{x} - z_j\vec{\theta}_l, t\right), \tag{2.1}$$

   where L_i is the ith phase screen with altitude z_i, DM_j the jth DM with conjugation altitude z_j, $\vec{x}$ the position vector on the pupil, and $\vec{\theta}$ the reference

star coordinate with respect to the center of the FoV. Each of the AO corrected wavefronts ψ_l represents a segment of the residual phase perturbation at the conjugation altitude of the wavefront sensor. The combination of these segments as a function of position and apparent magnitude of the reference star is used to calculate the next DM correction.

Since the wavefront sensor has to integrate over a certain (specifiable) period, the AO loop frequency has to be lower than the evolution frequency. And since the AO system responds with a certain latency, the DM correction is applied with the AO loop frequency but with a specifiable delay.

For diagnostic purposes, instantaneous PSFs at arbitrary positions defined by the user (e.g., on a symmetrical grid across the FoV) are calculated and the instantaneous Strehl ratio is derived for each evolution cycle. The diagnostic PSFs are coadded to determine long exposure PSFs.

3. Deduction of the results. After completion of the last iteration, several important parameters can be analyzed, such as long exposure Strehl distribution, temporal Strehl evolution or differential piston distribution and evolution. IDL routines are used to visualize the results.

2.2 Angular anisoplanatism of differential piston

In Sect. 1.2.4 the problem of angular anisoplanatism was introduced. Wavefronts propagating from two distinct directions pass through different regions in the atmosphere. The degree of correlation between the two wavefronts depends on the angular separation of the emitting sources and on the atmospheric turbulence in the different layers. The distance between a phase reference star and a science target, for which the correlation between the two phase distributions is still acceptable, is described with the isoplanatic angle θ_0. The region around a reference star with angular separations smaller than the isoplanatic angle is often called isoplanatic patch.

A similar quantity refers to the lowest order, large scale phase perturbations, that become apparent as differential piston (cf. Sect. 1.3.3), when using interferometers. The size of the patch around the fringe tracking reference star in which the spatial differential piston distribution is reasonably flat is denoted as *isopistonic angle*. A measure of the flatness is the RMS differential piston deviation with respect to the position of the fringe tracking reference. In the case of off-center fringe tracking, differences between piston values at the position of the science target and at the position of the fringe tracking reference star can not be determined and add to the residual piston. A large RMS deviation at the position

of the science target will, therefore, reduce the fringe contrast, even if the fringe tracker provides a good correction in the vicinity of its reference star.

The simulations presented in the following sections deal with the size of the isopistonic patch. The isopistonic angle obviously depends on the atmospheric conditions. But also the performance of the MCAO systems has a significant influence on the flatness of the differential piston distribution. To determine the importance of both influences, several simulations probing standard and extreme cases were performed.

2.2.1 Simulation setup

All simulations are based on atmospheric models consisting of seven layers. Each layer is represented by a perturbation phase screen that is randomly generated and obeys the power spectral density distribution of Kolmogorov. A two layer MCAO correction is considered in each simulation. In addition to the ground layer, corrections are applied for a second, high altitude layer at a conjugation altitude of 6000 m. Parameters that are common in all simulations are listed in Table. 2.1. Each simulation covers a period of 5.75 or 6.00 seconds with a resolution of 0.5 msec and required ~2 weeks of computing time on a 2.8 GHz PC. The time coverage was limited by the size of the main memory (4 GB). It is sufficient to investigate differential piston angular anisoplanatism, since these field dependent variations occur on much shorter time scales.

Differential piston is determined for a square grid of 25 positions in the central arcminute FoV – the region which can be accessed by the FFTS. The differential piston distribution is analyzed with respect to the value at the center of the FoV. This approach corresponds to a setup in which the fringe tracking reference star is in the center of the FoV and the angular distance is determined up to which a science target can be located at. In the natural observing strategy the positions of the targets are swapped: the science target is in the center of the FoV and the distance to the reference star must not exceed the isopistonic angle $\theta_{0,\mathrm{Piston}}$.

2.2.2 Atmospheres and asterisms

At the time when these simulations were done, C_n^2 and wind profile measurements for Mt. Graham did not exist. Since then, initial measurement campaigns at the site have been carried out (Egner 2006). The amount of data currently at hand provides only a tentative picture of the actual atmospheric conditions above Mt. Graham. In Sect. 2.3, these initial measurements are considered. In the simulations dealing with the differential piston variation, atmospheric input

Table 2.1: *Parameters that are common in all simulations*

telescope and system parameters:	
telescope diameter	8.2 m
central obscuration	not considered
zenith distance	0°
GWS FoV diameter	120″– 360″
MHWS FoV diameter	0″– 120″
λ_{science}	2.2 μm
number of DM	2 per channel, 4 total
conjugation altitudes	100 m , 6000 m
λ_{WFS}	0.75 μm
loop parameters:	
time step	$5{\cdot}10^{-4}$ s
number of steps	11500 or 12000
common atmospheric parameters:	
number of layers	7
power spectrum	Kolmogorov
noise parameters of MCAO CCDs:	
bandwidth integration	0.4 μm
overall quantum efficiency	0.3
RON	3.5 and 4.0 [e^- $pix^{-1}frame^{-1}$]
sky brightness (R-band)	20.0

parameters are based on data from two other sites: Data sets for $\frac{D}{r_0}$ and wind profiles were taken from Paranal and San Pedro Martir (private communication).

All parameter sets are based on a reference wavelength of λ=2.2 μm. The profiles representing Paranal are identical to the parameters used in the simulations quantifying the performance of LINC-NIRVANA (Arcidiacono 2005). They result in a seeing angle of ~0.73″ in the V-band. To consider worse atmospheric conditions, the annual mean of the C_n^2 and wind profile of the San Pedro Martir site in Mexico, ~550 km west of Mt. Graham and at similar altitude (2720 m vs. 3200 m at Mt. Graham) were used to obtain the necessary input parameters. The derived $\frac{D}{r_0}$ parameters result in a mean r_0=0.068 m and in a seeing angle of θ_{seeing} ~1.5″ at V-band. Both sites considered here are located close to the sea and all atmospheric profiles from these locations may not fully represent the conditions predominating at Mt. Graham. Therefore, the detailed results may not be directly transferable to the conditions at the LBT. However, the main intention behind the simulations, the study of the influence of seeing and MCAO on the size of the isopistonic patch, is not altered by the use of other atmospheric data.

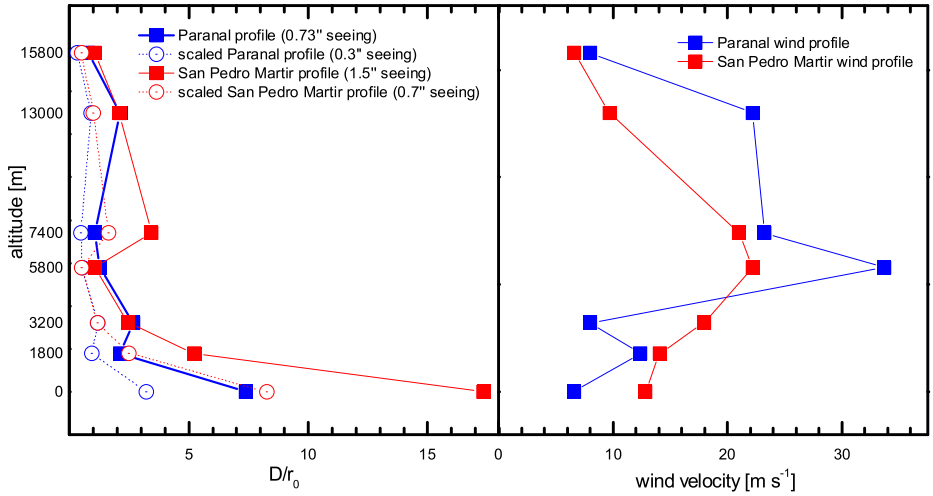

Figure 2.1: *Atmospheric parameters used for the simulations. The values for $\frac{D}{r_0}$ correspond to a wavelength λ=2.2μm. The profiles of the two sites both also have been scaled to represent better seeing conditions. For each profile the resulting seeing angle in the V-band is stated. The four profiles span the full range from extraordinary good to terrible seeing.*

Atmospheric screens were created for 7 altitudes (cf. Fig. 2.1). New screens were generated for each simulation, even for those with the same atmospheric parameters. These screens were moved according to the given wind velocities but with random directions for each layer. As a consequence, the resulting differential piston RMS maps of different simulations with identical parameter sets shown in Figures 2.3 and 2.4 vary slightly in their appearance.

Both $\frac{D}{r_0}$ profiles have also been scaled to represent better seeing conditions. This allowed the analysis of excellent seeing (Paranal atmosphere representing a seeing of 0.3″ at V-band) and the comparison of the San Pedro Martir atmosphere (scaled to a seeing of 0.7″) with the Paranal conditions.

The performance of an MCAO system (Arcidiacono 2005) is strongly coupled to the availability of bright reference stars. Since the layer oriented MCAO is able to optically combine the light of several reference stars for the determination of the correction matrix, the distribution in terms of position and apparent magnitude of the full asterism available to the system is relevant for the performance.

For the simulations presented in this section, two exemplary asterisms were considered: “lat 20” and “ngp 0-31” (cf. Fig. 2.2), roughly corresponding to fields at a galactic latitude of 20° and at the north galactic pole, respectively. With a total V-band magnitude within 6′ of 9.6 mag, lat 20 represents a rather

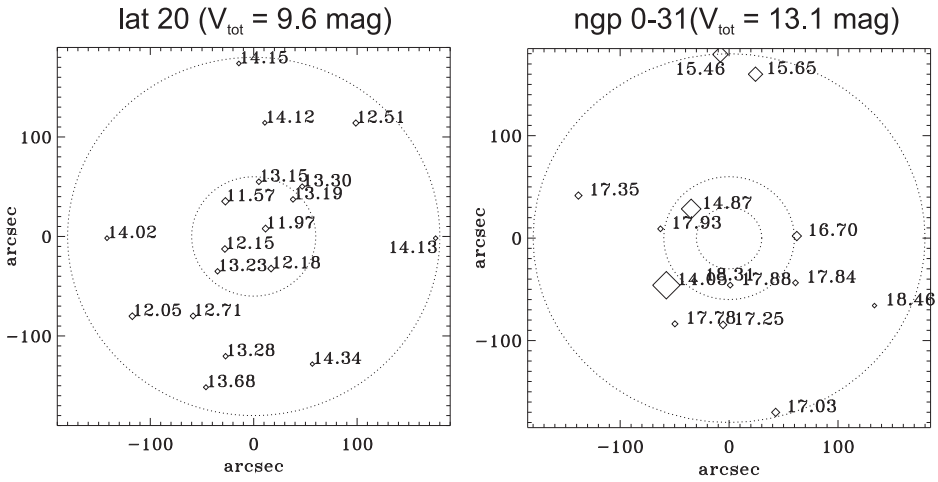

Figure 2.2: *Asterisms used for the simulations of the isopistonic patch size. The lat 20 case represents a bright asterism, for which a good MCAO performance can be assumed. ngp 0-31 is the contrary case resulting in low MCAO performance.*

Table 2.2: *Parameters that were adjusted to comply to the considered asterism.*

	lat 20	ngp 0-31
Gain DM1	0.55	0.6
Gain DM2	0.35	0.6
Spatial sampling WFS1	32	8
Spatial sampling WFS2	18	7
Integration time WFS1	2.5 ms	10 ms
Integration time WFS2	1.0 ms	20 ms

bright case that allows for good MCAO performance, ngp 0-31 (V_{tot}=13.1 mag), on the other hand, represents the faint end that has been considered. Details are given in Arcidiacono (2005).

Based on the results of optimization tests, several parameters had to be adjusted to the asterism to provide a better MCAO performance. The parameters that were specific to the considered asterism are listed in Table 2.2.

2.2.3 Results

Figures 2.3 and 2.4 summarize the results of the simulations in terms of spatial distribution of differential piston over the FoV. For each time step, the differential piston at any position is referenced to the differential piston value at the center of the FoV (cf. Fig. 2.5). The resulting maps, therefore, represent the RMS scatter

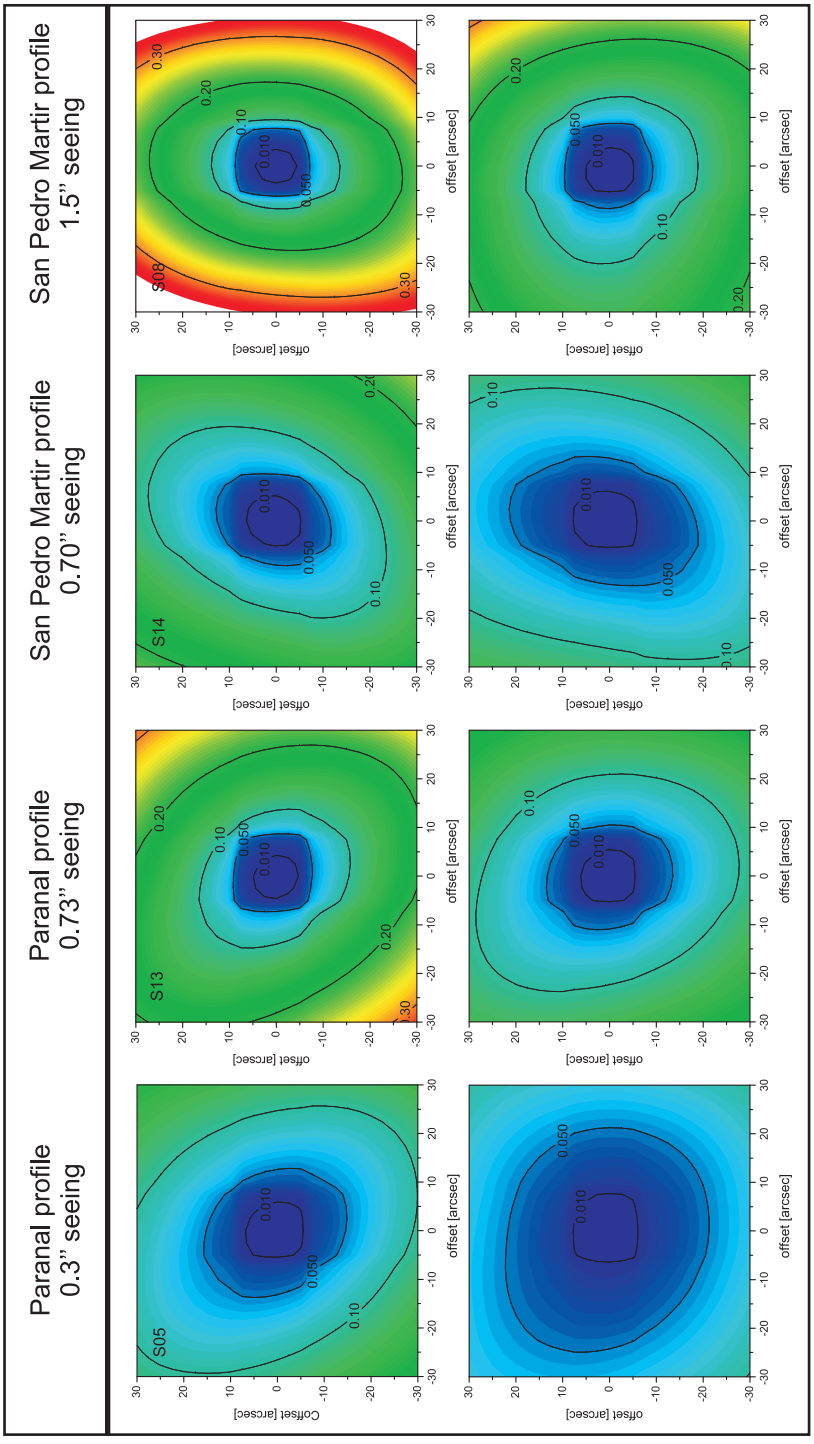

Figure 2.3: *Spatial distribution of atmospheric differential piston. The maps show the RMS deviation from the value at the center position. The contours represent multiples of λ (=2.20 μm). The maps in the bottom row show the spatial distribution with MCAO correction (using the bright asterism* ***lat 20****).*

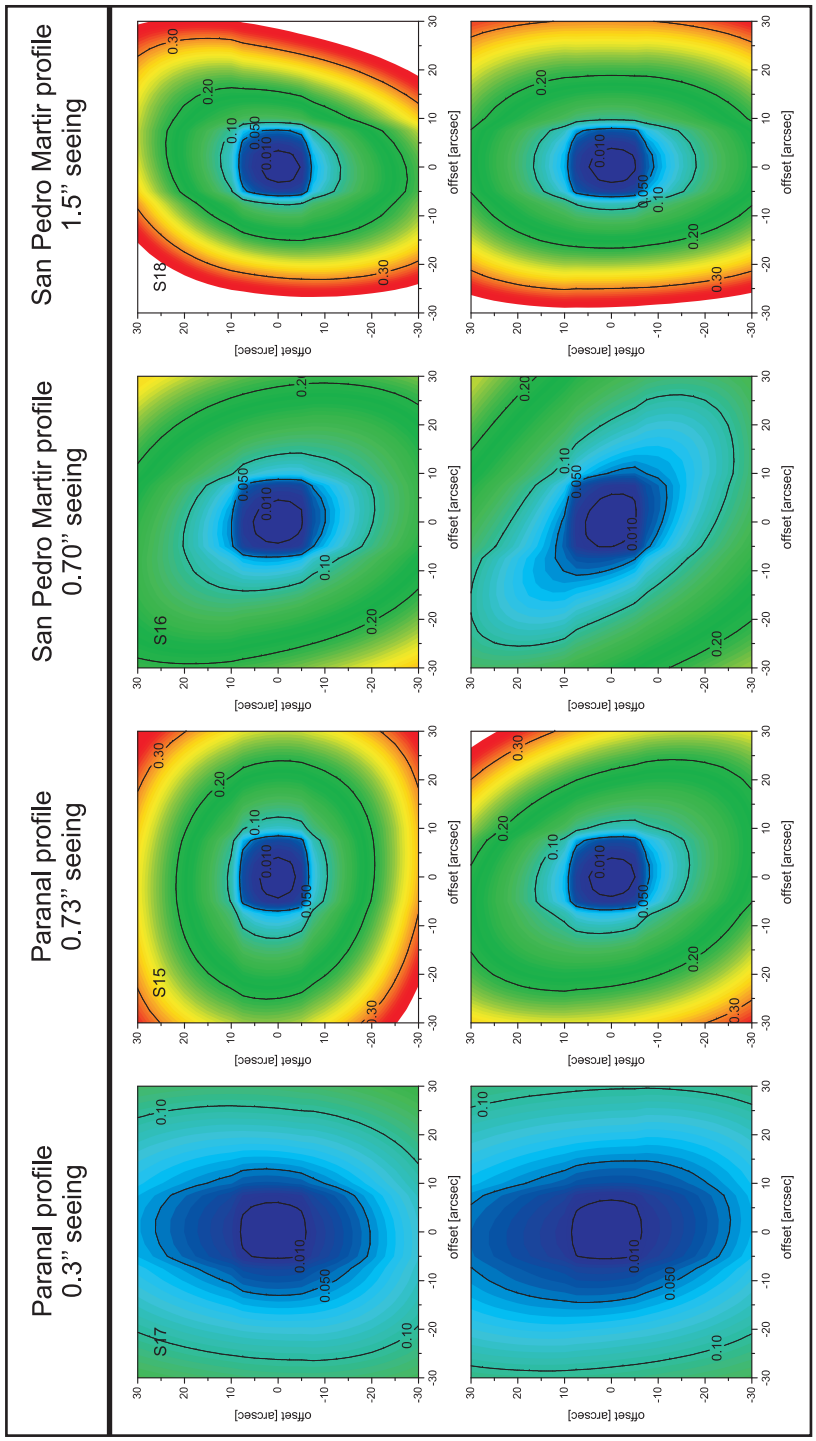

Figure 2.4: *Spatial distribution of atmospheric differential piston. The maps show the RMS deviation from the value at the center position. The contours represent multiples of λ (=2.20 μm). The maps in the bottom row show the spatial distribution with MCAO correction (using the asterism* ***ngp 0-31****).*

at any position with respect to the location of the science target. This RMS scatter is shown both with and without applied MCAO correction. A characteristic measure is the size of the region with a differential piston RMS smaller than the residual piston goal of 0.1 λ. Table 2.3 contains the corresponding patch sizes.

Table 2.3: *Radii of regions with RMS differential piston deviation from the central position of $\leq 0.1\lambda$. Values for patch sizes parallel and perpendicular to the direction of the baseline (BL) are given.*

θ_{seeing} (V-band)	atmosphere $\theta_{0,\text{Piston}}$		MCAO corrected $\theta_{0,\text{Piston}}$ (lat 20)		$\theta_{0,\text{Piston}}$ (ngp 0-31)	
[″]	∥ BL [″]	⊥ BL [″]	∥ BL [″]	⊥ BL [″]	∥ BL [″]	⊥ BL [″]
0.3	26	>30	>30	>30	30	> 30
0.73	13	14	21	28	11	17
0.7	15	24	26	>30	20	24
1.5	10	13	16	19	9	18

2.2.4 Discussion

Esposito et al. (2000) discuss the differential piston angular anisoplanatism analytically and base their analyses in the case of the LBT on a modified Hufnagel-Valley model for the atmospheric turbulence profile. They state values for the anisopistonic error (RMS) as a function of the distance to the center of the FoV and as a function of the outer scale. A median r_0(V-band)=0.133 m (which corresponds to a seeing angle of 0.78″) was derived.

Similar to the approach in the present study, they define a threshold of 0.1λ to determine the size of the isopistonic patch. For the K-band (2.2 μm) and an infinite outer scale (which is the assumption in the present study and which corresponds to a worst case scenario), they derive isopistonic patch radii of 12.6″ along the direction of the baseline and 16.8″ orthogonal to this direction. These values are in agreement with the findings in the simulations. For a seeing angle of 0.73″ at V-band isopistonic patch radii of 13″ and 14″ are derived. The systematic difference of the RMS isopistonic patch size parallel and perpendicular to the direction of the baseline is an innate feature of the geometry of the LBT aperture. In the study of Esposito et al., the influence of adaptive optics on the size of the isopistonic patch was not included. The MCAO systems flatten the incoming wavefronts in each of the two interferometric channels, and by doing this, reduce the spatial variation of differential piston in the FoV. The

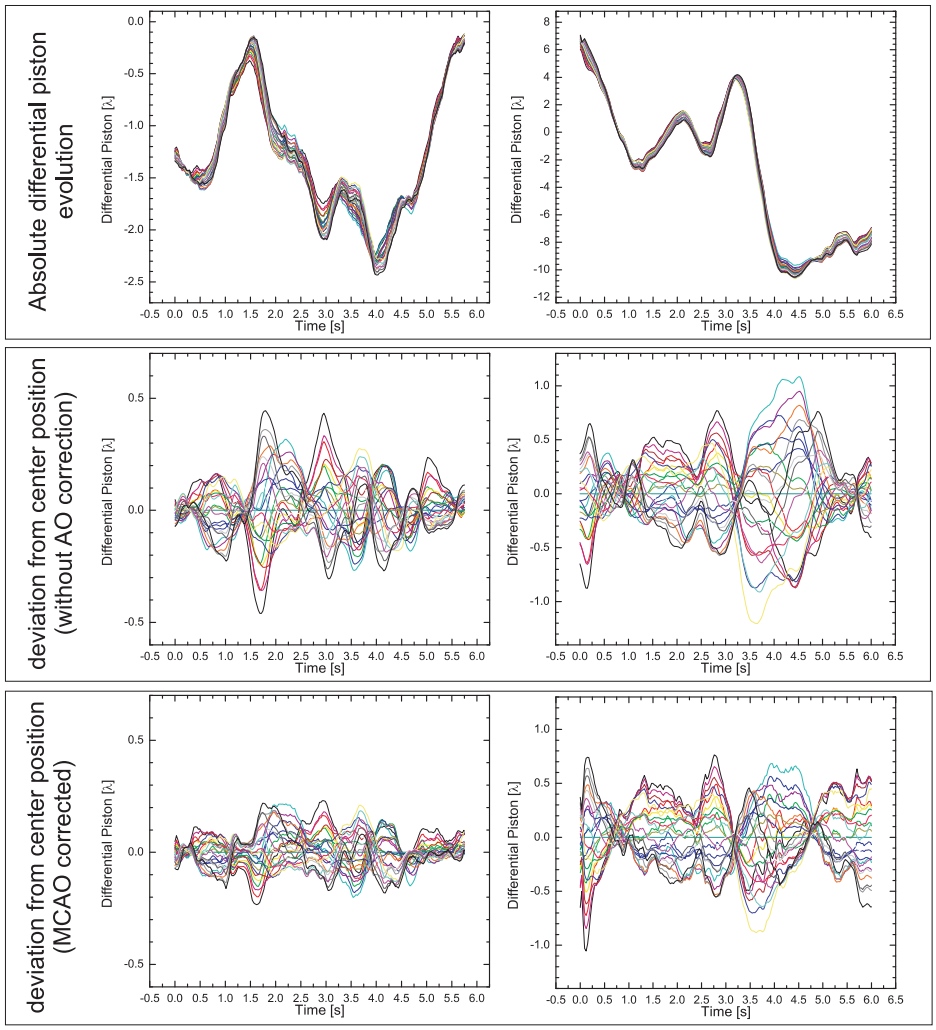

Figure 2.5: *Time sequences of differential piston for two extreme cases: the panels in the left column represent the best case scenario (0.3″ seeing case, bright lat 20 asterism), the panels in the right column the worst case scenario (1.5″ seeing, faint ngp 0-31 asterism). MCAO confines the range over which the piston values spread. The efficiency is dependent on the performance of MCAO.*

effectiveness of the flattening is dependent on the MCAO performance, which again depends on the asterism. It can be concluded, that:

- The isopistonic patch size is highly dependent on the degree of atmospheric turbulence. With the caveat of a missing mean atmospheric turbulence profile for the Mt. Graham site, both the present study and the study of Esposito et al. (2000) find representative RMS isopistonic patch sizes of $\sim 15''$ radius.
- The derived isopistonic patch sizes are based on an atmospheric model with infinite outer scale. This is a worst case assumption. The angular sizes increase significantly with decreasing outer scale.
- The isopistonic patch size can be increased significantly with the help of MCAO. The gain in the isopistonic patch size is depending on the MCAO performance, which is again dependent on the asterism that is used for reference.

2.3 The Galactic Center as target for LINC-NIRVANA

The Galactic Center has been subject to numerous studies covering a wide range of different wavelengths. In the NIR the investigation of the dynamics of stars has provided compelling evidence for the existence of a super-massive black hole at the center of the Milky Way (e.g., Eckart & Genzel 1996; Ghez et al. 1998). Additional strong evidence for a massive black hole at the center, the position of Sgr A*, is provided by the observation of variability with typically 60-100 minute flares in the X-ray and NIR wavelength domain (e.g., Baganoff et al. 2001; Genzel et al. 2003).

Since Sgr A* is remarkably faint also in the NIR, such studies would clearly benefit from the resolving power and sensitivity provided by LINC-NIRVANA. Figure 2.6 contains a comparison of current 8 m class resolution and the LINC-NIRVANA resolution element. A main drawback, however, is the low declination of the target. With $\delta \sim -29°$ the maximum elevation of the source is always less than 30°, when observed with a telescope at a latitude of +32° (cf. Fig. 2.7). For such an elevation the column of air between the telescope and the object is more than twice as long as the one for an object that is observed in the zenith (which corresponds to airmass=1). Therefore, approaching wavefronts have to propagate a longer distance through turbulent medium and suffer from stronger perturbations. The AO systems can only partially compensate for these perturbations – the Strehl ratio is decreased. Furthermore, low-elevation observations may suffer from increased instrumental flexure.

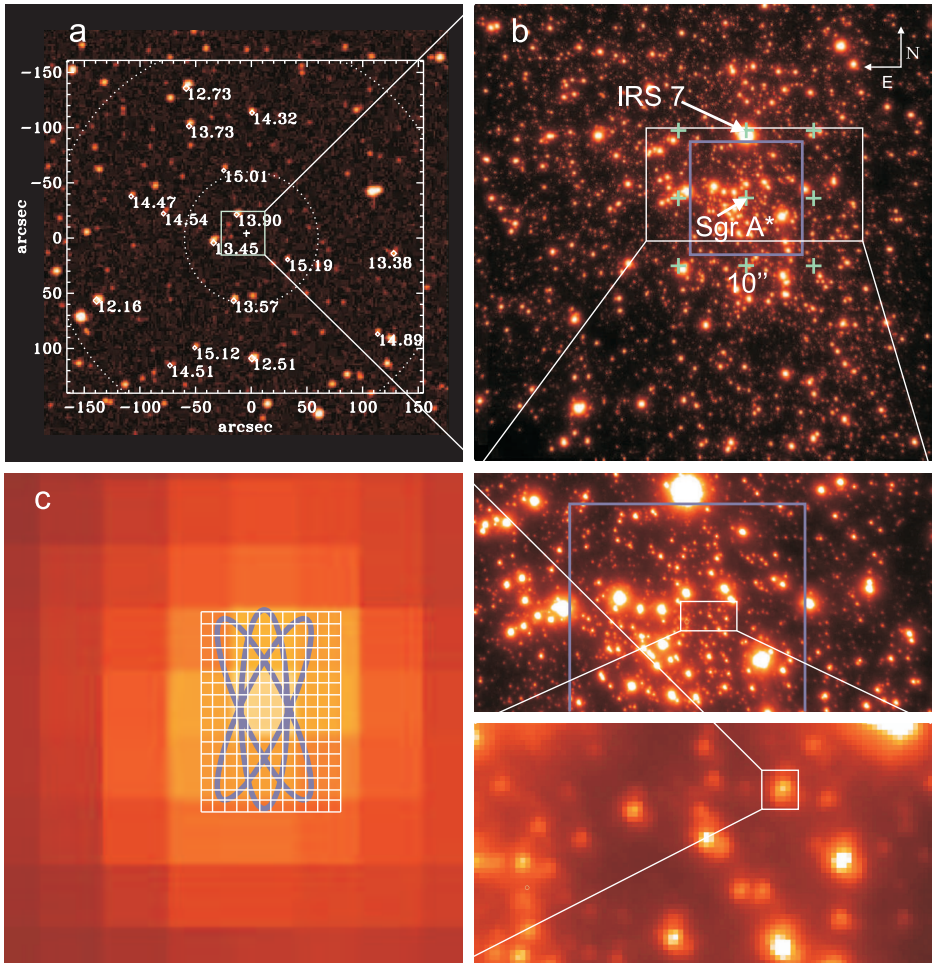

Figure 2.6: *a) Optimal asterism for (LINC-NIRVANA) MCAO supported observations of the Galactic Center. Underlying is a digitized sky survey image in the visible. With a total V-band magnitude V_{tot} =10.55 the asterism is relatively bright. b) K-band image (NACO) of the central 40.5″×40.5″. The blue box indicates the size of the scientific FoV of LINC-NIRVANA. IRS 7, located about 7″ north of Sgr A*, is the brightest star in the NIR in the vicinity. It is well suited as reference star for fringe tracking. The green crosses indicate the positions for which the imaging performance of LINC-NIRVANA was probed in the simulation presented here. c) Comparison of the spatial resolution capabilities in the K-band of LINC-NIRVANA and current 8 m class AO supported telescopes. Shown is the size of a K-band fringe, that is rotated by ±25° to indicate the range for the direction of maximum resolution. This direction is defined by the parallactic angle. The range of parallactic angles that are coverable with the LBT is limited by the low declination of the target (cf. Fig 2.7) The white grid represents the pixel scale of LINC-NIRVANA. Each pixel corresponds to 5 mas.*

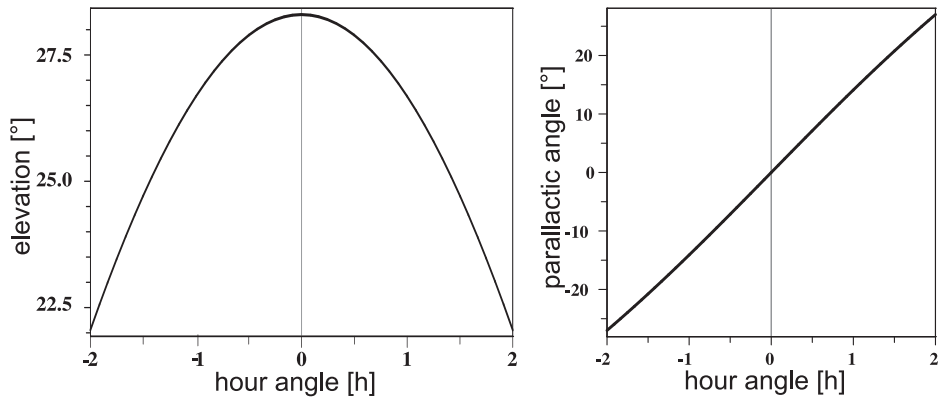

Figure 2.7: *Elevation and parallactic angle of the Galactic Center as a function of the hour angle. Because of its low declination, the Galactic Center is difficult to observe from the northern hemisphere. A low elevation is equivalent to a high airmass, which reduces the image quality.*

Another, related aspect limiting the spatial resolution that is achievable, is the limited coverage of the parallactic angle (cf. Sect. 1.4.2). The Galactic Center is observable for approximately 4 hours (depending on the minimum elevation that is feasible). Within this period, the parallactic angle changes by only about 50°. As a consequence, it is not possible to achieve the same maximum resolution in all directions. Reconstructed images based on data representing the full range of observable parallactic angles will show elongated point sources.

2.3.1 Simulation setup

The simulation of the imaging performance of LINC-NIRVANA using the Galactic Center as target includes a set of atmospheric parameters, that were actually measured on Mt. Graham by Egner (2006, pp 108). The author distinguishes between representative "good", "average" and "bad" C_n^2 profiles. For each of the 3 cases he states a set of r_0 values for seven different altitudes and the average wind velocity at each of these altitudes. In the simulations presented here, the required $\frac{D}{r_0}$ were retrieved from the "good" dataset, which represents the C_n^2 profiles resulting in r_0 values in the top 20% to 30% of the cumulative distribution. The resulting seeing in this case is θ_{seeing} =0.56″(at V-band). Since the stated r_0 values correspond to $\lambda = 0.5\ \mu$m, they had to be scaled to correspond to $\lambda = 2.2\ \mu$m (cf. Sect. 1.2.2). The resulting values for $\frac{D}{r_0}$ are shown in Fig. 2.8.

The profile corresponds to airmass 1, i.e., a zenith distance $\theta = 0$. To be more realistic, a further scaling factor was applied to take the high airmass in the

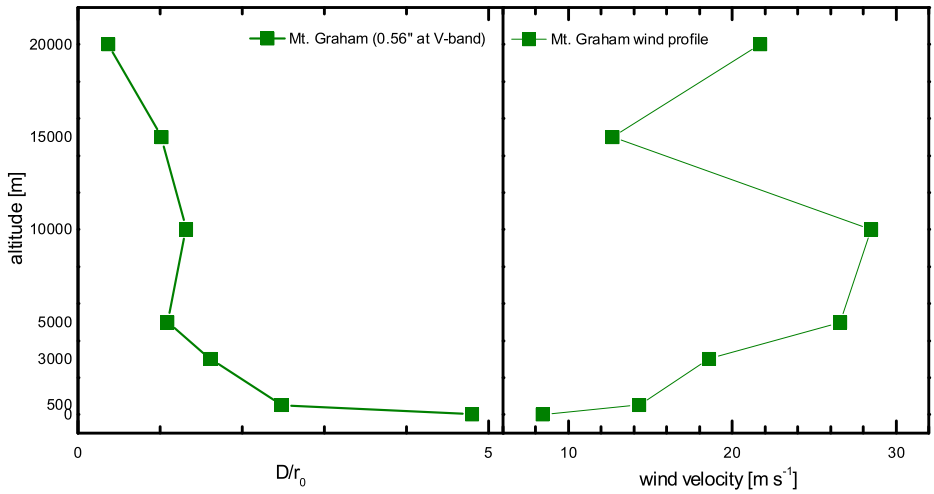

Figure 2.8: *Atmospheric parameters used for the simulation of the Galactic Center. $\frac{D}{r_0}$ correspond to $\lambda = 2.20\ \mu m$. The values were derived from C_n^2 profiles measured on Mt. Graham (Egner 2006). The values considered here represent the low r_0 tail of the SCIDAR measurements (good atmospheric conditions). A detailed discussion, also of the heights of the different layers can be found in Egner (2006).*

case of the Galactic Center into account:

$$\frac{D}{r_0}\left(\theta\right) = \frac{D}{r_0}\left(\theta = 0\right) \cdot \cos\left(\theta\right)^{-3/5} \tag{2.2}$$

A mean zenith distance of $\theta = 65°$ was chosen (cf. Fig.2.7). The conjugation altitudes of the DMs were adjusted correspondingly.

Several short test simulations have been performed to identify the optimum asterism that should be used in the case of the Galactic Center. It turns out that the constellation of reference stars, which can be exploited by GWS and MHWS, is in favor of a good MCAO performance. A total V-band magnitude of 10.55 is available, for the layer-oriented MCAO concept, in which the light of several reference stars is optically coadded.

2.3.2 Results

In total, 10000 temporal steps were simulated, each corresponding to 1 ms. The achievable Strehl ratio was determined for a square grid of 9 positions with a spacing of 6″(cf. Fig. 2.6, panel b). The grid spacing was chosen such that it includes the position of the NIR bright source IRS 7, which is ideally suited as a reference target for fringe tracking. At this position the differential piston is

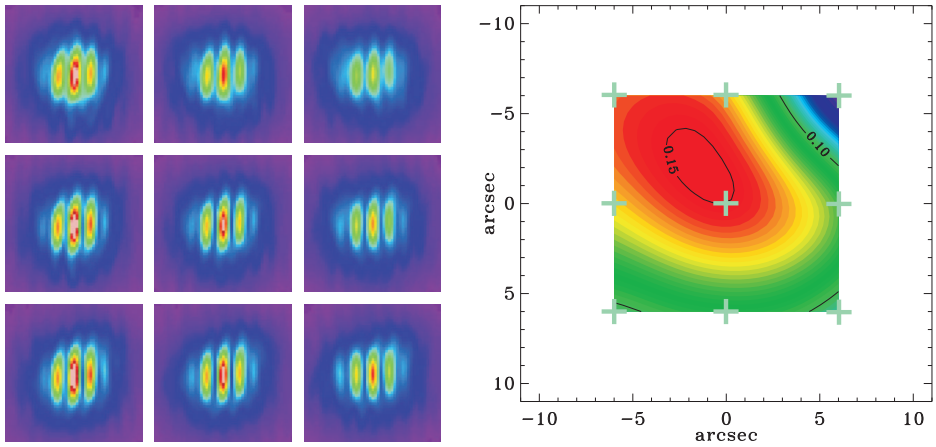

Figure 2.9: *Long exposure PSFs (at $\lambda = 2.2$ μm) and Strehl map for a 12″×12″ field around Sgr A*. The diagnostic PSFs are determined in a rectangular grid marked by the green crosses. The distribution of the Strehl ratio across the scientific FoV provided by LINC-NIRVANA is relatively flat (10%-15%). The simulation considers good but realistic atmospheric conditions on Mt. Graham and an angular zenith distance of θ =65°. It assumes that all systems still work properly at low elevation.*

determined and corrected every 5 ms. The full OPD correction is applied, neglecting residual differential piston caused by measurement uncertainties, control loop performance etc. For each of the 9 positions, long exposure PSFs were determined (cf. Fig. 2.9). Since a fringe tracking reference is used, the resulting diagnostic PSFs not only contain the effects of not perfectly corrected high-order perturbations but also of differential piston angular anisoplanatism.

Figure 2.9 shows, that the distribution of the Strehl ratio across the scientific FoV of LINC-NIRVANA targeting Sgr A* is relatively flat. The achievable Strehl ratio under the aforementioned conditions of ≈10%–15% is sufficiently high for the reconstruction of diffraction limited images.

2.3.3 Potential next steps

The simulation presented here demonstrates the principal usefulness of observations of the Galactic Center with LINC-NIRVANA, assuming the technical feasibility of observations at an elevation of 25°. Its relevance suggests the further use of the Galactic Center as challenging showcase for the performance of LINC-NIRVANA. Several extentions to the presented simulation of the Galactic Center are possible. The ability to determine the long exposure PSFs at any position in the FoV allows to simulate the PSF right at the position of important stellar sources in the vicinity of Sgr A*. Based on existing source maps, images

of the Galactic Center region with field dependent variations of the PSF and different parallactic angles can be generated. Furthermore, the gain in sensitivity provided by the LBT can be considered by adding a simulated faint star field to the known source list. The performance of deconvolution and image reconstruction algorithms may be tested with these images.

CHAPTER 3

Cophasing LINC-NIRVANA

As already pointed out in the preceding chapters, fringe tracking is indispensable for cophased imaging with LINC-NIRVANA. The following discussion of the FFTS will focus on the principle of operation, the opto-mechanical design and the fringe detection algorithm. The control loop and the software design are outlined and preliminary results of a fringe tracking experiment in the laboratory are reported. At the time of this thesis (summer 2007), the system is still under development. Especially the control loop optimization is not yet completed. Therefore, a comprehensive performance analysis is not yet possible. Furthermore, the discussion is limited to the fringe tracking task of the FFTS. With increasing knowledge of the mechanical behavior of various components in the instrument the flexure tracking issue has recently gained in importance, too.

3.1 Principle of operation

Among the Adaptive Optics systems within LINC-NIRVANA, FFTS is tailored to deal with the lowest order Zernike modes: the real-time detection and compensation of differential piston and the correction of misalignment due to instrumental flexure. For the first task, the most challenging of the three fringe tracking modes (cf. Sect. 1.3.3) will be implemented in order to provide the best possible image quality: cophasing. This is the only mode that allows for a stable fringe pattern with highest possible fringe contrast on the science detector over a longer period of time.

In order to take measures against a continuously varying differential piston, the phase delay information has to be retrieved at the position at which the beam combination takes place. As part of a homothetic imaging interferometer with beam combination in the image plane, a FPA at the combined focus is needed as sensor for the fringe tracker. Furthermore, to be able to respond to differential piston, an actuator has to be part of the servo loop, that allows to introduce controlled changes of the optical path length in one or both arms of the interferometer. This is the task of the piston mirror. The individual components in the fringe tracking loop are introduced in more detail in Sect. 3.1.4.

3.1.1 FFTS cophasing in a nutshell

A suitably bright reference point source in the FoV is used to analyze its PSF in the focal plane of the beam combiner. A filter wheel in front of the FFTS detector allows to select the NIR band that is used for fringe tracking and allows to switch between broadband filters with a small coherence length or narrow-band filters with a longer coherence length. The FFTS detector samples the PSF with a frame rate of 50 Hz – 200 Hz. Each frame is averaged perpendicular to the fringe direction to obtain a PSF profile. An analytic model is fitted to this one-dimensional intensity profile. The resulting differential piston is fed into a piston control algorithm that calculates, based on this and preceding values, as well as on model parameters, the actuating variable in the control loop. To actually compensate for the measured differential piston, the piston mirror is moved according to the actuating variable and introduces controlled path-length variations. The result should be a time-stable fringe pattern across the imaged sources on the science detector with the white light fringe in the center of each PSF and a time varying residual piston of less than $\frac{\lambda}{10}$.

3.1.2 PSF acquisition in the FoV

The great advantage of LINC-NIRVANA being a homothetic imager is that a large FoV can be exploited in the search for a suitably bright reference source. In general, the size of the usable FoV is limited by:

- The differential piston angular anisoplanatism (cf. Sect. 2.2). The size of the isopistonic patch is mainly influenced by the seeing and the performance of the mid/high layer MCAO system.
- The influence of optical aberrations on the interferometric PSF. The degree of static misalignment of the two LBT single eye Airy patterns depends on the position in the FoV. It varies with the distance to the optical axis and with its direction to the interferometric baseline. The alignment of the two Airy patterns is better parallel to the direction of the baseline than perpendicular to the baseline. This results in an elliptical shape of the usable FoV.

An increase in the usable FoV directly has a positive impact on the sky coverage of the full instrument. The larger the FoV, the higher the probability to find a suitable reference star. See Table 3.2 for the dimensions of the FFTS FoV. Since it is far too expensive to cover the full usable FoV with FPAs, the FFTS FPA has to be moved to the position of the reference star PSF in the focal plane. The FFTS will acquire images of this PSF at frame rates of up to 200 Hz. These

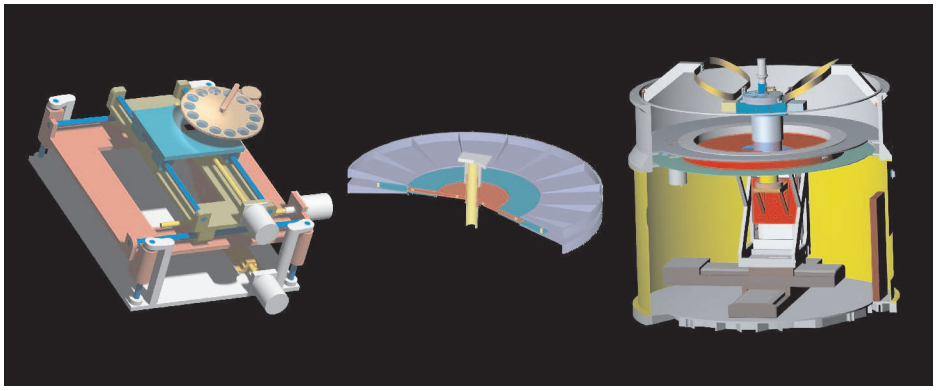

Figure 3.1: *Different detector positioning and shielding concepts studied as solutions for the FFTS hardware. Left: design study of a cryogenic positioning device. A one-dimensional prototype was built and tested. Because of demanding positioning requirements it was decided to employ ambient temperature micro positioning stages. Center: shield design with nested sliding disks. Right: current design (cf. Sect. 3.3).*

frame rates can only be realized for a small subwindow of the FFTS detector. In order to be able to continuously acquire the light of the reference star, the FFTS detector subwindow needs to follow the trajectory of the PSF in the focal plane. A recurring repositioning of the detector followed by a continuous shifting of the subwindow on the stationary detector itself was considered to be not feasible for many reasons (such as detector size, readout speed, clock-pattern upload). Therefore, the detector chip with a fixed subwindow has to be moved continuously along the PSF trajectory (note that it can stay fixed for an on-axis reference). The fringe tracking performance is dependent on the level of precision to which the position of the PSF on the subwindow is known (cf. Sect. 3.5). Therefore, it is desirable to keep deviations from the actual position of the PSF due to positioning inaccuracies of the detector as small as possible. Subpixel (1 pixel = 18.5 μm) positioning accuracy of the detector is a challenge for any positioning device with a large travel range like in this application. But much stronger are the constraints imposed by the need of a cryogenic environment for the detector. After intense studies and negotiations with companies that have experience in the field of micro positioning, building a cryogenic positioning device that provides the required accuracies had to be considered as infeasible in the framework of this project (cf. Fig. 3.1). It was decided to search for a solution that allows to implement off-the-shelf micro positioning stages. In such a solution the detector has to be mechanically connected to, but thermally isolated and shielded from, the positioning device, which needs to be kept at ambient temperature. In Sect. 3.3 the mechanical design of such a solution is presented.

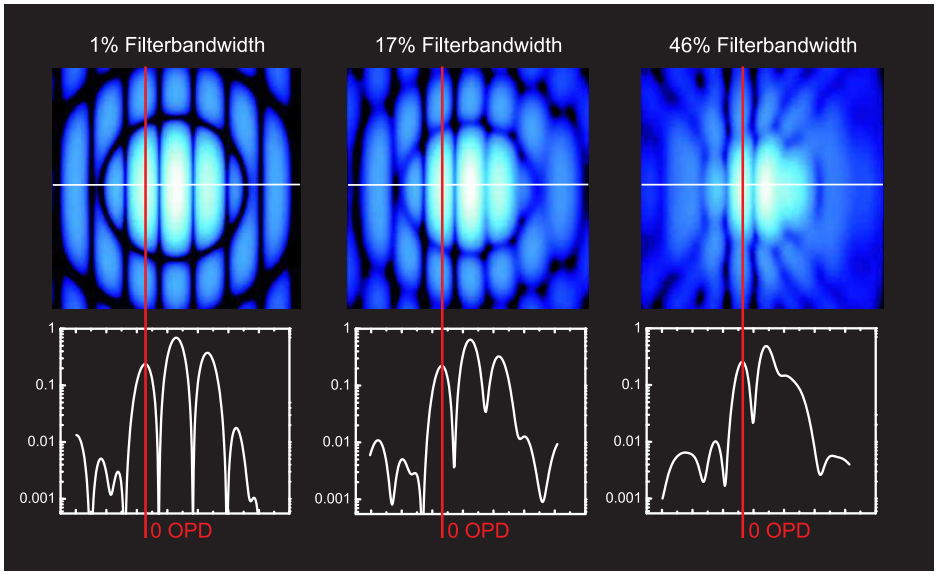

Figure 3.2: *Polychromatic PSF profiles contain information on the absolute differential piston between the two arms of the interferometer. This is an important difference to monochromatic PSFs, for which the infinite coherence length and the resulting λ-periodicity does not allow to distinguish between differential piston values with an integer multiple of λ. For cophasing the knowledge of the absolute differential piston value is required to identify the zeroth fringe. The PSFs and profiles shown here (in logarithmic scale) result from a differential piston of 1λ. The broader the polychromatic bandwidth, the clearer is the identification of the white light fringe.*

3.1.3 Image analysis

Differential piston can be identified in the position of the fringes with respect to the Airy envelope function. The direction of the white light fringe in the case of a large differential piston of several λ can also be determined directly in the PSF of the reference star. A larger differential piston gives rise to a more asymmetric PSF as can be seen in Fig. 3.2. The degree of asymmetry is determined by the coherence length l_c of the source-filter system (cf. Eq. 1.34). If the differential piston is of the order of or larger than the coherence length, the interference fringes vanish.

Column averages of the two-dimensional frames result in one-dimensional PSF intensity profiles (cf. Fig. 3.3). The profile of a monochromatic PSF of the LBT along the direction of the interferometric baseline can be expressed as:

$$I(\theta) = 2I_0 \left(\frac{2J_1(\theta)}{\theta} \right)^2 \cdot \left[1 + \cos\left(2\frac{b}{d}\theta + 2\pi P \right) \right], \tag{3.1}$$

with $\theta = 1.22\pi \frac{x - x_0}{r_A}$, I_0 and r_A representing the peak intensity and radius of a

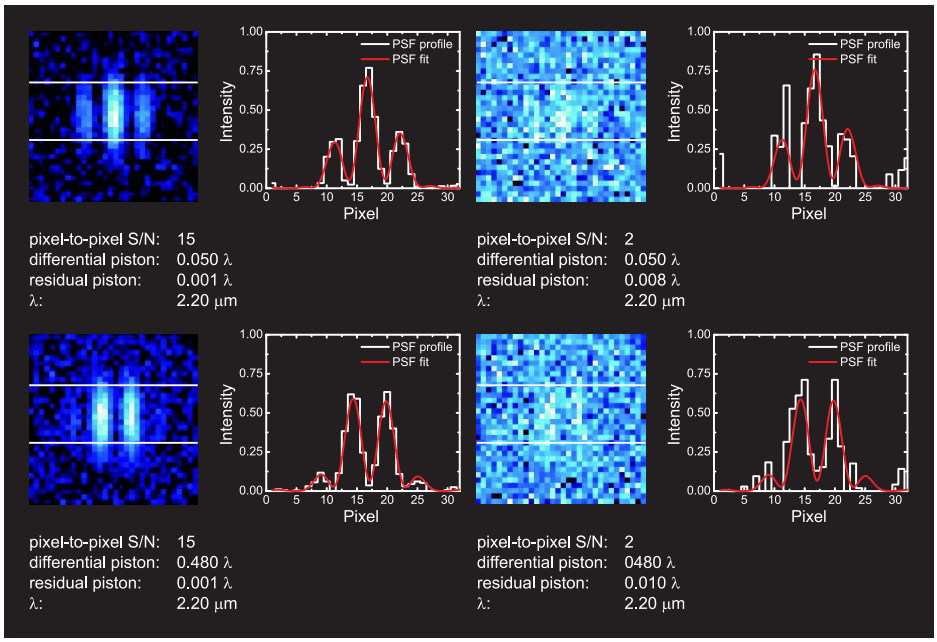

Figure 3.3: *Piston analysis in simulated PSFs with a pixel sampling and image size corresponding to the FFTS plate scale and window size. Superposed is a Gaussian noise contribution resulting in pixel-to-pixel signal to noise ratios of 15 and 2. The PSF profiles contain the pixel column averages calculated for the pixel rows in between the white lines. Although the fringe patterns in the low S/N cases become almost invisible, the frames contain sufficient information for obtaining reasonable results with the differential piston fitting algorithm.*

single channel Airy distribution, and b/d the ratio of the separation of the mirror centers and the mirror diameters. P denotes the differential piston in wavelengths between the two channels.

This analytic expression was implemented in a multidimensional fitting algorithm based on the Levenberg-Marquardt method (Huber, P.J. 1981; Press et al. 2002). The robust method is a standard approach for nonlinear least-squares optimization problems since it minimizes the χ^2 merit function in a minimum amount of iterations. Besides the parameters describing the geometry of the pupil (b,d), the single channel Airy distribution (center position x_0, I_0, r_A) and the differential piston P, the background level was considered as additional parameter. The results of a performance test are shown in Sect. 3.5. With a polychromatic modification of this algorithm it is possible to determine differential piston also greater than λ with a low pixel-to-pixel Signal-to-Noise ratio.

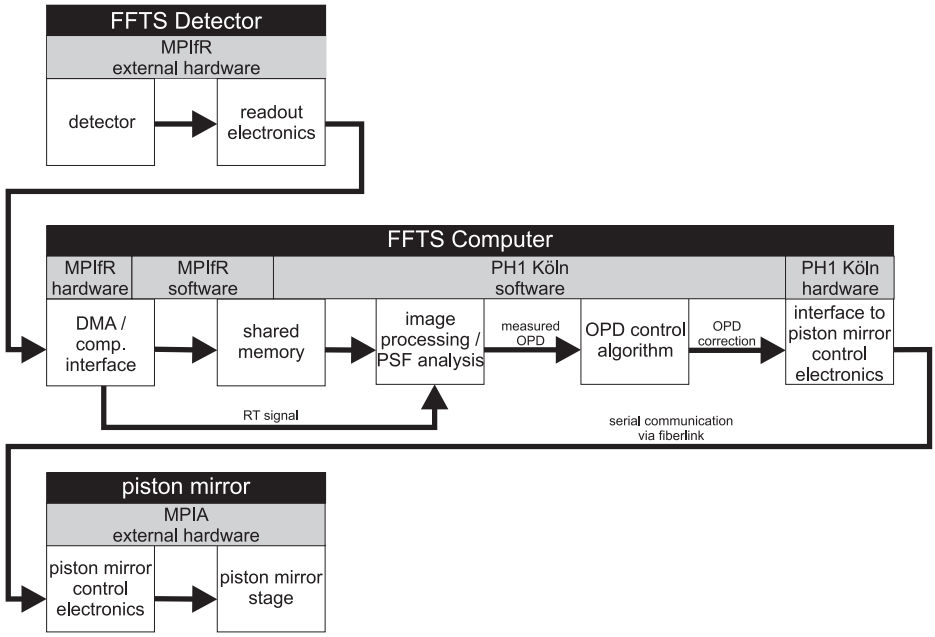

Figure 3.4: *Hard- and software components in the FFTS control loop. The arrows indicate the direction of information flow. Also shown are the institutes that are responsible for the individual components: Max-Planck-Institut für Radioastronomie (MPIfR), 1. Physikalisches Institut d. Universität zu Köln (PH1), and Max-Planck-Institut für Astronomie (MPIA)*

3.1.4 Fringe tracking control loop

The fringe tracking control loop consists of several hard- and software components. Figure 3.4 shows the 3 main parts of the servo loop (FFTS detector, FFTS computer and piston mirror) and the sequence in which the various components interact with each other.

Detector and readout electronics

The FFTS detector and associated readout electronics will be provided by the Max-Planck-Institut für Radioastronomie (MPIfR). Currently forseen is an engineering grade HAWAII-I NIR FPA to be used as FFTS detector. At this detector grade one quadrant (512×512 pixel) is fully operational, which is sufficient, since only a small subwindow will be used for fringe tracking. The detector and its fanout board is part of the detector head that is moved along the focal plane of the beam combining camera within the cryostat of LINC-NIRVANA (cf. Sect. 3.3). The fanout board is connected to the ambient temperature part of the readout electronics that is directly mounted to the vacuum recipient of

LINC-NIRVANA. Here the analog signal is amplified and digitized. A fiber link is used to transmit the obtained image data to a data interface box located next to the FFTS Computer. The data enters the FFTS Computer via a PCI DMA board. More detailed information can be found in Behrend (2005).

FFTS Computer

All image analysis, piston fitting and control tasks run on the FFTS workstation. It will be a multi-processor or multi-core system with Linux as operating system. Several software processes that are associated with the fringe tracking control loop are time critical and require high scheduling priority. These processes can be assigned to designated processors or cores. The software will take advantage of real-time functionality that is implemented in the 2.6 Kernel. An investigation of a 3rd party soft real-time extension to the Kernel (RTAI) has shown no significant advantage in addition to the functionality provided directly by the Kernel, when the software is designed to run in user space. The tests of the real-time solutions were carried out with a setup that was specific to the requirements of the FFTS software. The results of these tests are documented in Wang et al. (2006).

The control engine will also be realized as process on the FFTS computer. The choice of the control strategy that will be implemented depends on the actual differential piston power spectrum that is to be dealt with. Many instrumental factors may contribute to the power spectrum in addition to the atmosphere. These additional factors are currently under investigation. A preliminary discussion of the power spectrum and the simulated system response is given in Rost et al. (2006). In Sect. 3.4 the software design for the FFTS is outlined.

Piston mirror

The piston mirror (cf. Fig. 3.5) is the actuator in the fringe tracking servo loop. Each of the two reflective surfaces is part of the optical path of the left or the right interferometric arm respectively. The two collimated beams are approaching the mirror from almost diametrically opposed directions and are redirected in parallel towards the beam combining telescope (cf. also Fig. 1.5). The common structure is mounted on a piezo-electric nanopositioning stage. An axial motion along the direction of the approaching beams shortens one of the two optical paths while lengthening the other path by the same amount at the same time. This effect is used by the FFTS to introduce controlled path-length variations for the compensation of differential piston. The piezo stage from Physik Instrumente has a stroke of 75 μm – this corresponds to an overall OPD correction range of 150 μm. The mirror assembly consists of aluminium (AlSi35) and

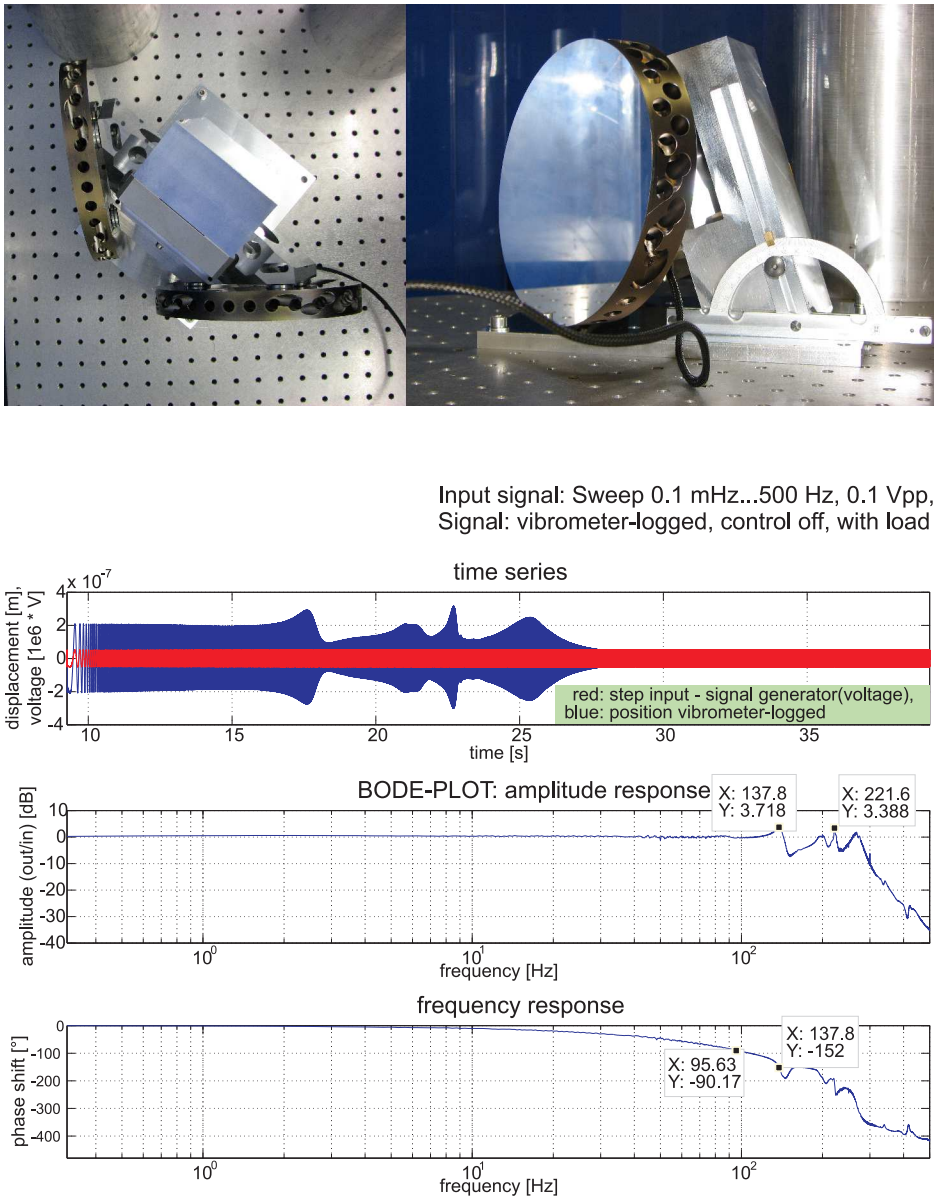

Figure 3.5: *The piston mirror and its Bode-Plot (both courtesy: Mario Brix, MPIA). Made of light-weighted aluminium, the movable load with the two reflecting surfaces is mounted to a piezo-electric nanopositioning stage. The open loop measurements show that the first resonance peak of the piston mirror assembly is at ~140 Hz. This value resembles an upper limit of the actuating bandwidth of the piston mirror hardware. A vibrometer was used to determine actual distance variations of the actuator as response to an analog signal with continuously increasing frequency. The measurements have been carried out at the MPIA.*

has a mass of 3350 g that is to be moved by the stage. It is clear that such a high mass limits the frequency response of the actuator in the servo loop and with this the control bandwidth that is achievable. Figure 3.5 shows the Bode Plot of the piston mirror. It was obtained in open loop and represents the mechanical response neglecting further bandwidth limitations imposed by the position control electronics of the device. The first resonance peak appears at ~ 140 Hz. A reliable operation of the piston mirror can only be realized below this limit.

3.2 Technical requirements

The cophasing task imposes some fundamental constraints on the correction bandwidth of the control loop as well as on the stroke of the actuator. Further top level requirements result from the need to follow the trajectory of the PSF in the FoV.

3.2.1 Amplitude

To be able to dimension the required stroke of the piston mirror, the range in which OPD variations occur has to be known. Equation 1.17 allows to derive the standard deviation for atmospheric OPD between the two apertures of the interferometer for different seeing conditions. Exemplary values are shown in Table 3.1. In these estimates the applicability of Kolmogorov statistics with an infinite outer scale L_0 is assumed. A small outer scale would result in a saturation of σ_{OPD} at smaller values. However, existing measurements of the outer scale at other sites resulted in values that are typically larger than the 14.4 m baseline of the LBT. Kolmogorov statistics, therefore, most likely provides adequate estimates.

Equation 1.17 describes the standard deviation of phase fluctuations between two points in the pupil plane. The piston value for each of the two telescopes

Table 3.1: *σ_{OPD} for different seeing conditions (cf. Eqs. 1.17 and 1.30) and a baseline B=14.4 m. The seeing angles correspond to $\lambda = 0.5\ \mu$m. θ_{seeing} values for Mt. Graham are from Egner (2006).*

$\theta_{\mathrm{seeing}}[''] $	σ_{OPD} [μm]	comment
0.3	4.7	OPD simulations, best case
0.56	7.9	Mt. Graham, 'good' seeing
0.68	9.3	Mt. Graham, 'average' seeing
0.82	10.8	Mt. Graham, 'bad' seeing
0.94	12.1	used for GC simulation
1.5	17.9	OPD simulations, worst case

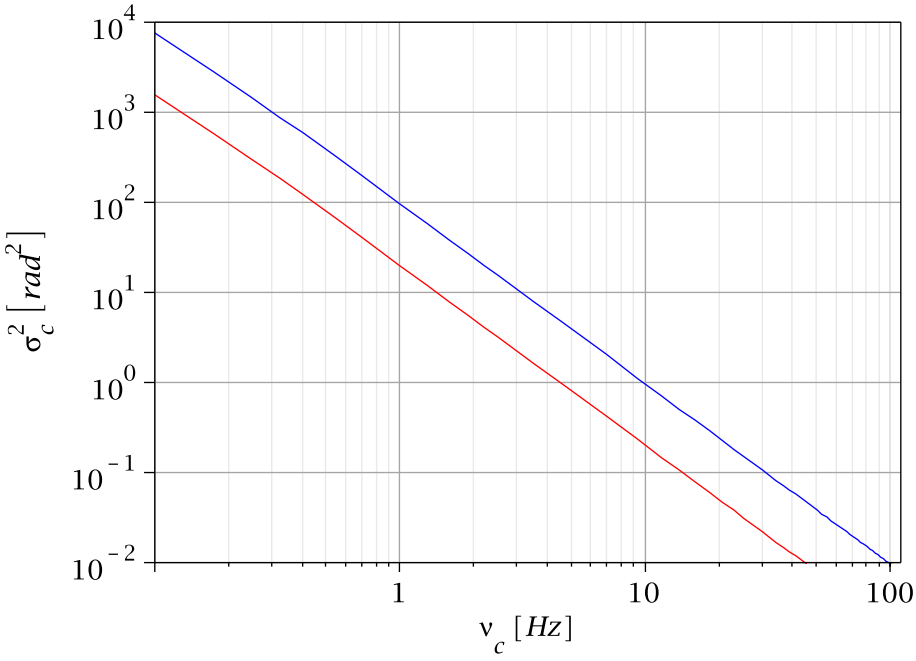

Figure 3.6: *Residual piston variance for a simple fringe tracker as function of the control bandwidth. A wind velocity of 10 m/s and an aperture diameter of 8.3 m is assumed. The lines correspond to a mean r_0 for the LBT site at 1.0 μm (blue) and 2.2 μm (red).*

in the interferometer, however, is the phase average over the full aperture. Especially for large aperture telescopes with several Fried cells across the entrance pupil differential piston does not fully correspond to the phase variations between the center positions of the apertures. Therefore, the values derived with Eq. 1.17 represent upper limits for σ_{OPD}.

3.2.2 Bandwidth

The temporal power spectrum $\omega_\phi(\nu)$ of the atmospheric fringe motion of a two-element interferometer has been derived by Conan et al. (1995). Based on their results, Kellerer & Tokovinin (2007) discuss the response of a simple fringe tracking device with an error transfer function

$$T(\nu) = \frac{i\nu}{\nu_c + i\nu}, \tag{3.2}$$

where ν_c is the closed-loop 3 dB bandwidth of the fringe tracker. The power-spectrum of the remaining, corrected fringe motion is

$$\omega_c(\nu) = |T(\nu)|^2 \, \omega_\phi(\nu) \tag{3.3}$$

A quantity characterizing the performance of the fringe tracker is the residual piston variance

$$\sigma_c^2(\nu_c) = \int_{-\infty}^{\infty} \frac{\nu^2}{\nu_c^2 + \nu^2} \omega_\phi(\nu) \mathrm{d}\nu \tag{3.4}$$

Kellerer & Tokovinin (2007) approximate this residual piston error as function of the bandwidth with

$$\sigma_c^2(\nu_c) \approx (2\pi\nu_c t_1)^{-2}, \tag{3.5}$$

where t_1 is the modified differential piston time constant given in Eq. 1.22. In Fig. 3.6 $\sigma_c^2(\nu_c)$ is plotted for $r_0 = 0.35$ m (blue line) and $r_0 = 0.90$ m (red line). A wind velocity of 10 m s^{-1} and an aperture diameter of 8.3 m are assumed. The fried parameters are based on a value of 0.15 m at a wavelength of 0.5 μm, which is the mean value of what was measured for the LBT site by Egner (2006) [seeing 0.68″ at $\lambda = 0.5$ μm]. They represent the same atmospheric conditions at $\lambda = 1.0$ μm (blue line) and $\lambda = 2.2$ μm (red line). This plot suggests that a correction bandwidth of few Hz is sufficient to achieve a residual piston variance of ~ 1 rad^2 in the NIR. To be able to remain below the 1 rad^2 limit also at stronger wind conditions, the system should allow for a correction bandwidth of a few 10 Hz.

3.2.3 Detector positioning

The sub-window on the detector used to acquire the PSF of the reference star has to continuously follow its trajectory as the field rotates. A mechanical solution must fulfill this requirement for every position within the FoV that is exploited by the FFTS and for all zenith distances the telescope supports. The velocity of the detector translation in the focal plane varies with the declination and the hour angle of the target the telescope is following. The shorter the angular distance to the zenith, the faster the field rotation. At meridian transit the zenith distance is at its minimum and the angular velocity of the parallactic angle $\left|\frac{\mathrm{d}}{\mathrm{dt}}\eta\right|$ at its maximum. In Fig. 3.7 $\left|\frac{\mathrm{d}}{\mathrm{dt}}\eta\right|$ at culmination is plotted as function of the declination of the target of interest when observed with the LBT. $\frac{\mathrm{d}}{\mathrm{dt}}\eta$ and azimuth velocity $\frac{\mathrm{d}}{\mathrm{dt}}az$ are very similar, especially for low zenith distances (cf. Fig. 3.7). The highest value for $\frac{\mathrm{d}}{\mathrm{dt}}az$ (and also for $\frac{\mathrm{d}}{\mathrm{dt}}\eta$) is $\sim 1^\circ\mathrm{s}^{-1}$. This limit is introduced by the telescope dome, which needs to be synchronously moved with the azimuth

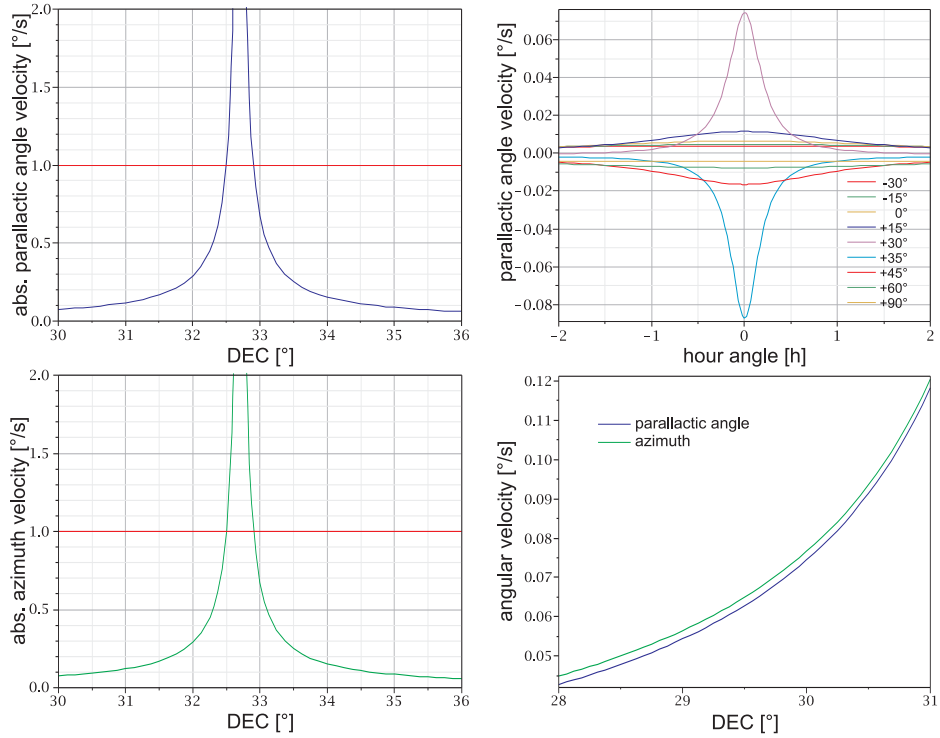

Figure 3.7: *Left: Absolute parallactic angle velocity (top) and absolute azimuth angle velocity (bottom) at meridian transit vs. declination. Top right: Parallactic angle velocity for different declinations vs. hour angle. Bottom right: comparison of azimuth and parallactic angle velocity. All panels: a latitude of 32.7°(the latitude of the LBT) is considered.*

angle of the telescope. $1°s^{-1}$ corresponds to a translation velocity of 2.6 mm s^{-1} at the largest distance (150 mm) to the optical axis in the focal plane (cf. Table 3.2).

3.3 Mechanical design

The mechanical design of FFTS is driven by the mechanical requirements discussed in Sect. 3.2, decisions on the feasibility of cryogenic positioning, limitations on detector readout capabilities, the history of the system design also of other components (especially the cooling system), and resources at hand during the system design phase. It is not the only thinkable solution for the given task and combines several advantages and some disadvantages. The mechanical model was developed with Pro/Engineer, a parametric 3D design program. In

Table 3.2: *The FFTS field of view*

Focal plane	
focal ratio (22.8 m)	f/31.5
focal plane curvature	spherical
curvature radius	-217 mm
scale	~ 3.48 mm $('')^{-1}$
FFTS field of view (angular ⌀)	
$\perp$ baseline	$60''$
$\parallel$ baseline	$90''$
FFTS focal plane dimensions	
$\perp$ baseline	200 mm
$\parallel$ baseline	300 mm
$\parallel$ optical axis	64 mm

the following the FFTS hardware components within the vacuum recipient are introduced together with the requirements they have to fulfill (cf. also Bertram 2004). Excluded from the discussion is the piston mirror, which, although directly associated with the FFTS, is considered as part of the warm optics on the optical bench of LINC-NIRVANA. Details can be found in Rohloff (2005). The FFTS mechanics will consist of the following assemblies (cf. Fig. 3.8):

- a detector head with FFTS detector, detector fanout board, and filter wheel.
- a moving baffle, that comprises the boundary between the cryogenic environment within the LINC-NIRVANA camera dewar and the ambient temperature environment of the detector positioning unit.
- a detector positioning unit (DPU). This is a remote controllable 3D-stage with high positional repeatability. It allows to position the detector anywhere within the usable FoV and to follow the trajectories of fringe tracking reference stars.
- an interlock protection, that prevents mechanical damage of the hardware in case of erroneous asynchronous motion of the moving baffle and the detector positioning unit.
- a support structure, that forms the mechanical outer skeleton of the FFTS to which moving baffle and detector positioning unit are mounted.
- a multi-core or multi-processor Linux workstation. It will carry out all real-time tasks such as detector positioning, PSF image processing and analysis, differential piston determination and piston mirror control.

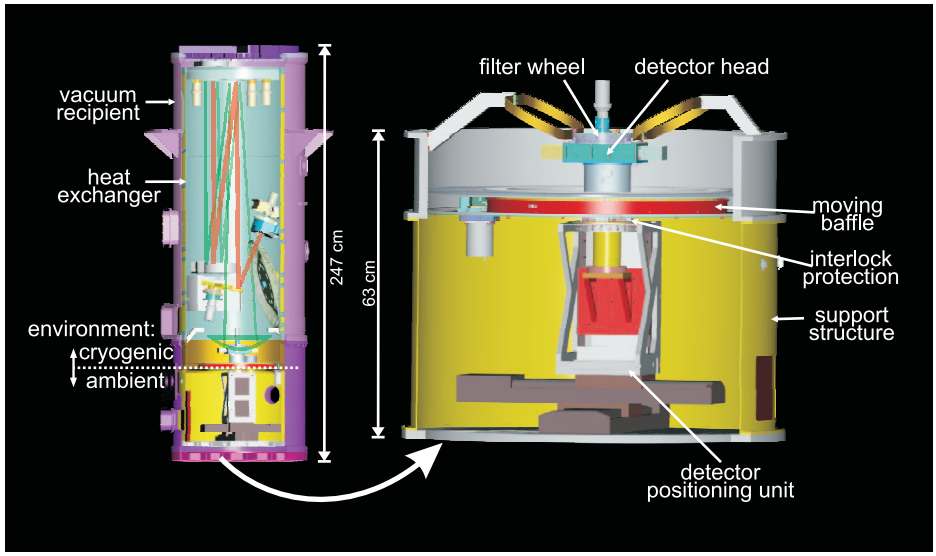

Figure 3.8: *Main components of the FFTS hardware. With the exception of the piston mirror, FFTS computer and additional electronics, all hardware related to the FFTS is located in the bottom part of the LINC-NIRVANA vacuum recipient. Part of the hardware is located in an ambient temperature environment, other components have to be within the cryogenic environment of the beam combining camera. A moving baffle comprises the boundary between these two environments.*

Further electronics is needed for the detector readout, temperature monitoring and control as well as motion control.

3.3.1 Detector head

The detector head contains the FFTS detector with its fanout board and the filter wheel. It is mounted on top of the fiberglass tube of the detector positioning unit and has to fulfill the following requirements:

- It has to be positionable along the curved focal plane in the range of the usable FoV.
- The detector head needs to be in thermal contact with the LINC-NIRVANA heat exchanger. This connection needs to transfer a constant heat load on detector head of <1W. The heat load will temporarily increase whenever the filter wheel motor is in use.
- Detector and fanout board have to be protected from stray light by a light-tight enclosure.

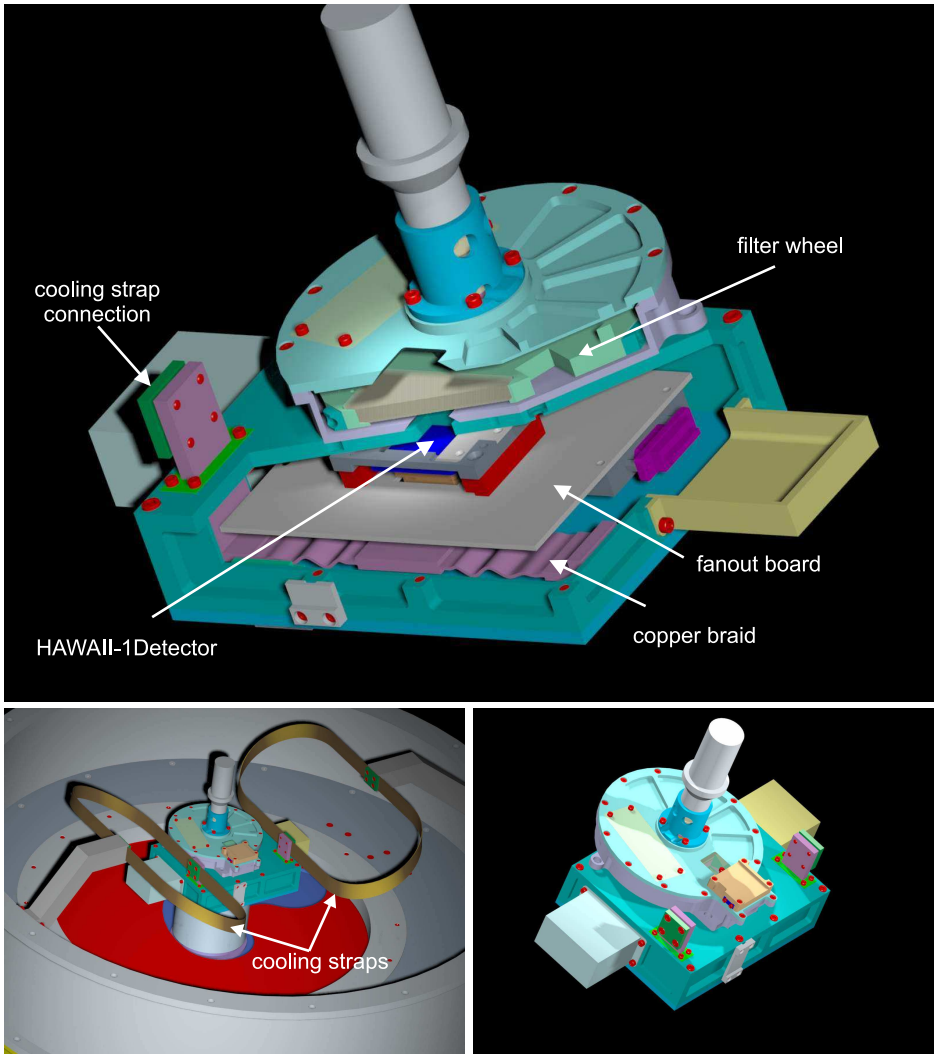

Figure 3.9: *The detector head contains the fanout board with the HAWAII-1 detector array and a filter wheel. A housing shields these components from stray light. The filter wheel provides 8 filter positions, an open and a blind position. Because of its isolated position on top of a fiberglass tube, the detector head has to be connected to the heat exchanger via copper cooling straps. Within the housing copper braids connect the cooling straps with a heat sink on the back side of the fanout board. A control loop is forseen to keep the detector at a constant temperature.*

- The direction of fast readout of the detector should coincide with the direction of minimum resolution. Possible spill-over effects in between individual pixels at high readout frequencies are then constrained to this direction.
- The detector head has to be easily removable in order to access the warm part of the FFTS mechanics.
- A compact, lightweight design is required to reduce mechanical flexure.
- The center of gravity should be in the center of the fiberglass tube of the DPU.

As shown in Fig. 3.9, thermal contact to the LINC-NIRVANA heat exchanger is provided via 4 flexible copper cooling straps made of many thin layers. Their sandwich sheet structure (no braids are used) prevents the straps from hanging down, their length allows the detector head to access any point in the specified volume. Within the housing, a copper braid directly connects the cooling block at the bottom side of the fanout board with the cooling straps and provides direct heat transfer from the fanout board to the LINC-NIRVANA heat exchanger. The detector quadrant which is to be placed underneath the opening to the filter wheel can be chosen by mounting the fanout board to one of four positions. All cables enter the box through the inside of the fiberglass tube of the DPU. Dismountable covers allow easy access to the cable connectors of the fanout board. Once the cables are unplugged, the whole detector head assembly, including the fanout board, can be removed from the base plate.

The filter wheel provides 8 positions for J, H, K, J+H and H+K broadband filters and 3 filters with 1% bandwidths and central wavelengths corresponding to J, H and K. In addition the filter wheel provides an open and a blind position. It is optimized in terms of weight and compactness. A cam disk and limit switch combination is implemented for filter position reference. In order to minimize weight, the option of absolute position encoding was abandoned. Instead, an additional reference position is defined by a second cam-switch combination. Filter positions will be counted from this reference.

3.3.2 Moving baffle

The moving baffle separates the cryogenic environment of the dewar from the ambient temperature environment. It prevents intrusion of thermal radiation into the interior of the camera. Furthermore, it has to allow the DPU to access the cryogenic environment via a hole, which can be moved to any position within

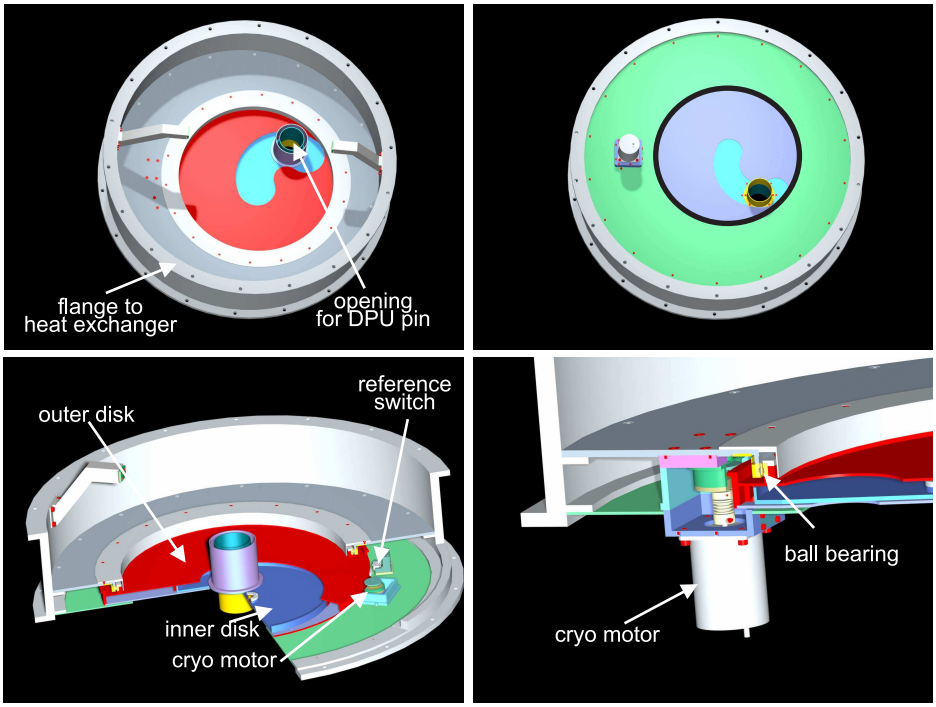

Figure 3.10: *top left: moving baffle, view on the cryogenic temperature side. top right: moving baffle, view on the ambient temperature side. The outer annulus is in thermal contact with the heat exchanger. Radiation heat transfer on the rotating disk is restricted to the encircled surface in the center. bottom left: Two nested disks shield the cryogenic environment from the warm. The vertical tube can be positioned everywhere within a radius of 150 mm from the center of the baffle by rotating the two disks. bottom right: A Phytron stepper motor actively drives the outer disk of the baffle.*

the region of the focal plane projected to the baffle plane that corresponds to the usable FoV. The following requirements have to be fulfilled:

- Light tight baffle. The shield has to suppress the intrusion of NIR photons into the camera environment.
- Moving access hole. The area of the FFTS FoV projected onto the XY reference plane of the baffle has to be accessible by the moving access hole. This hole allows the DPU to access the cryogenic environment.
- Baffle and DPU should be mechanically decoupled. The baffle system should not add additional gravitational load or vibrations to the fiberglass tube of the detector head.

- Synchronous motion of DPU and moving baffle.
- Cold shield. The shield has to prevent the intrusion of thermal photons into the cryogenic environment of the dewar. This includes photons radiated from the shield itself. The science detector is oriented in a way that it is facing the moving shield. Emitted or unshielded photons will directly increase the background of the detector. Therefore, the shield itself has to be cooled.
- Compact design. The baffle should not define the radius of the dewar.

The moving baffle consists of two nested disks (cf. Fig. 3.10). The outer disk is centered on the symmetry axis of the DPU. It is guided by a ball bearing with a central clearance that is larger than the positioning range of the DPU. This disk needs to be actively driven synchronously with the DPU. It covers the full area which needs to be accessible, except for a narrow circular arc shaped opening. This opening is covered by the second disk, which is located inside the double layered outer disk (cf. bottom left panel in Fig. 3.10). The inner disk allows for radial positioning of the DPU. It can be moved by the DPU itself without an active drive mechanism (a balanced mass distribution and a constant distance to the disk's center results in a constant torque which is dependent only on the friction of the ball bearing. Furthermore, there will be no radial movement while tracking a reference source). The outer disk, however, needs to be driven by a cryo motor (cf. right panels in Fig. 3.10), since the torque is dependent on the radial position of the DPU. Its motion has to be synchronized with the DPU motion. The design permits a positional discrepancy of 3 mm before triggering an interlock of the system. With this concept, any X-Y motion of the DPU is decomposed into two simple rotations. In the most common case of tracking a guide star, only circular trajectories centered on the DPU symmetry axis are followed, hence the number reduces to one rotation. The constraints upon the precision of the baffle motion are low due to the comfortable +/- 3 mm tolerance. In contrast to translational motion at cryogenic temperatures, rotational motion is easier to realize in such an environment. The current design assumes sufficient heat transfer via the ball bearing. To guarantee sufficient heat transfer in the cool-down period, the outer and not the inner rim of the bearing is attached to the heat exchanger. Differential contraction in radial direction, therefore, needs to be compensated to prevent the destruction of the bearing.

To minimize the radiation heat load onto the outer disk, all parts that do not interfere with the DPU are covered by a cold plate. Also, the surface of the disk facing the warm side will be coated to reduce absorption.

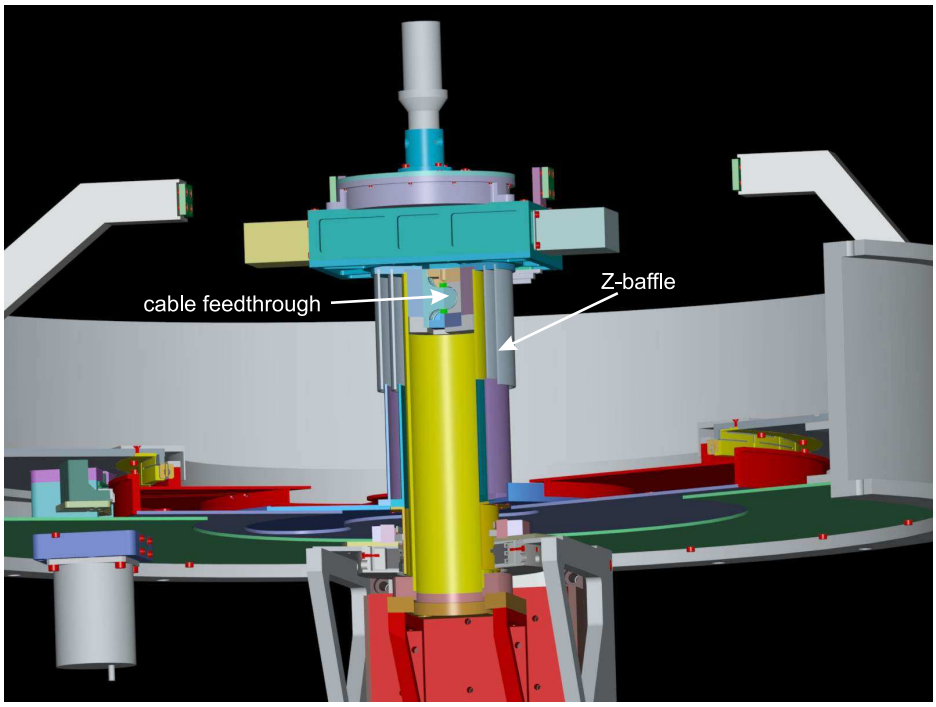

Figure 3.11: *A fiberglass tube is the connection between the Detector head in the cryogenic environment and the detector positioning unit in the ambient temperature environment. It fits through the hole in the moving baffle. All cables to the detector head go through the tube. To prevent radiation to enter the interior of the beam combining camera, a cable feedthrough has to be realized within the tube. For the same reason a Z-baffle surrounds the tube on the cold side. The CAD rendering shows the detector head in the highest Z position.*

3.3.3 Detector positioning unit

The DPU allows to move the detector head within the focal plane to the position of the reference source and to follow its trajectory. The following requirements have to be fulfilled:

- Travel range 200 mm x 300 mm x 70 mm.
- Maximum velocity for guide star tracking: 2.6 mm/s (cf. Sect. 3.2).
- Absolute positioning accuracy: <50 μm (for initial PSF acquisition).
- Relative positioning reproducibility: +/- 4 μm for PSF trajectory tracking. The quality of fringe tracking depends on the uncertainty of the PSF position. Knowing the central position of the PSF to sub-pixel precision

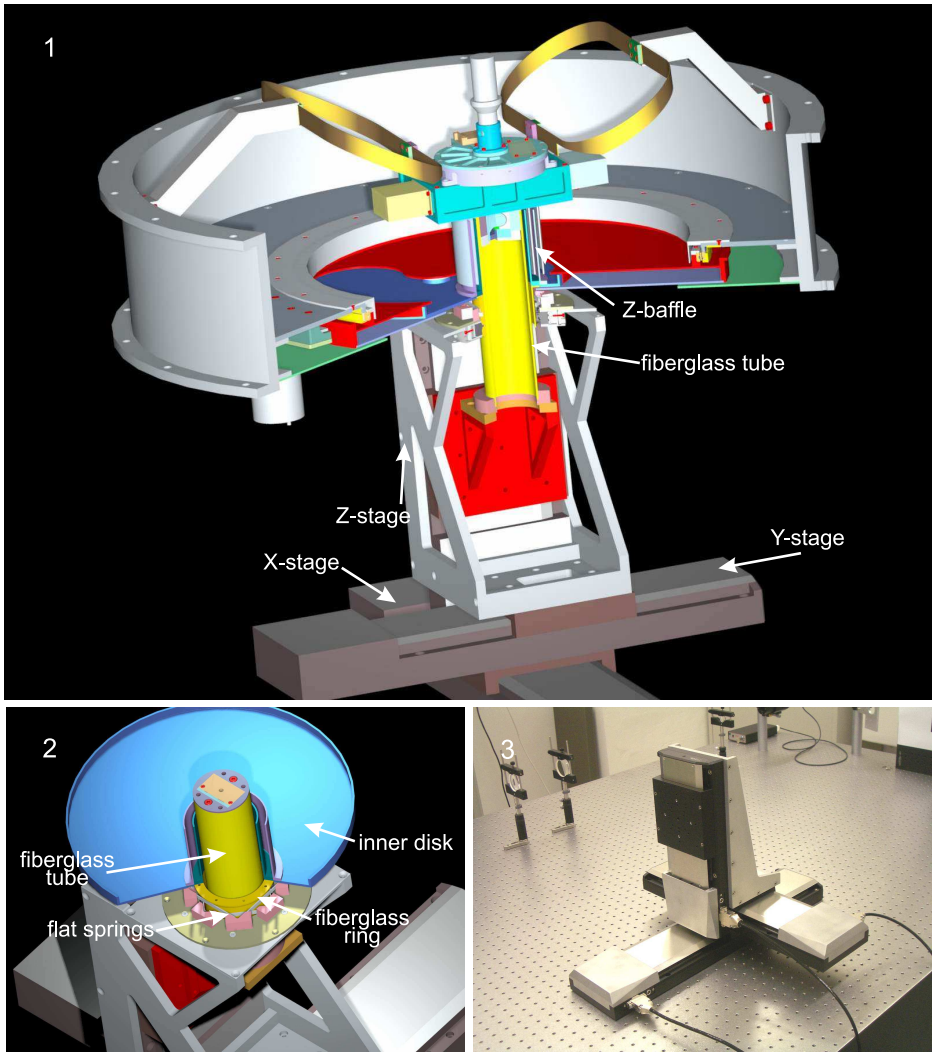

Figure 3.12: *1: The detector positioning unit (DPU) consists of 3 linear stages which allow positioning of the detector head anywhere within a volume of 200 x 300 x 70 mm^3. A fiberglass tube supports the detector head in the cryogenic part and connects it with the linear stages in the warm part of the dewar. 2: Flat springs attached to the detector positioning unit center the inner disk of the moving baffle on the tube axis. The detector head and the baffling tubes for motion in Z direction can be completely removed to disassemble the FFTS mechanics. 3: 3 linear stages from Physik Instrumente are assembled in a test setup for the detector positioning unit.*

allows us to reduce the number of free parameters that have to be fitted to the PSF profile, which in turn increases the performance of the fringe tracking algorithm significantly (cf. Sect. 3.5).

- Operation at vacuum conditions (10^{-6} mbar).
- Routing of all cables to the detector head through the DPU.
- Shielding of the Z-direction travel range below the detector head.

The DPU consists of 3 vacuum qualified micro positioning stages from Physik Instrumente (PI) with travel ranges corresponding to the volume that has to be accessible by the detector (cf. Fig. 3.12). A vertical fiberglass tube mounted to the Z-stage points through the moving hole in the baffle and carries the detector head (cf. Fig. 3.11). The travel range in Z-direction is shielded by a double layer shield of axial tubes. Tangential flat springs attached to the top of the Z-stage center the inner disk of the moving baffle around the fiberglass tube. A photon-tight cable feedthrough is integrated into the fiberglass tube. This has the advantage that all cables and the feedthrough itself can remain assembled when disassembling the moving baffle.

3.3.4 Interlock protection

A two-level (soft and hard limit) interlock protection is foreseen to prevent damage to the hardware in case of unsynchronized motion of DPU and moving baffle. It consists of a concentric circle of 24 micro switches (cf. Fig. 3.13) around the fiberglass tube of the moving baffle. Every second switch is dedicated to a hard limit level. The radial position of the switches can be adjusted. Both protection levels have to be realized within the 3mm mechanical tolerance between DPU and moving baffle. The microswitches that are forseen have a relatively large over-travel range past the activation position, which allows a second limit switch level (hard limit) in the radial direction before the physical limit of the switches is reached. The orientation of the limit switch circle is fixed with respect to the linear stages. A total of 12 switches per protection level allows assignment of 3 switches to each direction of the X- and Y-linear stage. These have their own limit switches implemented. A serial wiring of the 3 interlock protection switches and the linear stage limit switch allows us to always interrupt motion into the corresponding direction, regardless of the cause (asynchronous motion or physical limit) which triggered the actuation. With the spacing of 30° between neighboring soft limit switches, a geometrical response delay is reduced to 0.1mm (cf. Fig. 3.13).

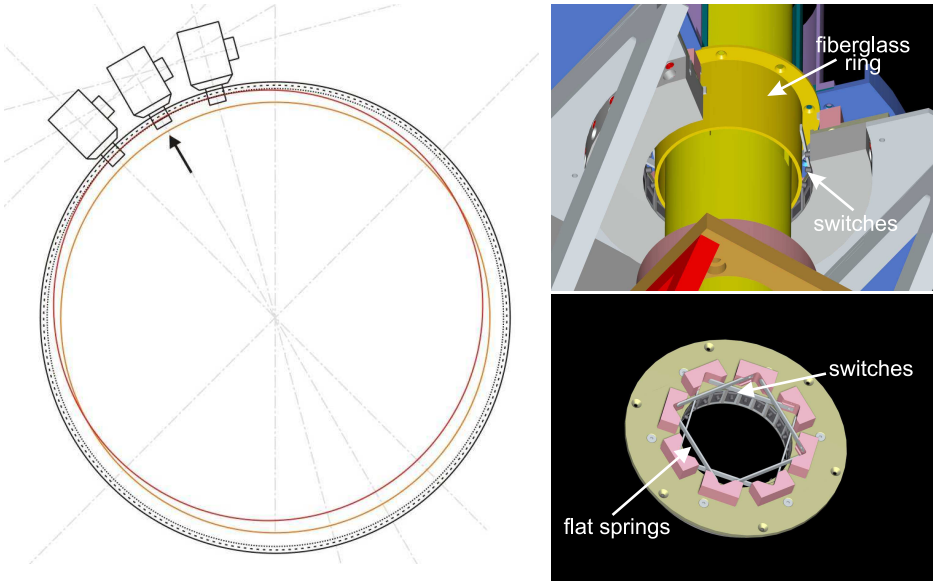

Figure 3.13: *To prevent damage to the mechanics in the case of unsynchronized motion of moving baffle and detector positioning unit, an interlock protection system will be implemented. It consists of micro switches that stop the motors in such an exceptional situation. The switches are arranged in a circle and are attached to the DPU. A fiberglass ring attached to the inner disk of the moving baffle will eventually hit a switch and trigger the emergency stop. Left: The spacing of the switches keeps geometrical response delays to a minimum (<0.1 mm). The switch in the center will be used for the hard limit, and will, therefore, have a slightly larger radial distance than shown here.*

3.3.5 Support structure

The support structure (cf. Fig. 3.14) is the mechanical outer skeleton of the FFTS. In the upper part, it supports the moving baffle (cf. Sect. 3.3.2), hence it forms the boundary between the cryogenic environment and the ambient temperature environment of the LINC-NIRVANA dewar. Its design has to include thermal insulation between these two environments. It also includes the mounting and thermal interface to the LINC-NIRVANA heat exchanger. Its main purposes are:

- mounting platform for the ambient temperature DPU.
- thermal bridge between cryogenic FFTS components and the heat exchanger of LINC-NIRVANA.
- mechanical interface to the heat exchanger of LINC-NIRVANA.

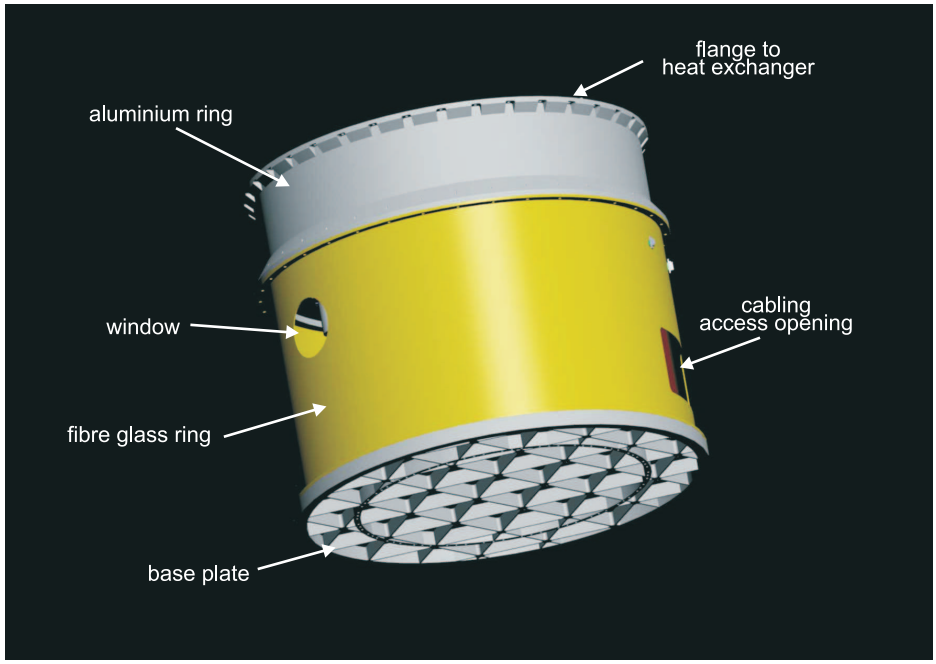

Figure 3.14: *The support structure consists of an aluminium ring in the top, cold part, a fiberglass ring in the warm, bottom part, and a base plate. It is mounted to the LINC-NIRVANA heat exchanger.*

3.4 Software design

A fundamental part of the FFTS is its software. Most hardware components have a software counterpart and crucial functionality, such as the fringe fitting or the OPD control algorithm has to be implemented as software. Furthermore, the FFTS is not a stand-alone entity but part of a complex system that receives input from and provides information to other subsytems of LINC-NIRVANA. The development of the FFTS software package, therefore, requires a thorough analysis and a design that takes into account all the different tasks and interfaces. A detailed description is beyond the scope of this thesis. Here, only a coarse listing of the modules in the FFTS software package is provided. More details can be found in Bertram (2007).

The FFTS software package consists of the following modules, which encapsulate the different FFTS tasks. The package itself is named LFFTS and all modules start with “lf”. (The awkward nomenclature follows a rule that was decided among the LINC-NIRVANA software group). All modules will be realized as separate processes.

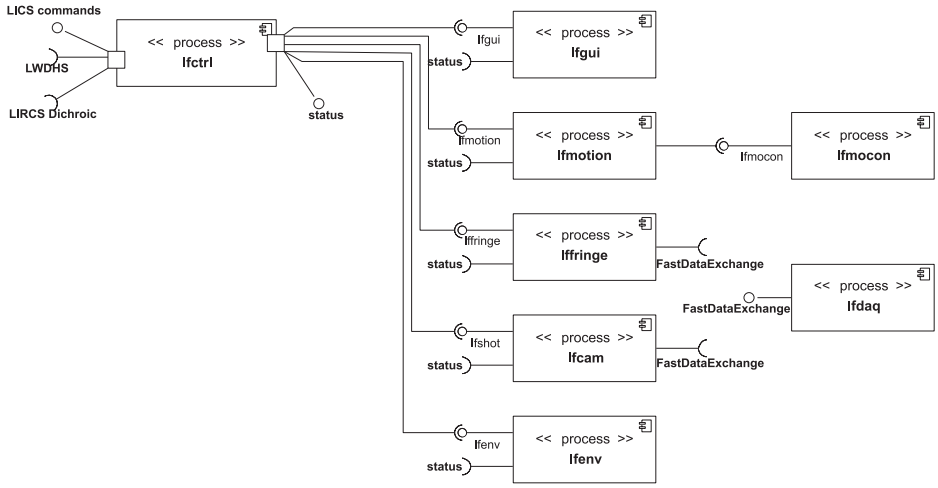

Figure 3.15: *LFFTS modules*

- **lfctrl:** the LFFTS master control module controls all other modules in the LFFTS package. It provides the interface to the instrument control software (LICS).
- **lfgui:** the LFFTS graphical user interface.
- **lfmotion:** the motion control module is a high-level software representation of all motor-driven components in the FFTS. It provides all functionality that is necessary to follow the reference star, to reposition the detector, to synchronize the motion of the detector positioning unit and the moving baffle, and to move the filter wheel.
- **lfmocon:** this module is a software representation of the motor controller. It interfaces exclusively to the lfmotion module and provides low-level motor control functionality.
- **lffringe:** this module contains the main control loops of the FFTS: the Fringe- and the Flexure Control Loop as well as the image processing loop for incoming raw data.
- **lfdaq:** the module that receives raw data from the PCI DMA board and provides it via the FastDataExchange Interface.
- **lfcam:** this module provides an interface to the FFTS camera and functionality to obtain and process single shot data.

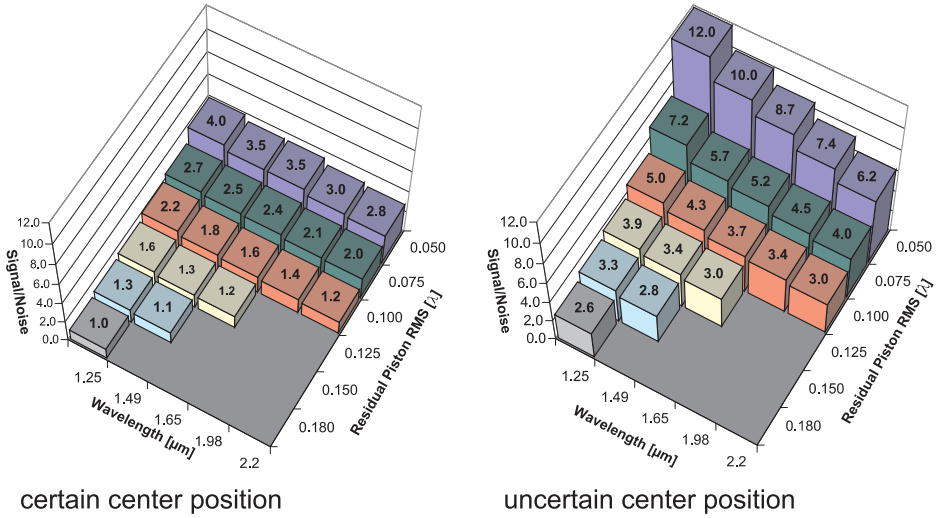

Figure 3.16: *S/N required for different combinations of central wavelengths and residual differential piston values.*

- **lffenv:** the environment module mainly deals with temperature monitoring and control tasks within LFFTS. It provides interfaces to the LakeShore hardware.

3.5 Performance of the fringe fitting algorithm

The fringe contrast, that can be achieved in each specific case, is the result of a detailed piston error calculation. It has to take into account numerous instrumental and atmospheric parameters. Part of this error budget is the performance of the fringe fitting algorithm, i.e., the part of the fringe tracking loop that realizes the OPD measurement. A residual piston (RMS) of 0.1 λ for the central wavelength of the science band at the position of the science target is a benchmark for the fringe tracking performance. This goal imposes constraints on the magnitude of the fringe tracking reference star.

The pixel-to-pixel S/N ratio required to achieve a certain residual piston RMS depends on the sampling of the PSF, i.e. on the wavelength at which the fringe tracking reference star is observed. At shorter wavelengths a higher S/N is needed to achieve the same residual piston RMS as for longer wavelengths (cf. Fig. 3.16). On the other hand, fringe tracking at shorter wavelengths has relaxed requirements on the residual piston RMS in the fringe tracking band when the science band is at longer wavelengths (cf. Table 3.3). The choice of the fringe

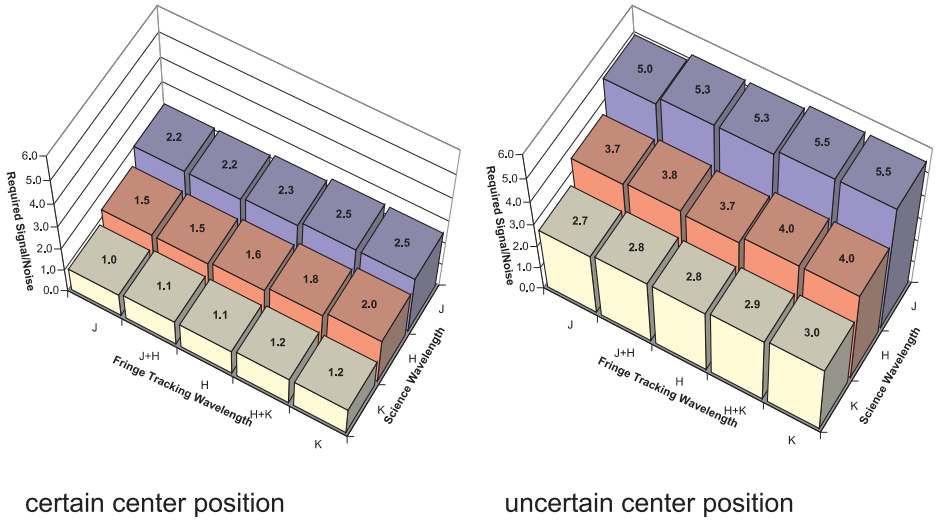

Figure 3.17: *S/N required to achieve a residual differential piston RMS of 0.1* λ_{Science}.

tracking band, therefore, is a trade-off between sampling and mandatory residual piston RMS at the fringe tracking band. Figure 3.17 shows, that the wavelength dependence on the required residual piston RMS actually outweighs the dependence on the PSF sampling. As a consequence, it is always preferable to chose a short wavelength band for fringe tracking. However, not all combinations of science and fringe tracking bands are available. In the central region of the FFTS FoV, part of the NIR wavelength range is reflected to the science detector by a dichroic and, therefore, not available to the FFTS.

The performance of the fringe tracking algorithm is dependent on the degree to which the center position of the PSF is known. If the position is unknown by more than half a pixel, the required S/N is much higher, since this parameter then has to be added to the parameters that are to be determined by the fit routine. For this reason, Figures 3.16, 3.17 and 3.18 also provide values for a multi-parameter fit including the central position.

The S/N requirements were used to derive estimates of limiting magnitudes for fringe tracking guide stars. Note that these estimates are based only on the requirements of the fringe tracking algorithm and do neither consider the piston rejection function of the full fringe tracking control loop nor any other effect contributing to the piston error budget. The values given here, therefore, represent upper limits of the actual limiting magnitudes achievable with the FFTS hardware that is currently planned to be used. The detector readout noise (RON) has by far the largest impact on the S/N ratio. Therefore, all other sources of noise

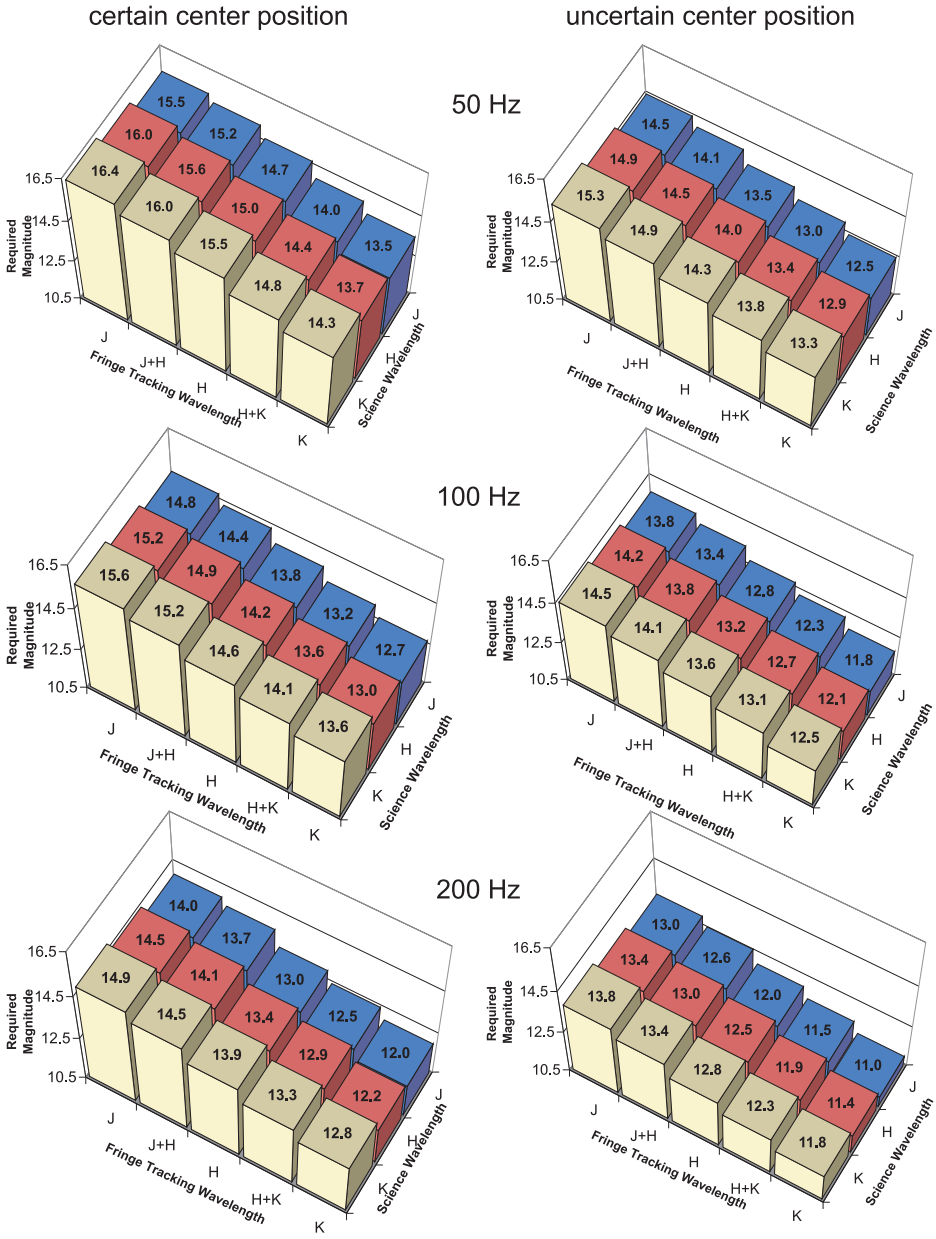

Figure 3.18: *Limiting magnitudes required to achieve a residual differential piston RMS of 0.1* λ_{Science} *for different combinations of fringe tracking and science wavelengths and frame rates of 50 Hz, 100 Hz and 200 Hz*

Table 3.3: *Residual piston RMS at the fringe tracking wavelength required to achieve an RMS value of 0.1 λ_{Science}.*

	Fringe tracking band				
λ_{Science}	J	J+H	H	H+K	K
J	0.100	0.085	0.076	0.063	0.057
H	0.132	0.112	0.100	0.083	0.075
K	0.176	0.150	0.133	0.111	0.100

Table 3.4: *Parameters considered for the limiting magnitude estimates shown in Fig. 3.18. Read-out noise is the dominating noise component, all others can be neglected.*

optical component	throughput
M1	0.95
M2	0.95
M3	0.95
collimator	$6 \cdot 0.98$
DM	$2 \cdot 0.98$
Dichroic	0.98
Dewar entrance window	0.98
Beam combiner	$2 \cdot 0.98$
Dichroic	0.98
Throughput excluding filter (R_{Tel})	0.66
Detector Quantum efficiency (R_{QE})	0.6
Detector RON (N_{RON}) [e^-]	15.5
Telescope area (A) [m^2]	105.6
Strehl (R_{Strehl})	0.4

Table 3.5: *Filter specific parameters considered for the limiting magnitude estimates shown in Fig. 3.18.*

Filter specific parameters	J	J+H	H	H+K	K
λ_{iso} [μm]	1.25	1.47	1.65	1.98	2.20
bandwidth FWHM ($\Delta\lambda$) [μm]	0.24	0.60	0.36	0.92	0.56
filter transmission (R_{Filter})	0.8	0.8	0.8	0.8	0.8
atmospheric transmission (R_{Atm})	1	0.6	1	0.6	1
F_0 [10^{-10} W $m^{-2}\mu m^{-1}$]	31.4	16.4	11.2	5.7	3.8
fract. of PSF in central pixel (f_{pixel}) [%]	4.7	3.4	2.8	2.0	1.6

(except for the Poisson distribution of the photon noise) have been neglected in this estimate:

$$\mathrm{S/N} \approx \frac{N'_{\mathrm{p}}}{\sqrt{N'_{\mathrm{p}} + N^2_{\mathrm{RON}}}}, \tag{3.6}$$

where N'_p is the number of photo electrons per frame in the central pixel of the PSF image and N_{RON} the number of readout noise electrons.

$$N'_p = \frac{1}{\mathrm{hc}} \cdot A \cdot F_\lambda \cdot \lambda_{\mathrm{iso}} \cdot \Delta\lambda \cdot R_{\mathrm{Atm}} \cdot R_{\mathrm{Tel}} \cdot R_{\mathrm{Strehl}} \cdot R_{\mathrm{Filter}} \cdot R_{\mathrm{QE}} \cdot \frac{f_{\mathrm{pixel}}}{\mathrm{Framerate}} \tag{3.7}$$

All parameters that have been considered are listed in Table 3.4. The resulting magnitude limits for different combinations of fringe tracking and science wavelengths are shown in Fig. 3.18.

3.6 Fringes in the laboratory

To be able to develop the control loop and to test the robustness of the fringe tracking concept that is forseen for the FFTS, it was decided to set up a laboratory experiment. The goal was to develop an image plane testbed interferometer that allows to actively introduce controlled low-order phase perturbations, namely OPD and differential tip/tilt. The geometry of the resulting intensity distribution should be similar to the LBT PSF. Furthermore, the setup should incorporate all components that are required in a fringe tracking servo loop: a sensor for fringe acquisition and an actuator to compensate for measured OPD. With such a setup it is intended to determine the performance with which a fringe tracking control loop is able to compensate for defined OPD sequences, to test different control algorithms, and to optimize the control parameters of a real existing servo system.

One key issue to be investigated is the cophasing accuracy. It should be tested how well the zeroth fringe is identified among the fringes that are measurable for a certain coherence length. Associated with this issue is the behavior of the system in a “fringe hopping” incident, i.e., when a sudden change of the OPD occurs. These tests require a white light solution to be able to vary the coherence length within the system.

With a first testbed interferometer set up at the MPIA it was possible to demonstrate the functioning of the fringe fitting algorithm not only with computer generated fringes but also with fringes that were actually acquired in a laboratory experiment. A slow fringe control loop was closed that allowed to compensate thermal OPD drifts. More detailed information on the first testbed interferometer can be found in Andersen et al. (2004).

Table 3.6: *The main hardware components of in the PSF simulator experiment (cf. Fig. 3.19).*

component	
white light source	halogen
pinhole ⌀	0.5 mm
bandpass filter	
1.) $\bar{\lambda}$, $\Delta\lambda$ (FWHM)	700 nm, 10 nm
2.) $\bar{\lambda}$, $\Delta\lambda$ (FWHM)	700 nm, 40 nm
3.) $\bar{\lambda}$, $\Delta\lambda$ (FWHM)	700 nm, 100 nm
4.) $\bar{\lambda}$, $\Delta\lambda$ (FWHM)	675 nm, 150 nm
achromatic collimator focal length	1000 mm
laser	
type	He-Ne, phase stabilized
$\bar{\lambda}$	632.8 nm
beam expander	30×
beam splitter	50%
telescope	
type	Celestron NexStar 5i
focal length	1250 mm
aperture ⌀	127 mm
camera	AVT Dolphin F-145c, CCD
piston mirror (and atmosphere) actuator	
type	PZT P753 (PI)
stroke	36 μm

3.6.1 PSF simulator setup

The experiment is realized on an optical table in a dust protected environment. Figure 3.19 shows the setup with all hardware components that are involved, Table 3.6 lists the key parameters of the individual components. It is equipped with two light sources: a monochromatic He-Ne laser and a halogen lamp in combination with several bandpass filters (cf. Fig. 3.20) for white light tests. To be able to use the halogen lamp in an interferometer, a pinhole has to be implemented to restrict the size of the effective emission region and to allow for coherent combination (cf. Fig. 3.21). An achromatic collimator lens group with a focal length of 1000 mm is used to produce a collimated beam that is spatially filtered by an iris aperture stop. This aperture stop defines the Airy diffraction pattern, i.e, the envelope distribution of the interferometric PSF. The beam of the laser is expanded by a factor of 30 and then also spatially filtered by an aperture stop to obtain a relatively uniform beam profile and to define the Airy pattern.

Once the beam profiles are defined in both cases (mono- and polychromatic), a 50% beam splitter is used to split the incoming light and distribute it between two paths. In the PSF simulator setup, the approaching monochromatic and poly-

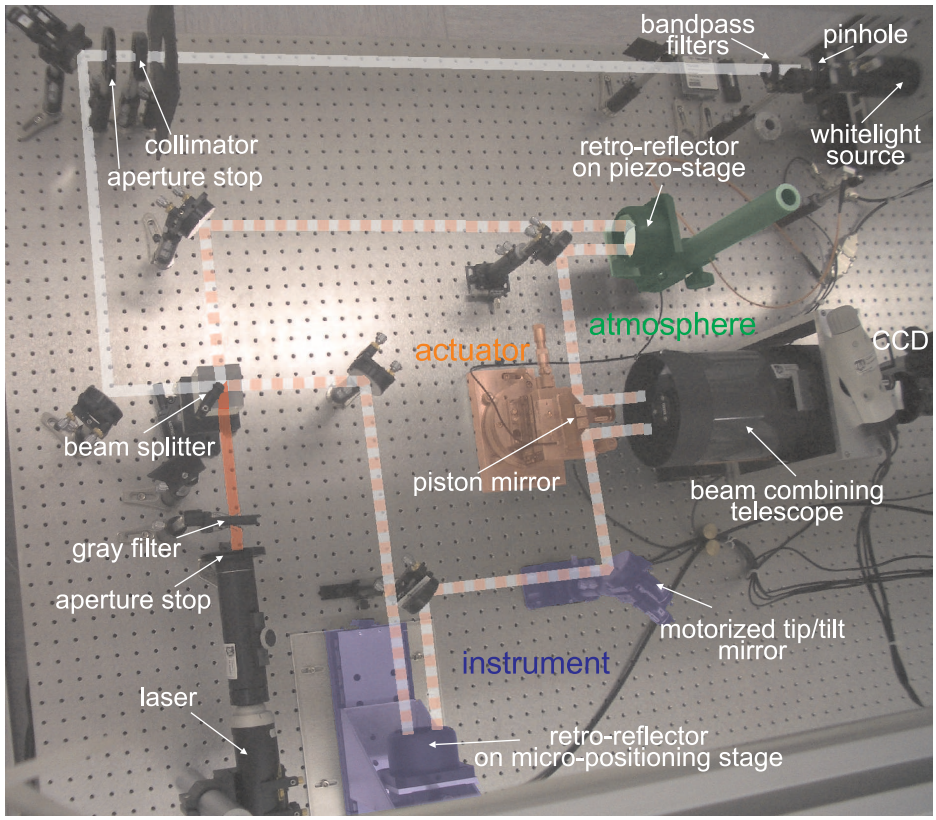

Figure 3.19: *The testbed interferometer in the laboratory. This experiment allows to produce monochromatic and white light PSFs of variable shape in the visible wavelength domain. Within this interferometer, time-variable atmospheric and instrumental OPD and instrumental differential tip/tilt can be simulated. Two light sources are available: a halogen white light source and a He-Ne laser. The light of the two sources is collimated and spatially filtered by aperture stops before a beam splitter divides each beam into the two arms of the interferometer. Starting at the beam splitter, white light and laser light share the same paths. In the upper path, a retro-reflector on a piezo nano-positioning stage (green parts) allows to introduce pathlength variations that follow an atmospheric power spectrum. The introduced OPD can be compensated by the piston mirror (orange parts), which is mounted to another piezo nano-positioning stage. The piston mirror directs the two beams into the beam-combining telescope. A CCD in the focal plane is used to obtain the resulting PSF. A micro-positioning stage with a stroke of ~ 100 mm and a motorized tip/tilt mirror (blue parts) in the lower path allow to introduce large instrumental OPD or a misalignment of the two arms of the interferometer.*

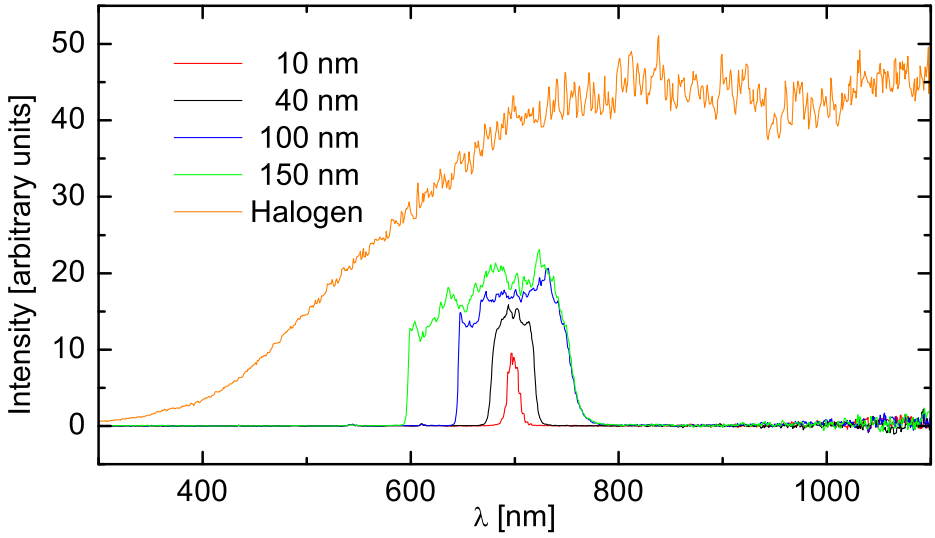

Figure 3.20: *Spectral distributions of light that can be used within the current setup of the PSF simulator experiment. The spectra show the part of the lamp spectrum that is transmitted by the broadband filters (in some cases also by a combination of high- and low-pass filters).*

.

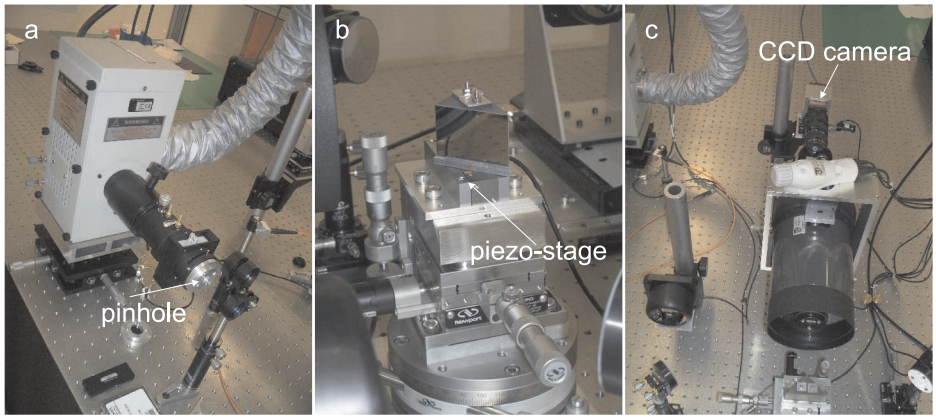

Figure 3.21: *Hardware components in the PSF simulator experiment. a) White light source with collimator optics, a liquid filter to reduce the thermal IR part of the spectrum, and the pinhole. To reduce potential turbulence or thermal pathlength variations, the hot exhaust air is directed away from the optical components. b) The piston mirror is mounted on top of a piezo nano-positioning stage. Several other degrees of freedom are adjustable for the alignment of this component. The translation of the mirror in direction of the beam-combining telescope is motorized. By moving the device along this direction it is possible to adjust the separation of the two parallel beams that are to be combined. This allows to control the geometry of the resulting PSF. c) The beam-combining telescope and the CCD camera in the back. Optics in between these two components allow to adjust the size of the PSF on the CCD.*

chromatic beams enter the beam splitter on two sides that are perpendicular to each other. The transmission direction of the polychromatic beam is the reflection direction of the laser beam and vice versa. This setup has the advantage, that both light sources can be used independently or even together, without any mechanical switching. From this point on, the polychromatic and monochromatic beams share the same two paths of the interferometer.

Retro-reflectors on actuators can be used for an adjustment of the optical length of each of both paths. In the upper path (cf. Fig 3.19) a piezo nano-positioning stage with an overall stroke of 36 μm allows to introduce fast varying OPD with a range of twice the stroke. The stages are specified to provide an actuation bandwidth of up to 200 Hz with the given load. With these parameters it is possible to replay differential piston sequences that correspond to atmospheric power spectra (cf. Sect 3.2) or certain combinations of atmospheric and instrumental power spectra. The lower path contains a retro-reflector that is mounted on a micro-positioning stage with a much larger range: $\sim$ 100 mm. By introducing OPD that is much larger than the coherence length it is possible to test alignment procedures. Furthermore, a motorized mirror allows to conveniently align the two beams such that the Airy distributions overlap in the focal plane. It can also be used to introduce defined differential tip/tilt to simulate not perfectly overlapping Airy distributions.

Similar to the piston mirror in the schematic view in Fig. 1.5 or the LINC-NIRVANA counterpart, the piston mirror in this testbed interferometer is the actuator in the fringe tracking servo loop. It is part of both optical paths - any translation in the plane of the paths and perpendicular to the optical axis of the beam-combining telescope reduces the length of one path and increases the length of the other path by the same amount. The piston mirror (cf. Fig. 3.21) is also moved by a piezo nano-positioning stage. It folds both beams towards the beam combining telescope. By adjusting the distance to the telescope, the separation of the two parallel beams can be varied and with this the fringe spacing in the focal plane, in which the beam combination takes place. A CCD camera in the focal plane acts as sensor for the fringe tracking servo loop. Here, the resulting PSFs are obtained. It is possible to adjust the window size and frame rate at which the PSFs are provided to the fringe tracking control loop.

3.6.2 First results

The optical components in the testbed interferometer were successfully aligned. Both beams coincide in the focal plane of the beam combining telescope and produce the desired fringe pattern. The geometry of the resulting intensity distribution is adjustable such that it corresponds to the LBT case. As proof of con-

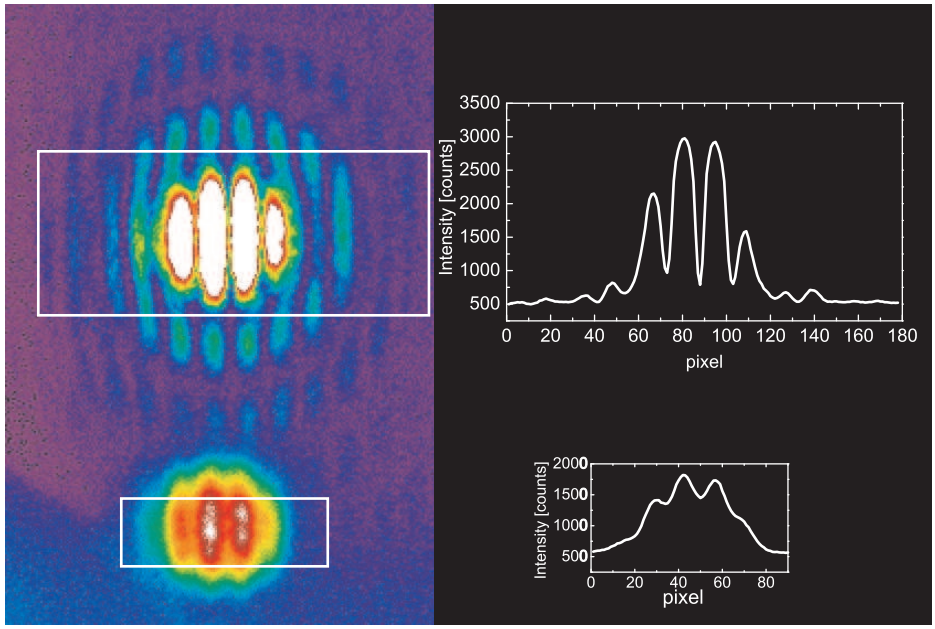

Figure 3.22: *Exemplary PSFs obtained with the PSF simulator experiment. Top: monochromatic PSF, bottom: polychromatic PSF. In the polychromatic case, a strong incoherent fraction of light significantly reduces the fringe contrast. The difference in the number of fringes per Airy radius results from different aperture geometries in the two cases. Column averages of the pixels enclosed in the white boxes are used for the profiles on the right side.*

cept, Figs. 3.22 and 3.23 show some of the first simulated PSFs. It is possible to introduce actuator controlled OPD with all stages in the setup. Furthermore, the motorized tip/tilt mirror allows to simulate non-overlapping Airy distributions, as can be seen in Fig. 3.23b and c.

The setup is highly sensitive to vibrations and even pressure variations, as caused by a motion of the walls of the dust protection enclosure. Therefore, the air-damping system of the optical table is absolutely mandatory. If the testbed interferometer is mechanically decoupled and the doors of the dust protection are closed and left untouched, the fringes remain stable to a level of $< 0.1\lambda$, which corresponds to OPD fluctuations of < 60 nm. This residual may be caused by turbulence within the dust enclosure, which also houses many electronic devices such as the piezo controller, the motor controller, the lamp's power supply and other equipment. All these devices emit heat and may cause a certain degree of turbulence within the enclosure, which is not designed to provide a laminar flow across the optical table. Nevertheless, the level of stability is satisfying for the purposes of the testbed interferometer.

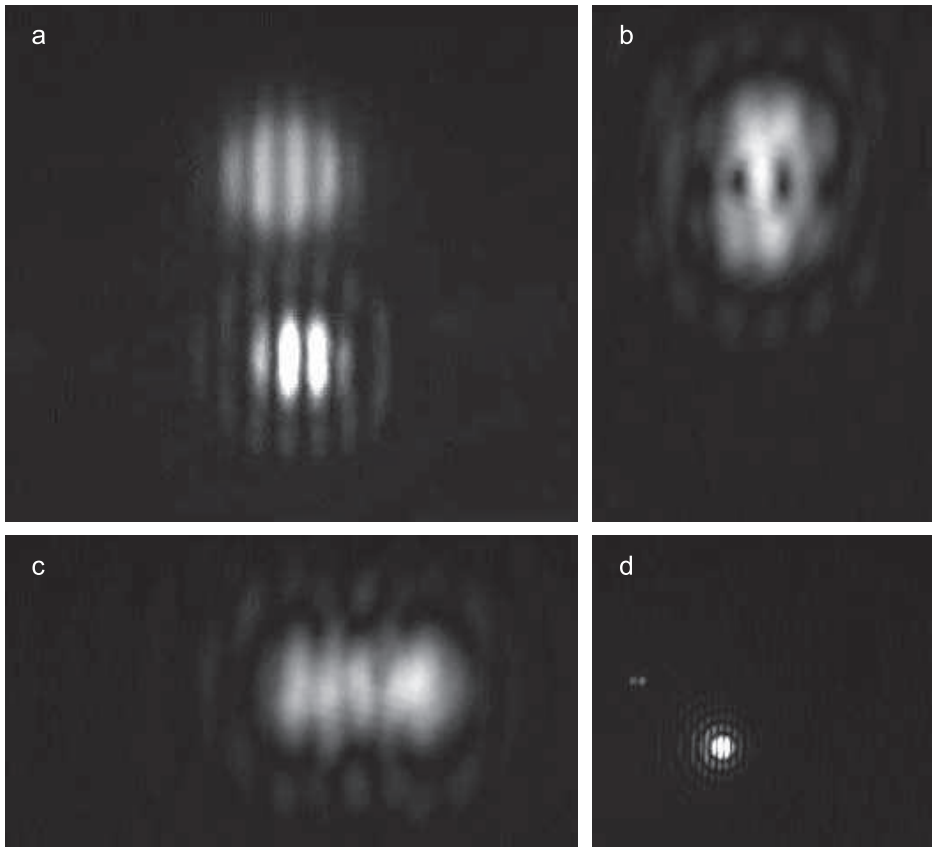

Figure 3.23: *a) Polychromatic PSF (top) with a higher fringe contrast than in Fig. 3.22 and monochromatic PSF in a well-aligned setup. b) Monochromatic PSF resulting from differential tip. c) Monochromatic PSF resulting from differential tilt. d) The size of the PSF on the detector is adjustable to simulate different plate scale situations.*

The polychromatic PSF in Fig. 3.22 is influenced by a high degree of incoherence, as the low fringe contrast indicates. It was taken as an example for the case of a finite coherence length and does not show the white light fringe. By moving the micro-positioning stage it is possible to identify the region in which the OPD in the system is smaller than the coherence length. The choice of the pinhole diameter has not yet been optimized for the optimum trade-off between fringe contrast and throughput.

The next steps mainly involve software development. All hardware components of the fringe tracking loop (CCD, piezo controller, motor controller) have to provide interfaces that can be accessed in a Linux environment. Once this is possible, the first version of a fringe tracking loop will be realized. The response

functions of the piezo actuators with their different loads and the latencies caused by the individual components in the control loop have to be determined. This input is then used to identify the control parameters. Several software components that will be used in the testbed interferometer are part of the FFTS software package.

CHAPTER 4

Interferometry on extragalactic targets

The final chapters of this thesis will deal with the purpose of the development of astronomical instrumentation: the observation of astronomical targets and the astrophysical interpretation of the obtained data. Chapters 5 and 6 contain two examples of extragalactic science, which will benefit from high-spatial resolution interferometric data at various wavelengths: quasistellar objects (QSOs) and interacting galaxies. Studies on the two classes of objects will take advantage of the capabilities that will be provided by the LBT and LINC-NIRVANA. The two studies presented here are based on unresolved observational data in the mm wavelength domain. Interferometric observations in this domain are a desirable next step, which provides important structural and dynamical information, especially on the molecular gas reservoirs in these objects. A multi-wavelength analysis of mm and future high-resolution NIR data will allow to draw a more profound picture of the processes that govern the appearance of these two classes of extragalactic objects. One major result of such high-resolution studies may be the proof that both classes are not independent phenomena but linked via an evolutionary sequence. Many indications for the inclusion of galaxy interaction in the history of QSO hosts have already been published.

Quasistellar objects and their host galaxies

At the time of their discovery, QSOs appeared to be unresolved objects with a starlike morphology but with a clearly nonstellar spectrum. This peculiar class of extragalactic objects attracts the attention of astronomers for almost 60 years now. The prominent and compact appearance results from their bright active galactic nuclei (AGN), which in the case of QSOs may completely dominate the brightness distribution of the galaxies hosting such objects. The spectral energy distribution of these objects extends over a wide range of the electromagnetic spectrum with roughly equal energy emitted in each waveband. Different approaches to search for AGN in various wavelength domains resulted in a large number of catalogs. Automated surveys like the Sloan Digital Sky Survey currently lead to a rapid growth of the number of known objects. Véron-Cetty & Véron (2006) list ~85 000 QSOs and ~22 000 low luminosity AGN in the 12th edition of their catalog. QSOs are among a large variety of AGN appearances

that have been phenomenologically classified. An incomplete selection is:

- *Seyfert galaxies*. These objects are low luminosity AGN that show highly exited strong emission lines originating in the nucleus. Such lines show a Doppler broadening of the order of 500 km s^{-1}. Seyferts can be further divided into two subclasses: Type II Seyfert galaxies only show the mentioned "narrow" line emission of both permitted and forbidden transitions. In addition to this feature the lines in Type I Seyferts also show very broad wings of the order of 1000 to 5000 km s^{-1} or beyond. Both types are strong emitters in the infrared wavelength domain. Often the spectra show a non-thermal power-law continuum component.

- *Radio galaxies*. These objects appear bright in the radio wavelength domain. For most of these radio-loud objects an optical counterpart was identified (normal elliptical galaxies in most cases). Their optical spectra again allow to distinguish between *narrow-line radio galaxies* similar to Type II Seyferts and *broad-line radio galaxies* with spectra comparable to the ones of Type I Seyferts. Radio galaxies are closely related to the jet phenomenon, a directed outflow of material originating from the AGN.

- *Quasistellar radio sources (Quasars) and QSOs*. For some radio-loud objects the search for an optical counterpart resulted in an unresolved powerful point source instead of an elliptical galaxy. These objects have been named Quasars. Quasar nuclei are exceptionally bright in the optical, other than that they do not differ from Type I Seyferts. The common but rather arbitrary borderline for Quasars is the absolute magnitude $M_B \sim -23$ mag, fainter objects are classified as Seyferts. Some definitions explicitely distinguish between radio-loud Quasars and radio-quiet QSOs. Others introduce the term "QSO" for optically bright Type I AGN and do not consider the radio properties of these objects. QSO surveys carried out in the visible wavelength domain generally do not introduce radio selection criteria. As the sample discussed in Chapter 5 is based on such a survey (Wisotzki et al. 2000), the latter interpretation of the term "QSO" is followed.

It can be assumed that most AGN systems are very similar in their physical properties. Binney & Merrifield (1998) state three factors that have a dominating influence on the different appearance of these sources: (I) the luminosity of some objects is significantly larger than that of others, (II) some objects possess jets whereas others don't, (III) anisotropic effects, i.e. different appearance depending on the objects' orientation relative to the line of sight. Orientation-based unification models (e.g. Antonucci 1993) try to explain the various appearances geometrically.

Since AGN are part of a galaxy, it is obvious to ask whether and how AGN are influenced by the character of the host galaxy and vice versa. Many questions related to AGN and their host galaxies are still not answered (cf. Barthel & Sanders 2006). To give some examples: The feeding mechanisms that provide the abundant supply of material needed to fuel the enormous luminosity of QSOs are still unclear. So is the role of galaxy mergers in the history of QSO host galaxies, the connection to ultraluminous infrared galaxies or the relation to circum-nuclear starburst activity in the host galaxies. In Chapter 5 global molecular gas properties of nearby low-luminosity QSO host galaxies are presented and a potential strong concentration of molecular gas in the centers of the hosts is discussed. This study has also been published in Bertram et al. (2007).

Interaction in galaxy clusters

Galaxies are found as relatively isolated systems or in pairs, in groups or in clusters with several 10 up to several 1000 galaxies. Rich galaxy clusters have typical diameters of several Mpc and are rather rare. Nevertheless, most galaxies are part of gravitationally bound systems of various sizes and, therefore, are exposed to their environment. Many aspects of galaxy interaction in clusters have been discussed in the literature, such as direct interaction with companions, with the cluster potential or with the intracluster medium. These interactions have consequences for all participants. Galaxies may show tidal signatures, lopsided gas distributions or even completely disturbed morphologies. The intracluster medium gains material which was initially bound in galaxies and was lost in the course of interaction. The largest known galaxies are found in the centers of the cluster potential. These so called cD galaxies are supergiant elliptical galaxies that probably gained their mass by cannibalizing neighboring galaxies.

Naturally, interaction is often discussed in the context of galaxy evolution. One important hint is given by Butcher & Oemler (1978) who show that rich galaxy clusters at $z \geq 0.5$ have a significantly higher fraction of blue, i.e., gas rich disk galaxies with active star formation than it is the case for $z = 0$. In other words: such dense environments may favor the transition from gas-rich disk galaxies into gas depleted ellipticals. The results of Giovanelli & Haynes (1985) point into the same direction. They show that galaxies in the centers of rich clusters are deficient in atomic hydrogen. This interaction affecting the interstellar medium of galaxies is commonly explained with ram pressure stripping in the core of a cluster. In Chapter 6 a similar, although much weaker effect on the molecular gas content is discussed for members of the galaxy cluster Abell 262. Part of the data discussed in Chapter 6 have been published in Bertram et al. (2006a).

Several indications also point to a link between the richness on the environment and the existence of QSOs. Close companions are commonly found in the vicinity of AGN hosting galaxies.

The benefits of NIR homothetic imaging

Because of the dominating contribution of the AGN to the overall brightness distribution of a QSO host galaxy, the identification of parameters of the host galaxy is often a big challenge. The environment in the vicinity of the AGN is even more difficult to observe. However, the central few 100 pc not only harbor the AGN itself but may also contain massive circum-nuclear starburst regions. In order to study the AGN – host connection, it is essential to separate starburst and AGN components from the underlying host galaxy. Such a separation is a non-trivial task with demanding requirements on observation and data reduction techniques. Spatial resolution is a key parameter in this context. An increase in spatial resolution narrows down the region of the galaxy image that is affected by the PSF of the AGN. But also the stability of the PSF and the exact knowledge of its shape play important roles in image analysis of AGN hosts.

Highest spatial resolution in the NIR can be achieved with stellar interferometers such as the VLT interferometer or the Keck interferometer. Baselines of more than 100 m allow for milli-arcsecond resolution. However, their optical designs do not support homothetic beam combination. Thus, the field of view of these interferometers is very small. Furthermore, the discrete sampling of the visibility function with the small number of available baselines currently does not permit the mapping of sources (at least not in a regular observing scheme). Therefore, experiments carried out with these specialized instruments mainly aim at measuring the angular sizes of a limited number of bright localized sources.

The Fizeau imaging interferometer LINC-NIRVANA at the LBT on the other hand is intended to be a general purpose instrument with a broad scientific scope. It will provide a tripled spatial resolution and doubled sensitivity compared to current 8 m class telescope technology. Its $10''$ field of view is ideally suited for extragalactic astronomy. Naturally, high spatial resolution and sensitivity is a common desire in most fields of observational astrophysics and in any wavelength domain. In the case of interacting galaxies, high spatial resolution NIR observations provide information on signs of interaction such as tidal tails, tidal bridges or more severely disturbed galaxy morphologies, stellar population or externally triggered star formation activity.

Interferometric observations of mm CO line emission

Emission lines carry important information about the excitation conditions that are prevalent in the environments of their origin. A lot of properties, such as gas densities, temperatures, composition or gas masses are derived in emission line analyses. Mapping of line emission allows to determine the gas distribution, line profiles provide information on velocities and dispersion. Because of its relative abundance, ^{12}CO is the most important line emitter in the mm wavelength domain. Except for H_2, it is the most common molecule in the universe. And other than cold H_2, which is difficult to detect in space, ^{12}CO has a permanent dipole momentum that allows for prominent rotational emission lines. The J=1−0 (115 GHz $\hat{=}$ 2.6 mm) and J=2−1 (230 GHz$\hat{=}$ 1.3 mm) transition lines are observable with ground based instruments through atmospheric transmission windows. Since CO is collisionally coupled to H_2, ^{12}CO(1−0) is used as a tracer for cold H_2.

Current local mm arrays allow to observe CO line emission with sub-arcsecond spatial resolution in long baseline configurations. But also maps with more moderate angular resolution resulting from observations with more compact array configurations can provide important structural information for both science cases. In Chapter 5 indications of a confinement of molecular gas in nearby low-luminosity QSO host galaxies are outlined. Such a confinement has been found in ultraluminous infrared galaxies, which are believed to be the predecessors of QSO hosts. Interferometric follow-up observations are required to confirm the presence of such a confinement. In the case of Abell 262 presented in Chapter 6, the indicated existence of a moderate environmental effect on the CO content of cluster galaxies can only be verified, if the gas distribution is known. The CO emission region may not be fully covered by the extent of a single-dish telescope beam at 115 GHz. To derive the overall intrinsic CO content, source size estimates were necessary. These estimates introduce a serious uncertainty in the gas mass estimates. High resolution information indicating the actual sizes of the CO emission regions are needed to overcome this problem. For one galaxy, UGC 1347, such an interferometric follow-up observation is exemplified in Sect. 6.3.2.

CHAPTER 5

Molecular gas in nearby low-luminosity QSO host galaxies

5.1 Introduction

The investigation of the molecular gas content and its distribution in the host galaxies of QSOs is a key issue in the understanding of evolutionary sequences and environments of AGN. All proposed sequences involve star formation and an abundant supply of material to fuel the starburst and the central engine.

Sanders et al. (1988) were the first to discuss a connection between ultraluminous infrared galaxies (ULIGs) and QSOs, suggesting that both represent different stages in an evolutionary sequence that starts with the collision of gas-rich spiral galaxies. In the course of the merger, circumnuclear starburst activity is triggered and a dominant part of available molecular gas is concentrated within the center of the merging galaxy. Several interferometric studies on individual ULIGs, like the archetypal ULIG Arp 220 (e.g. Scoville et al. 1991), reveal a massive concentration of molecular gas in the center ($\lesssim$ 1 kpc diameter). The bulk of H_2 in these gas rich objects seems to be associated with this central gas accumulation. This massive concentration not only favors starburst activity but may also be required to drive the nuclear activity that becomes apparent in the QSO phase of the sequence. The more distant and more gas-rich submillimeter galaxies (SMGs) resemble scaled-up versions of the local ULIG population, also showing compact CO emission regions confined to the center. Tacconi et al. (2006) state a median diameter of $\leq$ 4 kpc for 8 SMGs.

Contrary to the evolutionary model, Downes & Solomon (1998) question the need for an AGN to power the FIR emission in ULIGs. They argue that extreme starbursts in circumnuclear molecular disks or rings are fully accountable for the high FIR luminosity. Following their line of arguments implies that, although several ULIGs with AGN are known, AGN are not mandatory for the ULIG appearance and ULIGs are not necessarily the predecessors of QSOs.

A recent study of Dunlop et al. (2003) on the morphological properties of QSO host galaxies discusses a decrease of the number density of disk dominated host galaxies ending in a complete depletion at $M_V \leq -23$ mag (they are assum-

ing $H_0 = 50$ km s^{-1} Mpc^{-1}). From their analysis of Hubble space telescope and NIR data they conclude that QSO hosts have properties very similar to red, quiescent elliptical galaxies. These objects usually are gas depleted. Barthel (2006) argues for a more differentiated picture at least of intermediate luminosity QSO hosts and points to several indications of recent or ongoing star formation activity in these objects.

Little is known about molecular gas in nearby QSO hosts: Evans et al. (2001, 2006) and Scoville et al. (2003) discuss small samples of QSO host galaxies selected from the Palomar-Green (PG) Bright Quasar Survey (Schmidt & Green 1983). Few studies on individual sources add to the incomplete picture of molecular gas in local QSO hosts. A common denominator seems to be the presence of large amounts of molecular gas in the majority of these objects, which militates against a quiescent nature of host galaxies. The distribution of molecular gas, the extent and density of regions emitting CO line emission and similarities with or differences to local Seyfert I galaxies have not yet been studied on a solid statistical base. More detailed multi-wavelength investigations of a larger sample of nearby QSOs are certainly beneficial in the controversial debate on the nature and history of QSOs. Especially the separation of the starburst and the AGN component in extragalactic objects from the faint contribution of the underlying host galaxy require exceptionally high spatial resolution and sensitivity. The nearby QSOs with $z \leq 0.1$, therefore, represent an important link between the cosmologically local, less luminous AGN and the high redshift, high luminosity QSOs (at $z \geq 0.5$). Within this volume the accessibility of important structural information with state-of-the-art interferometers is technically feasible. In the millimeter domain, interferometers then provide sub-kpc resolutions that allow to probe the sizes of potentially compact circum-nuclear molecular gas reservoirs similar to the ULIG case (cf. Fig. 5.1). If the molecular gas is less confined to the center compared to the ULIG case it will be possible to study the distribution and potential signs of interaction on larger scales.

A sample of nearby UV excess QSOs or luminous Seyfert I galaxies was selected, that is not only suitable for interferometric imaging in the mm wavelength domain, but also allows for detailed imaging and spectroscopy in the NIR. For 41 members of the sample single-dish CO data were obtained (in one case also interferometric data). The sample is introduced in Sect. 5.2, together with a definition of the term "low-luminosity QSO" that is used throughout this study. The presentation of the results follows in Sect. 5.4. The data allows to draw conclusions on the total molecular gas content of low-luminosity QSOs and can be related to existing visible and far infrared quantities, as presented in Sect. 5.5. $H_0 = 75$ km s^{-1} Mpc^{-1} and $q_0 = 0.5$ are assumed throughout the chapter.

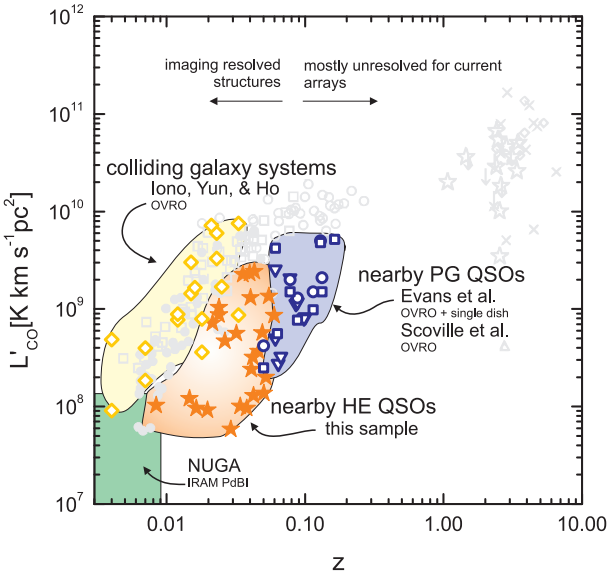

Figure 5.1: *L'_{CO}-z distribution of already existing interferometric imaging studies of AGN hosts / interacting galaxies (thick outlined symbols) and the distribution of the nearby low-luminosity QSO sample. The underlying light gray symbols represent a compilation of the most CO luminous objects ((U)LIGs/SMGs/HzRGs/QSOs) measured so far (Greve et al. 2005) for the corresponding redshifts. The objects in the nearby low-luminosity QSO sample have redshifts that allow to resolve structures on the sub-kpc scale in the ^{12}CO(1−0) transition with current mm-interferometers.*

5.2 The nearby low-luminosity QSO sample

The only selection criterion for the sample of nearby low-luminosity QSOs was their small cosmological distance: only objects with a redshift z < 0.060 were chosen. This redshift limit is based on a NIR spectroscopic constraint: It ensures the observability of the diagnostic CO(2−0) rotation vibrational band head absorption line in the NIR, which is important for the stellar population analysis. This line is then still accessible in the K-band.

The members were selected entirely from an extended catalog of sources found in the Hamburg/ESO survey (HES). The HES (Wisotzki et al. 2000) is a wide angle survey for optically bright QSOs, with a well-defined flux limit of $B_J \lesssim 17.3$ mag, varying from field to field, and a redshift coverage of 0 < z < 3.2. QSO candidates were identified in digitized objective prism plate data by applying a color- and spectral feature based selection scheme. With the exception of objects listed in the Véron-Cetty & Véron (1996) catalog, all candidates were subject to spectroscopic follow-up observations to confirm the object's identity and to reject false classifications.

The application of a starlike morphological criterion in many other QSO samples like the PG Bright Quasar Survey or the 10k catalog of the 2dF QSO Redshift Survey results in a significant degree of incompleteness at the low redshift end. One of the main advantages of the HES over other surveys is the consideration of extended objects. The HES sample, therefore, shows a high volume density of luminous type I AGN also at low cosmological distances. This circumstance makes the HES sample a valuable source of objects for a study of nearby QSOs. A total of 99 objects within the volume $0.01 \leq z \leq 0.06$ were identified by the HES. Thirty-nine of these form the subsample that is discussed in this study. The objects in the subsample all have $\delta > -30°$. To avoid potential selection biases, the composition of the subsample matches the full sample of nearby low-luminosity QSOs in terms of redshift distribution and percentage of IRAS detected sources.

It is important to note that no luminosity discrimination between QSOs and Seyfert I galaxies was applied by the HES – all luminous type I AGN showing broad emission lines (FWHM $\geq$ 1000 km s^{-1}) in their follow-up spectra were included in their catalog. This has a direct implication on the absolute brightness distribution of the subsample here referred to as "nearby low-luminosity QSO sample". The sample clearly probes the low luminosity tail of the local quasar luminosity function (Köhler et al. 1997). All objects in the sample have absolute B_J magnitudes exceeding (i.e., dimmer than) the traditional boundary[1] $M_B \sim$-22 mag between higher luminosity QSOs and lower luminosity Seyfert I galaxies. This boundary has no astrophysical motivation, as it was technologically induced at the time of its introduction (Schmidt & Green 1983). However, to respect the commonly used definition of the term "QSO", the term "low-luminosity QSO" is used throughout the study for objects identified in QSO surveys that may be fainter than the traditional boundary magnitude. Not only the HES but also the PG Bright Quasar Survey provide low-luminosity QSOs in their samples.

The restriction to type I AGN in the HES naturally resulted in the exclusion of type II AGN in the nearby low-luminosity QSO sample. For this reason the comparison with literature data in Sect. 5.5 was also restricted to type I AGN.

Several members of the nearby low-luminosity QSO sample were already subject to studies in the NIR and mm wavelength domain. First NIR imaging and spectroscopic results of nearby low-luminosity QSO sample members are presented in Fischer et al. (2006). A series of observations carried out with SEST and BIMA (Bertram et al. 2006b) preceded the observations presented in this study. In these first runs a slightly differently composed sample was scanned for millimetric CO emission. The primary goal was to identify the CO brightest

[1] translated to the cosmology used within this study

objects for high resolution interferometric follow-up observations. The resulting SEST spectra and CO properties of two detected nearby HES objects, HE 0108-4743 and HE 2211-3903, are included in Sections 5.4 and 5.5. However, due to the higher detection limit, they were not included in the FIR unbiased subsample discussed in Sect. 5.5.1. The third detection, HE 1029-1831, was included. Follow-up observations with the Plateau de Bure Interferometer allowed to resolve the central region in this exemplary case. A detailed analysis can be found in Krips et al. (2007).

5.3 Observations and data reduction

This chapter focuses on the results of sensitive observations carried out with the IRAM 30 m telescope on Pico Veleta (Spain) in September 2005, June 2006 and January 2007.

Twenty-six out of 38 observed sources were detected (cf. Table 5.1). In most cases the detection limits were much lower than in the preceding observing runs. However, part of the data obtained in June 2006 suffered from mediocre weather conditions and had to be excluded from further analysis. Moreover, in several cases the observing frequencies had to be based only on the redshifts provided by the HES. Although nominally uncertain by only 300 km s^{-1}, in some cases the Hamburg/ESO based systemic velocities deviated from the measured systemic velocity centroids by up to 750 km s^{-1} (cf. Sect. 5.5.2). A certain fraction of weak sources may not have been detected because of this de facto uncertainty.

The A and B receivers were used together with the 1 MHz and 4 MHz filter banks to acquire ^{12}CO(1−0) and ^{12}CO(2−1) emission line data in parallel. The configuration of the backends allowed for a velocity coverage Δv between 1300 km s^{-1} and 1400 km s^{-1} at the redshifted CO lines. The compactness of the sources allowed to take advantage of the wobbling secondary and the resulting excellent background stability. In the three observing runs useful data with a total of ∼65 h on-source integration time was obtained.

The data reduction was carried out using the IRAM software CLASS. Each polarization direction was analyzed individually and both directions were averaged whenever appropriate. In all cases it was sufficient to subtract linear baselines of background intensity. To increase the signal-to-noise ratio, most of the spectra (cf. Fig. 5.2) were hanning smoothed. In order to obtain main beam temperatures, the main beam efficiency $B_{\rm eff} = 0.75$ and the forward efficiency $F_{\rm eff} = 0.95$ were applied to $T_{\rm A}^*$ at ∼110 GHz and $B_{\rm eff} = 0.54$ and $F_{\rm eff} = 0.91$ to $T_{\rm A}^*$ at ∼220 GHz. The line intensities $I_{\rm CO}$ represent main beam temperatures integrated over the full velocity range of the emission line. The errors $\Delta I_{\rm CO}$ were

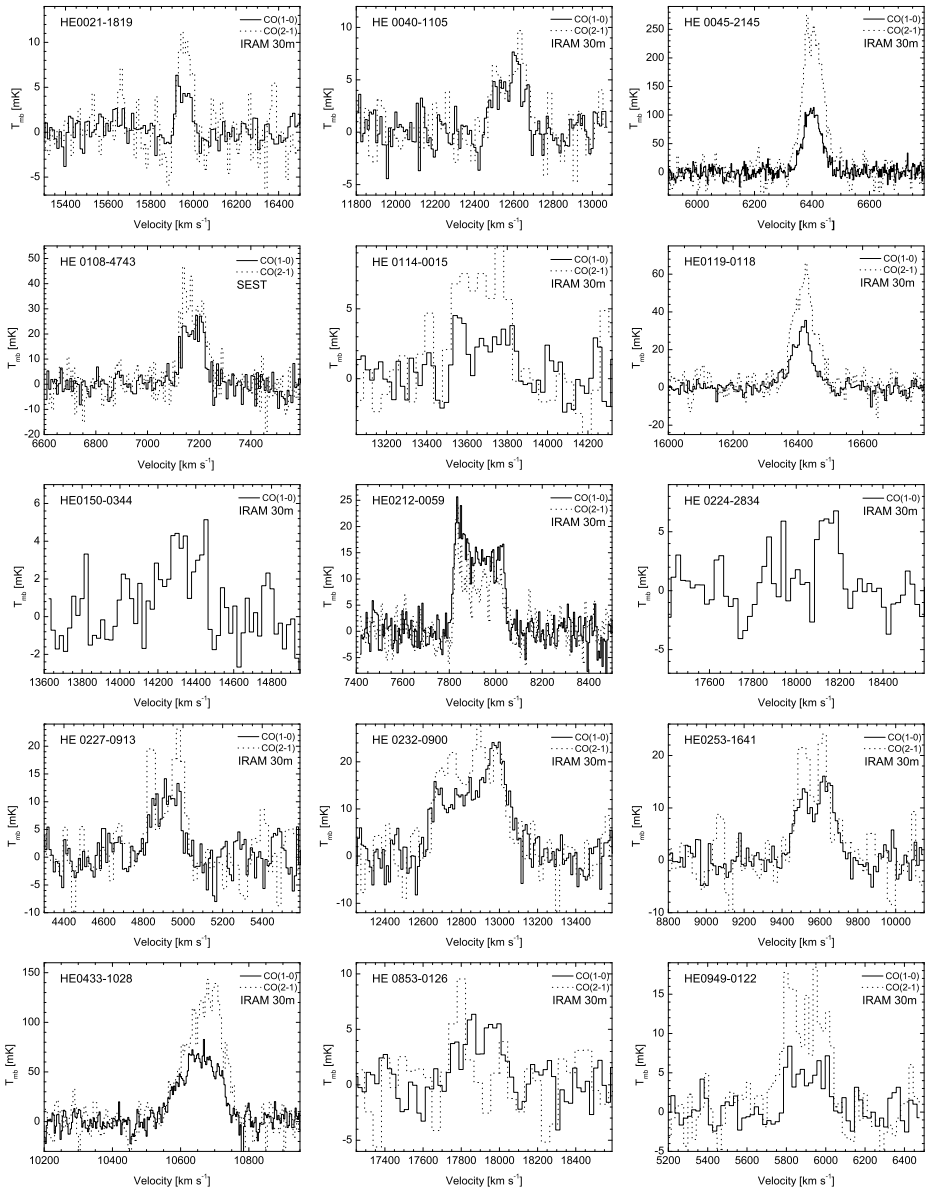

Figure 5.2: ^{12}CO *spectra of detected host galaxies.*

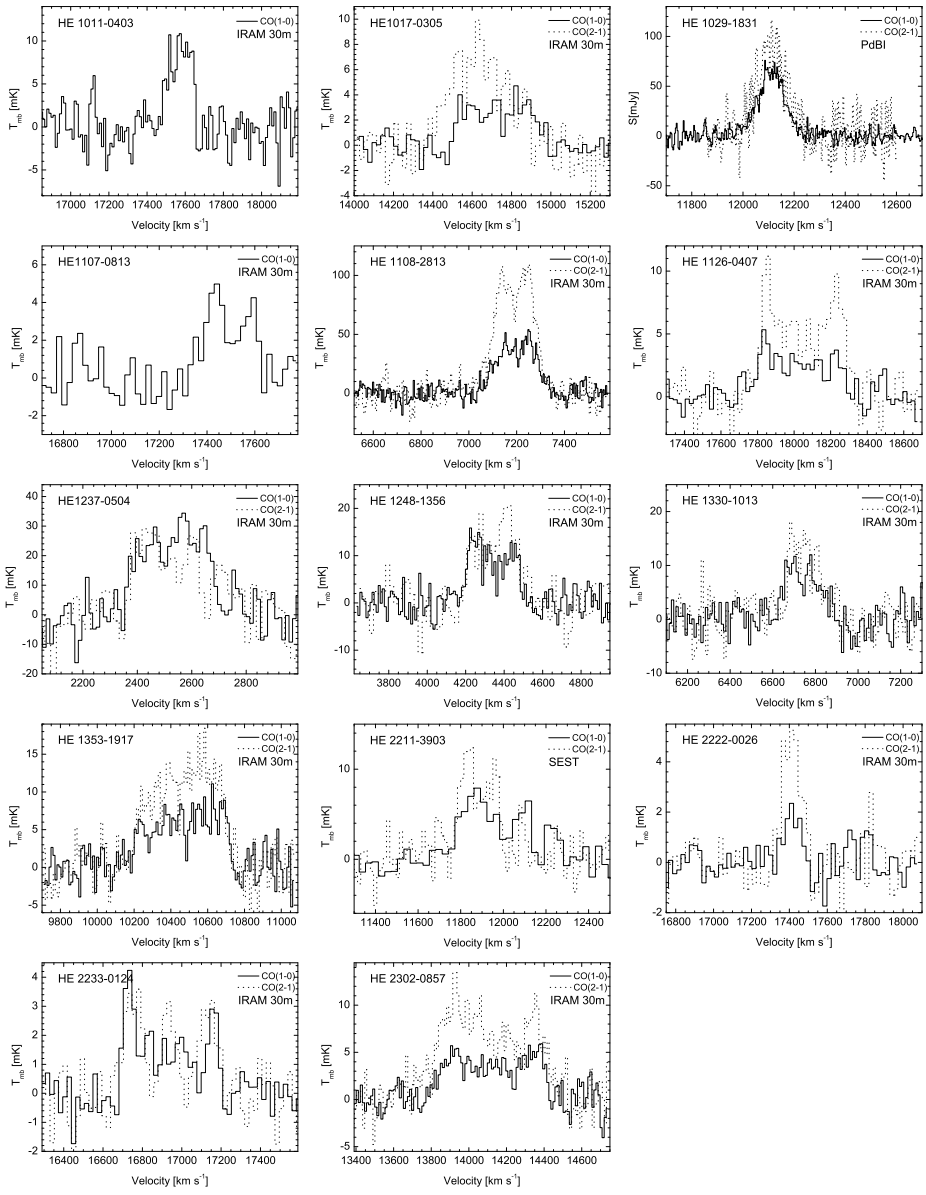

Figure 5.2: *—continued*

Table 5.1: *Journal of the observations carried out with the IRAM 30 m telescope in in September 2005, June 2006, and January 2007. Three previously detected sources are also listed. z was taken from the HES. t_{int} denotes the total on-source integration time for each receiver.*

Obj.	alt. name	R.A. (J2000) [h	m	s]	Dec. (J2000) [°	′	″]	z	Obs. run	t_{int} [min]
HE 0021-1810	VCV2001 J002339.2-175355	00	23	39.4	-17	53	53	0.053	’07	118
HE 0021-1819	NPM1G -18.0010	00	23	55.3	-18	02	50	0.052	’07	140
HE 0040-1105	VIII Zw 36	00	42	36.8	-10	49	21	0.041	’06	112
HE 0045-2145	IRAS 00452-2145	00	47	41.3	-21	29	27	0.021	’05	45
HE 0108-4743	IRAS 01089-4743	01	11	09.7	-47	27	36	0.029[1]	SEST	76
HE 0114-0015	SDSS J011703.58+000027.4	01	17	03.6	+00	00	27	0.046	’06	98
HE 0119-0118	II Zw 1	01	21	59.8	-01	02	25	0.054	’05	60
HE 0150-0344	IRAS 01505-0343	01	53	01.4	-03	29	24	0.046	’06	70
HE 0203-0031	Mrk 1018	02	6	15.9	-00	17	29	0.043	’06	56
HE 0212-0059	Mrk 590	02	14	33.6	-00	46	00	0.027	’05	60
HE 0224-2834	AM 0224-283	02	26	25.7	-28	20	59	0.060	’06	55
HE 0227-0913	Mrk 1044	02	30	05.4	-08	59	53	0.017	’06	46
HE 0232-0900	NGC 985	02	34	37.7	-08	47	16	0.043	’06	32
HE 0253-1641	NPM1G-16.0109	02	56	02.6	-16	29	16	0.032	’05	120
HE 0345+0056	IRAS 03450+0055	03	47	40.2	+01	05	14	0.029	’05	117
HE 0351+0240	VCV2001 J035409.4+024931	03	54	09.4	+02	49	30	0.034	’06	74
HE 0412-0803	MS 04124-0802	04	14	52.6	-07	55	41	0.038	’06	115
HE 0429-0247	RXS J04316-0241	04	31	37.0	-02	41	25	0.041	’06	61
HE 0433-1028	Mrk 618	04	36	22.2	-10	22	33	0.033	’05	25
HE 0853-0126		08	56	17.8	-01	38	07	0.060	’06	135
HE 0853+0102		08	55	54.3	+00	51	10	0.052	’06	120
HE 0934+0119	Mrk 707	09	37	01.0	+01	05	43	0.051	’06	72
HE 0949-0122	Mrk 1239	09	52	18.9	-01	36	44	0.019	’05	110
HE 1011-0403	PG 1011-040	10	14	20.6	-04	18	41	0.057	’06	122
HE 1017-0305	Mrk 1253	10	19	32.9	-03	20	15	0.048	’05	274
HE 1029-1831	NPM1G-18.0348	10	31	57.3	-18	46	34	0.040	PdBI	

Table 5.1: *continued*

Obj.	alt. name	R.A. (J2000) [h	m	s]	Dec. (J2000) [°	′	″]	z	Obs. run	t_{int} [min]
HE 1107-0813		11	09	48.5	-08	30	15	0.057	’07	80
HE 1108-2813	VCV2001 J111048.0-283004	11	10	48.0	-28	30	03	0.023	’05, ’07	41
HE 1126-0407	Mrk 1298, PG1126-041	11	29	16.6	-04	24	08	0.060	’05, ’07	41
HE 1237-0504	NGC 4593	12	39	39.4	-05	20	40	0.009	’05	35
HE 1248-1356		12	51	32.4	-14	13	17	0.015	’06	102
HE 1310-1051	PG 1310-108	13	13	05.7	-11	07	42	0.034	’07	64
HE 1330-1013		13	32	39.1	-10	28	53	0.022	’07	59
HE 1338-1423		13	41	12.9	-14	38	40	0.041	’07	85
HE 1353-1917	VCV2001 J135636.7-193144	13	56	36.7	-19	31	44	0.034	’07	97
HE 1417-0909		14	20	06.3	-09	23	13	0.044	’07	106
HE 2128-0221	6dF J2130499-020814	21	30	49.9	-02	08	15	0.052	’05, ’07	295
HE 2211-3903		22	14	42.0	-38	48	24	0.039	SEST	114
HE 2222-0026	SDSS J222435.29-001103.8	22	24	35.3	-00	11	04	0.058	’07	225
HE 2233-0124	VCV2001 J223541.9+013933	22	35	41.9	-01	39	33	0.056	’07	224
HE 2302-0857	Mrk 926	23	04	43.4	-08	41	09	0.046	’07	150

[1] The redshift for HE 0108-4743 was taken from Véron-Cetty & Véron (1996) and not spectroscopically verified by the HES. Since it differs significantly from other visual redshift data (Lawrence et al. 1999), the value was excluded from the redshift discussion in Sect. 5.5.2.

determined by the geometric average of the line error $\Delta I_{\rm L} = \sigma v_{\rm res} \sqrt{N_{\rm L}}$ and the baseline error $\Delta I_{\rm B} = \sigma v_{\rm res} N_{\rm L} / \sqrt{N_{\rm B}}$, where σ is the channel-to-channel RMS noise, $v_{\rm res}$ the spectral resolution, $N_{\rm L}$ the number of channels over which the line is distributed and $N_{\rm B}$ the number of channels used for the baseline fit.

5.4 Results

The CO line luminosity $L'_{\rm CO}$ of the ^{12}CO(1−0) transition can be expressed as (Solomon, Downes, & Radford 1992a):

$$L'_{\rm CO} = 23.5\ \Omega_{S*B}\ D_L^2\ I_{\rm CO}\ (1+z)^{-3}\ \left[\mathrm{K\ km\ s^{-1}\ pc^2}\right], \tag{5.1}$$

i.e., as a function of the velocity-integrated line intensity $I_{\rm CO}$ in units of K km s^{-1}, the luminosity distance $D_{\rm L}$ measured in Mpc, and the solid angle of the source convolved with the telescope beam $\Omega_{\rm S*B}$ in square arcseconds. For sources with solid angles much smaller than the telescope beam, $\Omega_{\rm S*B}$ can be approximated with $\Omega_{\rm Beam}$. The expression $L'_{\rm CO}$, commonly used in radio astronomy, and the general expression of the line luminosity $L_{\rm CO}$ are related by

$$L_{\rm CO} = \left(8\pi k \nu_{\rm rest}^3 / c^3\right) L'_{\rm CO} \tag{5.2}$$

(Solomon et al. 1992b). 1 K km s^{-1} corresponds to $\sim 1.9 \cdot 10^{29}$erg s^{-1} at the 115 GHz transition.

Established correlations (Young et al. 1995) between the 25.0 $B_{\rm mag}$ arcsec^{-2} isophotal diameter D_{25} of galaxies and the size of their CO emission region were used to confirm that, with the exception of HE 0212-0059 and HE 0232-0900, the sources should all be smaller than the ∼22″ telescope beam resulting at ∼115 GHz. For the two exceptional cases it is likely that the overall CO line luminosity is underestimated in the present study. In the case of HE 0232-0900, already published data (Horellou et al. 1995a, see below) allowed to determine a factor ∼1.7 by which the current luminosity is too low. Because of the very similar optical extent, a similar factor can be assumed for HE 0212-0059.

The integrated line intensity, the systemic velocity (represented by the flux-weighted centroid of the CO(1-0) line), the linewidth (FWZI), the resolution of the smoothed spectrum as well as the derived CO luminosity of each detected source are shown in Table 5.2. Also shown are estimates for the molecular gas masses. They were obtained by applying a $M(\mathrm{H_2})/L'_{\rm CO}$ conversion factor α to the CO luminosity. The determination of the H_2 content using $L'_{\rm CO}$ as tracer has to be handled with care. Commonly used is a value of α=4.8 $M_\odot$ (K km s^{-1} pc^2)$^{-1}$ (Solomon & Barrett 1991), derived from galactic molecular cloud observations. The common approach of using a 'standard' conversion factor derived

from galactic observations has the shortcoming of disregarding the dependency of α on the metalicity of the region of interest (Israel 1997). For a sample of ultra luminous infrared galaxies Downes & Solomon (1998) state a conversion factor that is 5 times lower. Within this study $\alpha = 4\ M_{\odot}$ (K km s^{-1} pc^2)$^{-1}$ is adopted to allow for direct comparison with the results of Evans et al. (2001, 2006) or Scoville et al. (2003).

A subset of the sources had been subject to molecular gas studies before. The published data confirm the results listed in Table 5.2. The ^{12}CO(1−0) emission of the extended source HE 0232-0900 was mapped with the IRAM 30 m telescope by Horellou et al. (1995a). The value for $I_{\rm CO}$ of the central position agrees within 18%. After correction for the different beam sizes, the ^{12}CO(1−0) detections of HE 0227-0913 with the NRO 45m telescope by Vila-Vilaró et al. (1998), of HE 1237-0504 with SEST by Curran et al. (2000), and of HE 0433-1028 with SEST by Strong et al. (2004) agree within 10% with the values presented in this study. HE 1237-0504 was also observed by Maiolino et al. (1997) with the NRAO 12m telescope. Their beam-size corrected values for this object, for HE 0212-0059, and for HE 0949-0122, however, exceed the values presented here by a factor 2-3. For HE 0212-0059, the difference may be explained with the extension of the galaxy and the different beam sizes. The other results, however, are in contrast with the good agreements of the 4 other independent measurements mentioned above, which provide a high level of confidence in the data presented here.

5.5 Discussion

5.5.1 Detection rate and molecular gas mass

About 60% of the mostly southern sources in the nearby low-luminosity QSO sample have a declination $\delta \geq -30^{\circ}$ and can be observed with the IRAM 30 m telescope. Of these, about 65% have been subject to this study. They show a redshift distribution similar to the full nearby low-luminosity QSO sample (Fig. 5.3). Within the restricted redshift range considered in this sample, the number of objects per redshift bin is purely volume dependent – the number increases with increasing z. When plotted against redshift (Fig. 5.4), the particular position of the sample in between previously studied local Seyfert I and more luminous QSO host galaxies becomes apparent. The omission of a far infrared (FIR) selection and the on average larger distance, compared to the local Seyfert I population, resulted in the inclusion of several objects with FIR flux densities below the IRAS detection limit (cf. Sect. 5.5.4). In several of these cases it was still possible to detect CO emission.

Table 5.2: *Summary of ^{12}CO properties. Unless otherwise noted, the data was acquired with the IRAM 30 m telescope.*

			^{12}CO(1–0)						^{12}CO(2–1)		
Obj.	v_0 (LSR) [km/s]	D_L [Mpc]	I_{CO} [1] [K km/s]	Δv_{FWZI} [km/s]	v_{res} [km/s]	LS [2]	$L'_{CO}/10^8$ [3] [K km/s pc^2]	$M(H_2)$ [$10^9 M_\odot$]	I_{CO} [1] [K km/s]	Δv_{FWZI} [km/s]	v_{res} [km/s]
HE 0021-1819	15954	215.5	0.39±0.04	110	11.0	∧	2.1	0.8	0.68 ± 0.1	121	11.0
HE 0040-1105	12578	169.4	0.96±0.08	238	10.8	⊓	3.2	1.3	1.19±0.15	238	22.0
HE 0045-2145	6403	85.8	8.20±0.18	133	9.0	∧	7.2	2.9	22.39±0.59	181	5.3
HE 0108-4743[4]	7175	96.2	2.24±0.21	118	7.4	⊓	10.4	4.2	3.67±0.31	160	7.4
HE 0114-0015	13682	184.5	0.92±0.13	326	21.8	⊓	3.6	1.5	2.24±0.38	305	43.5
HE 0119-0118	16412	221.7	2.38±0.09	165	5.5	∧	13.5	5.4	4.70±0.17	143	5.5
HE 0150-0344	14329	193.3	0.89±0.15	305	21.8	⊓	3.8	1.5	[7]		
HE 0212-0059	7921	106.3	3.51±0.11	240	5.3	⊓	4.7[8]	1.9[8]	2.42±0.12	251	5.3
HE 0224-2834	18150	245.6	0.71±0.11[5]	132	21.1	∧	4.9	2.0	< 0.46	132	22.1
HE 0227-0913	4914	65.8	1.86±0.17	254	10.6	⊓	1.0	0.4	2.96±0.31	254	21.1
HE 0232-0900	12886	173.6	6.92±0.34	597	10.9	⊓	24.3[8]	9.7[8]	8.13±0.66	586	22.0
HE 0253-1641	9580	128.7	2.89±0.15	282	13.4	⊓	5.6	2.3	3.89±0.37	301	21.0
HE 0433-1028	10651	143.3	9.42±0.27	252	3.4	∧	22.6	9.0	16.55±0.48	199	5.4
HE 0853-0126	17899	242.1	1.28±0.15	331	22.1	⊓	8.6	3.4	0.82±0.36	309	44.1
HE 0949-0122	5905	79.1	1.23±0.14	276	21.2	⊓	0.9	0.4	3.55±0.24	318	21.2
HE 1011-0403	17572	237.6	1.37±0.12	187	11.0	⊓	8.9	3.5	[7]		
HE 1017-0305	14737	198.9	1.25±0.10	458	21.8	⊓	5.7	2.3	2.44±0.23	458	21.8
HE 1029-1831[6]	12112	163.1	4.24 ± 0.2	254	3.4	∧	13.1	5.3	5.05 ± 0.2	254	3.4
HE 1107-0813	17481	236.4	0.82±0.10	308	22.0	⊓	5.2	2.1	< 0.3	310	44.0
HE 1108-2813	7198	96.5	8.32±0.28	309	5.3	⊓	9.2	3.7	18.84±0.47	320	5.3
HE 1126-0407	18006	243.6	1.52±0.15	640	22.1	⊓	10.3	4.1	3.02±0.20	551	22.1
HE 1237-0504	2531	33.8	7.52±0.57	302	13.1	⊓	1.0	0.4	6.04±1.01	315	21.0
HE 1248-1356	4338	58.0	2.96±0.19	348	10.5	⊓	1.2	0.5	4.23±0.39	338	21.1
HE 1330-1013	6744	90.4	1.82±0.16	266	10.6	⊓	1.8	0.7	2.4 ± 0.2	245	10.6
HE 1353-1917	10472	140.8	3.25±0.22	592	10.7	⊓	7.6	3.0	5.5 ± 0.3	549	10.8

Table 5.2: *continued*

Obj.	v_0 (LSR) [km/s]	D_L [Mpc]	^{12}CO(1–0) I_{CO} [1] [K km/s]	Δv_{FWZI} [km/s]	v_{res} [km/s]	LS [2]	$L'_{CO}/10^8$ [3] [K km/s pc^2]	$M(H_2)$ [$10^9 M_\odot$]	^{12}CO(2–1) I_{CO} [1] [K km/s]	Δv_{FWZI} [km/s]	v_{res} [km/s]
HE 2211-3903[4]	11945	160.8	1.87±0.34	466	30.0	⊓	23.2	9.3	1.85±0.19	260	15.1
HE 2222-0026	17414	235.5	0.21±0.04	154	22.0	∧	1.3	0.5	0.61±0.06	176	22.0
HE 2233+0124	16913	228.6	0.89±0.08	506	22.0	⊓	5.4	2.1	0.95±0.12	506	22.0
HE 2302-0857	14120	190.4	2.31±0.16	653	10.9	⊓	9.7	3.9	5.17±0.29	817	10.9
Non-detections											
HE 0021-1810	16039	216.6	< 0.07	315	43.8		< 1.1	< 0.5	< 0.12		43.8
HE 0203-0031	12723	171.4	< 0.16	315	43.4		< 1.6	< 0.6	< 0.51		43.4
HE 0345+0056	8994	120.8	< 0.15	315	42.9		< 0.8	< 0.3	< 0.26		42.9
HE 0351+0240	10793	137.0	< 0.19	315	43.1		< 1.2	< 0.5	[7]		
HE 0412-0803	11392	152.9	< 0.14	315	43.2		< 1.2	< 0.5	[7]		
HE 0429-0247	12441	165.5	< 0.31	315	43.4		< 2.9	< 1.2	[7]		
HE 0853+0102	15589	210.5	< 0.16	315	43.8		< 2.4	< 1.0	[7]		
HE 0934+0119	15091	203.7	< 0.12	315	43.7		< 1.7	< 0.7	< 0.24		43.7
HE 1310-1051	10193	137.0	< 0.16	315	43.0		< 1.0	< 0.4	< 0.23		43.0
HE 1338-1423	12528	168.8	< 0.15	315	43.4		< 1.5	< 0.6	< 0.21		43.4
HE 1417-0909	13191	177.8	< 0.09	315	43.4		< 1.0	< 0.4	< 0.18		43.4
HE 2128-0221	15828	213.8	< 0.08	315	43.8		< 1.3	< 0.5	< 0.12		43.8

[1] Upper limits and errors represent 1σ. [2] Line shape. ∧ denotes a triangular shaped line profile, as it is expected for turbulent line-of-sight velocity dispersion. ⊓ represents boxy or double-horn line profiles indicative for emission from an inclined, rotating disk. [3] For the upper L'_{CO} limits, the average linewidth Δv = 315km s^{-1} and 3σ detection limits were considered. [4] SEST 15m telescope measurement. A beam efficiency B_{eff} = 0.7 was applied to T_A^* and a 45″ beam was considered for L'_{CO}. [5] 3σ detection level for T_{mb}. [6] IRAM PdBI measurement (Krips et al. 2007), resulting in $S\,\Delta v$ = (21 ± 1)Jy km s^{-1} for ^{12}CO(1–0) and $S\,\Delta v$ = (25 ± 1)Jy km s^{-1} for ^{12}CO(2–1). S/T_{mb} = 4.95 Jy/K was used to compare the PdBI results with the 30 m telescope data. [7] 1mm data not reliable due to high water vapor. [8] Source is not compact. Values too low by a factor ∼1.7

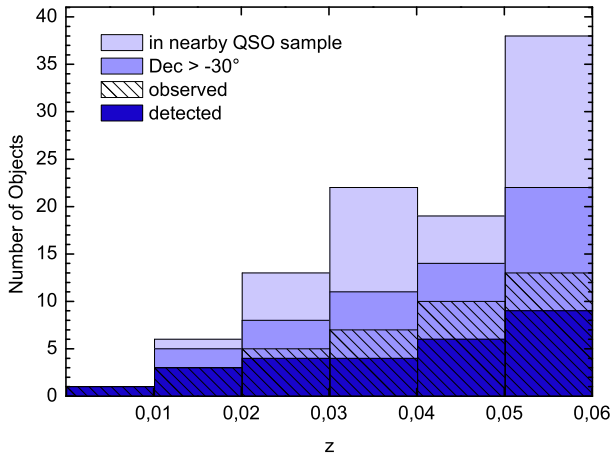

Figure 5.3: *The number of existing / observable with the IRAM 30 m telescope / observed / detected HE QSOs with increasing volume. At the distances discussed here, the frequency of occurrence is dominated by the size of the co-moving volume.*

The 3σ detection limits agree with the limits in the PG QSO host studies by Evans et al. (2001, 2006) and Scoville et al. (2003), carried out with the OVRO array and the IRAM 30 m telescope. Different from Evans et al. (2001, 2006), the volume limited sample of Scoville et al. (2003), consisting of 12 objects, is not confined to FIR selected sources. Therefore, a direct comparison with their results is appropriate. At redshifts exceeding 0.06, the common detection limit prevents the detection of galaxies with a molecular gas content of below 10^9 $M_\odot$ – only gas rich objects are then detectable. The redshifts of virtually all PG QSOs exceed this value. Nevertheless, the volume limited sample of Scoville et al. (2003) resulted in a detection rate of 75% which lets the authors conclude that the majority of luminous, low-redshift QSOs have gas-rich host galaxies. This picture may become more complicated when considering the incompleteness of the PG survey at low redshifts. The rejection of extended objects may cause an underrepresentation of bulge-dominated galaxies with a lower gas content. On the other hand, due to the arbitrariness of the $M_B \sim -22$ mag limit, low-luminosity QSOs above the line still may have host properties that are similar to their brighter equivalent. With 70% the detection rate of the IRAM 30 m observations presented here is almost identical to the rate of Scoville et al. (2003). The molecular gas masses of the detected host galaxies range from $0.4{\cdot}10^9 M_\odot$ to $9.7{\cdot}10^9 M_\odot$ with an average molecular gas mass of $2.8{\cdot}10^9 M_\odot$ ($3.0{\cdot}10^9 M_\odot$ when including the 2 sources that were detected with SEST).

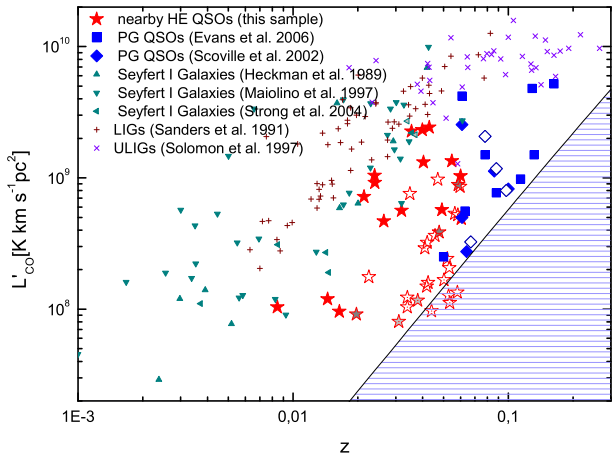

Figure 5.4: *CO luminosity versus redshift. For objects represented by filled shapes L_{FIR} is available, grey shapes indicate available upper limits for L_{FIR} and outlined shapes represent objects that have not been listed in the IRAS FSC. The shaded area in the bottom right corner indicates the region in which the determination of I_{CO} with the 30 m telescope falls below 0.315 K km s^{-1}. This value corresponds to a signal of 1 mK with a linewidth of 315 km s^{-1}, the average width of the detected lines.*

5.5.2 Comparison of CO and optical redshifts

Millimeter CO observations are well suited for the accurate measurement of systemic velocities of active galaxies. CO traces the cold and extended molecular gas distribution of the total host galaxy rather than the reservoir of highly excited gas in proximity to the central source. Features of the latter are commonly used to determine the redshift of active galaxies in the visible wavelength domain. These redshifts, however, can be affected by outflows, dust obscuration or other asymmetric phenomena that result in apparent velocities deviating from the actual systemic velocity.

For nearby objects like the sample discussed in this paper, the redshifts determined in the course of the HES follow-up spectroscopy program are mainly based on the narrow [O$_{\mathrm{III}}$] λ5007 emission line (Reimers et al. 1996). Boroson (2005) shows that the [O$_{\mathrm{III}}$] line is blue-shifted relative to the systemic velocity in up to 50% of all AGN. The emission peak shift may be as large as several hundred km s^{-1}. Fig. 5.5 shows the distribution of offsets between the velocities corresponding to the HE redshifts and the CO velocities measured in this study. Negative velocity differences imply blue-shifted visible emission features. On top of the nominal uncertainty of HE velocities ($\sim$300 km s^{-1}), the nearby low-luminosity QSOs indeed show a tendency for such a blue-shift with a mean velocity offset of -174 km s^{-1}.

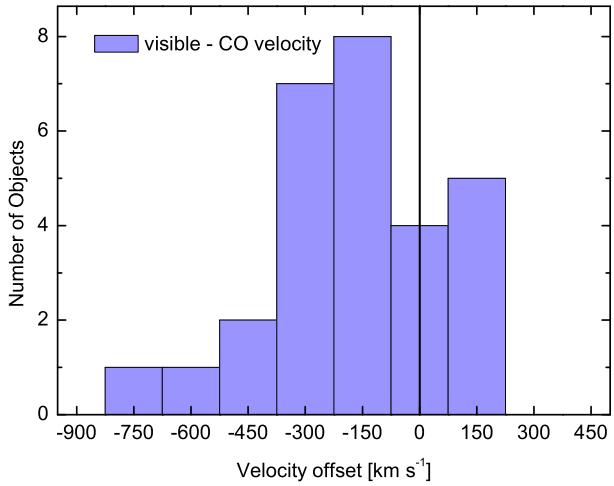

Figure 5.5: *The distribution of the differences between the CO velocity and the velocity derived from restframe visible spectroscopy. The systematic blueshift of the spectroscopic features determined in the visible is an indication for outflows or partial dust obscuration in the vicinity of the active nucleus.*

Table 5.3: *Mean CO(1–0) line widths and standard deviations of the mean for different line shapes and different absolute blue magnitudes. The numbers in parentheses represent the number of objects that fall into the corresponding category.*

	$\wedge$	$\sqcap$	$\wedge + \sqcap$
$M(B_J) > -20$	132 ± 13 (3)	301 ± 34 (11)	265 ± 33 (14)
$M(B_J) < -20$	200 ± 28 (4)	426 ± 49 (11)	367 ± 45 (15)
all	171 ± 22 (7)	364 ± 32 (22)	317 ± 29 (29)

5.5.3 Blue luminosity and CO line characteristics

Figure 5.6 shows the connection between absolute B_J brightness and CO luminosity. The B_J fluxes have a photometric uncertainty of ~0.2 mag and were determined by the HES group, based on their spectral plate data. Each value represents the flux within the central seeing disk, which for type I AGN at these redshifts is dominated by the nuclear contribution, with only small proportions from the host galaxy.

A more detailed description is given in Wisotzki et al. (2000). The magnitudes shown here are not corrected for extinction and, therefore, systematically too faint by a mean value of ~0.23 mag.

The data does not allow to distinguish between host and AGN contribution. Thus an increase of B_J luminosity can be the result of enhanced star formation

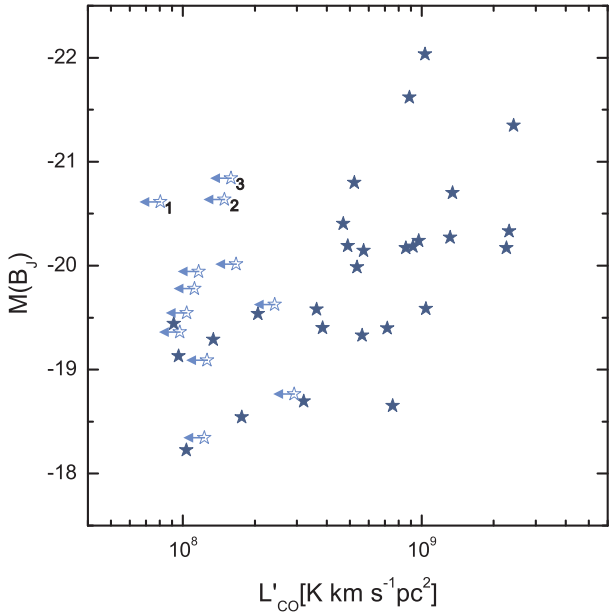

Figure 5.6: *Absolute B_J magnitude versus CO luminosity. The magnitudes shown here represent the central seeing disk, including contributions of both AGN and star formation in the central part of each galaxy. The majority of objects showing $M(B_J)$ brighter than -20 mag are also CO luminous. Exceptions are (1) HE 0345+0056, (2) HE 1338-1423, and (3) HE 0203-0031.*

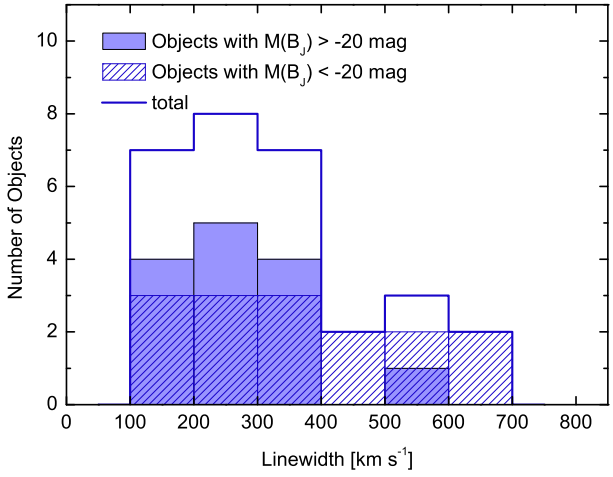

Figure 5.7: *Distribution of CO line widths (FWZI). Linewidths exceeding 400 km s^{-1} can be commonly found only in bright objects with absolute blue magnitudes < -20.*

activity in the central 1-2 kpc, enhanced AGN activity or both. In any way, the increase in activity comes along with larger reservoirs of molecular gas, as can be seen in Fig. 5.6. Except for 3 non-detected sources, low-luminosity QSOs with absolute central magnitudes brighter than $M(B_J) = -20$ mag all have CO luminosities of $\geq 5 \cdot 10^8$ K km s^{-1} pc^2, while the majority of fainter objects contain less molecular gas. This correlation seems to be intrinsic and not the result of a distance selection bias (with more luminous AGN being at larger distances with higher CO detection limits), as the small fraction of non-detections in the bright case shows. It remains unclear, whether the 3 B_J luminous non-detections are actually gas depleted or whether they were not detected because of an uncertain CO redshift. Upcoming HI observations, but also analyses of the morphologies in the visible/NIR will provide further information on the nature of these objects.

Not only the total CO content is higher but also the spread of the CO(1−0) line widths is wider for the brighter AGN hosts. Fig. 5.7 shows the distribution of line widths in all detected galaxies. With one exception, all objects showing FWZI line widths broader than 400 km s^{-1} have absolute central magnitudes of $M(B_J) \leq -20$ mag. The average line width of these bright objects is 367 km s^{-1}, ∼100 km s^{-1} broader than the fainter sources (cf. Table 5.3). The average signal-to-noise ratio (S/N) of the CO(1−0) detections in the B_J luminous case is only slightly (1.2 times) larger than the average S/N in the fainter case. Therefore, a significant S/N bias that potentially favors the identification of broader line profiles in more active objects is not present.

Such a different behavior could result from a selection effect in the optical identification process of QSO candidates. Objects with faint AGN activity may only be identified as type I AGN host when seen almost face-on, leaving the Seyfert I nucleus unobscured, while brighter AGN contributions can also be identified in objects with higher inclination.

A scenario of an intrinsically broader line width distribution, however, cannot be ruled out. A separation of sources into a class of triangular shaped and a second class of box shaped or double horn line profiles resulted in similar counts for each class (cf. Tables 5.2 and 5.3) in both the faint and the bright cases. The triangular shaped lines are indicative for a face-on view onto a turbulent gas distribution without a dominating disk component in the line-of-sight direction. The second class represents objects with rotating CO emission disks or rings at a certain inclination with respect to the line-of-sight. In several low-signal cases the assignment of a class was not obvious. Nevertheless, an aforementioned selection effect that favors low-inclination views on faint AGN candidates should yield a higher fraction of triangular shaped line profiles, which is not the case. Noting the caveat of small number statistics, the difference in

the mean line widths of triangular shaped line profiles should be pointed out. Bright objects with triangular shaped line profiles have a mean line width of 200 km s^{-1}, whereas in the faint cases the mean line width is only ~130 km s^{-1}. This difference could be a sign of higher velocity dispersion in the molecular gas distribution of the more active objects.

Most of the line profiles do not show strong asymmetries that can be used as indication for ongoing interaction. Clear asymmetries can be seen in the two sources that are probably larger than the telescope beam (HE 0212-0059 and HE 0232-0900). In these cases pointing errors are the likely explanation for the asymmetric line profile.

5.5.4 Far infrared luminosity and star formation efficiency

The correlation between molecular gas and far infrared emission is well known and often discussed in the context of CO studies. $L_{\rm FIR}/L'_{\rm CO}$ or $L_{\rm FIR}/M(H_2)$ is commonly referred to as Star Formation Efficiency (SFE) indicator, assuming that $L'_{\rm CO}$ traces the cold, gravitationally bound molecular gas reservoirs that form the birth places of young, dust enshrouded stars. However, CO is only an indirect measure as it actually traces the overall molecular gas content in galaxies rather than explicitly the dense cores that produce young stars (e.g., Gao & Solomon 2004). Furthermore, the far IR emission of galaxies is a composite of an active star formation and a quiescent cirrus-like component (Helou 1986). In the case of AGN hosts, AGN driven dust heating may also contribute significantly to the FIR luminosity.

Many samples are based on IR selection criteria and, therefore, represent only the IR and CO bright tail of the luminosity distribution. So do several studies of the molecular gas content of Seyfert galaxies (e.g. Heckman et al. 1989; Papadopoulos & Seaquist 1998; Strong et al. 2004) or the study of PG QSO host galaxies by Evans et al. (2001, 2006). For the sample discussed in this paper an IR selection criterion was not used. Only ~50% of the nearby HE QSOs sample are listed in IRAS catalogs. The subsample discussed here contains the same fraction of IRAS sources (cf. Table 5.4) – an IR bias was carefully avoided. 65% of the detected sources are listed in IRAS catalogs, while only for 2 of 12 non-detections IRAS flux densities are available. Only HE 2302-0857 is located in a field that was not scanned by IRAS.

Many of the IRAS detected sources only show 60 μm and 100 μm flux densities and several of them are close to the IRAS detection limit. Due to the limited data at hand, the following discussion will focus on $L_{\rm FIR}$. It is based on the 60 μm and 100 μm IRAS flux densities and represents the luminosity between 43 μm and 123 μm. Due to this bandwidth limit, warmer components peaking at

Table 5.4: *Far infrared properties of the IRAS detected sources in the subsample. The 60 and 100 μm IRAS flux densities are taken from the IRAS Faint Source Catalog (Moshir et al. 1990), or in few cases from Rice et al. (1988), Sanders et al. (1989), or Sanders et al. (2003).*

Obj.	$F_{60\mu m}$ [Jy]	$F_{100\mu m}$ [Jy]	L_{FIR} [$10^{10} L_{\odot}$]
HE 0045-2145	3.6	5.3	4.2
HE 0108-4743	1.0	2.2	1.7
HE 0119-0118	1.5	1.8	10.8
HE 0150-0344	0.5	<1.7	<4.4
HE 0212-0059	0.5	1.5	1.2
HE 0224-2834	0.4	0.4	3.3
HE 0227-0913	0.4	0.9	0.3
HE 0232-0900	1.4	1.9	6.5
HE 0253-1641	0.7	0.8	1.6
HE 0345+0056	0.5	<3.2	<2.7
HE 0412-0803	0.6	<1.4	<2.8
HE 0433-1028	2.7	4.2	9.1
HE 0949-0122	1.3	<2.4	<1.5
HE 1011-0403	0.2	<0.3	<1.5
HE 1017-0305	0.5	0.6	2.8
HE 1029-1831	2.6	3.7	10.8
HE 1108-2813	3.1	4.2	4.5
HE 1126-0407	0.7	1.2	6.8
HE 1237-0504	3.1	6.0	0.6
HE 1248-1356	0.8	1.3	0.5
HE 2211-3903	0.8	1.1	3.2

shorter wavelengths, especially potential AGN heated dust components remain less considered in L_{FIR}. In the context of LIGs/ULIGs or nearby galaxies, L_{IR} is often used instead of L_{FIR}. L_{IR} also includes the 12 μm and 25 μm IRAS bands and represents the total IR luminosity ranging from 8 to 1000 μm. For the definition of L_{FIR} and L_{IR} cf. Sanders & Mirabel (1996).

Figure 5.8 shows the distribution of the IRAS detected sources in the $L'_{CO} - L_{FIR}$ diagram, together with the CO data of a volume limited sample of nearby spiral galaxies (Sage 1993), Seyfert I galaxies (Heckman et al. 1989; Maiolino et al. 1997; Strong et al. 2004), luminous (LIGs, Sanders et al. 1991) and ultraluminous infrared galaxies (ULIGs, Solomon et al. 1997), and PG QSOs (Scoville et al. 2003; Evans et al. 2006). Also shown are linear regression fits (in log-log space) to normal and to luminous IR galaxy samples as well as to the PG QSO hosts.

The distribution of type I AGN hosts in the plot indicates the presence of two populations with differing power-laws: one population that follows the power-

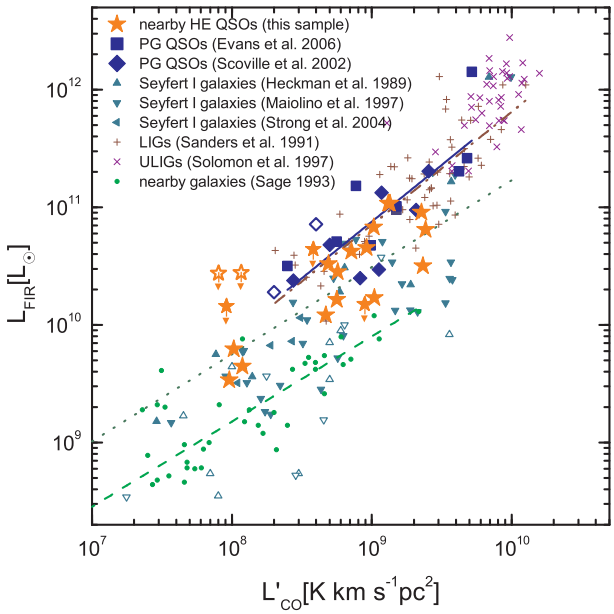

Figure 5.8: *FIR luminosity as a function of CO luminosity for the nearby QSO sample and various other Seyfert I, PG QSO host, luminous infrared galaxies and normal galaxies. The solid line represents a power law fit to the PG QSO hosts, the dashed line the distance limited sample of normal galaxies of Sage (1993), the dotted line a flux-limited sample of normal spiral galaxies (Solomon & Sage 1988), and the dashed-dotted line represents a power-law fit to the LIG sample of Sanders et al. (1991). Outlined symbols represent upper $L'_{\rm CO}$ limits.*

law of normal spiral galaxies and a second population that has $L_{\rm FIR}/L'_{\rm CO}$ properties very similar to LIGs.

The studies of Solomon & Sage (1988) and Sage (1993) are used to quantify the power law for normal galaxies: A fit to the distance limited sample of normal galaxies (excluding the upper limits considered in Sage (1993)) resulted in

$$L_{\rm FIR}/10^9 = 8 \cdot [L'_{\rm CO}/10^9]^{0.72(\pm 0.05)}, \tag{5.3}$$

while a fit to a FIR-selected sample of isolated spiral galaxies or spiral galaxies that do not show signs of interaction (Solomon & Sage 1988) yielded

$$L_{\rm FIR}/10^9 = 31 \cdot [L'_{\rm CO}/10^9]^{0.74(\pm 0.07)}. \tag{5.4}$$

Due to the FIR selection criterion, the latter sample is biased towards more active star formation with respect to average spiral galaxies. The bulk of local Seyfert I galaxies follows the trend described by these two fits, with a somewhat higher $L_{\rm FIR}/L'_{\rm CO}$ ratio for any given $L'_{\rm CO}$ than the Sage (1993) sample.

The power law fit to the PG QSO hosts, on the other hand, produces a slope of about unity:

$$L_{\rm FIR}/10^9 = 75 \cdot [L'_{\rm CO}/10^9]^{0.96(\pm 0.19)} \tag{5.5}$$

and is almost identical to the fit to the LIG data:

$$L_{\rm FIR}/10^9 = 71 \cdot [L'_{\rm CO}/10^9]^{0.96(\pm 0.09)}. \tag{5.6}$$

This common trend may be indicative for similar star formation activity in LIGs and luminous QSO hosts.

As for the low-luminosity QSO sample, Fig. 5.8 supports the picture of the sample being a link between the local Seyfert I population and luminous QSO host galaxies. The sample members seem to follow both trends, most of them can be found in a transition region between the two populations.

5.5.5 Opaque CO and FIR emission in (U)LIGs and QSO hosts?

In the following the various published results on the $L'_{\rm CO}$–$L_{\rm FIR}$ relation in normal and infrared luminous galaxies will be summarized together with the findings on the nature of the emission regions. Different pieces of information are combined to a simple qualitative model that explains geometrically the separation of type I AGN hosts into two populations in the $L_{\rm FIR}$ range between $10^9 L_\odot$ and $5 \cdot 10^{11} L_\odot$.

As discussed in Sect. 5.5.4, normal, undisturbed galaxies show a nonlinear $L'_{\rm CO}$–$L_{\rm FIR}$ relation with a slope < 1. For interacting galaxies (Solomon & Sage 1988) and LIGs (Sanders et al. 1991) the slope is approaching unity. In this case a linear relation between CO and FIR emission can be assumed. For ULIGs Solomon et al. (1997) also find a linear relation between FIR and CO emission, with a higher $L_{\rm FIR}/L_{\rm CO}$ ratio than in normal galaxies and LIGs. The increase of the $L_{\rm FIR}/L_{\rm CO}$ ratio towards ULIGs is well known (e.g., Sanders et al. 1986; Sanders & Mirabel 1996; Gao & Solomon 2004). It extends towards the even more luminous SMGs (Greve et al. 2005). Gao & Solomon (2004) point out, that a linear relation between CO and FIR luminosity remains valid only over two orders of magnitude in the lower $L_{\rm FIR}$ range (while a corresponding HCN – FIR relation extends over three orders of magnitude and includes the ULIG domain). Any fit to the CO luminosity over a wider range naturally yields a slope > 1. Gao & Solomon state a slope of 1.25 ± 0.08 for $L_{\rm FIR}$ between $10^{9.5} L_\odot$ and $10^{12.5} L_\odot$. Yao et al. (2003) even obtain a slope of 1.7 for $L_{\rm FIR}$ between $10^9 L_\odot$ and $10^{12} L_\odot$. [2]

[2] Their small projected beam size, however, may not cover the full CO content especially in the nearby, less infrared luminous galaxies. Thus, the slope may appear steeper than it actually is.

In interferometric CO data on nearby ULIGs Downes & Solomon (1998) show that most of the emission originates from rotating circumnuclear disks or rings. The disk gas forms a continuous medium rather than discrete virialized clouds. The linearity between FIR and CO emission in ULIGs and the dense environment resulting from the massive concentration of molecular gas suggest thermal excitation and optically thick emission. This is proposed by the same authors in an earlier paper (Solomon et al. 1997) but partially revised in Downes & Solomon (1998): According to their model fits the CO line emission is only moderately opaque and the CO(2–1)/CO(1–0) ratio indicates sub-thermal excitation.

If a connection between ULIGs and QSOs exists, as suggested in the evolutionary model, what does this imply for the molecular gas content in the evolved QSO phase of these objects? The model assumes a dispersion of the majority of gas and interstellar dust to clear the view onto the formerly dust enshrouded AGN. Indeed, low-z PG QSOs and nearby HE QSOs show CO and FIR luminosities and star formation efficiencies that are lower than it is the case for ULIGs in the same co-moving volume. Nevertheless, the majority of nearby low-luminosity QSOs is associated with large reservoirs of molecular gas (Sect. 5.5.1) and presumably also with ongoing star formation, as it is indicated by their $L'_{\rm CO}$–$L_{\rm FIR}$ distribution (Fig. 5.8). This might imply that the density of the formerly AGN obscuring medium in the central region is significantly reduced.

But how does the evolution affect the distribution of molecular gas? A confinement of the molecular gas to a compact region is still indicated also in high redshift QSOs (Riechers et al. 2006, in ground-state transition observations at z $\gtrsim$ 4). Spatially resolved data on QSOs in the local universe, however, is hardly available. For Mrk 231 Downes & Solomon (1998) report on an inner and an outer face-on disk within a radius of 1.15 kpc. Staguhn et al. (2004) present a ringlike structure with a radius of $\sim$ 1.2 kpc in the circumnuclear molecular gas distribution of I Zw 1. For the low-luminosity QSO HE 1029-1831 Krips et al. (2007) estimate a size of 6 ± 2 kpc for the CO source that is aligned with the optical bar. The data on low-z PG QSOs by Evans et al. (2001) and Scoville et al. (2003) do not permit to draw conclusions on the compactness of the emission.

The coincidence with the LIG population in the $\log L'_{\rm CO}$–$\log L_{\rm FIR}$ diagram with a power-law index 1 can be taken as indicator for a confinement of remaining H_2 content to a small and dense region. Based on this assumption, it is worth to revisit the idea of both bands being optically thick. If this is the case, the two different inclinations in the $\log L'_{\rm CO}$–$\log L_{\rm FIR}$ diagram may have a simple geometrical explanation: For normal galaxies, the CO distribution is less confined. The totality of individual gas clouds with varying line-of-sight velocities

contributes to the spectrum. In this case, it is appropriate to use the velocity-integrated CO line emission as tracer for the total molecular gas content of the galaxy. The FIR luminosity, on the other hand, is dominated by re-radiated dust emission, which originates from the densest regions in the ISM, the seeds of star formation. If the column densities in these compact regions result in $\tau > 1$ at the FIR bands, only the radiating surface contributes to the detectable FIR flux density. Let us assume a coarse, linear relation between the molecular gas content and the number of star formation seeds in a 3-dimensional gas distribution. Any surface of optically thick emission then scales with the power of $\frac{2}{3}$ of the overall volume. If L'_{CO} can be used as a measure for the total molecular gas content, L_{FIR} should scale with $L'^{0.67}_{\mathrm{CO}}$ and produce the corresponding inclination in the log–log plot. Once the density of the ISM reaches a threshold at which the CO emitting region (which may consist of a continuous medium) becomes opaque, both the CO and the FIR emitting surface scale linearly with the overall molecular gas and dust content. Under these circumstances the slope in the log–log plot is close to unity. An even higher density of star formation seeds in the ISM results in a larger surface filling factor within the galaxy, allowing for a higher $L_{\mathrm{FIR}}/L'_{\mathrm{CO}}$ ratio for each given CO luminosity. This effect causes the dispersion perpendicular to the power-law fit. As shown in Sect. 5.5.6 the different power-law fits for the individual source classes can be parameterized via the fractional source filling factor a of the material that participates in intense star formation or the source type f (QSO hosts and LIGs/ULIGs or normal galaxies).

The LIG/QSO scenario and the normal galaxy scenario describe the two extreme cases with power-laws 1 and 0.67 as upper and lower limit. These extreme cases seem to correspond well to the two populations described above. Furthermore, these scenarios do not exclude a transition region, in which the dense central region of a galaxy is optically thick for both bands while for the outer regions the full volume contributes to the detected CO emission.

5.5.6 Descriptive star formation model

Acknowledging the opaqueness of a dense, potentially continuous medium and the importance of the contribution of individual star formation regions to the overall emission leads to the consequence that the sources are characterized by the surface filling factor a of the star forming molecular gas in the host and a quantity β that describes the L_{FIR} and L'_{CO} contributions of the emitting regions (see below). Here L'_{CO} alone is not necessarily an adequate measure of the total molecular gas content in dense environments (as outlined in Sect. 5.5.4). Only if the standard assumptions are valid (virialized, i.e. gravitationally bound giant molecular clouds with different line-of-sight velocities), I_{CO} traces molecular

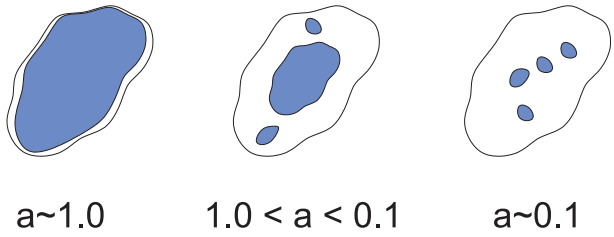

Figure 5.9: *Examples of molecular gas distributions with different fractions of molecular gas taking part in active star formation (dark areas). An inclined host is shown. The outer continuous line includes the majority of the molecular gas in the system.*

gas in both the LIG/ULIG/PG QSO case and the normal galaxy case.

The two extreme populations (LIG/ULIGs/PG QSOs and normal galaxies) in Fig. 5.8 can then be described as follows. For PG QSO hosts and LIGs CO and FIR luminosity are directly proportional:

$$\log(L'_{\rm CO}) \propto \log(L_{\rm FIR}). \tag{5.7}$$

For normal galaxies, additional quiescent molecular gas reservoirs contribute to the object's total CO luminosity but do not, or at least not as efficiently, produce dust emission in the FIR. The additional contribution grows non-linear with increasing total molecular mass. The portion of CO-luminosity per FIR-luminosity is higher by a factor $(1+\beta)$, with $\beta > 0$:

$$\log(L'_{\rm CO}) \propto [1+\beta]\log(L_{\rm FIR}) \sim 1.4\log(L_{\rm FIR}). \tag{5.8}$$

As a first step a smooth transition between the host properties of these different classes is assumed in the following, which can be parameterized by the value f with $0 \leq f \leq 1$. $f=1$ represents the case of QSO hosts and LIGs/ULIGs, while $f=0$ represents the case of normal galaxies. A direct proportionality between the CO and FIR luminosity in the $f=1$ case and in the star forming portions of normal galaxies is assumed. Furthermore it is assumed, that in the $f=1$ case the molecular gas of a dominant part of the host participates in the star formation process. In normal galaxies only a fraction a - for which $\log(L'_{\rm CO}) \propto \log(L_{\rm FIR})$ is valid - participates in that process. The quantity a can be identified as the surface filling factor of the star forming molecular gas in the host with $0<a<1$ (cf. Fig. 5.9). The remaining part gives rise to $\beta\log(L_{\rm FIR})$ as an additional portion of

CO-luminosity. Introducing a parameter C_0 allows to write:

$$\begin{aligned} \log(L'_{\rm CO}) &\cong f\log(L_{\rm FIR}) + \\ &\quad (1-f)[\log(aL_{\rm FIR}) + \beta\log((1-a)\,L_{\rm FIR})] + C_0 \\ &= [1+(1-f)\beta]\log(L_{\rm FIR}) + \\ &\quad (1-f)[\log(a) + \beta\log(1-a)] + C_0 \end{aligned} \tag{5.9}$$

In Fig. 5.10 the interdependency of a and f is shown, as they result in suitable power-law fits to the extreme and intermediate source classes in Fig. 5.8. Both quantities are linked via

$$log(a) \cong 3(f-1). \tag{5.10}$$

Within this model the two extreme source populations are represented by the following cases:
Case I: for $f = 1$, i.e. for QSO hosts and LIGs/ULIGs with $a \simeq 1$ follows:

$$\log(L'_{\rm CO}) \cong \log(L_{\rm FIR}) + C_0\ . \tag{5.11}$$

With a value of C_0∼-2, as suggested by Fig. 5.8, this corresponds to the heuristically derived expressions for LIGs/ULIGs and PG QSOs (Sanders et al. 1991; Solomon et al. 1997; Scoville et al. 2003; Evans et al. 2006).
Case II: For normal galaxies with $f = 0$, i.e. $0 < a \ll 1$, and $\beta \sim 0.4$ the model yields:

$$\log(L'_{\rm CO}) \cong 1.4\log(L_{\rm FIR}) - 5.0\ . \tag{5.12}$$

This corresponds to the heuristically derived expressions for samples of distance limited or non-interacting, isolated FIR-selected galaxies (Solomon & Sage 1988; Sage 1993, cf. Sect. 5.5.4).

It can be seen that the formalism described above naturally results in the heuristic relations for the extreme source populations as presented in Sect. 5.5.4 and shown in Fig. 5.8. It also allows to describe the mean properties of nearby QSO hosts discussed in this study as an intermediate population. The intermediate case of the nearby QSO hosts, for which $0.5 \lessapprox f \lessapprox 0.8$ or $\log a \sim -1$, can then be approximated by

$$\log(L'_{\rm CO}) \cong (1.1 \pm 0.05)\log(L_{\rm FIR}) - (2.5 \pm 0.3) \tag{5.13}$$

or

$$L_{\rm FIR}/10^9 \cong (50 \pm 20)\cdot[L'_{\rm CO}/10^9]^{0.91(\pm 0.04)}\ . \tag{5.14}$$

In total the model corresponds to a picture in which all hosts are similar in the amount of molecular gas (i.e. about 10% of $\sim 10^{12}$ $M_\odot$ of the total host mass)

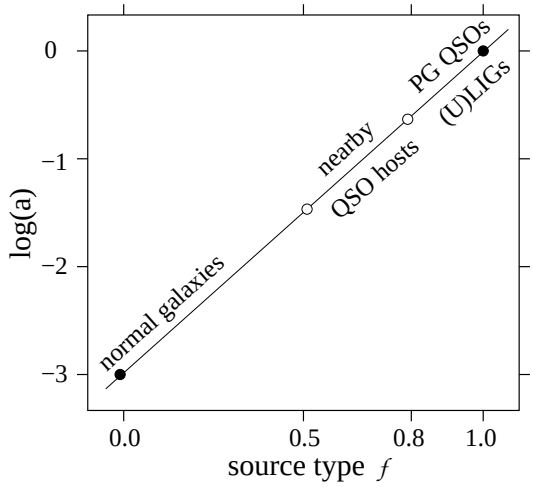

Figure 5.10: *Logarithm of the surface filling factor a of star-forming gas as a function of source type f as described in the text. The black filled circles mark the fits to the LIG/ULIG and the normal galaxies, respectively. The white filled circle indicate the region in which the nearby low-luminosity QSO hosts (discussed in this Chapter) are located.*

but different in the fraction of strong star forming regions. It also shows that the surface filling factor a and the value β that is linked to the FIR/CO emission properties of the source components are suitable parameters to describe a broad range of host galaxies.

5.6 Summary

This study deals with ^{12}CO observations of 41 nearby low-luminosity QSOs. Thirty-nine of them form a subsample that is not biased towards FIR emission. The results of this study can be summarized as follows:

1. 70% of the subsample have been detected in the ^{12}CO(1−0) transition. With a mean H_2 mass of $2.8 \cdot 10^9 M_\odot$ (assuming $\alpha = 4\ M_\odot$ (K km s^{-1} pc^2)$^{-1}$) the majority of low-luminosity QSO hosts is rich in molecular gas. This confirms previous results on PG QSOs by Scoville et al. (2003).

2. For the majority of detected objects, the redshift based on visible features is blueshifted with respect to the CO line centroid – probably as a result of

asymmetric phenomena in the vicinity of the nucleus, the emission region of the visible features.

3. The absolute B_J magnitude of the central seeing disk of the low-luminosity QSOs is used as an indicator for the total activity of AGN and circumnuclear starburst. Objects with $M(B_J) < -20$ mag not only show higher CO luminosities but also a wider distribution of linewidths than the fainter objects.

4. The connection between CO and FIR properties is discussed in the context of normal galaxies, local Seyfert I objects, LIGs, ULIGs and PG QSOs. Two populations with different power-laws in the $L'_{\rm CO}$–$L_{\rm FIR}$ plot are identified in the range between $L_{\rm FIR} = 10^9 M_\odot$ and $L_{\rm FIR} = 5 \cdot 10^{11} M_\odot$. The first population shows a power-law index of ~ 0.7 and contains normal, non- or weakly interacting galaxies and the bulk of Seyfert I objects. The second population with a power-law index of ~ 1 contains LIGs and the PG QSOs. The low-luminosity QSO sample seems to consist of objects of both populations and objects from a transition region.

5. For objects of the second population, i.e. also for galaxies hosting brighter QSOs, the linear relation between FIR and CO luminosity can be taken as indication for a concentration of the molecular gas in compact regions, similar to the case of ULIGs.

6. The idea of thermalized, optically thick FIR and CO emission, previously suggested in the context of ULIGs, is revisited. The two different slopes in the $L'_{\rm CO}$–$L_{\rm FIR}$ plot are discussed as a potential result of different optical properties of the ISM in the two populations.

CHAPTER 6

Abell 262 – Molecular gas stripping in cluster galaxies?

6.1 Introduction

A large number of mechanisms in rich galaxy clusters have been discussed (Butcher & Oemler 1978; Couch et al. 1998), and found to favor the transition from spiral-dominated, blue galaxy populations at higher redshifts towards the domination of early, red populations as observed at z $\sim$ 0. The most detailed view of galaxy cluster members has been obtained for the Coma and Virgo galaxies. Studies of these and other targets suggest interaction with either other cluster members or the cluster potential or the hot intra-cluster medium (ICM) seen as the main cause of both the truncation of the star-formation rate and the morphological transition. Strong evidence of interaction between the interstellar medium (ISM) and the ICM is shown by the lack of atomic gas (Giovanelli & Haynes 1985) in those spiral galaxies that are in the vicinity of the centers of rich clusters with respect to similar, but isolated objects. This HI deficiency is commonly explained by ram pressure stripping or sweeping, as the galaxy moves through the dense and hot gas in the core of the cluster. Studies of the global CO distribution of cluster galaxies (Kenney & Young 1989; Casoli et al. 1991, 1998; Boselli et al. 1997; Lavezzi & Dickey 1998), on the other hand, show either no or insignificant dependence of the molecular gas content on its location or on the degree of HI deficiency. Molecular clouds do not seem, or at least seem less, affected by the gas stripping mechanisms. The higher column densities and the concentration in the center of the disks and, therefore, the stronger binding within the galaxies' potential may allow molecular gas to better resist environmental influences.

Despite this negative global result, CO observations with high spatial resolution can provide important clues to the mechanisms that may influence the evolution of galaxies within a cluster. Vollmer et al. (2001), for example, discuss the indirect consequences of HI stripping by studying the lopsided molecular gas distribution in the case of the Coma galaxy NGC 4848. Although ram pressure stripping, in the long term, leads to an overall decrease in the gas mass, and

hence to a reduced star-formation rate (SFR), it can cause a temporary increase in the gas density and, along with this, an increased SFR. Molecular gas can be regarded as required for the star-formation process. Since CO is the most important tracer for molecular gas, CO observations provide information on whether the environment within cluster members favors enhanced star formation activity or not.

In this chapter of the thesis the results of CO observations of a sample of Abell 262 cluster galaxies are presented and indications for environmental effects on the total molecular gas content of the sample members are discussed. The tentative findings indicating a dependency of the global molecular gas mass on the distance to the cluster core are substantiated with $L_{\rm FIR}$ data. For a more profound analysis of the total molecular gas content of Abell 262 galaxies, it is essential to determine the extent and distribution of the CO emission regions with high spatial resolution interferometric observations. The results of such interferometric CO observations of the Abell 262 cluster member UGC 1347 are presented as an example of a more detailed analysis of the galaxy's CO distribution.

6.1.1 Abell 262

The spiral rich cluster Abell 262 has been subject to a variety of studies in different wavelength domains. Abell (1958) first analyzed Palomar observatory sky survey (POSS) photographic plates, and defined cluster richness classes by the number of galaxies in the cluster that are not more than 2 magnitudes fainter than the third brightest member. With 40 galaxies (Abell, Corwin, & Olowin 1989, corrected for background contamination) meeting this richness criterion, Abell 262 falls into richness class 0, and is far less densely populated then e.g. the Coma cluster with 106 members and richness class 2. However, the cluster consists of many more members. Struble & Rood (1999) consider a total number of 151 galaxies that are associated with Abell 262. As it is embedded in the main ridge of the Pisces-Perseus supercluster (Haynes & Giovanelli 1986), Abell 262 has a conspicuous appearance. Its center [R.A. (J2000) = $01^{\rm h}\ 52^{\rm m}\ 50^{\rm s}$, Dec. (J2000) = $36^\circ\ 08.8'$] coincides with the position of the cD galaxy NGC 708. [1]

The value for the cluster redshift of z=0.0163 (Struble & Rood 1999) results in a heliocentric velocity of v=c·z= 4887 km s^{-1} and a distance to the cluster of 49 h^{-1} Mpc. An angular separation of $1''$ then corresponds to 238 h^{-1} pc. The Abell radius (corresponding to $\sim$1.5 h^{-1} Mpc) follows $r_{\rm A}$=1.7′· z^{-1} $\simeq$ 1.75°. In these and the following calculations, whenever required, H_0 =

[1] Based on ROSAT PSPC observations, David, Jones, & Forman (1996) argue that the position of the central galaxy deviates slightly from center of the cluster potential.

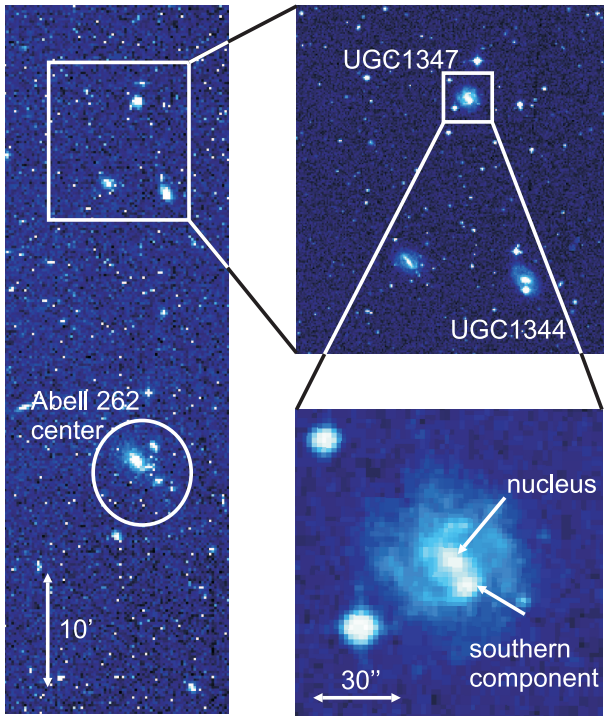

Figure 6.1: *The location of UGC 1347 within the Abell 262 cluster – visual images from the Palomar Observatory Sky Survey (POSS). The bottom right image shows the nucleus and the bright southern source at the tip of the bar.*

100 h km s^{-1} Mpc^{-1} and $q_0 = 0.5$ were used, unless otherwise stated. Fadda et al. (1996) state a line-of-sight velocity dispersion for Abell 262 members of $\sigma = 525^{+47}_{-33}$ km s^{-1}, which is similar to the result of Neill et al. (2001) ($\sigma = 548 \pm 36$ km s^{-1} for a sample of 101 Abell 262 member galaxies) and is only slightly higher than the average low-velocity dispersion ($\sigma = 485 \pm 45$ km s^{-1}) of clusters in the richness class 0 (Fadda et al. 1996).

Several groups have investigated the properties of the hot ICM of Abell 262 (e.g. Neill et al. 2001; David et al. 1996; MacKenzie et al. 1996). Jones & Forman (1984) identified Abell 262 as a dynamically young XD cluster, similar to Virgo, that shows the typical signs of a less evolved system with a stationary, dominant galaxy at its center: low X-ray luminosity ($3.07 \cdot 10^{43}$ ergs s^{-1}), low ICM temperature (2.8×10^7 K), high central gas density/cooling flow, high spiral fraction, low central galaxy density, irregular shape.

Since Abell 262 apparently is not yet in a relaxed state, the transformation mechanisms that are discussed in the context of higher redshift galaxy and cluster

evolution may still be active. And due to the cluster's low redshift, they can be studied with high spatial resolution. Several studies of the signatures of galaxy interaction have included the case of Abell 262. Similar to clusters such as Virgo, Coma, and several others, Abell 262 galaxies are deficient in atomic gas towards the center (Giovanelli, Haynes, & Chincarini 1982; Solanes et al. 2001). Bravo-Alfaro et al. (1997) used the Westerborg Synthesis Radio Telescope to map the spatial HI distribution of 11 Abell 262 members. They show that, in a few cases, the gas distribution is asymmetrical – again a sign of ISM-ICM interaction. A few Abell 262 galaxies were included in CO(1−0) observations by Lavezzi & Dickey (1998), and Hα emission of several members was investigated by Amram et al. (1994) and Moss & Whittle (2000). They discuss the Hα emission of Abell 262 member galaxies together with other cluster galaxies in the context of tidally induced star formation, whereas Amram et al. (1994) provide maps and rotation curves of six Abell 262 galaxies – among them UGC 1347.

6.1.2 UGC 1347

The SBc galaxy UGC 1347 [R.A. (J2000) = $01^{\rm h}\ 52^{\rm m}\ 45.9^{\rm s}$, Dec. (J2000) = $36°37'09''$], is located about $28'$ north of the cluster center (cf. Fig. 6.1). Based on HI observations, Haynes et al. (1997) found the galaxy's redshift to be z = 0.01849, corresponding to a systemic velocity of 5543 km s^{-1}. The difference between the cluster velocity of 4887 km s^{-1} and the systemic velocity of UGC 1347 of about 650 km s^{-1} ($\simeq$ 1.2 times the cluster's velocity dispersion) can be explained as a motion of the galaxy within the cluster.

UGC 1347 is the first extragalactic target that was observed with a laser-guide-star assisted adaptive optics system. Hackenberg et al. (2000) used the MPIA-MPE ALFA AO system at the Calar Alto 3.5 m telescope to obtain NIR images at subarcsecond resolution. They discuss their results in the context of published radio, FIR, and Hα data. Since millimetric CO observations had not been carried out for this object by that time, quantities related to the molecular gas content and distribution had to be estimated.

Besides a bright nuclear source, UGC 1347 features a second prominent component about $9''$ south of the center at the tip of the bar (cf. Fig. 6.1). Hackenberg et al. (2000) found this region to be compact in the NIR and identified it with a region of recent active star formation in the disk.

6.2 Observations and data reduction

For several members of the Abell 262 cluster, millimeter CO-emission line data were obtained for different transitions and, in the case of UGC 1347, also for different isotopomeres. The observations were carried out with the BIMA interferometer as well as the IRAM 30 m, Nobeyama 45 m, and Onsala 20 m single dish telescopes.

6.2.1 BIMA data

^{12}CO(1−0) observations of UGC 1347 were carried out at the Berkeley-Illinois-Maryland Association (BIMA) observatory at Hat Creek, CA, USA in July 2000. The local millimeter-wave radio interferometer, consisting of 10 antennae with a diameter of 6.1m each, was used in C configuration. Every 24 minutes the series of observations with this setup was interrupted by measurement of the phase calibrator 0136+478 located 11.5° north of UGC 1347. The good uv coverage obtained in the overall on-source integration time of 257 minutes resulted in an approximate beam size of 6.6″ FWHM. Because of the good data quality, it was possible to apply all standard reduction steps in an almost straightforward manner. The image reconstruction was performed with the software package MIRIAD provided by the BIMA consortium. The phase- and amplitude calibrated visibility samples were inverted into a spectral line cube by applying a natural weighting scheme. A hybrid Högbom/Clark/Steer CLEAN algorithm was applied to the image data obtained. A comparison with single dish data is shown in Fig. 6.2. Only about 70% of the total flux is expected to be recoverable from observations of sources with small angular extensions, such as UGC 1347 in BIMA's C configuration (Helfer et al. 2002).

The following remarks on smaller problems in the dataset may be helpful for archive users. An inspection of the uv dataset revealed that the first channel of each of the 16 spectral windows was malfunctioning. Both channels neighboring a malfunctioning channel showed reduced dynamics with respect to the other channels. While the spectral information of the malfunctioning channels was completely corrupted and therefore lost, the data of the neighboring channels with damped performance was recoverable by applying a correction factor. One of the malfunctioning channels unfortunately represents the 8.3 km/s wide spectral region starting at -4 km/s – right in the center of the emission line region of UGC 1347. In order to obtain a reasonably integrated intensity distribution of the galaxy and the integrated flux of the central source, the missing channel map was interpolated.

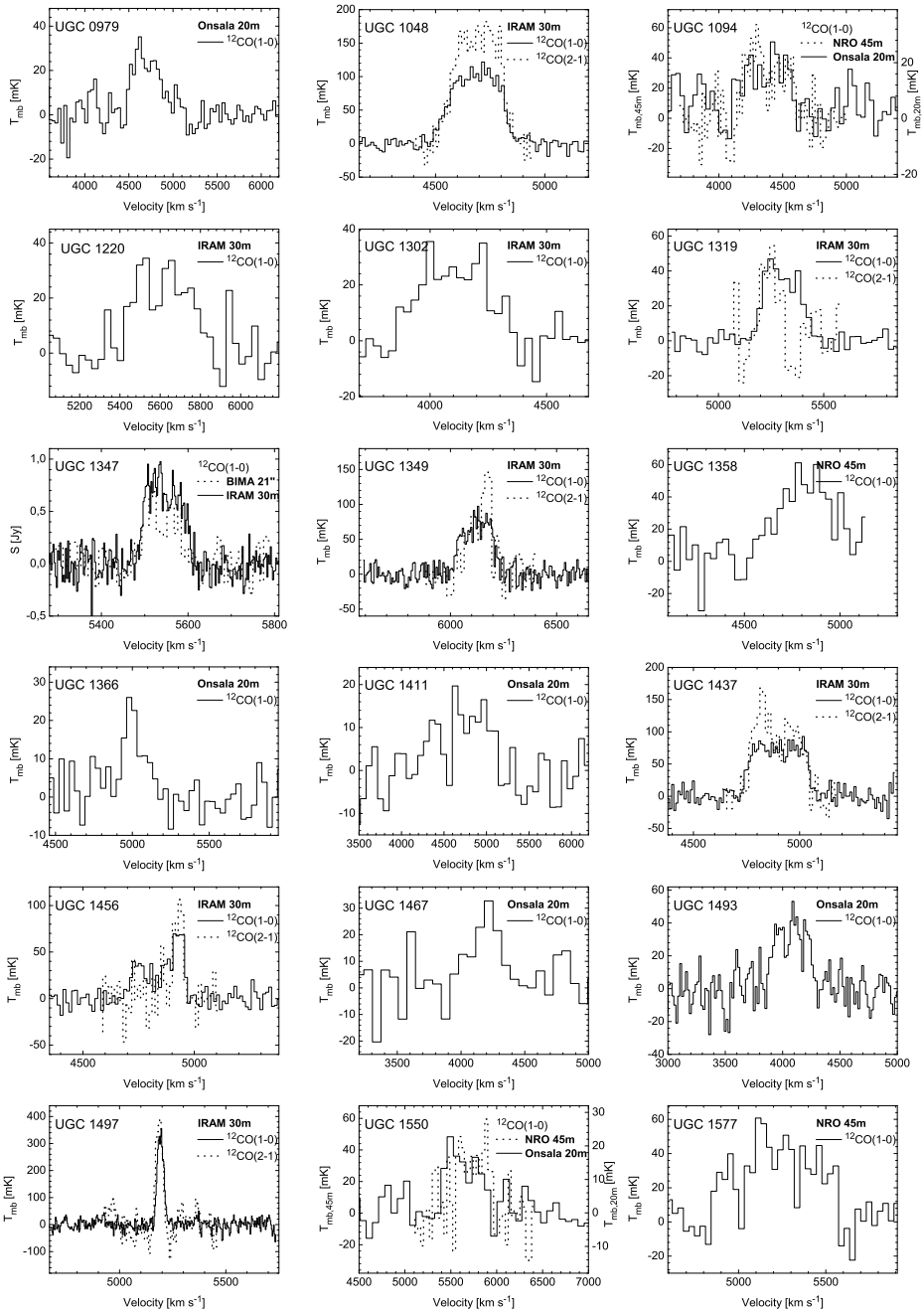

Figure 6.2: *^{12}CO(1–0) spectra of Abell 262 galaxies measured with the IRAM 30 m, the Onsala 20 m, or the Nobeyama 45 m telescope. With the 30 m telescope it was possible to obtain ^{12}CO(2–1) in parallel. The cases in which the ^{12}CO(2–1) emission line region extended over the bandwidth of the receiver have been excluded.*

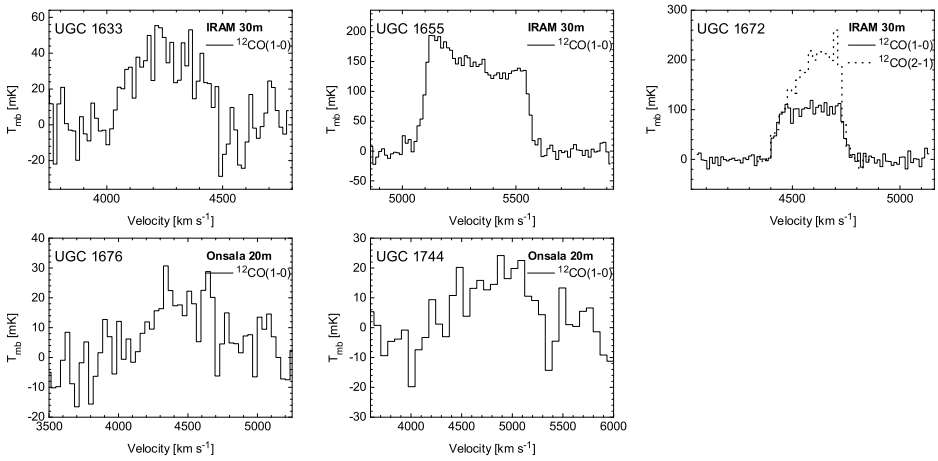

Figure 6.2: *—continued*

6.2.2 IRAM 30 m telescope data

Initial measurements with the IRAM 30 m telescope on Pico Veleta (Spain) of the ^{12}CO(1−0) and ^{12}CO(2−1) emission of UGC 1347 were performed in June 2000, prior to the BIMA observations. In July 2003 the IRAM 30 m telescope was used to acquire ^{12}CO(2−1) and ^{13}CO(1−0) emission line data of UGC 1347 in parallel. Further 11 Abell 262 cluster galaxies were observed for ^{12}CO(1−0) and ^{12}CO(2−1) emission during the same campaign. UGC 1347 was mapped on a regular grid of 8×7 positions with a spacing of $5''$ in between adjacent pointings, thus achieving Nyquist sampling for the ^{12}CO(2−1) beam. The Vespa backend was tuned to a spectral resolution of 1.25 MHz for each of the then 337 channels.

The spectra (see Fig. 6.2) were processed using the CLASS/GILDAS Software packages provided by IRAM. Except for a few cases in which the line emission extended over the spectral range of the receiver, linear baselines were subtracted from the spectra and peak temperatures, as well as line intensities, were determined. In order to obtain main beam temperatures, the main beam efficiencies B_{eff} and the forward efficiencies F_{eff} given in Table 6.1 were applied to T_A^*. The resulting values for I_{CO} and peak T_{MB}, as well as the velocity ranges over which the lines were integrated, are shown in Table 6.2. The errors of T_{MB} in Table 6.2 represent the RMS per channel after smoothing the spectra.

To compare the two ^{12}CO(1−0) spectra obtained with BIMA and the IRAM 30 m telescope shown in Fig. 6.2, the IRAM 30 m telescope T_{MB} spectrum was converted using the factor $S/T_{MB} = 4.95$ Jy K^{-1}. The inverse conversion of

Table 6.1: *Telescope parameters related to the CO observations of Abell 262 galaxies with the IRAM 30 m telescope, the Nobeyama 45 m telescope and the Onsala 20 m telescope. The main beam efficiencies (and forward efficiencies) stated below were used to convert antenna temperatures in main beam temperatures.*

obs. date	Telescope	line	rest frequency [GHz]	θ_{Beam} FWHM [″]	B_{eff}	F_{eff}
Jun. 00	30 m	^{12}CO(1–0)	115	21.5	0.80	0.93
Jul. 03	30 m	^{12}CO(2–1)	230	10.5	0.52	0.91
Jul. 03	30 m	^{12}CO(1–0)	115	21.5	0.74	0.95
Jul. 03	30 m	^{13}CO(1–0)	110	22.0	0.75	0.95
Mar. 05	45 m	^{12}CO(1–0)	115	14.7	0.38	
Mar. 05	20 m	^{12}CO(1–0)	115	33	0.43	

integrated flux densities measured by BIMA into I_{CO}, as given in Table 6.4, was done analogously with a factor $S/T_{\mathrm{MB}} = 0.46$ Jy K^{-1}.

6.2.3 Nobeyama 45 m telescope data

Altogether 14 Abell 262 galaxies were observed with the Nobeyama Radio Observatory's (NRO) 45 m telescope in Japan in March 2005. The observations partially suffered from bad weather. The observing conditions prevented observations at 115 GHz in ~50% of the assigned observing time. In several cases the pointing was problematic due to strong wind. In these cases the data is unreliable. In 8 cases the obtained datasets are reliable. Of these, 5 objects have been detected with the 45 m telescope.

The single-beam receiver S100 was used for CO data, S40 was used for SiO line observation of pointing sources. The acusto-optic spectrometers (AOS) provide a bandwidth corresponding to only about 600 km s^{-1}, which is too narrow for many extragalactic linewidths. Therefore, the autocorrelator (AC) A25, which covers 1200 km s^{-1}, was chosen as one backend. Simultaneously the two standard AOS (W5 and W6) where used.

Archive users should be aware of two technical details: the velocity axis of the AOS data is shifted by approximately 65 km s^{-1} with respect to the AC data. The AC data represent the correct values. Secondly, the AC is not optimized to be used together with the S100 receiver. The measured flux density is higher than the flux density of the AOS by a factor 1.26. This factor is considered in the data reduction.

The data reduction was done on-site with the NRO Software "Newstar". For the AC data, the edges are zero by definition. In several cases, this behavior resulted in scans with S-shaped baselines. Whenever this feature was domi-

nant, the useful range of the AC data had to be confined to the central region. The S-shaped baselines were not flagged (unless they showed other reason to be flagged) and only the central region was used for baseline subtraction. If shown beyond the confined region, such a spectrum may feature edges which deviate from the baseline.

6.2.4 Onsala 20 m telescope data

In further 9 sources ^{12}CO(1–0) emission was detected with the Onsala 20 m telescope in Sweden. These observations were also carried out in March 2005, at the same time as the observations with the 45 m telescope in Nobeyama. Similar weather conditions again resulted in a low atmospheric transmission at 115 GHz for a significant share of the assigned observing time. For the majority of objects observed, the prevailing high noise conditions were not sufficient to detect CO line emission. Due to the radome enclosure and the larger beam size, the pointing of the telescope was not problematic.

In most of the measurements a narrow interference line is visible in the spectra. The origin of the interference could not be determined. In few cases this artificial line coincided with the line emission of the target. A separation of the source flux density and the disturbance was not possible then. In all other cases the channels affected by the interference line were excluded from the line flux calibration. CLASS/GILDAS was used for the data reduction. Linear fits to the baselines were subtracted.

6.3 Results

6.3.1 Global CO and L_{FIR} properties of Abell 262 galaxies

The primary goal of the single dish observations was to determine the global CO content of a set of gas rich galaxies in the Abell 262 cluster and to investigate a possible dependency on the distance to the cluster center. The CO bright galaxies are candidates for interferometric high resolution follow-up observations that allow detailed studies of the spatial distribution of molecular gas. In the case of UGC 1347, such observations have been carried out using BIMA. They represent an example of how detailed investigations should be carried out on a much larger sample. For this reason a description of the results is presented in Sect. 6.3.2.

A possible impact of the galaxies' environment on the gas distribution and star-formation properties may be investigated most easily for the brightest candidates. In order to maximize the chances of detection, the CO-IR correlation (Stark et al. 1986; Sanders, Scoville, & Soifer 1991) was used in the selection.

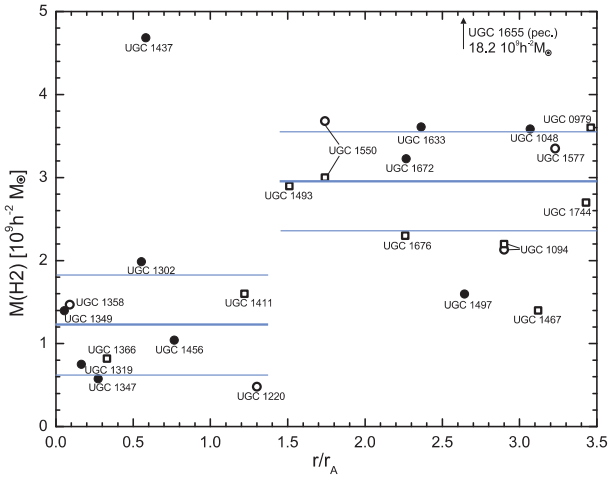

Figure 6.3: *Molecular mass vs. the distance to the cluster center. The horizontal lines represent the median value for each of the two subsamples and the common median absolute deviation. To be able to compare the mass estimates of a homogeneous sample, the peculiar galaxy UGC 1655 and the FIR weak galaxy UGC 1344 were not considered (see text).*

All selected galaxies show IRAS 100 μm fluxes of more than 2.5 Jy, with the exception of UGC 1344, which was included because it was discussed by Hackenberg et al. (2000). In addition to the FIR criterion, only galaxies of known HI content were chosen, as determined by Giovanelli & Haynes (1985).

The sample was composed to contain both a subset of 10 galaxies located close to the cluster center and a subset of 13 galaxies with a distance to the center that exceeds 1.5 Abell radii. The results of the measurements are shown in Fig. 6.2 and listed in Table 6.2 and a discussion follows in Sect. 6.4.

Molecular gas content

The CO emission region can extend somewhat beyond the region covered by the beams especially of the 30 m and 45 m telescopes. This can be seen in the case of UGC 1347 in Sect. 6.3.2, and it is also indicated by the off-center measurements in other cases. To estimate the overall intrinsic CO content and to derive molecular gas masses, certain assumptions on source sizes and distributions were necessary – namely both beam and sources were assumed to be Gaussian. The need for source-size estimates introduces a serious uncertainty in the gas mass estimates. Better statistics and high resolution information indicating the actual sizes of the CO emission regions, as obtained with BIMA for the case of UGC 1347, are mandatory to verify the results of this study.

Table 6.2: *Measured ^{12}CO properties of the centers of selected Abell 262 member galaxies and the molecular gas mass estimates of the sample. The corresponding parameters of the observation are shown in Table 6.1. For the mass estimates the sources are assumed do be Gaussian with a FWHM θ_S = 0.2·D_{25}, with the exception of UGC 1347, for which a more accurate FWHM could be determined from the interferometric measurements. The CO deficiency indicator CODEF follows the definition given in Casoli et al. (1998).*

Obj.	Telescope	v_0 [km s^{-1}]	Δv [km s^{-1}]	$I_{CO(1-0)}$ [K km s^{-1}]	$I_{CO(2-1)}$ [K km s^{-1}]	θ_S [″]	M(H_2) [$10^9 h^{-2}$ M$_\odot$]	L_{FIR}/M(H_2) [L$_\odot$/M$_\odot$]	CODEF
UGC 0979	20 m	4775	645	10.6 ± 0.9		30.1	3.6	2.6	
UGC 1048	30 m	4650	400	28.2 ± 0.4	40.7 ± 0.9	19.0	3.59	4.4	−0.08
UGC 1094	45 m	4385	465	14.7 ± 1.5		26.9	2.1	2.6	0.08
	20 m	4355	540	7.7 ± 1.0			2.2	2.6	0.07
UGC 1220	45 m	5660	510	9.9 ± 1.6		10.0	0.5	18.6	
UGC 1302	30 m	4125	550	9.7 ± 0.8		29.5	1.99	2.9	0.15
UGC 1319	30 m	5325	350	8.4 ± 0.4	5.0 ± 1.2	10.7	0.75	6.5	
UGC 1344	30 m	4170	N.D.			19.5	< 0.65		
UGC 1347	30 m	5650	200	4.6 ± 0.3	11.2 ± 1.3	18.9	0.57	12.6	0.39
UGC 1349	30 m	6125	250	12.9 ± 0.4	13.8 ± 1.3	15.5	1.39	4.7	−0.02
UGC 1358	45 m	4800	475	17.0 ± 1.5		18.6	1.5	0.3	−0.56
UGC 1366	20 m	5030	235	3.5 ± 0.5		20.9	0.8		
UGC 1411	20 m	4870	475	6.8 ± 1.3		21.8	1.6	1.5	−0.1
UGC 1437	30 m	4890	340	22.1 ± 0.6	28.4 ± 1.0	30.1	4.68	4.1	−0.06
UGC 1456	30 m	4825	350	9.8 ± 0.5	5.7 ± 0.6	15.1	1.04	3.7	0.01
UGC 1467	20 m	4186	340	7.4 ± 1.4		10.0	1.4	6.7	
UGC 1493	20 m	4080	390	12.2 ± 0.9		21.8	2.9	2.2	−0.18
UGC 1497	30 m	5200	100	12.6 ± 0.4	12.8 ± 1.0	19.0	1.60	6.6	0.12
UGC 1550	45 m	5775	415	14.4 ± 2.0		37.9	3.7	2.3	−0.16
	20 m	5665	475	7.6 ± 0.9			3.0	2.8	−0.07
UGC 1577	45 m	5225	730	24.0 ± 1.5		26.3	3.4	1.4	
UGC 1633	30 m	4250	500	13.6 ± 0.8		35.4	3.61	2.9	0.06
UGC 1655	30 m	5325	550	71.1 ± 0.7		34.6	18.2	2.7	
	45 m	5130	414	54.8 ± 2.2		34.6	11.8	4.1	
UGC 1672	30 m	4600	400	32.9 ± 0.5	56.4 ± 1.3	13.2	3.23	8.6	
UGC 1676	20 m	4425	505	9.5 ± 1.1		21.3	2.3	2.0	−0.17
UGC 1744	20 m	4820	675	11.7 ± 1.9		20.4	2.7	1.2	−0.33

Young et al. (1995) found the CO emission region of galaxies to be confined to the center of the disk and correlated with the 25.0 $B_{mag}/arcsec^2$ isophotal diameter D_{25}. The mean ratio of the CO scale length of a simple exponential model to D_{25} was determined to be 0.10. Similar to the approach of Young et al. (1995), the FWHM of the sources were taken as $0.2 \cdot D_{25}$, except for the case of UGC 1347, in which the interferometric measurements allowed a more accurate determination of the source size. The size estimates were then used to determine beam filling factors $F_{gauss} = 1 + (\theta_{Beam}/\theta_{Source})^2$ that were applied to correct the measured values of I_{CO}.

Lavezzi & Dickey (1998) observed UGC 1302, UGC 1319, and UGC 1456 in $^{12}CO(1-0)$ line emission using the 12m NRAO telescope with a beam size of 55″and obtained values for I_{CO} of 1.4 ± 0.21 K km s^{-1} (9.68 ± 0.76 K km s^{-1} in this study), 2.48 ± 0.21 K km s^{-1} (8.43 ± 0.35 K km s^{-1}), and 2.56 ± 0.29 K km s^{-1} (9.77 ± 0.48 K km s^{-1}) respectively. The differences of the values presented in this study result from different beam sizes. Considering the different sizes by correcting with F_{gauss} yields intrinsic I_{CO} values of 6 K km s^{-1} (15 K km s^{-1} in this study) for UGC 1302, 68 K km s^{-1} (42 K km s^{-1}) for UGC 1319, and 37 K km s^{-1} (31 K km s^{-1}) for UGC 1456. The remaining differences are explicable with uncertainties in the source-size estimates. Especially UGC 1302 is likely to be resolved in the IRAS 30 m telescope beam.

Determination of the H_2 content using I_{CO} (especially optically thick line emission) as the tracer has to be handled with care. The common approach of using a 'standard' $N(H_2)/I_{CO}$ conversion factor X derived from galactic observations has the shortcoming of disregarding the dependency of X on the metallicity of the region of interest (Israel 1997). Nevertheless, since only global mass estimates can be derived and since they are caused by the lack of information on metallicity, a 'standard' conversion factor $2.3 \cdot 10^{20} cm^{-2}$ (K km s^{-1})$^{-1}$ (Strong et al. 1988) was adopted. This also allows the results to be compared to published data. The resulting molecular mass estimates are listed in Table 6.2, where a linewidth of 500 km s^{-1} was assumed for the upper mass limit of UGC 1344, and plotted against their projected distance to the cluster center in Fig. 6.3. In this plot the horizontal lines represent the median molecular gas estimates and the common median absolute deviation for the two subsamples. To compare a more homogenous set of galaxies, the peculiar galaxy UGC 1655 with its outstanding flux density was not considered in the calculation of the median. Nor was UGC 1344, which does not meet the 100 μm selection criterion. If both galaxies were included, the median values of the two subsamples would be even further separated.

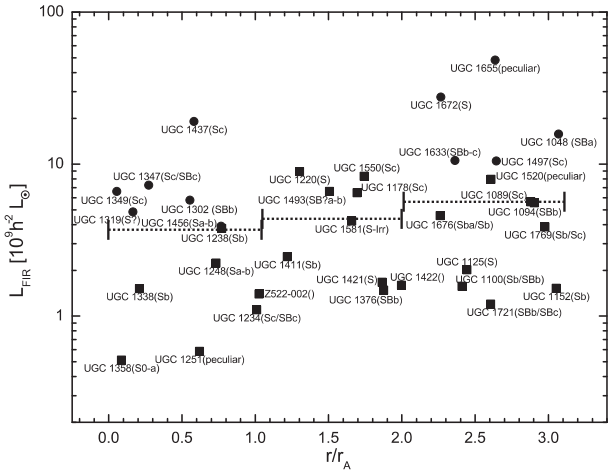

Figure 6.4: *FIR luminosity as function of the distance to the cluster center. The plot contains all Abell 262 galaxies down to the IRAS flux limit, with distances to the cluster core not exceeding 3 Abell radii. The filled circles represent the objects for which CO data were obtained. Median values of 3 regions are shown by the horizontal lines.*

L_{FIR} properties

To be able to discuss a possible selection bias due to the FIR selection criterion, FIR luminosities were calculated for all Abell 262 galaxies in the Giovanelli & Haynes sample within 3 Abell radii down to the IRAS flux limit (Table 6.3). Following Helou et al. (1988) the FIR luminosity can be written as:

$$L_{\mathrm{FIR}} = 3.94 \cdot 10^5 D[\mathrm{Mpc}]^2 (2.58 \cdot \mathrm{S}_{60\mu\mathrm{m}}[\mathrm{Jy}] + \mathrm{S}_{100\mu\mathrm{m}}[\mathrm{Jy}]). \qquad (6.1)$$

In Fig. 6.4 this luminosity is plotted against the projected distance to the cluster center.

6.3.2 Interferometric observations of UGC 1347

The overlay of the POSS-II Red[2] image and the BIMA CO map in Fig. 6.5 clearly shows that CO emission extends over almost the entire inner disk of UGC 1347. Continuum emission was not detected. A comparison of the two CO(1−0) spectra can be found in Fig. 6.6. With the high resolution ^{12}CO(1−0) observations obtained with BIMA, it was possible to identify reservoirs of molecular gas at the positions of the nucleus and in the southern component. Figure 6.5 shows maps of the two components. Only channel maps with a contribution of

[2]Second Palomar Observatory Sky Survey (POSS-II)

Table 6.3: *Properties of the IRAS FIR flux limited sample of Abell 262 galaxies with a distance to the cluster core of less than 3 Abell radii, as observed in HI by Giovanelli & Haynes . The morphological classification, as well as the inclination estimate (with respect to the line of sight), were taken from Nilson (1973), D_{25} from de Vaucouleurs et al. (1991), $S_{60\mu m}$ and $S_{100\mu m}$ IRAS flux densities from Moshir et al. (1990), and HI deficiency from Giovanelli & Haynes (1985). An inclination value of 1 indicates a face-on, and a 7 indicates an edge-on view onto the galaxy.*

Obj.	Class	Incl. class	D_{25} [′]	$S_{12\mu m}$ [Jy]	$S_{25\mu m}$ [Jy]	$S_{60\mu m}$ [Jy]	$S_{100\mu m}$ [Jy]	L_{FIR} $[10^9 h^{-2}\, L_\odot]$	HI deficiency	r/r_A
UGC 1048	SBa	1	1.58	0.14	0.47	3.75	6.95	15.76	0.2	3.07
UGC 1089	Sc	1	1.15	0.12	0.19	1.08	3.17	5.65	0.14	2.88
UGC 1094	SBb	6	2.24	0.11	0.16	1.03	3.19	5.55	0.07	2.9
UGC 1100	Sb/SBb	6	2.19	< 0.11	< 0.08	0.25	1.02	1.57	0.29	2.41
UGC 1125	S			< 0.08	< 0.12	0.42	1.05	2.02	−0.2	2.44
UGC 1152	Sb	5	1.05	< 0.08	< 0.10	0.32	0.79	1.53	−0.12	3.05
UGC 1178	Sc	7	1.82	0.14	0.12	1.23	3.66	6.48	−0.27	1.69
UGC 1220	S		0.83	0.14	0.26	1.88	4.6	8.95	0	1.3
UGC 1234	Sc/SBc		1.12	< 0.07	< 0.09	0.23	0.56	1.1	−0.14	1.01
UGC 1238	Sb	3	1.78	0.08	0.12	0.75	2.05	3.78	0.03	0.77
UGC 1248	Sa-b	6	3.16	0.09	< 0.12	0.28	1.63	2.24	0.77	0.73
UGC 1251	peculiar		0.91	< 0.10	0.18	0.03	0.55	0.59	0.83	0.62
UGC 1302	SBb	3	2.45	0.11	1.29	1.29	2.78	5.79	0.1	0.55
UGC 1319	S?		0.89	0.12	< 0.20	0.92	2.74	4.85	0.27	0.16
UGC 1338	Sb	2	0.89	< 0.13	< 0.13	0.29	0.85	1.52	> 0.79	0.21
UGC 1344	SBa	5	1.62						> 0.78	0.21
UGC 1347	Sc/SBc	1	1.26	0.12	0.19	1.49	3.84	7.28	−0.07	0.27
UGC 1349	Sc	1	1.29	0.14	0.21	1.44	3.26	6.61	0.38	0.05
UGC 1358	S0-a	6	1.55	0.07	< 0.04	0.09	0.31	0.51	> 0.79	0.09
UGC 1376	SBb	4	1.7	< 0.10	< 0.11	0.26	0.9	1.48	0.22	1.88
UGC 1411	Sb	6	1.82	< 0.11	0.01	0.44	1.45	2.46	−0.3	1.22
UGC 1421	S	7	1.62	< 0.08	< 0.09	0.3	0.98	1.67	0.48	1.86
UGC 1422			1.17	< 0.09	< 0.11	0.31	0.87	1.6	0.17	2.00
UGC 1437	Sc	3	2.51	0.29	0.38	3.36	11.4	19.04	−0.15	0.58

Table 6.3: *continued*

Obj.	Class	Incl. class	D_{25} [′]	$S_{12\mu m}$ [Jy]	$S_{25\mu m}$ [Jy]	$S_{60\mu m}$ [Jy]	$S_{100\mu m}$ [Jy]	L_{FIR} $[10^9 h^{-2}\ L_\odot]$	HI deficiency	r/r_A
UGC 1456	Sa-b	3	1.26	0.09	< 0.18	0.62	2.5	3.9	0.46	0.77
UGC 1493	SB?a-b	6	1.82	0.16	0.16	1.29	3.65	6.61	0.75	1.51
UGC 1497	Sc	2	1.58	0.17	0.29	2.02	5.85	10.49	−0.09	2.64
UGC 1520	peculiar		0.63	0.14	< 0.22	1.67	4.07	7.95	−0.08	2.61
UGC 1550	Sc	6	3.16	0.13	0.22	1.45	5.06	8.34	0.1	1.74
UGC 1581	S-Irr		1.66	< 0.11	0.80	0.8	2.4	4.22	−0.29	1.66
UGC 1633	SBb-c	6	2.95	0.21	0.25	1.91	6.2	10.55	0.21	2.36
UGC 1655	peculiar		2.88	0.70	1.03	10.89	22.83	48.3	0.25	2.64
UGC 1672	S	6	1.1	0.37	0.75	6.43	12.54	27.62	−0.06	2.27
UGC 1676	Sba/Sb	5	1.78	< 0.10	< 0.12	0.86	2.6	4.57	0.06	2.26
UGC 1721	SBb/SBc	1	2	< 0.11	< 0.12	0.19	0.77	1.2	−0.14	2.61
UGC 1769	Sb/Sc	4	1	0.08	< 0.14	0.68	2.33	3.86	−0.31	2.98
Z522-002			0.74	< 0.10	< 0.07	0.3	0.71	1.4	−0.21	1.02

at least 2σ to the individual components were used for compiling the integrated intensity maps. This resulted in corresponding velocity ranges of 5464 - 5589 km s^{-1} for the central component, 5555 - 5613 km s^{-1} for the southern component, and 5456 - 5613 km s^{-1} for the total galaxy (Fig. 6.5). The IRAM 30 m ^{12}CO(2−1) flux densities were integrated over the same velocity ranges as the BIMA maps. To coincide better with the BIMA contour map and the POSS-II Red data, the IRAM maps were shifted by 1.6″ towards north-east – a correction which agrees with the pointing accuracy of the 30 m telescope.

Table 6.4 lists the molecular line emission data determined for both regions, based on the BIMA ^{12}CO(1−0) and the IRAM 30 m ^{12}CO(2−1) observations. Their sizes were determined in the BIMA integrated intensity maps (Figure 6.5, white contours) assuming a Gaussian brightness distribution with an additional underlying disk, both contributing to the total flux density. For the central region, the 65% peak intensity contour was chosen, while for the southern component the 60% contour was chosen to represent the FWHM of the distribution. The nucleus remains unresolved at the BIMA beam with a FWHM ~ 6.6″, whereas the southern region shows extended CO emission at this resolution. To consider the error caused by the uncertainty in the determination of the size of the southern component, the 50% and 70% contours were taken as upper and lower limits.

The derived intrinsic ^{12}CO(2−1)/^{12}CO(1−0) line ratios R are listed in Table 6.5, together with the observed line ratios $R_{\rm Obs}$ and the corresponding correction factors $f_{\rm gauss}$, where

$$R = f_{\rm gauss} \cdot R_{\rm Obs}; \quad f_{\rm gauss} = \frac{1 + (10.5"/\Theta_{\rm S})^2}{1 + (6.6"/\Theta_{\rm S})^2} \tag{6.2}$$

and $\Theta_{\rm S}$ represents the FWHM of the source. In both regions, the CO lines are optically thick – under normal conditions an indication of cold, subthermally excited and dense ($\lesssim 10^4$ cm^{-3}, Eckart et al. 1990b) molecular gas.

Due to the lack of any information on metallicity in UGC 1347, the estimate of the molecular gas mass $M(H_2)$, as listed in Table 6.6, has a significant uncertainty. To account for the higher metallicity in galaxy centers, the value of $M(H_2)$ for the central region given in Table 6.6 was based on a lower conversion factor than the other two values, as suggested in Israel (2001).

Amram et al. (1994) investigate the Hα velocity field and the Hα rotation curve of UGC 1347. They derive an approximate inclination of 30°, as well as a position angle of 20°. As shown in Fig. 6.7, the Hα rotation curve is in good agreement with the ^{12}CO(1−0) velocity pattern along the same axis. The Hα rotation curve was scaled by a factor of 0.5 along the velocity axis to compensate for the inclination correction that was applied to the Amram et al. (1994) data.

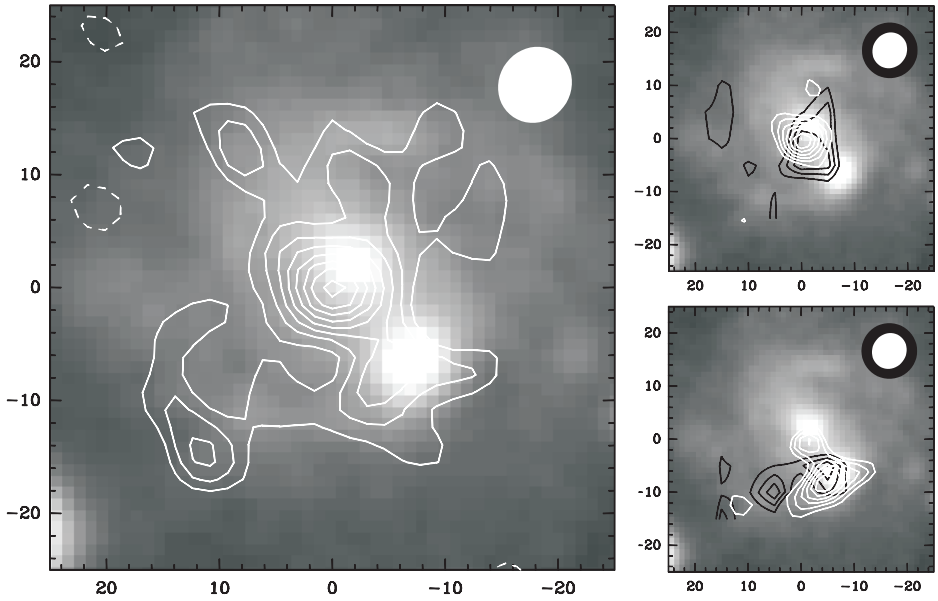

Figure 6.5: *Left: Overlay of the ^{12}CO map obtained with BIMA and the POSS-II Red image. The contours have an increment of $1\sigma = 1.80$ Jy beam$^{-1}\cdot$ km s^{-1} starting at 2σ. The CO emission extends over most of the inner disk of UGC 1347. Right: Integrated intensity maps of the central and the southern component. The black contours represent the ^{12}CO(2−1) emission obtained with the IRAM 30 m telescope. Contours represent 10% steps of the peak emission.*

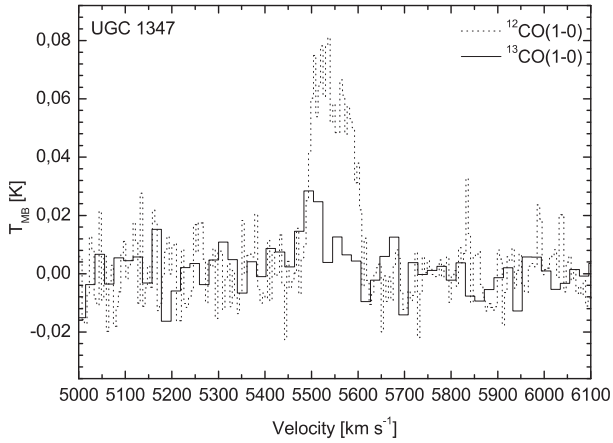

Figure 6.6: *Global ^{12}CO(1−0) and ^{13}CO(1−0) spectra of UGC 1347, obtained with the IRAM 30 m telescope*

Table 6.4: *Integrated temperatures for both CO-bright components and for the disk of UGC 1347. Both components were assumed to be Gaussian. A disk flux contribution was taken into account in the determination of the source sizes. The central component is not resolved. The values for the total galaxy represent IRAM 30 m single-beam measurements centered on the galaxy. A comparison of the two CO(1–0) spectra can be found in Fig. 6.6.*

	$\Theta_{S,Obs}$ [″]	$I_{^{12}CO(1-0)}$ [K km s^{-1}]	$I_{^{12}CO(2-1)}$ [K km s^{-1}]	$I_{^{13}CO(1-0)}$ [K km s^{-1}]
nucleus	<6.6	40.1 ± 1.3	8.4 ± 1.0	
southern	$8.5^{+1.4}_{-1.6}$	$24.1^{+5.5}_{-0.6}$	4.0 ± 0.6	
total galaxy	18.9	4.6 ± 0.3		1.7±0.3

Table 6.5: *^{12}CO(2–1)/^{12}CO(1–0) line ratio R for both CO-bright components of UGC 1347. The listed ratios R and source sizes θ_S are intrinsic values based on the integrated temperatures and observed sizes given in Table 6.4 and assuming Gaussian distributions for the beams and sources.*

	FWHM θ_S [″]	R_{Obs}	f_{gauss}	R
nucleus	6.6	0.21 ± 0.03	1.77	0.37
	0		2.50	0.53
southern	$5.4^{+2.0}_{-3.4}$	$0.17^{-0.03}_{+0.00}$	$1.92^{-0.24}_{+0.48}$	$0.33^{-0.09}_{+0.08}$

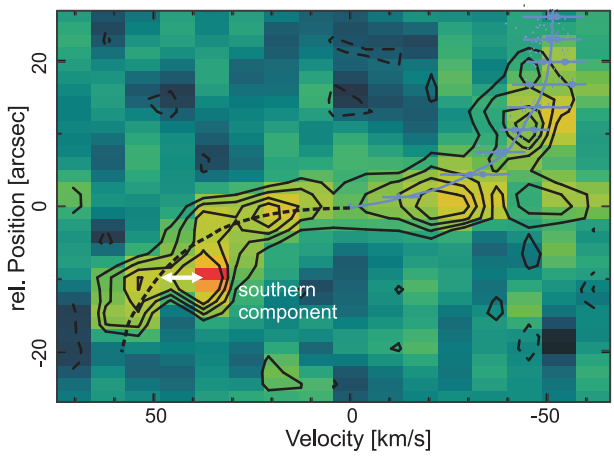

Figure 6.7: *^{12}CO(1–0) position-velocity diagram of UGC 1347 with the origin in the center of the galaxy and a position angle of 20°. Superimposed in the top right corner is the Hα rotation curve obtained by Amram et al. (1994) (see text). The southern component is blue-shifted by approximately 10 km s^{-1} with respect to the disk radiation at that position (indicated by the arrow).*

Table 6.6: *Molecular gas masses of the nucleus, southern component, and total galaxy. The size estimates given in Table 6.5 were applied.*

	X $[\mathrm{cm}^{-2}\ (\mathrm{K\ km\ s}^{-1})^{-1}]$	$M(\mathrm{H}_2)$ $[\mathrm{M}_\odot]$
nucleus	$4{\cdot}10^{19}$	$4.7{\cdot}10^{7}h^{-2}$
south.	$2{\cdot}10^{20}$	$9.4{\cdot}10^{7}h^{-2}$
total galaxy	$2{\cdot}10^{20}$	$5.7{\cdot}10^{8}h^{-2}$

However, the coincidence of both curves is valid only relative to each other, since Amram et al. find a systemic velocity of only 5478 km s^{-1}.

Another remarkable feature visible in the position-velocity diagram is a discrepancy in the velocity of the southern component and the disk at the same position. The gas appears to be blue-shifted by approximately 10 km s^{-1} with respect to the underlying disk. A weak evidence of a component, which is to a lesser extent red-shifted at that position is also indicated in the diagram. This may be explained by an expected cloud-cloud velocity dispersion of $\sigma \lesssim 10$ km s^{-1}. However, the blue-shifted (as well as the indicated red-shifted) emission coincides with the position of the southern component. Therefore, the shift may alternatively be explained by the model of an asymmetrically expanding gas shell or of large scale outflow with a substantial amount of entrained molecular gas. It supports the hypothesis of enhanced star formation in that region, as indicated by Hackenberg et al. (2000).

As expected, the largest velocity dispersion can be found at the position of the nuclear source. An upper limit for the dynamical mass confined in the unresolved center can be derived by considering the maximum velocity measured at the center position in the position-velocity diagram of $\sim$ 50km s^{-1}. When accounting for an inclination of 30° (resulting in $v_{\mathrm{max}} = 100$ km s^{-1}) and assuming a maximum radius of $< 1.5''$, an upper limit of $8.3{\cdot}10^{8}h^{-1}$ $\mathrm{M}_\odot$ can be derived.

6.4 Discussion

In the following the question about possible environmental influence on the global molecular mass content of cluster galaxies is revisited. In Sect. 6.4.1 several indicators of the presence of a molecular gas deficiency in the cluster core are presented. This deficiency is discussed further in the framework of a cirrus model in Sect. 6.4.4. Sect. 6.4.2 comments on a previously introduced CO deficiency parameter and in Sect. 6.4.3 the morphological composition of the subsamples of Abell 262 is discussed.

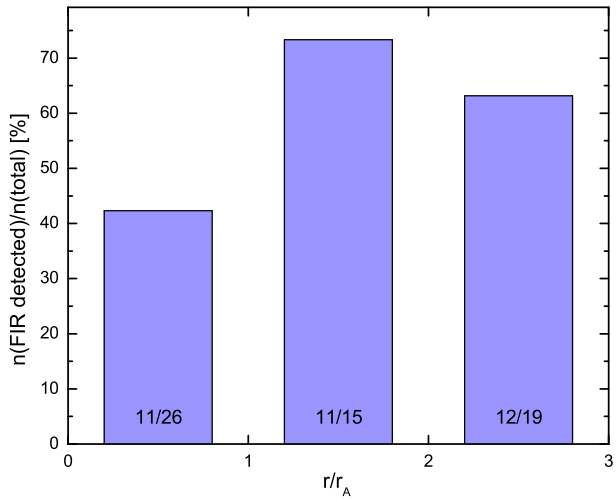

Figure 6.8: *The ratio of galaxies detected by IRAS varies with the distance to the cluster core.*

6.4.1 Signatures of environmental influences

The molecular gas mass estimates shown in Fig. 6.3 indicate a dependency of the total molecular gas content in Abell 262 galaxies on the projected distance to the cluster core. The median molecular gas mass of the sample members located in the vicinity of the cluster center was found to be $1.2 \pm 0.6 \cdot 10^9 h^{-2} M_\odot$, whereas a value of $3.0 \pm 0.6 \cdot 10^9 h^{-2} M_\odot$ was determined for the more distant subsample. The difference in the two median values is 3 times larger than the median absolute deviations.

Figure 6.4 shows that the application of the FIR selection criterion results in the inclusion of galaxies (such as the peculiar galaxy UGC 1655, UGC 1672, or UGC 1437) with outstanding L_{FIR} compared to the bulk of IRAS galaxies in Abell 262. The strong FIR flux density of UGC 1437, the location within the IRAS color-color diagram (cf. Sect. 6.4.4), and the fact that it is not HI deficient, taken together indicate that this galaxy is a more distant object that is projected into the central region.

Other indicators can be found in the L_{FIR} data that support the presence of an environmental influence on the molecular gas content of cluster galaxies. With the exception of UGC 1437 mentioned above, the L_{FIR} brightest Abell 262 galaxies are found at distances that exceed one Abell radius, whereas the faintest sources detected by IRAS are located close (in projection) to the core of the cluster. Moreover, the ratio of sources detected by IRAS in the Abell 262 sample of Giovanelli & Haynes drops from $\sim 65\%$ within the region of the annulus from 1

to 3 Abell radii to ~ 45% in the central region of the cluster (cf. Fig. 6.8). Due to projection effects, the intrinsic fraction of FIR-detected sources in the center (n_c) appears to be overestimated. There $n_c = n_{total} - n_{fg}$, where $n_{total}(= 26)$ represents all galaxies found within the central Abell radius, including a number of foreground or background galaxies n_{fg} that are projected along the line of sight into the central region. This number can be approximated by the product of the surface number density of galaxies of the outer region and the area of the central region:

$$n_{fg} \approx \frac{n_{outer}}{r^2_{outer} - r^2_{inner}} \cdot r^2_{inner} \tag{6.3}$$

where n_{outer} (=34) represents the number of galaxies within the projected region between 1 Abell radius (r_{inner}) and 3 (r_{outer}) Abell radii. This approximation leads to an upper limit for the number n_c of galaxies within r_{inner}, since the cluster profile has not been taken into account. The application of this correction yields a ratio of IRAS detected sources to n_c of below 38% within the cluster core in comparison with ~ 65% in the outer regions.

Aside from the IRAS detection rate, the median L_{FIR} value of detected galaxies in Abell 262 also varies with the projected distance to the cluster core. While in the region between 2 and 3 Abell radii, the median value amounts to $5.6 \cdot 10^9 L_\odot$, it drops to $3.8 \cdot 10^9 L_\odot$ (cf. Fig. 6.4) in the region of the central Abell radius. Again, the intrinsic value is likely to be lower, since more distant galaxies with higher L_{FIR} values are projected into the core region.

Assuming the validity of the $M(H_2) - L_{FIR}$ correlation, the drop in the IRAS detection rate and median L_{FIR} value in the center may imply a loss of molecular gas of galaxies in the core region of the cluster. This tentative result is not expected from previously published studies of molecular gas in galaxy clusters. However, the results are not necessarily inconsistent with previous investigations. The existing studies are rather inhomogeneous in terms of selection criteria and focus – the results are difficult to compare. A conclusion common to all studies is that the influence of the environment on the molecular gas content of cluster galaxies is minor (in many cases insignificant) and not comparable to the environmental impact on HI abundances. Kenney & Young (1989) study the CO content of a blue-magnitude limited sample of Virgo galaxies as a function of the HI deficiency of these objects. Casoli et al. (1991) take a similar approach and analyze the CO content of a FIR-selected sample of 9 HI-deficient Coma galaxies with 9 HI normal Coma galaxies. Horellou, Casoli, & Dupraz (1995b) focus on the fact that FIR or blue-magnitude selected samples are biased towards strong CO emission. They detected 11 of 21 Fornax cluster galaxies in CO emission. All 3 studies suffer from a very limited number of observations.

In contrast, Boselli et al. (1997) present a study on an optically selected sample of 27 galaxies in the Coma and Abell 1367 clusters and compare their CO content with a sample of 37 relatively isolated galaxies. Their search for a CO deficiency of cluster galaxies as a function of the distance from the cluster center shows a higher dispersion in the central region, thus leaving room for a minor environmental influence on the CO content. With a total of 582 galaxies from their own observations and from the literature, the study of Casoli et al. (1998) is based on the broadest statistical base. Their definition of the CO deficiency is discussed in the following.

6.4.2 The CODEF parameter

Similar to the definition of the HI deficiency in Giovanelli & Haynes (1985), Casoli et al. (1998) propose a CO deficiency parameter:

$$\mathrm{CODEF} = \log((\mathrm{M(H_2)}/\mathrm{D}_{25}^2)_{\mathrm{expected}}) - \log((\mathrm{M(H_2)}/\mathrm{D}_{25}^2)_{\mathrm{obs}}). \qquad (6.4)$$

As before, $M(\mathrm{H_2})$ is assumed to be directly proportional to I_{CO}. In order to compare the CO emission of observed galaxies with values obtained for isolated reference galaxies, Casoli et al. (1998) introduce a CO-emission predictor, which makes use of the FIR to optical-size relation $\log(L_{\mathrm{FIR}}/D_{25}^2)$:

$$\log((M(\mathrm{H_2})/D_{25}^2)_{\mathrm{expected}}) = \mathrm{a}(T)\log(L_{\mathrm{FIR}}/D_{25}^2) + \mathrm{b}(T), \qquad (6.5)$$

where a and b depend on the morphological type. The morphological type and optical size are already used by Haynes & Giovanelli (1984) to compare the HI content of galaxies to a standard of normalcy for isolated galaxies. In addition to these two parameters, Casoli et al. (1998) use L_{FIR} in their extended standard of normalcy for the molecular gas content of isolated galaxies. However, the use of L_{FIR} has the shortcoming of being correlated with the CO content of a galaxy. A CO deficiency may result in reduced FIR emission, as indicated in Sect. 6.4.1. In this case, the CO emission predictor will yield lower values for the 'expected' normalized CO emission $\log((M(\mathrm{H_2})/D_{25}^2)_{\mathrm{expected}})$ than what it ideally should, which in turn reduces the value of CODEF. In other words, L_{FIR} is well known for not being orthogonal to the CO emission. Therefore, this parameter is not well-suited to defining a standard of normalcy in a CO-deficiency study.

In the way it is defined above, CODEF instead forms a morphology dependent parameter that is similar to the star-formation efficiency $L_{\mathrm{FIR}}/M_{\mathrm{H_2}}$ (cf. Fig. 6.9 and Solomon & Sage (1988) and references therein). The SFE can be regarded as an indicator of the morphological type of galaxies and, therefore, is

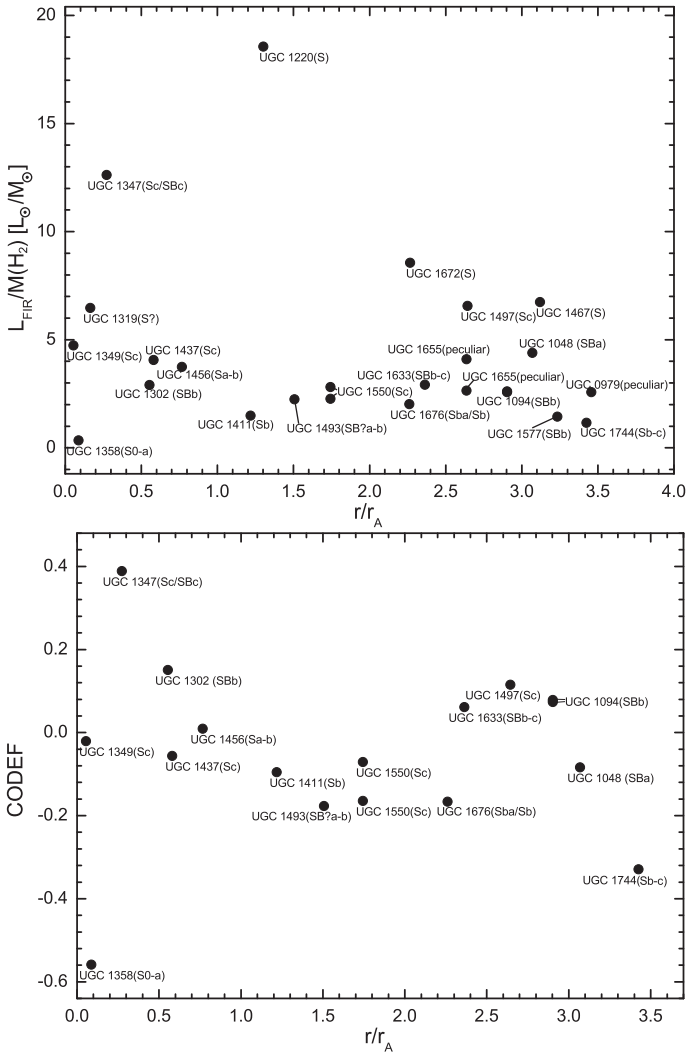

Figure 6.9: *Star-formation efficiency and CODEF parameter as a function of the distance to the cluster core.*

likely to be an indirect measure of their overall molecular gas content rather than their deficiency.

The CODEF values for the Abell 262 sample galaxies of known galaxy type are shown in Table 6.2 and plotted in Fig. 6.9. A Hubble constant $H_0 = 75\text{km s}^{-1}$ Mpc^{-1} was assumed to comply with the Casoli et al. (1998) parameters. Because of the restriction to non-peculiar galaxies, the number of galaxies in this sample for which CODEF can be derived is even smaller than the number of galaxies with measured CO-line intensities. For the remaining galaxies, a dependency of CODEF on the distance to the cluster core cannot be identified.

6.4.3 Morphological distribution

A more detailed analysis of a possible influence of the environment on the global molecular gas content has to include the morphological distribution of galaxies within the cluster. The Giovanelli & Haynes (1985) sample of Abell 262 galaxies indeed shows segregation between Sa/b and Sc galaxies as a function of position within the cluster. Twenty-six of 63 galaxies within 3 Abell radii are located within the central Abell radius. In this region, 5 objects were clearly classified by Nilson (1973) as early spiral galaxies, but only 3 early-type objects were identified in the region between 1 and 3 Abell radii. Therefore, early-type spiral galaxies, are predominantly found within the center of the cluster. For late-type spiral galaxies, the ratio changes towards a deficiency in the core: 6 late-type galaxies were clearly identified within the central Abell radius, but 11 were identified between 1 and 3 Abell radii. Five Sb/SBb galaxies were found in both the inner and the outer regions, thus resulting in a higher fraction for the center when referring to the total number of objects. Three galaxies were identified as peculiar, another 3 as dwarf galaxies. The remaining 22 galaxies were either identified as spirals without any further characterization or were not categorized at all.

However, for the L_{FIR} bright subsample and the CO subsample discussed in this study, such a clear segregation is not visible. Thirteen of the 36 objects with known FIR flux densities are located in the central Abell radius – 4 late-type and 3 early-type galaxies – whereas 7 late-type and 5 early type galaxies are found in the outer region between 1 and 3 Abell radii. Of the 12 objects that have been observed in CO emission, 7 are located in the central region. Of these, 2 are early and 3 are late-type galaxies. One SBa and 2 late-type classifications were found for the outer objects. Neglecting the morphological distribution of the subsamples, therefore, should not result in a misinterpretation of L_{FIR} or CO-line intensity based quantities in terms of environmental influences.

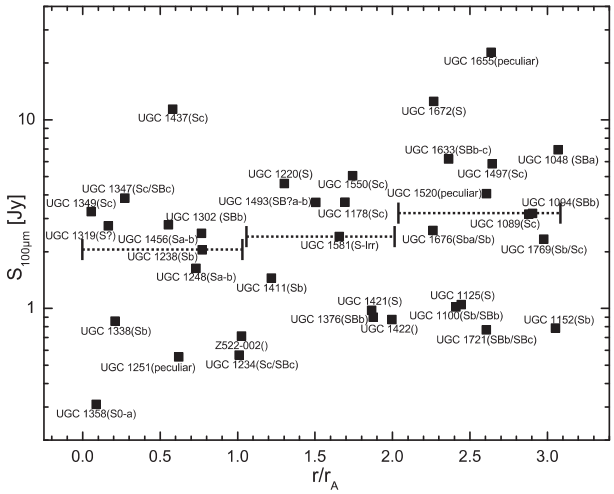

Figure 6.10: *IRAS 100 μm flux densities of Abell 262 galaxies as a function of the distance to the cluster center. The plot contains all Abell 262 galaxies down to the IRAS flux limit with distances to the cluster core not exceeding 3 Abell radii. Median values of 3 distance ranges are represented by the horizontal lines.*

6.4.4 H_2 loss by stripping of a cirrus-like component?

Gas clouds do not consist of atomic gas alone; molecular gas and cold dust are also associated with them. Several authors (e.g. Helou 1986; Rowan-Robinson 1992) have discussed the presence of cold dust in the ISM resulting in multiple-component models of galaxy emission in the IRAS wavelength domain. Besides warmer emission from active star-forming regions and eventually a Seyfert component, a relatively constant disk or cirrus-like component from cold interstellar dust contributes to the IRAS colors of galaxies.

In the course of the HI removal processes, which these cirrus-like clouds in cluster galaxies are subjected to, it is likely that the associated molecular gas and cold dust are also lost. This is supported by Doyon & Joseph (1989), who convincingly show the existence of dust deficiency in HI deficient galaxies in the core region of Virgo. By analyzing the FIR properties of the galaxies, they discuss the lack of dust in the context of the HI removal. Since dust must be associated with molecular gas, there must be a CO deficiency present at a low level, too. As shown in Sect. 6.4.1, a FIR deficiency is indeed present in the set of IRAS detected galaxies in the core of Abell 262. A total difference of $\Delta S_{100\,\mu\mathrm{m}} \sim 1.1$ Jy (Fig. 6.10) between the median values of the core ($r < r_\mathrm{A}$) and outer galaxies ($2r_\mathrm{A} < r < 3r_\mathrm{A}$) can be identified. HI and FIR deficiency, as well as the other indications of a core distance dependency of the molecular gas

content in Abell 262 galaxies, suggests the applicability of a model for cirrus-like cloud stripping. This model is introduced in Sect. 6.4.4 and applied to the case of Abell 262 in Sect. 6.4.4. The derived estimates are not inconsistent with the presence of simultaneously occurring CO-deficiency in the core region.

Another indication that supports the stripping hypothesis of cirrus-like clouds can be found in the IRAS color-color diagram (cf. Fig. 6.11). IRAS colors of normal galaxies are influenced by several factors. While the cirrus-like contribution is fairly constant for all galaxies, the importance of star formation varies and may significantly influence the galaxy's position within the color-color diagram. The presence of varying star-formation components on top of the cirrus-like component creates a distribution of galaxies within the color-color diagram that is non-Gaussian (cf. Helou 1986). Therefore, mean values are not adequate measures for comparing the colors of the cirrus-like components of central and more distant galaxies. Objects with a strong star-formation component should be excluded from the analysis. For the remaining objects, the median value of the core galaxies differs slightly from the value for the more distant galaxies, with the latter closer to that of typical cirrus colors.

The galactic cirrus cloud model of de Vries et al. (1987)

Galactic cirrus clouds, which are predominantly found at high galactic latitudes, consist of atomic and molecular gas. Embedded in the gas is cold dust, which re-radiates absorbed energy in the FIR. For the galactic cirrus in Ursa Major, de Vries, Thaddeus, & Heithausen (1987) have proposed a two-component model to explain its infrared emission as a function of the total hydrogen column density, $N(\mathrm{H})=N(\mathrm{HI})+2N(\mathrm{H_2})$:

$$I_{100\ \mu\mathrm{m}}[\mathrm{MJy\ sr^{-1}}] = aN(\mathrm{HI}) + bI_{\mathrm{CO}} + I_{100\ \mu\mathrm{m,BG}}, \tag{6.6}$$

where $I_{100\ \mu\mathrm{m,BG}}$ represents the flux density of the background emission. Again I_{CO} is used as tracer for $\mathrm{H_2}$: $X=N(\mathrm{H_2})/I_{\mathrm{CO}}=b/2a$. Then de Vries et al. (1987) derive a value for a of $(1.0 \pm 0.4) \cdot 10^{-20}$MJy sr^{-1} cm^2 and for b of (1.0 ± 0.5) MJy sr^{-1} K^{-1} km^{-1}s. In the cases of Centaurus A (Eckart et al. 1990a) and NGC 2903 (Jackson et al. 1991), the scope of this model has already been successfully extended to extragalactic sources.

Application of the model to the case of Abell 262

Due to the large IRAS beam, $S_{100\mu\mathrm{m}}$ comprises the source-integrated flux density for each Abell 262 galaxy. In order to extend the de Vries et al. (1987) model to

extragalactic sources, two assumptions are necessary: 1. the 100μm flux density traces N(H) on galactic scales, and 2. the background emission is similar over the whole extension of the cluster. A difference between representative values of $S_{100\mu\mathrm{m}}$ for the cluster core and for the outer region may be proportional to:

$$\Delta S_{100\ \mu\mathrm{m}} \propto \left\langle \int_{\mathrm{Sou}} N(H)\mathrm{d}\Omega \right\rangle_{\mathrm{out}} - \left\langle \int_{\mathrm{Sou}} N(H)\mathrm{d}\Omega \right\rangle_{\mathrm{core}} . \qquad (6.7)$$

The source-integrated H column density splits into an HI and an H_2 component, which are directly related to the respective HI and H_2 masses. So does $\Delta S_{100\ \mu\mathrm{m}}$ in the model. A direct determination of $\int N(H)\mathrm{d}\Omega$ can be only made for the few galaxies with existing H_2 mass estimates, but it is possible to obtain separate estimates for the $\Delta S_{100\ \mu\mathrm{m,HI}}$ and $\Delta S_{100\ \mu\mathrm{m,H_2}}$ components of $\Delta S_{100\ \mu\mathrm{m}}$, as is shown in the following.

The HI-deficiency HIDEF of galaxies in Abell 262, as defined and determined by Giovanelli & Haynes (1985), amounts to an average value of 0.33 for galaxies in the cluster's core region, with projected distances to the center of less than 1 Abell radius. For galaxies in the outer region, with distances exceeding 1 Abell radius, the average value for HIDEF is 0. HIDEF refers to a comparison sample of isolated galaxies (Haynes & Giovanelli 1984), for which the authors claim the average mass of all galaxies to be $\log(h^2 M_{\mathrm{HI}})$=9.39 ± 0.52. HIDEF and the average mass of a galaxy in the comparison sample can be used to derive an average HI-mass difference between the core and the outer region, and hence a value for $\Delta S_{100\ \mu\mathrm{m,HI}}$ of $0.68^{+1.58}_{-0.55}$Jy. The error mainly results from the uncertainties in the average HI mass and the factor a. The H_2 mass estimates given in Sect. 6.3.1 were used to obtain a gross estimate for $\Delta S_{100\ \mu\mathrm{m,H_2}}$ of 0.22 ± 0.15 Jy. Indeed, the estimates for the two components are in agreement with the the total difference $\Delta S_{100\ \mu m} \sim 1.1$ Jy found in the IRAS data of Abell 262 galaxies.

6.5 Summary and conclusions

Abell 262 is a spiral-rich cluster. Based on the classification given in Table 6.3, no clear tendency toward morphological segregation can be identified in the samples discussed in this study (cf. Sect. 6.4.3). The trend that the galaxies with less luminous CO-line emission and FIR-emission are located towards the center of the cluster (i.e. within the Abell radius) suggests that these objects show a deficiency in molecular gas and dust. Such an effect has not been reported so far. As in the case of the HI-deficiency, a CO-deficiency may be a result of

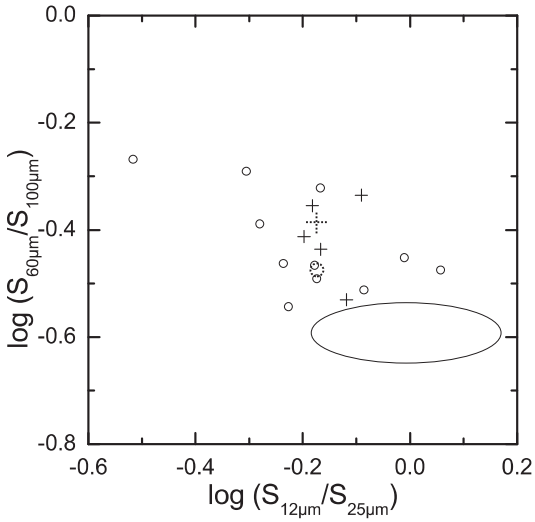

Figure 6.11: *Color-color diagram of Abell 262 galaxies detected in all four IRAS bands. Objects with a projected distance to the cluster core of less than 1 Abell radius are represented by a cross, and objects exceeding this distance are represented by open circles. The dotted symbols represent the respective median values. The ellipse marks the region of cirrus colors (cf. references in Helou 1986). The lowest cross belongs to UGC 1437, which is most likely a distant galaxy that is projected into the center. Therefore, it was neglected in the median. In the median value of the more distant galaxies, only the objects with* $\log S_{60\mu m}/S_{100\mu m} < -0.4$ *were considered. For the other objects a contribution of star formation to the FIR colors has to be assumed in addition to the cirrus-like component.*

interaction between neighboring galaxies or of interaction with either the central cluster potential or the central cluster gas reservoir.

The model by de Vries et al. (1987), explaining the FIR emission of galactic cirrus clouds, can be generalized to the case of a global cirrus/disc component in galaxies. One prediction of this model is a drop in the 100 μm flux density ($\Delta S_{100\,\mu m}$), which indeed is indicated in the existing IRAS data for the cluster. A small part of the decrease in $\Delta S_{100\,\mu m}$ can be expected to be caused by a deficiency of molecular gas mass in the cluster, which is traced by I_{CO}. The derived contributions to $\Delta S_{100\,\mu m}$ of 0.22 ± 0.15 Jy for the molecular gas mass deficiency and of $0.68^{+1.58}_{-0.55}$ Jy for the atomic gas mass deficiency is consistent with the overall drop in the median 100 μm flux density of ~ 1.1 Jy. It can be expected that a certain amount of molecular gas is associated with the more diffuse HI material. This is especially the case for high-latitude cirrus clouds that are also bright in their FIR emission. The weak indications of a CO- and L_{FIR}-deficiency observed in Abell 262 may, therefore, be a direct consequence of the HI-deficiency found by Giovanelli, Haynes, & Chincarini (1982).

As for UGC 1347, a second bright source south of the nucleus can be identified not only in the visual and NIR but also in the mm wavelength domain. Both sources are optically thick in their CO line emission. The velocity profile is in good agreement with a previously published Hα rotation curve. Within the position-velocity diagram, the southern component deviates from the rotation curve of the disk. This may indicate an asymmetrically expanding gas shell or a large scale outflow at the position of the southern source, which supports a scenario of enhanced star formation in that region, as was indicated by Hackenberg et al. (2000).

Abbreviation

2dF	two degree Field (survey)
A&A	Astronomy and Astrophysics
A&AS	Astronomy and Astrophysics Supplement Series
ADC	analog to digital converter
AGN	active galactic nucleus
AJ	Astronomical Journal
ALMA	Atacama Large Millimeter Array
AO	adaptive optics
ARA&A	Annual Review of Astronomy and Astrophysics
ApJ	Astrophysical Journal
ApJS	Astrophysical Journal Supplement Series
BIMA	Berkeley Illinois Maryland Association
CCD	charge-coupled device (detector)
CLASS	Continuum and Line Analysis Single-dish Software
DM	deformable mirror
DPU	detector positioning unit
DSS	Digitized Sky Survey
ESO	European Southern Observatory
FDR	Final Design Review
FIR	far-infrared
FoV	field of view
FPA	focal plane array
FT	fringe tracker
FWHM	full width at half maximum
FWZI	full width at zero intensity
GWS	ground-layer wavefront sensor
HE / HES	Hamburg/ESO survey
HzRG	highly redshifted radio galaxy
IRAM	Institut für Radioastronomie im Millimeterbereich
IRAS	Infrared Astronomical Satellite
ICM	intracluster medium
IDL	Interactive Data Language
ISM	interstellar medium

JOSA	Journal of the Optical Society of America
KI	Keck Interferometer
LBT	Large Binocular Telescope
LBTI	Large Binocular Telescope Interferometer
LIG	luminous infrared galaxy
LINC	LBT INterferometric Camera
LOST	Layer-Oriented Simulation Tool
mas	milli-arcsecond
MHWS	mid/high-layer wavefront sensor
MIRIAD	Multichannel Image Reconstruction, Image Analysis & Display
MNRAS	Monthly Notices of the Royal Astronomical Society
MPIA	Max-Planck-Institut für Astronomie, Heidelberg
MPIfR	Max-Planck-Institut für Radioastronomie, Bonn
Mrk	Markarian catalog of galaxies with UV-continuum
NIR	near-infrared
NIRVANA	Near-IR/Visible Adaptive iNterferometer for Astronomy
OVRO	Owens Valey Radio Observatory
PASP	Publications of the Astronomical Society of the Pacic
PG	Palomar-Green Bright Quasar Survey
PH1	1. Physikalisches Institut der Universität zu Köln
POSS	Palomar Observatory Sky Survey
PSF	point-spread function
PdBI	Plateau de Bure Interferometer
QSO	quasistellar object
RMS	root mean squared
RT	real-time
SDSS	Sloan Digital Sky Survey
SEST	Swedish-ESO Submillimetre Telescope
SF	star formation
SFE	star formation efficiency
SMG	submillimeter galaxy
SPIE	Society of Photo-Optical Instrumentation Engineers
ULIG	ultraluminous infrared galaxy
VLTI	Very Large Telescope Interferometer
I Zw	first Zwicky list of galaxies

Bibliography

Abell, G. O. 1958, *The Distribution of Rich Clusters of Galaxies*, ApJS, 3, 211

Abell, G. O., Corwin, H. G., & Olowin, R. P. 1989, *A catalog of rich clusters of galaxies*, ApJS, 70, 1

Amram, P., Marcelin, M., Balkowski, C., Cayatte, V., Sullivan, W. T., & Le Coarer, E. 1994, *H_α velocity fields and rotation curves of galaxies in clusters*, A&AS, 103, 5

Andersen, D. R., Bertram, T., Bizenberger, P., Egner, S., Herbst, T. M., Ragazzoni, R., & Straubmeier, C. 2004, *The LINC-NIRVANA testbed Fizeau interferometer*, in Proc. SPIE, Vol. 5491, New Frontiers in Stellar Interferometry, ed. W. A. Traub, 1760–+

Antonucci, R. 1993, *Unified models for active galactic nuclei and quasars*, ARA&A, 31, 473

Arcidiacono, C. 2004, *MultiConjugate Adaptive Optics for Large Telescopes*, PhD thesis, Università degli Studi di Firenze, Italy

—. 2005, *MCAO simulations*, Tech. Rep. LN-INAFA-FDR-AO-003, MPIA, Heidelberg, Germany

Arcidiacono, C., Diolaiti, E., Ragazzoni, R., Baruffolo, A., Brindisi, A., Farinato, J., & Vernet-Viard, E. 2003, *Sky coverage and Strehl ratio uniformity in layer-oriented MCAO systems*, in Proc. SPIE, Vol. 5169, Astronomical Adaptive Optics Systems and Applications, ed. R. K. Tyson & M. Lloyd-Hart, 169–180

Arcidiacono, C., Diolaiti, E., Tordi, M., Ragazzoni, R., Farinato, J., Vernet, E., & Marchetti, E. 2004, *Layer-oriented simulation tool*, Applied Optics, 43, 4288

Baganoff, F. K., Bautz, M. W., Brandt, W. N., Chartas, G., Feigelson, E. D., Garmire, G. P., Maeda, Y., Morris, M., Ricker, G. R., Townsley, L. K., & Walter, F. 2001, *Rapid X-ray flaring from the direction of the supermassive black hole at the Galactic Centre*, Nature, 413, 45

Barthel, P. D. 2006, *Star-forming QSO host galaxies*, A&A, 458, 107

Barthel, P. D. & Sanders, D. B. 2006, *Summary and key questions*, New Astronomy Review, 50, 840

Behrend, J. 2005, *Design Report of the Fringe and Flexure Tracker Detector*, Tech. Rep. LN-MPIFR-FDR-ELEC-001, MPIfR, Bonn, Germany

Bertram, T. 2004, *Fringe and Flexure Tracking System*, Tech. Rep. LN-KOELN-SWDR-ICS-001, PH1, Cologne, Germany

—. 2007, *FFTS Software*, Tech. Rep. LN-KOELN-SWDR-ICS-001, PH1, Cologne, Germany

Bertram, T., Eckart, A., Fischer, S., Zuther, J., Straubmeier, C., Wisotzki, L., & Krips, M. 2007, *Molecular gas in nearby low-luminosity QSO host galaxies*, A&A, 470, 571

Bertram, T., Eckart, A., Krips, M., Staguhn, J. G., & Hackenberg, W. 2006a, *Molecular gas in the galaxy cluster Abell 262. CO observations of UGC 1347 and other galaxies of the cluster*, A&A, 448, 29

Bertram, T., Eckart, A., Krips, M., Straubmeier, C., Fischer, S., & Staguhn, J. G. 2006b, *Molecular gas in QSO host galaxies*, New Astronomy Review, 50, 712

Binney, J. & Merrifield, M. 1998, Galactic Astronomy, Princeton Series in Astrophysics (Princeton, NJ: Princeton University Press), 251

Bizenberger, P., Andersen, D., Baumeister, H., Beckmann, U., Diolaiti, E., Herbst, T. M., Laun, W., Mohr, L., Naranjo, V., & Straubmeier, C. 2004, *The LINC-NIRVANA cryogenic interferometric camera*, in Proc. SPIE, Vol. 5492, Ground-based Instrumentation for Astronomy, ed. A. F. M. Moorwood & M. Iye, 1461–1470

Bizenberger, P., Diolaiti, E., Egner, S., Herbst, T. M., Ragazzoni, R., Reymann, D., & Xu, W. 2006, *LINC-NIRVANA: optical design of an interferometric imaging camera*, in Proc. SPIE, Vol. 6269, Ground-based and Airborne Instrumentation for Astronomy., ed. I. S. McLean & M. Iye, 62690D

Boroson, T. 2005, *Blueshifted [O III] Emission: Indications of a Dynamic Narrow-Line Region*, AJ, 130, 381

Boselli, A., Gavazzi, G., Lequeux, J., Buat, V., Casoli, F., Dickey, J., & Donas, J. 1997, *The molecular gas content of spiral galaxies in the Coma/A1367 supercluster*, A&A, 327, 522

Bravo-Alfaro, H., Szomoru, A., Cayatte, V., Balkowski, C., & Sancisi, R. 1997, *The HI distribution of spiral galaxies in the cluster A 262*, A&AS, 126, 537

Butcher, H. & Oemler, A. 1978, *The evolution of galaxies in clusters. II - The galaxy content of nearby clusters*, ApJ, 226, 559

Casoli, F., Boisse, P., Combes, F., & Dupraz, C. 1991, *Are H I-deficient galaxies of the Coma supercluster deficient in molecular gas?*, A&A, 249, 359

Casoli, F., Sauty, S., Gerin, M., Boselli, A., Fouque, P., Braine, J., Gavazzi, G., Lequeux, J., & Dickey, J. 1998, *Molecular gas in spiral galaxies*, A&A, 331, 451

Conan, J.-M., Rousset, G., & Madec, P.-Y. 1995, *Wave-front temporal spectra in high-resolution imaging through turbulence*, Journal of the Optical Society of America A, 12, 1559

Conan, R., Avila, R., Sánchez, L. J., Ziad, A., Martin, F., Borgnino, J., Harris, O., González, S. I., Michel, R., & Hiriart, D. 2003, *Wavefront outer scale measurements at San Pedro Mártir Observatory. Its impact on Adaptive Optics performances*, in Revista Mexicana de Astronomia y Astrofisica Conference Series, ed. I. Cruz-Gonzalez, R. Avila, & M. Tapia, Vol. 19, 31–36

Couch, W. J., Barger, A. J., Smail, I., Ellis, R. S., & Sharples, R. M. 1998, *Morphological Studies of the Galaxy Populations in Distant "Butcher-Oemler" Clusters with the Hubble Space Telescope. II. AC 103, AC 118, and AC 114 at $Z = 0.31$*, ApJ, 497, 188

Cox, A. N., ed. 1999, Allen's Astrophysical Quantities (AIP press), 262

Curran, S. J., Aalto, S., & Booth, R. S. 2000, *Dense molecular gas in Seyfert galaxies*, A&AS, 141, 193

David, L. P., Jones, C., & Forman, W. 1996, *ROSAT PSPC Observations of Cool Rich Clusters*, ApJ, 473, 692

de Vaucouleurs, G., de Vaucouleurs, A., Corwin, H. G., Buta, R. J., Paturel, G., & Fouque, P. 1991, Third Reference Catalogue of Bright Galaxies (Berlin Heidelberg New York: Springer-Verlag)

de Vries, H. W., Thaddeus, P., & Heithausen, A. 1987, *Molecular and atomic clouds associated with infrared cirrus in Ursa Major*, ApJ, 319, 723

Desiderá, G., Anconelli, B., Bertero, M., Boccacci, P., & Carbillet, M. 2006, *Application of iterative blind deconvolution to the reconstruction of LBT LINC-NIRVANA images*, A&A, 452, 727

Downes, D. & Solomon, P. M. 1998, *Rotating Nuclear Rings and Extreme Starbursts in Ultraluminous Galaxies*, ApJ, 507, 615

Doyon, R. & Joseph, R. D. 1989, *Dust deficiency in Virgo spirals*, MNRAS, 239, 347

Dunlop, J. S., McLure, R. J., Kukula, M. J., Baum, S. A., O'Dea, C. P., & Hughes, D. H. 2003, *Quasars, their host galaxies and their central black holes*, MNRAS, 340, 1095

Eckart, A., Cameron, M., Rothermel, H., Wild, W., Zinnecker, H., Rydbeck, G., Olberg, M., & Wiklind, T. 1990a, *Observations of CO isotopic emission and the far-infrared continuum of Centaurus A*, ApJ, 363, 451

Eckart, A., Downes, D., Genzel, R., Harris, A. I., Jaffe, D. T., & Wild, W. 1990b, *Warm gas and spatial variations of molecular excitation in the nuclear region of IC 342*, ApJ, 348, 434

Eckart, A. & Genzel, R. 1996, *Observations of stellar proper motions near the Galactic Centre*, Nature, 383, 415

Egner, S. 2006, *Multi-Conjugate Adaptive Optics forLINC-NIRVANA – Laboratory tests of a Ground-Layer Adaptive Optics System and Vertical Turbulence Measurements at Mt. Graham*, PhD thesis, Ruperto-Carola University of Heidelberg, Germany

Esposito, S., Riccardi, A., & Femenía, B. 2000, *Differential piston angular anisoplanatism for astronomical optical interferometers*, A&A, 353, L29

Evans, A. S., Frayer, D. T., Surace, J. A., & Sanders, D. B. 2001, *Erratum: "Molecular Gas in Infrared-Excess, Optically Selected Quasars and the Connection with Infrared-luminous Galaxies" [Astron. J. 121, 1893 (2001)]*, AJ, 121, 3285

Evans, A. S., Solomon, P. M., Tacconi, L. J., Vavilkin, T., & Downes, D. 2006, *Dense Molecular Gas and the Role of Star Formation in the Host Galaxies of Quasi-stellar Objects*, AJ, 132, 2398

Fadda, D., Girardi, M., Giuricin, G., Mardirossian, F., & Mezzetti, M. 1996, *The Observational Distribution of Internal Velocity Dispersions in Nearby Galaxy Clusters*, ApJ, 473, 670

Fischer, S., Iserlohe, C., Zuther, J., Bertram, T., Straubmeier, C., Schödel, R., & Eckart, A. 2006, *Nearby AGN and their hosts in the near infrared*, A&A, 452, 827

Fried, D. L. 1966, *Optical resolution through a randomly inhomogeneous medium for very long and very short exposures,*, J. Opt. Soc. Am., 56, 1372

—. 1982, *Anisoplanatism in adaptive optics,*, J. Opt. Soc. Am., 72, 52

Gao, Y. & Solomon, P. M. 2004, *The Star Formation Rate and Dense Molecular Gas in Galaxies*, ApJ, 606, 271

Genzel, R., Schödel, R., Ott, T., Eckart, A., Alexander, T., Lacombe, F., Rouan, D., & Aschenbach, B. 2003, *Near-infrared flares from accreting gas around the supermassive black hole at the Galactic Centre*, Nature, 425, 934

Ghez, A. M., Klein, B. L., Morris, M., & Becklin, E. E. 1998, *High Proper-Motion Stars in the Vicinity of Sagittarius A*: Evidence for a Supermassive Black Hole at the Center of Our Galaxy*, ApJ, 509, 678

Giovanelli, R. & Haynes, M. P. 1985, *Gas deficiency in cluster galaxies - A comparison of nine clusters*, ApJ, 292, 404

Giovanelli, R., Haynes, M. P., & Chincarini, G. L. 1982, *The neutral hydrogen deficiency of the cluster A262*, ApJ, 262, 442

Greve, T. R., Bertoldi, F., Smail, I., Neri, R., Chapman, S. C., Blain, A. W., Ivison, R. J., Genzel, R., Omont, A., Cox, P., Tacconi, L., & Kneib, J.-P. 2005, *An interferometric CO survey of luminous submillimetre galaxies*, MNRAS, 359, 1165

Hackenberg, W., Eckart, A., Davies, R. I., Rabien, S., Ott, T., Kasper, M., Hippler, S., & Quirrenbach, A. 2000, *Near-infrared adaptive optics observations of galaxy clusters: Abell 262 at z=0.0157, J1836.3CR at z=0.414, and PKS 0743-006 at z=0.994*, A&A, 363, 41

Haynes, M. P. & Giovanelli, R. 1984, *Neutral hydrogen in isolated galaxies. IV – Results for the Arecibo sample*, AJ, 89, 758

—. 1986, *The connection between Pisces-Perseus and the Local Supercluster*, ApJ, 306, L55

Haynes, M. P., Giovanelli, R., Herter, T., Vogt, N. P., Freudling, W., Maia, M. A. G., Salzer, J. J., & Wegner, G. 1997, *21 cm H1 Line Spectra of Galaxies in Nearby Clusters*, AJ, 113, 1197

Heckman, T. M., Blitz, L., Wilson, A. S., Armus, L., & Miley, G. K. 1989, *A millimeter-wave survey of CO emission in Seyfert galaxies*, ApJ, 342, 735

Helfer, T. T., Vogel, S. N., Lugten, J. B., & Teuben, P. J. 2002, *Imaging Simulations of Large-Scale Flux Recovery at Millimeter Wavelengths*, PASP, 114, 350

Helou, G. 1986, *The IRAS colors of normal galaxies*, ApJ, 311, L33

Helou, G., Khan, I. R., Malek, L., & Boehmer, L. 1988, *IRAS observations of galaxies in the Virgo cluster area*, ApJS, 68, 151

Hill, J. M., Green, R. F., & Slagle, J. H. 2006, *The Large Binocular Telescope*, in Proc. SPIE, Vol. 6267, Ground-based and Airborne Telescopes, 62670Y

Hill, J. M. & Salinari, P. 2004, *The Large Binocular Telescope project*, in Proc. SPIE, Vol. 5489, Ground-based Telescopes, ed. J. M. Oschmann, Jr., 603–614

Hofmann, K.-H., Driebe, T., Heininger, M., Schertl, D., & Weigelt, G. 2005, *Reconstruction of aperture-synthesis images from LBT LINC-NIRVANA data using the Richardson-Lucy and space-variant Building Block method*, A&A, 444, 983

Horellou, C., Casoli, F., Combes, F., & Dupraz, C. 1995a, *The CO emission of ring galaxies.*, A&A, 298, 743

Horellou, C., Casoli, F., & Dupraz, C. 1995b, *The CO and HI emission of spiral and lenticular galaxies in the Fornax cluster.*, A&A, 303, 361

Huber, P.J. 1981, Robust Statistics (New York: Wiley-Interscience)

Ishimaru, A. 1978, Wave Propagation and Scattering in Random Media (New York: Academic)

Israel, F. 2001, *Extragalactic H_2 and its Variable Relation to CO*, in Molecular hydrogen in space, ed. F. Combes & G. Pineau des Forêts (Cambridge, UK: Cambridge University Press), 293

Israel, F. P. 1997, *H_2 and its relation to CO in the LMC and other magellanic irregular galaxies*, A&A, 328, 471

Jackson, J. M., Eckart, A., Cameron, M., Wild, W., Ho, P. T. P., Pogge, R. W., & Harris, A. I. 1991, *The interstellar medium of the hot-spot galaxy NGC 2903*, ApJ, 375, 105

Jones, C. & Forman, W. 1984, *The structure of clusters of galaxies observed with Einstein*, ApJ, 276, 38

Kellerer, A. & Tokovinin, A. 2007, *Atmospheric coherence times in interferometry: definition and measurement*, A&A, 461, 775

Kenney, J. D. P. & Young, J. S. 1989, *The effects of environment on the molecular and atomic gas properties of large Virgo cluster spirals*, ApJ, 344, 171

Köhler, T., Groote, D., Reimers, D., & Wisotzki, L. 1997, *The local luminosity function of QSOs and Seyfert 1 nuclei.*, A&A, 325, 502

Kolmogorov, A. N. 1961, *The local structure of turbulence in incompressible viscous fluids for very large Reynolds numbers*, in Turbulence, Classic Papers on Statistical Theory, ed. S. K. Friedlander & L. Topper (New York: Wiley-Interscience), 151–155

Krips, M., Eckart, A., Neri, R., Bertram, T., Straubmeier, C., Fischer, S., Staguhn, J. G., & Vogel, S. N. 2007, *Barred CO emission in HE 1029-1831*, A&A, 464, 187

Labeyrie, A. 1970, *Attainment of diffraction limited resolution in large telescopes by Fourier analysing speckle patterns in star images*, A&A, 6, 85

Laun, W., Baumeister, H., & Bizenberger, P. 2006, *The LINC-NIRVANA IR cryostat*, in Proc. SPIE, Vol. 6269, Ground-based and Airborne Instrumentation for Astronomy, ed. I. S. McLean & M. Iye, 626956

Lavezzi, T. E. & Dickey, J. M. 1998, *Observations of ^{12}CO (J = 1–0) in 44 cluster galaxies*, AJ, 115, 405

Lawrence, A., Rowan-Robinson, M., Ellis, R. S., Frenk, C. S., Efstathiou, G., Kaiser, N., Saunders, W., Parry, I. R., Xiaoyang, X., & Crawford, J. 1999, *The QDOT all-sky IRAS galaxy redshift survey*, MNRAS, 308, 897

Linfield, R. P., Colavita, M. M., & Lane, B. F. 2001, *Atmospheric Turbulence Measurements with the Palomar Testbed Interferometer*, ApJ, 554, 505

MacKenzie, M., Schlegel, E. M., & Mushotzky, R. 1996, *Broad Band X-Ray Telescope Observations of the Clusters of Galaxies Abell 262 and Abell 496*, ApJ, 468, 86

Maiolino, R., Ruiz, M., Rieke, G. H., & Papadopoulos, P. 1997, *Molecular Gas, Morphology, and Seyfert Galaxy Activity*, ApJ, 485, 552

Mariotti, J.-M. 1992, *Prospects for Earth-based interferometry*, in ESA Special Publication, Vol. 354, Targets for Space-Based Interferometry, ed. C. Mattok, 35–41

Moshir, M. et al. 1990, IRAS Faint Source Catalogue, Version 2.0 (Passadena: JPL)

Moss, C. & Whittle, M. 2000, *An Hα survey of eight Abell clusters: the dependence of tidally induced star formation on cluster density*, MNRAS, 317, 667

Neill, J. D., Brodie, J. P., Craig, W. W., Hailey, C. J., & Misch, A. A. 2001, *The Beta Problem: A Study of Abell 262*, ApJ, 548, 550

Nightingale, N. S. & Buscher, D. F. 1991, *Interferometric seeing measurements at the La Palma Observatory*, MNRAS, 251, 155

Nilson, P. 1973, *Uppsala General Catalogue of Galaxies*, Universitatis Upsalienis, Nova Acta Regiae Societatis Upsaliensis, Series V: A, Vol. 1

Noll, R. 1976, *Zernike polynomials and atmospheric turbulence*, JOSA, 66, 207

Papadopoulos, P. P. & Seaquist, E. R. 1998, *Physical Conditions of the Molecular Gas in Seyfert Galaxies*, ApJ, 492, 521

Press, W. H., Teukolsky, S. A., Vetterling, W. T., & Flannery, B. P. 2002, Numerical Recipes in C++ : the art of scientific computing (Cambridge, New York, Melbourne, Madrid, Cape Town: Cambridge University Press)

Ragazzoni, R. 1996, *Pupil plane wavefront sensing with an oscillating prism*, Journal of Modern Optics, 43, 289

Ragazzoni, R., Farinato, J., & Marchetti, E. 2000, *Adaptive optics for 100-m-class telescopes: new challenges require new solutions*, in Proc. SPIE, Vol. 4007, Adaptive Optical Systems Technology, ed. P. L. Wizinowich, 1076–1087

Reimers, D., Köhler, T., & Wisotzki, L. 1996, *The Hamburg/ESO survey for bright QSOs. II. Follow-up spectroscopy of 160 quasars and Seyferts*, A&AS, 115, 235

Rice, W., Lonsdale, C. J., Soifer, B. T., Neugebauer, G., Kopan, E. L., Lloyd, L. A., de Jong, T., & Habing, H. J. 1988, *A catalog of IRAS observations of large optical galaxies*, ApJS, 68, 91

Riechers, D. A., Walter, F., Carilli, C. L., Knudsen, K. K., Lo, K. Y., Benford, D. J., Staguhn, J. G., Hunter, T. R., Bertoldi, F., Henkel, C., Menten, K. M., Weiss, A., Yun, M. S., & Scoville, N. Z. 2006, *CO(1-0) in $z \gtrsim 4$ Quasar Host Galaxies: No Evidence for Extended Molecular Gas Reservoirs*, ApJ, 650, 604

Roggemann, M. C., Welsh, B. M., & Fugate, R. Q. 1997, *Improving the resolution of ground-based telescopes*, Reviews of Modern Physics, 69, 437

Rohloff, R. R. 2005, *Piston Mirror Unit*, Tech. Rep. LN-MPIA-FDR-MECH-002, MPIA, Heidelberg, Germany

Rost, S., Bertram, T., Straubmeier, C., Wang, Y., & Eckart, A. 2006, *The LINC-NIRVANA fringe and flexure tracker: piston control strategies*, in Proc. SPIE, Vol. 6274, Advanced Software and Control for Astronomy, ed. H. Lewis & A. Bridger, 62741P

Rowan-Robinson, M. 1992, *Interstellar dust in galaxies*, MNRAS, 258, 787

Sage, L. J. 1993, *Molecular gas in nearby galaxies – I. CO observations of a distance-limited sample*, A&A, 272, 123

Sanders, D. B., Mazzarella, J. M., Kim, D.-C., Surace, J. A., & Soifer, B. T. 2003, *The IRAS Revised Bright Galaxy Sample*, AJ, 126, 1607

Sanders, D. B. & Mirabel, I. F. 1996, *Luminous Infrared Galaxies*, ARA&A, 34, 749

Sanders, D. B., Phinney, E. S., Neugebauer, G., Soifer, B. T., & Matthews, K. 1989, *Continuum energy distribution of quasars - Shapes and origins*, ApJ, 347, 29

Sanders, D. B., Scoville, N. Z., & Soifer, B. T. 1991, *Molecular gas in luminous infrared galaxies*, ApJ, 370, 158

Sanders, D. B., Scoville, N. Z., Young, J. S., Soifer, B. T., Schloerb, F. P., Rice, W. L., & Danielson, G. E. 1986, *Molecular gas in high-luminosity IRAS galaxies*, ApJ, 305, L45

Sanders, D. B., Soifer, B. T., Elias, J. H., Madore, B. F., Matthews, K., Neugebauer, G., & Scoville, N. Z. 1988, *Ultraluminous infrared galaxies and the origin of quasars*, ApJ, 325, 74

Schmidt, M. & Green, R. F. 1983, *Quasar evolution derived from the Palomar bright quasar survey and other complete quasar surveys*, ApJ, 269, 352

Scoville, N. Z., Frayer, D. T., Schinnerer, E., & Christopher, M. 2003, *The Host Galaxies of Optically Bright Quasi-stellar Objects: Molecular Gas in z≤0.1 Palomar-Green Quasi-stellar Objects*, ApJ, 585, L105

Scoville, N. Z., Sargent, A. I., Sanders, D. B., & Soifer, B. T. 1991, *Dust and gas in the core of ARP 220 (IC 4553)*, ApJ, 366, L5

Solanes, J. M., Manrique, A., García-Gómez, C., González-Casado, G., Giovanelli, R., & Haynes, M. P. 2001, *The H I Content of Spirals. II. Gas Deficiency in Cluster Galaxies*, ApJ, 548, 97

Solomon, P. M. & Barrett, J. W. 1991, *The CO – H_2 Mass Conversion Factor*, in IAU Symp. 146: Dynamics of Galaxies and Their Molecular Cloud Distributions, ed. F. Combes & F. Casoli, 235

Solomon, P. M., Downes, D., & Radford, S. J. E. 1992a, *Warm molecular gas in the primeval galaxy IRAS 10214 + 4724*, ApJ, 398, L29

Solomon, P. M., Downes, D., Radford, S. J. E., & Barrett, J. W. 1997, *The Molecular Interstellar Medium in Ultraluminous Infrared Galaxies*, ApJ, 478, 144

Solomon, P. M., Radford, S. J. E., & Downes, D. 1992b, *Molecular gas content of the primaeval galaxy IRAS 10214 + 4724*, Nature, 356, 318

Solomon, P. M. & Sage, L. J. 1988, *Star-formation rates, molecular clouds, and the origin of the far-infrared luminosity of isolated and interacting galaxies*, ApJ, 334, 613

Staguhn, J. G., Schinnerer, E., Eckart, A., & Scharwächter, J. 2004, *Resolving the Host Galaxy of the Nearby QSO I Zw 1 with Subarcsecond Multitransition Molecular Line Observations*, ApJ, 609, 85

Stark, A. A., Knapp, G. R., Bally, J., Wilson, R. W., Penzias, A. A., & Rowe, H. E. 1986, *Molecules in galaxies. III - The Virgo cluster*, ApJ, 310, 660

Strong, A. W., Bloemen, J. B. G. M., Dame, T. M., Grenier, I. A., Hermsen, W., Lebrun, F., Nyman, L.-A., Pollock, A. M. T., & Thaddeus, P. 1988, *The radial distribution of galactic gamma rays. IV - The whole galaxy*, A&A, 207, 1

Strong, M., Pedlar, A., Aalto, S., Beswick, R. J., Curran, S., & Booth, R. 2004, *Molecular gas properties of 12-μm Seyfert galaxies - I. The southern sample*, MNRAS, 353, 1151

Struble, M. F. & Rood, H. J. 1999, *A Compilation of Redshifts and Velocity Dispersions for ACO Clusters*, ApJS, 125, 35

Tacconi, L. J., Neri, R., Chapman, S. C., Genzel, R., Smail, I., Ivison, R. J., Bertoldi, F., Blain, A., Cox, P., Greve, T., & Omont, A. 2006, *High-Resolution Millimeter Imaging of Submillimeter Galaxies*, ApJ, 640, 228

Traub, W. A. 1986, *Combining beams from separated telescopes*, Applied Optics, 25, 528

Véron-Cetty, M.-P. & Véron, P. 1996, A Catalogue of quasars and active nuclei, ESO Scientific Report, 7th edn. (Garching, Germany: European Southern Observatory)

Véron-Cetty, M.-P. & Véron, P. 2006, *A catalogue of quasars and active nuclei: 12th edition*, A&A, 455, 773

Vila-Vilaró, B., Taniguchi, Y., & Nakai, N. 1998, *CO Survey of a Distance-limited Seyfert Sample. I. The Data*, AJ, 116, 1553

Vollmer, B., Braine, J., Balkowski, C., Cayatte, V., & Duschl, W. J. 2001, *^{12}CO(1-0) observations of NGC 4848: A Coma galaxy after stripping*, A&A, 374, 824

Wang, Y., Bertram, T., Straubmeier, C., Rost, S., & Eckart, A. 2006, *The LINC-NIRVANA fringe and flexure tracker: Linux real-time solutions*, in Proc. SPIE, Vol. 6274, Advanced Software and Control for Astronomy, ed. H. Lewis & A. Bridger, 62741O

Wisotzki, L., Christlieb, N., Bade, N., Beckmann, V., Köhler, T., Vanelle, C., & Reimers, D. 2000, *The Hamburg/ESO survey for bright QSOs. III. A large flux-limited sample of QSOs*, A&A, 358, 77

Yao, L., Seaquist, E. R., Kuno, N., & Dunne, L. 2003, *CO Molecular Gas in Infrared-luminous Galaxies*, ApJ, 588, 771

Young, J. S., Xie, S., Tacconi, L., Knezek, P., Viscuso, P., Tacconi-Garman, L., Scoville, N., Schneider, S., Schloerb, F. P., Lord, S., Lesser, A., Kenney, J., Huang, Y., Devereux, N., Claussen, M., Case, J., Carpenter, J., Berry, M., & Allen, L. 1995, *The FCRAO Extragalactic CO Survey. I. The Data*, ApJS, 98, 219

List of Figures

List of Tables

Danksagung

Die Dissertation ist geschrieben und damit einige Jahre voll spannender Arbeit zu Papier gebracht. An dieser Stelle möchte ich mich herzlich bei allen bedanken, die auf die ein oder andere Weise an dieser Arbeit mitgewirkt und zu ihrem erfolgreichen Abschluss beigetragen haben.

An erster Stelle danke ich meinem Doktorvater, Herrn Prof. Dr. Andreas Eckart, der mir die Möglichkeit gegeben hat, die Arbeit in seiner Gruppe anzufertigen. Ich habe von der Vielzahl an Ideen und kreativen Lösungsansätzen, aber auch von der humorvollen Atmosphäre der Zusammenarbeit sehr profitiert.

Bedanken möchte ich mich des weiteren bei:

Christian Straubmeier, der mir stets mit Rat, Tat und inspirierenden Diskussionen zur Seite stand, nicht nur, aber gerade auch in der Pionierphase des FFTS.

der Kölner FFTS Mannschaft, die zum Glück in letzter Zeit um einige Mitglieder gewachsen ist und mit deren Hilfe nun viele Fortschritte an den zahlreichen Baustellen des FFTS erzielt werden. Vielen Dank an Bettina Lindhorst, Steffen Rost, Yeping Wang, Imke Wank und an Gunther Witzel.

der Feinmechanikwerkstatt unter der Leitung von Herrn Matthias Mondt für die stets kompetente Beratung und die zügige und perfekte Bearbeitung der unterschiedlichsten Aufträge. Die Zusammenarbeit hat immer ausgesprochen gut funktioniert.

Herrn Prof. Dr. J. Jolie, der sich bereit erklärt hat, das Zweitgutachten zu übernehmen, bei Herrn Prof. Dr. J. Saur für die Übernahme des Prüfungsvorsitzes und bei Frau Prof. apl. Dr. S. Pfalzner für die Übernahme des Prüfungsbeisitzes.

Many thanks to Carmelo Arcidiacono who never was lost when dealing with LOST. In various sessions in Cologne, Florence and Garching he helped to answer the questions discussed in Chapter 2 by adapting his code, providing examples, discussing results etc.

Sebastian Egner für die Bereitstellung der C_n^2 Profile und für die Diskussionen im Zusammenhang mit den Atmosphärenparametern.

Many thanks to the staff of the IRAM 30 m telescope and to KUNO Nario from the Nobeyama Radio Observatory for their support during the observations.

der Ingenieursriege des MPIA, speziell Harald Baumeister, Peter Bizenberger, Mario Brix, Werner Laun und Lars Mohr für die zahlreichen Diskussionen und Hilfestellungen im Zusammenhang mit der Realisierung der Hardware des FFTS.

Christian Straubmeier, Sabine König, Sebastian Fischer, Steffen Rost und Bettina Lindhorst für das intensive Korrekturlesen der Arbeit.

dem "OoE", Jens Zuther, Sabine König und Sebastian Fischer für die gute Stimmung, die zahlreichen Diskussionen und die exzellenten Antworten auf viele spontan gestellte Fragen.

der "aegroup" für die ausgesprochen gute Atmosphäre.

meinen Eltern, ohne deren Unterstützung in vielerlei Hinsicht das Studium und die Arbeit nicht möglich gewesen wären.

Ein besonders großer und liebevoller Dank geht an meine Frau Sünne, die mich immer unterstützt hat in dem, was ich tue, mich aufgemuntert hat, wenn Dinge nicht auf Anhieb funktioniert haben und dabei sicherlich auch einiges ertragen musste. Danke für die Geduld und das Verständnis!

Erklärung

Ich versichere, dass ich die von mir vorgelegte Dissertation selbständig angefertigt, die benutzten Quellen und Hilfsmittel vollständig angegeben und die Stellen der Arbeit – einschließlich Tabellen, Karten und Abbildungen –, die anderen Werken im Wortlaut oder dem Sinn nach entnommen sind, in jedem Einzelfall als Entlehnung kenntlich gemacht habe; dass diese Dissertation noch keiner anderen Fakultät oder Universität zur Prüfung vorgelegen hat; dass sie – abgesehen von unten angegebenen Teilpublikationen – noch nicht veröffentlicht worden ist sowie, dass ich eine solche Veröffentlichung vor Abschluss des Promotionsverfahrens nicht vornehmen werde. Die Bestimmungen dieser Promotionsordnung sind mir bekannt. Die von mir vorgelegte Dissertation ist von Herrn Prof. Dr. Andreas Eckart betreut worden.

Köln, den 28. August 2007

Teile der Dissertation sind in den folgenden Publikationen enthalten:

Bertram, T., Eckart, A., Fischer, S., Zuther, J., Straubmeier, C., Wisotzki, L., & Krips, M. 2007, *Molecular gas in nearby low-luminosity QSO host galaxies*, A&A, 470, 571

Bertram, T., Arcidiacono, C., Straubmeier, C., Rost, S., Wang, Y., & Eckart, A. 2006a, *The LINC-NIRVANA fringe and flexure tracker: image analysis concept and fringe tracking performance estimate*, in Proc. SPIE, Vol. 6268, Advances in Stellar Interferometry, ed. J. D. Monnier, M. Schöller, & W. C. Danchi, 62683P

Bertram, T., Baumeister, H., Laun, W., Straubmeier, C., Rost, S., Wang, Y., & Eckart, A. 2006b, *The LINC-NIRVANA fringe and flexure tracker: cryo-ambient mechanical design*, in Proc. SPIE, Vol. 6268, Advances in Stellar Interferometry, ed. J. D. Monnier, M. Schöller, & W. C. Danchi, 62683L

Bertram, T., Eckart, A., Krips, M., Staguhn, J. G., & Hackenberg, W. 2006c, *Molecular gas in the galaxy cluster Abell 262. CO observations of UGC 1347 and other galaxies of the cluster*, A&A, 448, 29

Weitere Veröffentlichungen:

Krips, M., Eckart, A., Neri, R., Bertram, T., Straubmeier, C., Fischer, S., Staguhn, J. G., & Vogel, S. N. 2007, *Barred CO emission in HE 1029-1831*, A&A, 464, 187

Zuther, J., Iserlohe, C., Pott, J.-U., Bertram, T., Fischer, S., Voges, W., Hasinger, G., & Eckart, A. 2007, *Mrk 609: resolving the circumnuclear structure with near-infrared integral field spectroscopy*, A&A, 466, 451

Bertram, T., Eckart, A., Krips, M., Straubmeier, C., Fischer, S., & Staguhn, J. G. 2006d, *Molecular gas in QSO host galaxies*, New Astronomy Review, 50, 712

Briegel, F., Berwein, J., Kittmann, F., Volchkov, V., Mohr, L., Gaessler, W., Bertram, T., Rost, S., & Wang, Y. 2006, *The LINC-NIRVANA Common Software*, in Proc. SPIE, Vol. 6274, Advanced Software and Control for Astronomy, ed. H. Lewis & A. Bridger, 62741M

Eckart, A., Schödel, R., Straubmeier, C., Bertram, T., Pott, J.-U., Muzic, K., Meyer, L., Moultaka, J., Viehmann, T., Rost, S., & Herbst, T. 2006, *Interferometric observations of the galactic center: LBT and VLTI*, in Proc. SPIE, Vol. 6268, Advances in Stellar Interferometry, ed. J. D. Monnier, M. Schöller, & W. C. Danchi, 62681J

Fischer, S., Iserlohe, C., Zuther, J., Bertram, T., Straubmeier, C., & Eckart, A. 2006a, *NIR imaging and spectroscopy of AGN hosts at $z \leq 0.06$*, New Astronomy Review, 50, 736

Fischer, S., Iserlohe, C., Zuther, J., Bertram, T., Straubmeier, C., Schödel, R., & Eckart, A. 2006b, *Nearby AGN and their hosts in the near infrared*, A&A, 452, 827

Rost, S., Bertram, T., Straubmeier, C., Wang, Y., & Eckart, A. 2006, *The LINC-NIRVANA fringe and flexure tracker: piston control strategies*, in Proc. SPIE, Vol. 6274, Advanced Software and Control for Astronomy, 62741P

Straubmeier, C., Bertram, T., Eckart, A., Rost, S., Wang, Y., Herbst, T., Ragazzoni, R., & Weigelt, G. 2006, *The imaging fringe and flexure tracker of LINC-NIRVANA: basic opto-mechanical design and principle of operation*, in Proc.

SPIE, Vol. 6268, Advances in Stellar Interferometry, ed. J. D. Monnier, M. Schöller, & W. C. Danchi, 62681I

Wang, Y., Bertram, T., Straubmeier, C., Rost, S., & Eckart, A. 2006, *The LINC-NIRVANA fringe and flexure tracker: Linux real-time solutions*, in Proc. SPIE, Vol. 6274, Advanced Software and Control for Astronomy, ed. H. Lewis & A. Bridger, 62741O

Bertram, T., Eckart, A., Krips, M., & Staguhn, J. 2005, *Molecular Gas in the Abell 262 Cluster Galaxy Ugc 1347*, Ap&SS, 295, 303

Krips, M., Eckart, A., Neri, R., Pott, J.-U., Zuther, J., Scharwächter, J., & Bertram, T. 2005, *Feeding Monsters - A Study of Active Galaxies*, Ap&SS, 295, 95

Zuther, J., Eckart, A., Voges, W., Bertram, T., & Straubmeier, C. 2005, *Selection of Extragalactic Targets for AO and VLTI Observations*, in Science with Adaptive Optics, ed. W. Brandner & M. E. Kasper, pp 375

Andersen, D. R., Bertram, T., Bizenberger, P., Egner, S., Herbst, T. M., Ragazzoni, R., & Straubmeier, C. 2004, *The LINC-NIRVANA testbed Fizeau interferometer*, in Proc. SPIE, Vol. 5491, New Frontiers in Stellar Interferometry, ed. W. A. Traub, pp 1760

Bertram, T., Andersen, D. R., Arcidiacono, C., Straubmeier, C., Eckart, A., Beckmann, U., & Herbst, T. M. 2004, *The LINC-NIRVANA fringe and flexure tracking system: differential piston simulation and detection*, in Proc. SPIE, Vol. 5491, New Frontiers in Stellar Interferometry, ed. W. A. Traub, pp 1454

Eckart, A., Zuther, J., Mouawad, N., Schodel, R., Straubmeier, C., Bertram, T., Pott, J.-U., Scharwachter, J., & Herbst, T. M. 2004, *Scientific potential for LINC NIRVANA observations of galactic nuclei*, in Proc. SPIE, Vol. 5491, New Frontiers in Stellar Interferometry, ed. W. A. Traub, pp 106

Gaessler, W., Bertram, T., Briegel, F., Driebe, T. M., Heininger, M., Nussbaum, E., Storz, C., Wang, J., Zealouk, L., Herbst, T. M., Ragazzoni, R., Eckart, A., & Weigelt, G. P. 2004, *UML modeling of the LINC-NIRVANA control software*, in Proc. SPIE, Vol. 5496, Advanced Software, Control, and Communication Systems for Astronomy, ed. H. Lewis & G. Raffi, 79–87

Straubmeier, C., Bertram, T., Eckart, A., & Herbst, T. 2004a, *LINC-NIRVANA - The Interferometric Near-Infrared Imaging Camera for the Large Binocular Telescope*, in The Dense Interstellar Medium in Galaxies, ed. S. Pfalzner, C. Kramer, C. Staubmeier, & A. Heithausen, pp 317

Straubmeier, C., Bertram, T., Eckart, A., Wang, Y., Zealouk, L., Herbst, T. M., Andersen, D. R., Ragazzoni, R., & Weigelt, G. P. 2004b, *The fringe and flexure tracking system for LINC-NIRVANA: basic design and principle of operation*, in Proc. SPIE, Vol. 5491, New Frontiers in Stellar Interferometry, ed. W. A. Traub, pp 1486

Eckart, A., Bertram, T., Mouawad, N., Viehmann, T., Straubmeier, C., & Zuther, J. 2003, *Long Range Science Perspectives for the VLTI*, Ap&SS, 286, 269

Straubmeier, C., Eckart, A., Bertram, T., Zealouk, L., & Wang, Y. 2003, *The correction of pistonic aberrations at the LBT: A near-infrared Fringe and Flexure Tracker for LINC*, in Proc. SPIE, Vol. 4838, Interferometry for Optical Astronomy II, ed. W. A. Traub, 1271–1281

Eckart, A., Mouawad, N., Krips, M., Straubmeier, C., & Bertram, T. 2002, *Scientific potential for interferometric observations of the Galactic Center*, in Proc. SPIE, Vol. 4835, Future Research Direction and Visions for Astronomy, ed. A. M. Dressler, 12–21